COOL STAR MAGNETIC FIELD TOPOLOGIES

CONNECTING SIMULATIONS AND OBSERVATIONS FOR SOLAR-LIKE STARS

Lisa Theres Lehmann

A Thesis Submitted for the Degree of PhD
at the
University of St Andrews

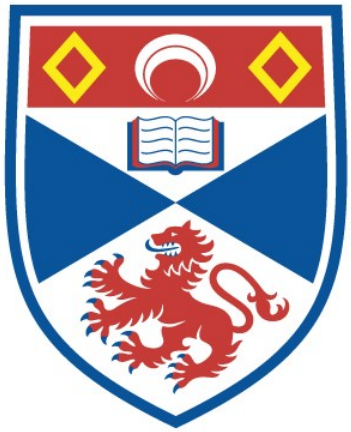

2020

Cool star magnetic field topologies

Connecting simulations and observations for solar-like stars

by

Lisa Theres Lehmann

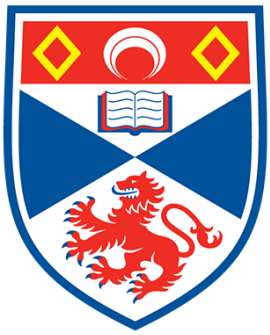

University of
St Andrews

This thesis is submitted in partial fulfilment for the degree of
Doctor of Philosophy (PhD)
at the University of St Andrews

September 2019

Declaration

I, Lisa Theres Lehmann, do hereby certify that this thesis, submitted for the degree of PhD, which is approximately 47,000 words in length, has been written by me, and that it is the record of work carried out by me, or principally by myself in collaboration with others as acknowledged, and that it has not been submitted in any previous application for any degree.

I was admitted as a research student at the University of St Andrews in November 2015.

I received funding from an organisation or institution and have acknowledged the funder(s) in the full text of my thesis.

27th September 2019

Date Signature of candidate

I hereby certify that the candidate has fulfilled the conditions of the Resolution and Regulations appropriate for the degree of PhD in the University of St Andrews and that the candidate is qualified to submit this thesis in application for that degree.

27 Sept 2019

Date Signature of supervisor

Permission for publication

In submitting this thesis to the University of St Andrews we understand that we are giving permission for it to be made available for use in accordance with the regulations of the University Library for the time being in force, subject to any copyright vested in the work not being affected thereby. We also understand, unless exempt by an award of an embargo as requested below, that the title and the abstract will be published, and that a copy of the work may be made and supplied to any bona fide library or research worker, that this thesis will be electronically accessible for personal or research use and that the library has the right to migrate this thesis into new electronic forms as required to ensure continued access to the thesis.

I, Lisa Theres Lehmann, have obtained, or am in the process of obtaining, third-party copyright permissions that are required or have requested the appropriate embargo below.

The following is an agreed request by candidate and supervisor regarding the publication of this thesis:

Printed copy

No embargo on print copy.

Electronic copy

Embargo on part (Chapter 5) of electronic copy for a period of 2 years on the following ground(s):

- Publication would preclude future publication

Supporting statement for electronic embargo request

The publication of the Chapter 5 is in progress and will be submitted soon.

Title and Abstract

- I agree to the title and abstract being published.

27th September 2019

Date Signature of candidate

27 Sept 2019

Date Signature of supervisor

Underpinning research data or digital outputs

Candidate's declaration

I, Lisa Theres Lehmann, understand that by declaring that I have original research data or digital outputs, I should make every effort in meeting the University's and research funders' requirements on the deposit and sharing of research data or research digital outputs.

27th September 2019

Date Signature of candidate

Permission for publication of underpinning research data or digital outputs

We understand that for any original research data or digital outputs which are deposited, we are giving permission for them to be made available for use in accordance with the requirements of the University and research funders, for the time being in force.

We also understand that the title and the description will be published, and that the underpinning research data or digital outputs will be electronically accessible for use in accordance with the license specified at the point of deposit, unless exempt by award of an embargo as requested below.

The following is an agreed request by candidate and supervisor regarding the publication of underpinning research data or digital outputs:

No embargo on underpinning research data or digital outputs.

27th September 2019

Date Signature of candidate

27 Sept 2019

Date Signature of supervisor

Collaboration statement

This thesis is the result of my own work conducted at the University of St Andrews between November 2015 and September 2019. Parts of the work presented here have been published in scientific journals as part of the peer review process. The whole text in this thesis is written entirely by me as well as all figures in this thesis are produced by me unless explicitly stated in the figure's caption.

- Chapter 3 is based on: *"The energy budget of stellar magnetic fields: comparing non-potential simulations and observations"*, L. T. Lehmann, M. M. Jardine, A. A. Vidotto, D. H. Mackay, V. See, J.-F. Donati, C. P. Folsom, S. V. Jeffers, S. C. Marsden, J. Morin, P. Petit, 2017, Monthly Notices of the Royal Astronomical Society, 446, L24-L28 and on *"Connecting the large- and the small-scale magnetic fields of solar-like stars"*, L. T. Lehmann, M. M. Jardine, D. H. Mackay, A. A. Vidotto, 2018, Monthly Notices of the Royal Astronomical Society, 478, 4390-4409. The photospheric magnetic field maps from the 3D non-potential flux transport simulations were provided by D. H. Mackay. All required codes for the analysis are written by me. All co-authors provided comments on the final manuscript.

- Chapter 4 is based on: *"Observing the simulations: applying ZDI to 3D non-potential magnetic field simulations"*, L. T. Lehmann, G. A. J. Hussain, M. M. Jardine, D. H. Mackay, A. A. Vidotto, 2019, Monthly Notices of the Royal Astronomical Society, 483, 5246-5266. The photospheric magnetic field maps from the 3D non-potential flux transport simulations were provided by D. H. Mackay. The Zeeman-Doppler-Imaging code was provided by G. A. J. Hussain which I adapted and run to model the Stokes profiles and to determine the resulting magnetic field maps. All required codes for the analysis are written by me. All co-authors provided comments on the final manuscript.

- Chapter 5 will be submitted as *"The magnetic field vector of the Sun-as-a-star – III. Evolution of the large-scale vector field of the 3D non-potential flux-transport simulated activity cycle 23 and its reconstruction with ZDI"*, L. T. Lehmann, G. A. J. Hussain, A. A. Vidotto, M. M. Jardine, D. H. Mackay to Monthly Notices of the Royal Astronomical Society. The

photospheric magnetic field maps from the 3D non-potential flux transport simulations were provided by D. H. Mackay. The Zeeman-Doppler-Imaging code was provided by G. A. J. Hussain which I adapted and run to model the Stokes profiles and to determine the resulting magnetic field maps. A. A. Vidotto provided scientific advice mainly in context of the comparison with the observations of solar cycle 24. All required codes for the analysis are written by me.

Abstract

Good knowledge about cool star magnetic activity, topology and cycles is crucial to find a second solar system and to better understand ours. The Zeeman-Doppler-Imaging (ZDI) surveys, which unveil the stellar magnetic field topology, have now run for long enough to detect solar-like activity cycles. This is a good point to review what ZDI detects robustly and how to interpret the resulting ZDI maps. As ZDI only detects the large-scale magnetic field an important question to answer is: What can we learn from the large-scale field topology about the small-scale field for solar-like stars?

I connect 3D non-potential flux transport simulations based on the Sun with the observational ZDI technique. First, I decomposed the magnetic field topology of the simulations into different length-scales. I discovered that the large-scale field reflects global properties of the small-scale field emergence for slowly-rotating solar-like stars. Second, I used synthetic line profiles modelled from the simulations as input for ZDI. I showed that ZDI can recover the hints of the small-scale flux emergence in the observable large-scale field for slow rotators but recovers approximately one order of magnitude lower magnetic energy. The maximum entropy regularisation used in ZDI prevents the correct reconstruction of the magnetic energy distribution but ZDI can recover the fractions of the different field components reasonably well.

To examine if ZDI can recover solar-like cycles, I applied ZDI to non-potential flux transport simulations modelling the solar magnetic field over 15 years. I discovered that the axisymmetric poloidal fraction and the axi- and non-axisymmetric energy are the best parameters to track solar-like activity cycles while the averaged large-scale field or the total energy show no or misleading trends.

Acknowledgements

General acknowledgements

My biggest thanks need to go to my supervisor Professor Moira Jardine. I could not imagine a better supervisor than she has been for me during my whole stay and especially in the last year of my PhD. Her constant enthusiasm to solve and to investigate each detail of a scientific problem combined with her constant support and understanding makes her a role-model of a supervisor. I am extremely grateful that I got the chance to do my PhD under her supervision.

Further, this PhD project would not have been so successful without the constant support and the fruitful discussions with Gaitee Hussain, Duncan Mackay and Aline Vidotto. Thank you very much for introducing me to your topics and your support and advice during the writing process of the papers and PhD thesis.

I also would like to thank my office mates and friends in St Andrews filling my PhD time with lots of laughs and curios discussions. Especially thanks to Carolina but also to Nina, Gerardo, Nicole, Gabi, Kirstin, Laith, Victor and Rose. Also a big thank you to my best friends Anne and Lisa standing beside me especially during the writing process of this thesis.

Thank you, Eugen, for always believing in me, especially if I don't believe in me. Thanks for going through all ups and downs of my (PhD) life, for encouraging and grounding me again and again and for making our time in Scotland so joyful.

Life occurs and next to the happiest event also the hardest time of my life started. I would not be able to write these words without the huge support of my parents and my mother-in-law and the great help of Christiane and Peter in the beginning. Especially, I want to thank my father proofing ones more that he is always there and undoubtedly supports me wherever I am.

For the bottom of my heart, I want to thank my mother for her unfailing support and encouragement during my whole life and especially during the last year. I would not have achieved to dream my dream without your heartening. I am more grateful than I can ever express.

Funding

I acknowledge support from the Scottish Universities Physics Alliance (SUPA) prize studentship and the University of St Andrews Higgs studentship. Further, I received supplementary founding for travelling from SUPA and the European Southern Observatory (ESO) for a 8-weeks short term visit at the ESO Headquarters in 2017 and the ESO for supporting a second visit (1-month) in 2018. Further, I received a travel grant to visit the Cool Stars 20 Conference in Boston to present the work displayed in Chapter 4 from the Royal Astronomical Society (RAS).

Research Data/Digital Outputs access statement

Research data underpinning this thesis are available at https://doi.org/10.17630/ae078167-03ea-4af6-9055-c3147e13c286

For Annabell

Contents

List of Figures

List of Tables

1 Introduction

1.1 Motivation

The magnetic activity of stars plays a key role to answer topical questions in stellar evolution (e.g. Folsom et al. 2018), the behaviour of the stellar wind (e.g. Finley et al. 2019) or in exoplanet research (e.g. Klein & Donati 2019). The signal of an earth-like planet around a solar-like star has same amplitude as the signal coming from the host star's magnetic activity, Haywood et al. (2014). To detect a second earth or solar system and to better understand our own, we need a good and deep understanding about cool stars magnetic activity.

One open question is to find an explanation for the detection of strong, often dominant, toroidal fields on cool stars. They often appear in the shape of unidirectional azimuthal magnetic fields or even closed rings which is a completely different magnetic field topology as seen at our Sun. These azimuthal fields are observed for very active stars in the saturated dynamo regime (Donati et al., 1992; Donati & Brown, 1997) as well as for less active stars (e.g. Dunstone et al. 2008) and in several other spectral classes (e.g. Marsden et al. 2006b; Petit et al.

2008). Their origin is part of current research. Stellar winds were excluded by Jardine et al. (2013). Possible theories are grounded in the dynamo theory (e.g. Donati & Brown 1997; Brandenburg 2005; Brown et al. 2011), in the inter-network (e.g. Schüssler & Vögler 2008) or in star spots, as I analysed in my master thesis using a simple star spot model, (Lehmann, 2015).

The determination of magnetic field maps is possible due to the Zeeman-Doppler-Imaging technique (ZDI), which is able to detect the stellar large-scale field topology. However, we could show in See et al. (2019) that ZDI only observes less than 20 % of the total magnetic field of F, G, K and M dwarfs, see also Reiners & Basri (2009); Morin et al. (2010) for previous studies focusing on M dwarfs. It is difficult to interpret the large-scale field topologies if the majority of the magnetic field is hidden in the small-scale structures, see e.g. Johnstone et al. (2010); Arzoumanian et al. (2011); Lang et al. (2014). Stellar small-scale field distributions are still unknown but exoplanet studies start to unveil scale sizes and distributions of surface spots. For example a transiting planet can be used as probe to stellar surface structures, see e.g. Morris et al. (2017).

This raises questions about what ZDI robustly detects and how to interpret the observed large-scale field topologies. What can we learn from the large-scale field topology about the small-scale field distribution and how are they linked for solar-like stars? My PhD thesis aims to answer these questions. I am using solar-based 3D non-potential flux transport simulations to understand the link between solar-like small-scale flux emergence and their effects on the observable large-scale field, see Chapter 3. In the next step, I examine the detectability of the large-scale field topologies of solar-like stars with the ZDI technique, see Chapter 4. Finally, I investigate what would be the best strategy to observe solar-like activity cycles, see Chapter 5. My results will help by the interpretation of the stellar magnetic field maps and to find a second Sun in terms of activity (cycle).

Parts of the following sections are based on or paraphrased from the introductions of my publications.

1.2 Description of the magnetic field

In this section, I describe and derive the magnetic field equations on which the methods and techniques, applied in this thesis, are based. I am using the magnetic field description

grounded on the spherical harmonic modes and restrict the equations mostly to the stellar surface[1], see Section 1.2.1. In Section 1.2.2 I introduce the potential and non-potential field equations. The derivations in both sections can be found in many textbooks.

1.2.1 Magnetic field description using spherical harmonics

If no electric currents are present, Ampere's law can be written as $\nabla \times \mathbf{B} = 0$. The magnetic field is then potential. A potential magnetic field $\mathbf{B}$ defined as $\mathbf{B} = -\nabla\Psi$ must satisfy the Laplace equation,

$$\nabla^2\Psi = 0, \tag{1.1}$$

in any volume, where $\Psi(r,\theta,\phi)$ is a 3D flux function. Further Gauß's law ($\nabla \cdot \mathbf{B} = 0$) needs to be fulfilled. Magnetic fields are always divergence free as no magnetic monopoles exist.

I want to find a solution for Eq. 1.1 in spherical polar coordinates and use the spherical harmonics for this purpose. Laplace's Equation in spherical polar coordinates is

$$\nabla^2\Psi = \frac{1}{r^2}\frac{\partial}{\partial r}\left(r^2\frac{\partial\Psi}{\partial r}\right) + \frac{1}{r^2\sin\theta}\frac{\partial}{\partial\theta}\left(\sin\theta\frac{\partial\Psi}{\partial\theta}\right) + \frac{1}{r^2\sin^2\theta}\frac{\partial^2\Psi}{\partial\phi^2} = 0. \tag{1.2}$$

I insert the trial solution

$$\Psi(r,\theta,\phi) = R(r)\Theta(\theta)\Phi(\phi) \tag{1.3}$$

into Eq. 1.2 and multiply it by $\frac{r^2\sin^2\theta}{\Psi(r,\theta,\phi)}$. The result is:

$$\frac{\sin^2\theta}{R(r)}\frac{\partial}{\partial r}\left(r^2\frac{\mathrm{d}R(r)}{\mathrm{d}r}\right) + \frac{\sin\theta}{\Theta(\theta)}\frac{\partial}{\partial\theta}\left(\sin\theta\frac{\mathrm{d}\Theta(\theta)}{\mathrm{d}\theta}\right) + \underbrace{\frac{1}{\Phi(\phi)}\frac{\mathrm{d}^2\Phi(\phi)}{\mathrm{d}\phi^2}}_{\text{(I)}} = 0. \tag{1.4}$$

Term (I) only depends on ϕ and shall be set to $-m^2$

$$\frac{1}{\Phi(\phi)}\frac{\mathrm{d}^2\Phi(\phi)}{\mathrm{d}\phi^2} = -m^2. \tag{1.5}$$

The variable m must not be a function of any of the three variables r,θ,ϕ as

$$\underbrace{\frac{1}{\Phi(\phi)}\frac{\partial^2\Phi(\phi)}{\partial\phi^2}}_{\text{LHS is only a function of } \phi} = \underbrace{-\frac{\sin^2\theta}{R(r)}\frac{\partial}{\partial r}\left(r^2\frac{\partial R(r)}{\partial r}\right) - \frac{\sin\theta}{\Theta(\theta)}\frac{\partial}{\partial\theta}\left(\sin\theta\frac{\partial\Theta(\theta)}{\partial\theta}\right)}_{\text{RHS is only a function of } \theta \text{ and r}} = -m^2 \tag{1.6}$$

[1]The magnetic field observations based on ZDI are only using the photospheric spectral lines, so that my analysis of the stellar magnetic field is focused on the photosphere $r = R_\star$.

but needs to hold for all values of r, θ and ϕ. Eq. 1.5 has the commonly known solution

$$\Phi(\phi) = C_1 e^{im\phi}, \tag{1.7}$$

where C_1 is a constant. The function $\Phi(\phi)$ needs to be unchanged under 2π rotation ($\Phi(\phi) = \Phi(\phi + 2\pi)$) to be rotationally symmetric. This restricts m to integer values.

Putting the solution for Φ (Eq. 1.7) into Eq. 1.4 and dividing it by $\sin^2\theta$ separates the Laplace equation in two terms, which only depend on r or θ.

$$\underbrace{\frac{1}{R(r)}\frac{\partial}{\partial r}\left(r^2\frac{\partial R(r)}{\partial r}\right)}_{\text{(III)}} + \underbrace{\frac{1}{\sin\theta}\frac{1}{\Theta(\theta)}\frac{\partial}{\partial\theta}\left(\sin\theta\frac{\partial\Theta(\theta)}{\partial\theta}\right) - \frac{m^2}{\sin^2\theta}}_{\text{(II)}} = 0 \tag{1.8}$$

I set term (II) equal to $-\ell(\ell+1)$ and term (III) equal to $\ell(\ell+1)$, while ℓ must not be a function of any of the three variables r, θ, ϕ following the same argument as for m, see Eq. 1.6. In the following, I derive the solution for the terms (II) and (III) separately and the choice of $\ell(\ell+1)$ will be comprehensible.

Term (II) gives

$$\frac{1}{\sin\theta}\frac{1}{\Theta(\theta)}\frac{\partial}{\partial\theta}\left(\sin\theta\frac{\partial\Theta(\theta)}{\partial\theta}\right) - \frac{m^2}{\sin^2\theta} = -\ell(\ell+1). \tag{1.9}$$

Substituting Eq. 1.9 with $\mu = \cos\theta$ and $\frac{\mathrm{d}}{\mathrm{d}\theta} = \frac{\mathrm{d}\mu}{\mathrm{d}\theta}\frac{\mathrm{d}}{\mathrm{d}\mu} = -\sin\theta\frac{\mathrm{d}}{\mathrm{d}\mu}$ results in:

$$\frac{\partial}{\partial\mu}\left((1-\mu^2)\frac{\partial\Theta(\mu)}{\partial\mu}\right) + \left[-\frac{m^2}{1-\mu^2} + \ell(\ell+1)\right]\Theta(\mu) = 0, \tag{1.10}$$

which is the associated Legendre differential equation. It has solutions of the form

$$\Theta(\theta) = C_2 P_{\ell m}(\cos\theta) + C_3 Q_{\ell m}(\cos\theta), \tag{1.11}$$

where C_2 and C_3 are constants and $P_{\ell m}(\cos\theta)$ and $Q_{\ell m}(\cos\theta)$ are the associated Legendre functions of the first and second kind. The solution should be finite at $\theta = 0$, so that $Q_{\ell m}(\cos\theta)$ needs to be dismissed by setting $C_3 = 0, \forall \ell, m$. I receive then the following solution for Eq. 1.10:

$$\Theta(\mu) = P_{\ell m}(\mu) = (-1)^m \frac{1}{2^\ell \ell!}(1-\mu^2)^{\frac{m}{2}}\frac{\mathrm{d}^{\ell+m}}{\mathrm{d}\mu^{\ell+m}}(\mu^2-1)^\ell. \tag{1.12}$$

The highest order of μ in $(\mu^2-1)^\ell$ is 2ℓ, so the derivative $\frac{\mathrm{d}^{\ell+m}}{\mathrm{d}\mu^{\ell+m}}(\mu^2-1)^\ell$ vanishes for $m>\ell$. Further, I restrict $m \geq -\ell$, so that no negative order derivatives occur. Thus, $-\ell \leq m \leq \ell$.

Term (III), which only depends on r, can be rearranged into the form of a second order Euler-Cauchy equation using the product rule:

$$\frac{1}{R(r)}\frac{\partial}{\partial r}\left(r^2\frac{\partial R(r)}{\partial r}\right)=\ell(\ell+1) \tag{1.13}$$

$$\Leftrightarrow r^2\frac{\partial^2 R(r)}{\partial r^2}+2r\frac{\partial R(r)}{\partial r}-\ell(\ell+1)R(r)=0 \tag{1.14}$$

The Euler-Cauchy equation is known to have solutions of the form $R(r)=r^n$. To determine n I put $R(r)=r^n$ and its derivatives $\frac{\partial R(r)}{\partial r}=nr^{n-1}$ and $\frac{\partial^2 R(r)}{\partial r^2}=n(n-1)r^{n-2}$ into Eq. 1.14 and get

$$n(n-1)r^n+2nr^n-\ell(\ell+1)r^n=0 \tag{1.15}$$

$$\Leftrightarrow (n(n-1)+2n-\ell(\ell+1))r^n=0 \tag{1.16}$$

$$\Rightarrow n^2+n=\ell(\ell+1) \tag{1.17}$$

$$\Rightarrow n=\begin{cases}\ell\\ -(\ell+1)\end{cases} \tag{1.18}$$

The weighted sum of solutions is itself a solution to differential equations, so that a solution for term (III) is:

$$R(r)=C_4r^\ell+C_5r^{-(\ell+1)}, \tag{1.19}$$

where C_4 and C_5 are constants.

I combine the solutions for the single variables (Eq. 1.7,1.12,1.19) and receive the full solution for the Laplace equation in the spherical polar coordinates:

$$\Psi(r,\theta,\phi)=R(r)\Theta(\theta)\Phi(\phi)=\sum_{\ell=0}^{\infty}\sum_{m=-\ell}^{\ell}\left[a_{\ell m}r^\ell+b_{\ell m}r^{-(\ell+1)}\right]P_{\ell m}(\cos\theta)e^{im\phi}. \tag{1.20}$$

As the magnetic field is defined as $\mathbf{B}=-\nabla\Psi$, I get the following expression for the magnetic

field in spherical polar coordinates based on the spherical harmonics:

$$B_r(r,\theta,\phi) = -\frac{\partial \Psi}{\partial r} = -\sum_{\ell=0}^{\infty}\sum_{m=-\ell}^{\ell}\left[a_{\ell m}\ell r^{\ell-1} - b_{\ell m}(\ell+1)r^{-(\ell+2)}\right]P_{\ell m}(\cos\theta)e^{im\phi},$$
$$B_\theta(r,\theta,\phi) = -\frac{1}{r}\frac{\partial \Psi}{\partial \theta} = -\sum_{\ell=0}^{\infty}\sum_{m=-\ell}^{\ell}\left[a_{\ell m}r^{\ell-1} + b_{\ell m}r^{-(\ell+2)}\right]\frac{\mathrm{d}P_{\ell m}(\cos\theta)}{\mathrm{d}\theta}e^{im\phi},$$
$$B_\phi(r,\theta,\phi) = -\frac{1}{r\sin\theta}\frac{\partial \Psi}{\partial \phi} = -\sum_{\ell=0}^{\infty}\sum_{m=-\ell}^{\ell}\left[a_{\ell m}r^{\ell-1} + b_{\ell m}r^{-(\ell+2)}\right]P_{\ell m}(\cos\theta)\frac{im}{\sin\theta}e^{im\phi}. \quad (1.21)$$

1.2.2 Field modelling at stellar surface

I can simplify Eq. 1.21 with the following assumptions: First, I let $\mathbf{B} \to 0$ for $r \to \infty$ and set the terms $a_{\ell m} \to 0$ to prevent $r^{\ell-1} \to \infty$ for $r \to \infty$. Furthermore, I can neglect $\ell = 0$ in general as there are no magnetic monopoles. The amplitudes with negative m are equal to the ones with positive m, so that the sum $\sum_{m=-\ell}^{\ell}$ can be reduced to $\sum_{m=0}^{\ell}(2-\delta_{m,0})$, where $\delta_{m,0}$ is the Kronecker delta function, (Johnstone, 2012). My work focusses on the magnetic field at the stellar surface, so I set $r = \mathrm{R}_\odot$. Applying these simplifications and defining $c_{\ell m} = b_{\ell m}(\ell+1){\mathrm{R}_\odot}^{-(\ell+2)}$, I get for the magnetic field at the stellar surface:

$$B_r(\theta,\phi) = \sum_{\ell=0}^{\infty}\sum_{m=0}^{\ell}(2-\delta_{m,0})c_{\ell m}P_{\ell m}(\cos\theta)e^{im\phi},$$
$$B_\theta(\theta,\phi) = -\sum_{\ell=0}^{\infty}\sum_{m=0}^{\ell}(2-\delta_{m,0})\frac{c_{\ell m}}{\ell+1}\frac{\mathrm{d}P_{\ell m}(\cos\theta)}{\mathrm{d}\theta}e^{im\phi},$$
$$B_\phi(\theta,\phi) = -\sum_{\ell=0}^{\infty}\sum_{m=0}^{\ell}(2-\delta_{m,0})\frac{c_{\ell m}}{\ell+1}P_{\ell m}(\cos\theta)\frac{im}{\sin\theta}e^{im\phi}. \quad (1.22)$$

The coefficient $c_{\ell m}$ can be determined by solving

$$c_{\ell m} = \frac{(2\ell+1)[(\ell-m)!]}{4\pi(2-\delta_{m,0})[(\ell+m)!]}\int_0^{2\pi}\int_0^{\pi} B_r(\theta,\phi)P_{\ell m}(\cos\theta)e^{-im\phi}\sin\theta\,\mathrm{d}\theta\,\mathrm{d}\phi, \quad (1.23)$$

which only depends on the radial surface field[2].

The Eq. 1.22 expresses the magnetic field **B** for potential surface fields but potential fields are often insufficient to describe the surface magnetic field for solar-like stars, see e.g. Jar-

[2]The derivation of $c_{\ell m}$ uses the polynomial orthogonality conditions and can be derived by inserting $B_r(\theta,\phi)$ from Eq. 1.22 into $\int_0^{2\pi}\int_0^{\pi} B_r(\theta,\phi)P_{\ell' m'}(\cos\theta)e^{-im'\phi}\sin\theta\,\mathrm{d}\theta\,\mathrm{d}\phi$, see e.g. Johnstone (2012).

dine et al. (2013); Lehmann et al. (2019) or Chapter 2.4.1. A non-potential field expression is needed. I use the expressions based on Elsasser (1946) and Chandrasekhar (1961, Appendix III):

$$\begin{aligned} B_r(\theta,\phi) &= \sum_{\ell m} \alpha_{\ell m} P_{\ell m} e^{im\phi}, \\ B_\theta(\theta,\phi) &= \sum_{\ell m} \beta_{\ell m} \frac{1}{\ell+1} \frac{\mathrm{d}P_{\ell m}}{\mathrm{d}\theta} e^{im\phi} + \sum_{\ell m} \gamma_{\ell m} \frac{imP_{\ell m} e^{im\phi}}{(\ell+1)\sin\theta}, \\ B_\phi(\theta,\phi) &= \sum_{\ell m} \beta_{\ell m} \frac{imP_{\ell m} e^{im\phi}}{(\ell+1)\sin\theta} - \sum_{\ell m} \gamma_{\ell m} \frac{1}{\ell+1} \frac{\mathrm{d}P_{\ell m}}{\mathrm{d}\theta} e^{im\phi}. \end{aligned} \tag{1.24}$$

The normalisation constant is defined as

$$c_{\ell m} = \sqrt{\frac{2\ell+1}{4\pi} \frac{(\ell-m)!}{(\ell+m)!}}, \tag{1.25}$$

and is now included in the associated Legendre polynomial $P_{\ell m} \equiv c_{\ell m} P_{\ell m}(\cos\theta)$. The sums $\sum_{\ell=0}^{\infty} \sum_{m=0}^{\ell} (2-\delta_{m,0})$ are summarised to $\sum_{\ell m}$.

I am changing now from a right-handed coordinate system[3] to a left-handed coordinate system, which results in the change of the direction of the ϕ-component. From now onwards the radial field component B_r points towards outwards, the meridional field B_θ runs with co-latitude (from north to south) and the azimuthal component B_ϕ runs in the clockwise direction as viewed from North pole[4]. Eq. 1.24 changes accordingly to:

$$\begin{aligned} B_r(\theta,\phi) &= \sum_{\ell m} \alpha_{\ell m} P_{\ell m} e^{im\phi}, \\ B_\theta(\theta,\phi) &= \sum_{\ell m} \beta_{\ell m} \frac{1}{\ell+1} \frac{\mathrm{d}P_{\ell m}}{\mathrm{d}\theta} e^{im\phi} + \sum_{\ell m} \gamma_{\ell m} \frac{imP_{\ell m} e^{im\phi}}{(\ell+1)\sin\theta}, \\ B_\phi(\theta,\phi) &= -\sum_{\ell m} \beta_{\ell m} \frac{imP_{\ell m} e^{im\phi}}{(\ell+1)\sin\theta} + \sum_{\ell m} \gamma_{\ell m} \frac{1}{\ell+1} \frac{\mathrm{d}P_{\ell m}}{\mathrm{d}\theta} e^{im\phi}. \end{aligned} \tag{1.26}$$

This was done to be consistent with the left-handed coordinate system used by Vidotto (2016), see Eq. 1-6 or 26-31, in the following chapters, e.g., for the spherical harmonic decomposition, see Chapter 2.1.

The vector magnetic field can be described in different coordinate systems. Until now, I

[3]Right-handed spherical coordinate system means: $\mathbf{e_r} \times \mathbf{e_\theta} = \mathbf{e_\phi}$.

[4]For the right-handed coordinate system the azimuthal component B_ϕ runs in the anti-clockwise direction. The radial and meridional component remain the same.

used the spherical polar coordinates: radial r, meridional θ and azimuthal ϕ. Beside that, the magnetic field can be described by using the poloidal and toroidal component. The following expression in the toroidal and poloidal field will also help to better understand the origin of Eq. 1.26.

Chandrasekhar (1961) showed, that a solenoidal field $\mathbf{B}$ ($\nabla \cdot \mathbf{B} = 0$) can be expressed by the toroidal $\mathbf{B_{tor}}$ and poloidal field $\mathbf{B_{pol}}$, $(\mathbf{B_{tor}} + \mathbf{B_{pol}}) = \mathbf{B}$,

$$\begin{aligned} \mathbf{B_{tor}} &= \nabla \times \left(\frac{\Psi}{r} \mathbf{r} \right), \\ \mathbf{B_{pol}} &= \nabla \times \left(\nabla \times \frac{\Phi}{r} \mathbf{r} \right), \end{aligned} \tag{1.27}$$

where Ψ and Φ are arbitrary scalar functions of position. Expressing Ψ and Φ in spherical harmonics with the help of the coefficients $T(r)$ and $S(r)$, that can be functions of r, one receives:

$$\begin{aligned} \Psi &= T(r) P_{\ell m} e^{im\phi}, \\ \Phi &= S(r) P_{\ell m} e^{im\phi}. \end{aligned} \tag{1.28}$$

To get Eq. 1.26 again, I solve Eq. 1.27 by relating the poloidal field coefficient $S(r)$ to the two coefficients $\alpha_{\ell m}$ and $\beta_{\ell m}$ and the toroidal field coefficient $T(r)$ to the $\gamma_{\ell m}$ coefficient of Eq. 1.26. I receive then the following expressions for the toroidal and poloidal field by restricting the expressions to the stellar surface again and still applying a left-handed coordinate system:

$$\mathbf{B_{pol}} = (B_{r,\mathrm{pol}}, B_{\phi,\mathrm{pol}}, B_{\theta,\mathrm{pol}}), \tag{1.29}$$

$$\begin{aligned} B_{r,\mathrm{pol}}(\theta, \phi) &= \sum_{\ell m} \alpha_{\ell m} P_{\ell m} e^{im\phi}, \\ B_{\theta,\mathrm{pol}}(\theta, \phi) &= \sum_{\ell m} \beta_{\ell m} \frac{1}{\ell + 1} \frac{\mathrm{d}P_{\ell m}}{\mathrm{d}\theta} e^{im\phi}, \\ B_{\phi,\mathrm{pol}}(\theta, \phi) &= -\sum_{\ell m} \beta_{\ell m} \frac{im P_{\ell m} e^{im\phi}}{(\ell + 1) \sin\theta}, \end{aligned} \tag{1.30}$$

$$\mathbf{B_{tor}} = (B_{r,\mathrm{tor}}, B_{\phi,\mathrm{tor}}, B_{\theta,\mathrm{tor}}) \tag{1.31}$$

$$\begin{aligned} B_{r,\mathrm{tor}}(\theta,\phi) &= 0, \\ B_{\theta,\mathrm{tor}}(\theta,\phi) &= \sum_{\ell m} \gamma_{\ell m} \frac{imP_{\ell m} e^{im\phi}}{(\ell+1)\sin\theta}, \\ B_{\phi,\mathrm{tor}}(\theta,\phi) &= \sum_{\ell m} \gamma_{\ell m} \frac{1}{\ell+1} \frac{\mathrm{d}P_{\ell m}}{\mathrm{d}\theta} e^{im\phi}, \end{aligned} \tag{1.32}$$

where $(\mathbf{B_{pol}}, \mathbf{B_{tor}}) = \mathbf{B}$. These expressions for the toroidal and poloidal field were orginally given in a right-handed coordinate system by Chandrasekhar (1961). To receive the right-handed expressions again, the sign of the ϕ-component in Eq. 1.30 and 1.32 needs to be reversed.

One can now describe any surface magnetic field with the help of the coefficients $\alpha_{\ell m}, \beta_{\ell m}$ and $\gamma_{\ell m}$ as this magnetic field description has no a-priori assumptions. One has the description of the potential surface magnetic field again by setting $\gamma_{\ell m} = 0$. The potential field is also a pure poloidal field in this case. The restriction of $\alpha_{\ell m}$ and $\beta_{\ell m}$ provides advantages by extrapolating the surface magnetic field to outer radii $r > \mathrm{R}_\odot$, see Chapter 2.4.1. The components of both coordinate systems (radial, azimuthal, meridional and toroidal, poloidal) are mutually orthogonal to each other.

In this description the magnetic field is a composition of several spherical harmonic modes, that are specified by the ℓ and m modes. The ℓ-mode indicates the order of the multipole, e.g. dipole for $\ell = 1$, quadrupole for $\ell = 2$, octopole for $\ell = 3$ and so on. The m-mode indicates the axisymmetry of the mulitpole, i.e. the alignment of the multipole with the rotation axis. I use the common definition, that the axisymmetric modes are only the modes where $m = 0$. In the literature the axisymmetric modes are sometimes defined as all modes where $m < \ell/2$, which is a less strict definition than I apply. The modes imply the number of nodal crossings or polarity switches in the meridional and azimuthal direction[5]. Fig. 1.1 presents the radial magnetic field for the first three ℓ and m-modes.

1.3 Detection of the stellar magnetic field

The first detection of a stellar magnetic field was achieved by George Ellery Hale (1908). He uncovered the magnetic field in sunspots by observing the Zeeman splitting and broadening

[5]The number of nodal crossings for the meridional direction is given by $\ell - m$ and for the azimuthal direction by m.

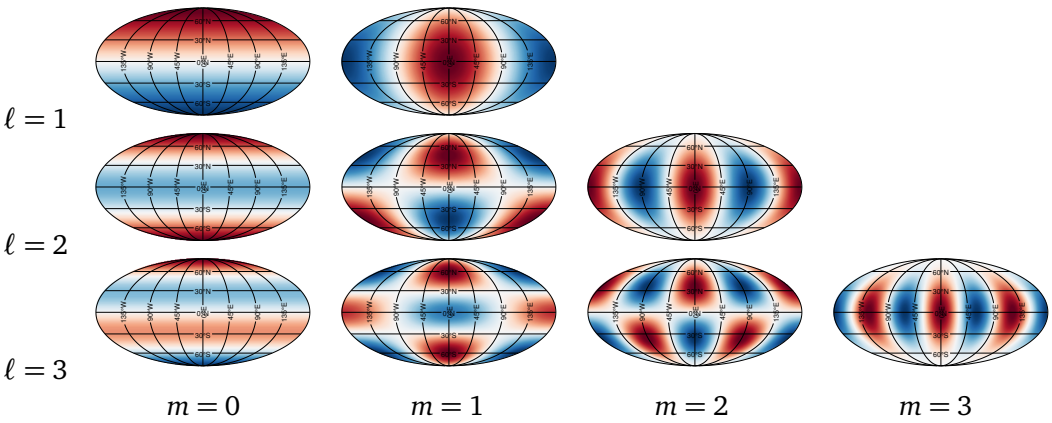

Figure 1.1: An illustration of the radial magnetic field of Eq. 1.26 for the first three ℓ and m-modes. The magnetic field is colour coded from red to blue representing positive to negative radial magnetic field values. The spherical harmonic function $P_{\ell m}$ dominates the radial magnetic field and characterises the nodal crossing.

in absorption lines at Mount Wilson. Babcock (1947) detected the first stellar magnetic field on a star other than the Sun, which was at the Ap star 78 Vir showing a magnetic field of 1.5 kG. More than 30 years later Robinson et al. (1980) compared spectral lines of different Landé factors and achieved the first detection of magnetic fields on solar analogous for 70 Oph A (K0 V) and ξ Boo A (G8 V). Nowadays, we have detected cool star magnetic fields on M Dwarfs (Donati et al., 2008b; Morin et al., 2008a, 2010), solar-like and young solar-type stars (Marsden et al., 2006a; Petit et al., 2008; Folsom et al., 2016; Folsom et al., 2018), T Tauri stars (Carroll et al., 2012; Hill et al., 2017, 2019), planet-host stars (Fares et al., 2013) and gaints (Konstantinova-Antova et al., 2010; Tsvetkova et al., 2019). They show magnetic field strengths over several orders of magnitudes and the Zeeman-Doppler-Imaging technique enables us to get magnetic field maps of the photospheric field.

This thesis focusses on the magnetic field topologies of cool stars. It should be mentioned that also hot and degenerated stars show magnetic fields and that the stellar magnetic field evolves with age in general. The appearence and the origin of the magnetic field for hot and degenerated stars is very different from cool stars. A good summary about the stellar magnetic fields of different spectral classes, masses and ages is given by Berdyugina (2009).

1.3.1 Zeeman effect and spectropolarimetry

Pieter Zeeman (1897) opened the window for detecting magnetic fields by measuring the broadening of emission and absorption lines in polarised light under the influence of strong magnetic fields. The Zeeman effect enables us to detect magnetic fields from μG in molecular

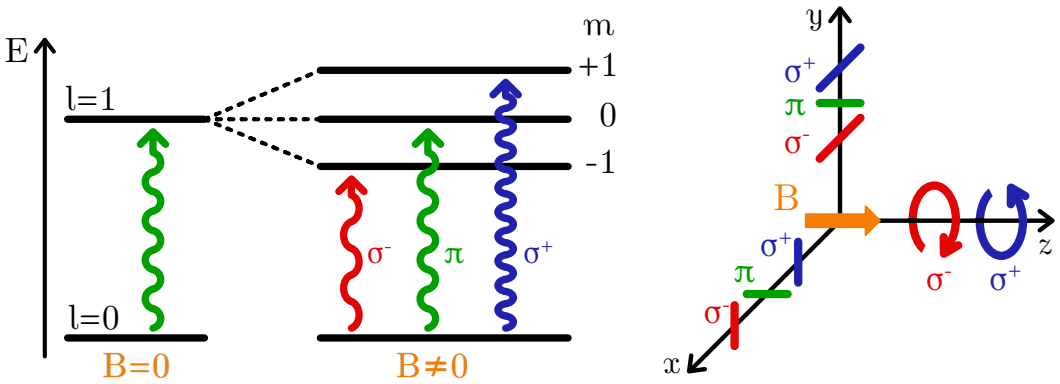

a. **b.**

Figure 1.2: a. A schematic illustration of the atomic energy level degeneration during the Zeeman effect allowing the transition for $m = -1, 0, +1$ corresponding to the σ^-, π and σ^+ component, where the $\sigma^\pm$ components are red or blue wavelength shifted. **b.** An illustration of the different polarisations of the Zeeman components. By observing the magnetic field **B** longitudinal (z-direction) the $\sigma^\pm$ components are circularly polarised and π is forbidden. By observing the magnetic field **B** transversal (x- or y-direction) the three different components are linearly polarised.

clouds to 10^{15} G in Neutron stars. If an isolated atom is affected by a magnetic field **B**, the magnetic Hamiltonian

$$H_B = \mu_0(\mathbf{L} + 2\mathbf{S}) + \frac{e^2}{8mc^2}(\mathbf{B} \times \mathbf{r})^2 \tag{1.33}$$

needs to be added to the undisturbed Hamiltonian H_0, where $\mu_0 = \frac{eh}{4\pi mc}$ is the Bohr magneton (m is the electron mass and e the electron charge, h the Planck constant, c the speed of light), **L** and **S** describe the total orbital angular momentum and spin, and **r** is the position operator of the electronic cloud. The diamagnetic term $\frac{e^2}{8mc^2}(\mathbf{B} \times \mathbf{r})^2$ needs only be taken into account for strong magnetic fields found in white dwarfs or neutron stars and can be neglected for non-degenerates stars, (Donati & Landstreet, 2009). The atomic energy levels degenerate under the influence of magnetic fields and split into $2J + 1$ sublevels, where J is total angular momentum quantum number of the atom. The degenerated energy levels are shifted by

$$\Delta E = \mu_0 g B M, M = -J, -J+1, \cdots, J+1, J, \tag{1.34}$$

where g is the dimensionless Landé factor[6] and M the magnetic quantum number. A dipole transition between two energy levels and therefore the emission or absorption of photons is only allowed for $\Delta M = -1, 0, 1$, see Fig. 1.2a. These three groups of transitions obtain different polarisation signatures depending on the angle between the magnetic field vector and observer, see Fig. 1.2b. The spin of a circularly polarised photon absorbed by an atom causes a change of $\Delta M = \pm 1$. The spin of a linearly polarised photon is zero and allows the transition with $\Delta M = 0$. Transitions with $\Delta M = \pm 1$ are called $\sigma^{\pm}$ components, which are circularly polarised by observing the magnetic field longitudinal (parallel to **B**) and linearly polarised by observing the magnetic field transversal (perpendicular to **B**). Transitions with $\Delta M = 0$ are called π components and vanish by observing the magnetic field longitudinal and are linearly polarised by observing transversal. The π component has the same wavelength as the undisturbed spectral line λ_0 but the $\sigma^{\pm}$ are red/blue wavelength shifted by

$$\Delta\lambda_B = \mu_0 g \lambda_0^2 B = 4.67 \cdot 10^{-13} g \lambda_0^2 \left[\mathring{\mathrm{A}}^2\right] B[\mathrm{G}]. \tag{1.36}$$

An example: the spectral line Fe I $\lambda_0 = 6173.34\,\mathring{\mathrm{A}}$ has an effective Landé factor of $g = 2.5$. The corresponding Zeeman splitting in the intensity profile would be $5.78\,\mathrm{pm} = 2.81\,\mathrm{kms}^{-1}$ for a magnetic field of 1.3 kG in contrast to $2.16\,\mathrm{ms}^{-1}$ for a magnetic field of 1 G, see also Fig. 1.3. The splitting increases for longer wavelengths with $\Delta\lambda_B \propto \lambda_0^2$, which makes the near infrared spectrum attractive for magnetic field detection, (Valenti et al., 1995). The molecular Zeeman effect becomes more important for the detection and analysis of magnetic fields in very cool stars and magnetic structures, e.g. Berdyugina et al. (2000); Afram et al. (2007); Berdyugina et al. (2008).

The Zeeman splitting into the three components is affected by several other processes and parameters of the stellar atmosphere. The photons undergo several absorption and emission processes. They are affected by the temperature, gravitation, micro- and macro-turbulence and the magnetic field of the respective layer of the atmosphere. Other broadening effects like the thermal broadening ($\lambda_{\mathrm{therm}} \sim \lambda_0 \sqrt{k_B T / mc^2}$, where k_B is the Boltzmann constant, T

[6]For light atoms the Landé factor can be estimated via the Russell-Saunders (or L-S) coupling,

$$g = 1 + \frac{J(J+1) + S(S+1) - L(L+1)}{2J(J+1)} \tag{1.35}$$

where g is mostly between 0−3, (Donati & Landstreet, 2009). For transitions where the Russell-Saunders coupling is no longer appropriate the effective Landé factor (Beckers, 1969) based on laboratory measurements (e.g., Reader & Sugar 1975) provides good results.

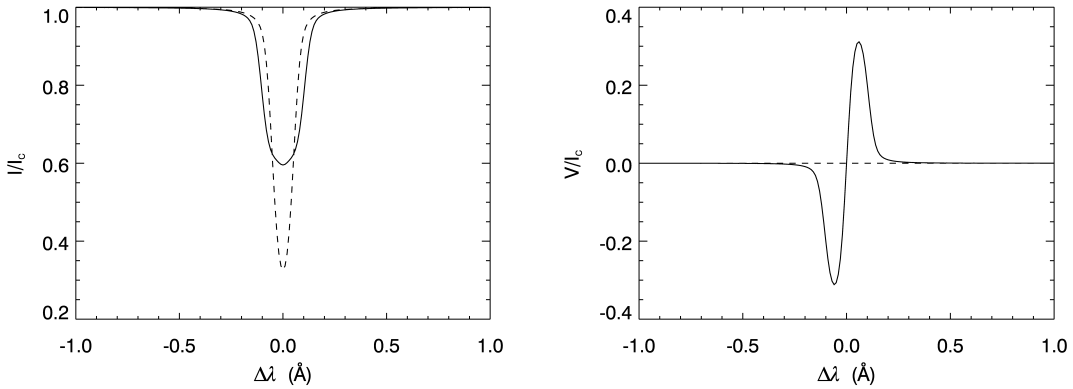

Figure 1.3: The simulated spectral line Fe I 6173 Å in Stokes I (left) and Stokes V (right) without a magnetic field (dashed line) and under the influence of a magnetic field of 1.3 kG (solid line). Figure reproduced from Lehmann (2013, fig. 2.9) with permission.

the effective temperature, m the average particle mass) and the rotational broadening ($\lambda_{\rm rot} = \lambda_0 \frac{v_e \sin i}{c}$, v_e is the equatorial rotation velocity and i the inclination angle) can affect (and even hide) the Zeeman splitting and therefore need to be taken into account.

To actually see the splitting of the spectral line into the three components in the unpolarised light the magnetic field needs to be typically stronger than a few kG. In the case of cool stars the spectral lines are only broadened in the wings and decrease in depth as the Zeeman shift λ_B is smaller than the width of the undisturbed line, see Fig. 1.3. In the case of circularly polarised light, $\sigma^{\pm}$ only appears if a magnetic field is present (if other circular polarisation effects can be neglected which is normally the case). This allows the detection of magnetic fields down to a few G in optical wavelengths or down to μG in radio.

George Gabriel Stokes (1852) introduced the following Stokes vectors to characterise the different polarisations:

$$\begin{aligned} I &= A_x^2 + A_y^2 & I &= \updownarrow + \leftrightarrow \\ Q &= A_x^2 - A_y^2 & Q &= \updownarrow - \leftrightarrow \\ U &= 2A_xA_y \cos\epsilon & U &= \nearrow - \nwarrow \\ V &= 2A_xA_y \sin\epsilon & V &= \circlearrowleft - \circlearrowright . \end{aligned} \tag{1.37}$$

where $A_{x,y}$ is the amplitude of the electromagnetic wave[7] and ϵ the phase difference between

[7]The electric field (E_x, E_y) of a polarised electromagnetic wave propagating in the z-direction can be described as

$$\begin{aligned} E_x &= A_x \cos\phi \\ E_y &= A_y \cos(\phi + \epsilon), \end{aligned} \tag{1.38}$$

the x and y component of the electric field vector. The unpolarised light is then described by Stokes I, the linear polarisations by Stokes QU and the circular polarisations by Stokes V, see also the visualisation of the Stokes vector on the right hand side of Eq. 1.37.

The Stokes V component typically has an amplitude of 5 % of the Stokes I (Piskunov & Kochukhov, 2002) and is nowadays widely observed, e.g., with ESPaDOnS@CFHT, NARVAL@TBL or HARPSPol. The Stokes QU reach typically only 0.5 % of the Stokes I (Piskunov & Kochukhov, 2002) but it was possible to detect the full Stokes vector IQUV for the active star II Peg by Rosén et al. (2015). However, currently only the brightest stars can be observed in all four Stokes parameters.

A magnetic field measurement can be made from the unpolarised light (Stokes I) using the Zeeman Broadening (ZB) technique, (Robinson et al., 1980; Saar, 1988; Reiners & Basri, 2006; Lehmann et al., 2015; Scalia et al., 2017). The spectral line profiles of magnetically insensitive lines (effective Landé factor $g \simeq 0$) and magnetically sensitive lines ($g > 0$) are compared to determine the total average unsigned magnetic field $B_I = B \cdot f$, where f is the filling factor of the magnetic field B. The ZB technique detects the mean field strength over the projected stellar disc including the magnetic field at all length scales. For relatively inactive stars similar to the Sun the broadening is small and competes with other broadening effects. For fast rotating stars the rotational broadening can hide even stronger magnetic fields and high signal-to-noise ratio levels (S/N) are necessary[8], (Reiners & Basri, 2006). However, the ZB provides no information about the distribution of the magnetic field morphology or their polarity.

1.3.2 Zeeman-Doppler-Imaging

The Doppler Imaging technique is able to resolve (indirectly) stellar discs for brightness and abundance distributions, (Deutsch, 1958; Vogt & Penrod, 1983; Vogt et al., 1987). The stellar rotation causes a specific Doppler-shifted contribution across the visible stellar disc. Spotted regions lead to a rotationally modulated Doppler-shifted distortion in the spectral line profile depending on their positions on the projected stellar discs, see also review of Rice (2002). The faster the star rotates, the greater the projected equatorial velocity $v_e \sin i$ and the greater the range of Doppler-shifted contributions and therefore the spatial resolution. However, for fast

were $A_{x,y}$ are the amplitudes, ϕ the phase and ϵ the phase difference between E_x and E_y.

[8] In fact, ZB cannot be used for stars with projected rotational velocity higher than $\approx 35\,\mathrm{km\,s^{-1}}$, (Reiners & Basri, 2006).

rotators the rotational broadening makes the line profiles increasingly shallower. A higher S/N is then required to detect structures in the broadened line profiles while at the same time one needs to ensure that the exposure times are kept within a few percent of the rotation period to reduce phase blurring (and hence more flux cancellation).

Applying the Doppler Imaging principles to polarised Stokes profiles enables the detection of large-scale stellar magnetic field morphologies. Semel (1989) first proposed the technique of Zeeman Doppler Imaging to map magnetic field distributions across the stellar surface of rapidly rotating stars by tracing the rotationally modulated Stokes V signatures in spectral time series. The first stellar magnetic field detection with ZDI was achieved by Donati et al. (1989) followed by the first map by Donati et al. (1992). The circularly polarised Stokes V signal is sensitive to the longitudinal component of the magnetic field, which allows us to recover not only the location but also the orientation of the magnetic field. Fig. 1.4 shows schematically how the Stokes V profiles vary if dot-like magnetic field regions of different field components cross the stellar disc. Also the linearly polarised Stokes QU profiles can be included to use the full Stokes vector, which reduces the cross-talk between the field vectors in the resulting magnetic field map provided phase coverage is not compromised, (Wade et al., 2000; Kochukhov et al., 2004; Rosén et al., 2015). See also figure 3 and 4 of the review of Reiners (2012) for a good example of how Stokes IQUV are rotationally modulated by magnetic structures.

The Stokes V profiles only appear if a magnetic field is present, which makes it ideal to detect the large-scale stellar magnetic field. ZDI is only sensitive to the large-scale field as the resolution is given by the range of Doppler distributions determined by $v_e \sin i$. Within a resolution element the opposite polarities are cancelled, which restricts the detection to the large-scale magnetic field. ZDI and ZB are in a sense complementary when applied to generally slower rotating stars: ZDI can detect the location and orientation of the large-scale field and the resolution gains from faster rotation periods. ZB can detect the unsigned magnetic field of all length scales but without information about distribution or orientations and decreases in sensitivity at faster rotation periods[9]. Both techniques are subject to inclination effects as no signature is received from the unobserved obscured hemisphere.

For cool stars, even if they are relatively active, the Stokes V signal is still very weak. To

[9]For stars with projected equatorial rotation velocities $v_e \sin i \gg 25\,\mathrm{km\,s^{-1}}$.

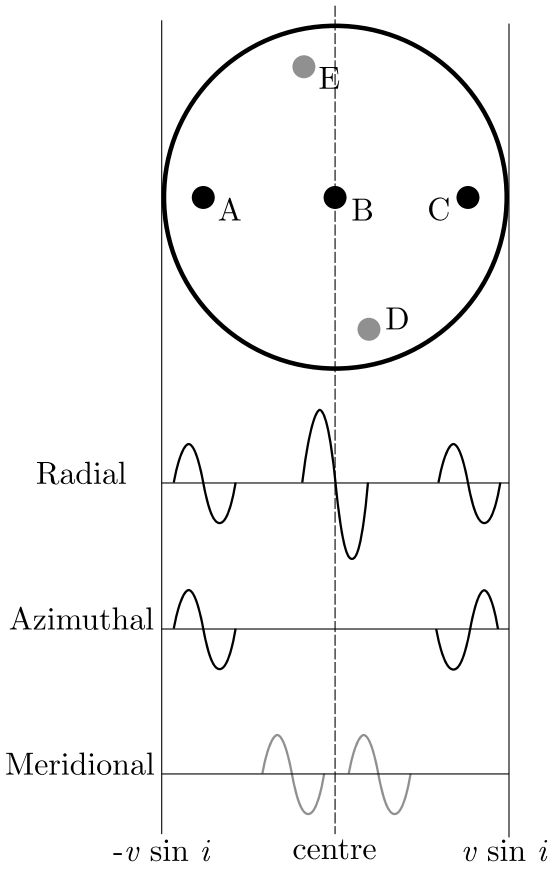

Figure 1.4: A schematic representation of the variation in Stokes V for dot-like magnetic regions of different magnetic field vector components. Contain the dots A, B, C radial field the Stokes V profile is largest at the centre as the magnetic field is longitudinal observed. Contain the dots A, B, C azimuthal field the field is longitudinal observed at the limb while showing opposite polarity. The meridional component (gray dots E, D) is best observed polewards for higher inclined stars ($i = 60°$). ZDI is affected by cross-talk between the meridional and radial component as both components show similar signatures on the right and left hemisphere. The figure is based on Hussain (2004, fig. 1) and reproduced from Lehmann (2015, fig. 2.2) with permission.

enhance the signal, spectropolarimeters[10] observe a large fraction of the visible spectrum to collect the polarised light of thousands of photospheric lines which are cross-correlated. The signal from typically 1000–2000 photospheric lines is used to model a "mean" profile with higher S/N. Currently, the Least Squares Deconvolution (LSD) (Donati et al., 1997) or the Single Value Decomposition (Carroll et al., 2012) are the most commonly applied techniques. The result of applying these cross-correlation techniques is to produce a mean profile that has a S/N of several thousand if the peak input S/N is ≈ 100. Such high S/N is typically what is needed to robustly detect and map magnetic fields in solar-type stars. One next possible step is to determine a mean profile for a zero stellar magnetic field ($\mathbf{B}_{\rm Sim} = 0$) and cross-correlate it with the observed one. The corresponding reduced χ^2 is determined and minimised by iteratively changing $\mathbf{B}_{\rm Sim}$ of the simulated mean profile.

This is an ill-posed problem as in principle an infinite number of magnetic field configurations would fit the observed profile within a specified level of agreement (usually measured as χ^2). The first implementations of ZDI filled the stellar surface with spots of independent magnetic field components (radial, azimuthal (east-west) and meridional (north-south), Donati & Collier Cameron 1997; Donati & Brown 1997; Hussain et al. 2000). The problem is here that unphysical solutions with $\nabla \cdot \mathbf{B} \neq 0$ are possible as the three field components are not related. Also simple field configurations like dipolar fields could not be reconstructed. Today most codes use therefore the spherical harmonics description, (Hussain et al., 2002; Donati et al., 2006b; Kochukhov, 2015). They fulfil Gauß's law for magnetism ($\nabla \cdot \mathbf{B} = 0$) automatically and are able to recover all field configuration from dipolar fields to highly complex fields. The spherical harmonic description was introduced in Section 1.2.1. The coefficients $\alpha_{\ell m}, \beta_{\ell m}, \gamma_{\ell m}$ (Eq. 1.26) are fitted to the mean profile, where further restrictions can be applied, e.g. axi-/non-axisymmetric or potential/non-potential field configurations, see also Chapter 2.4.1.

A regularisation function is still needed to restrict the solution of the possible magnetic field configurations. The maximum entropy approach with different implementations (Donati & Brown, 1997; Hussain et al., 2000) is commonly used or alternatively a Levenberg-Marquardt minimisation constrained by a Tikhonov regularisation (Piskunov & Kochukhov, 2002) or more recently an iterative Landweber method (Carroll et al., 2012).

Next to all of the advantages of ZDI, it has a number of limitations:

[10]The most commonly used optical spectropolarimeters are currently ESPADONS at CFHT, NARVAL at TBL and HARPSpol at the ESO 3.6m telescope. Just recently, SPIROU at CFHT become available.

- The most important one is the restriction of the large-scale field detection. The Stokes V profiles can only detect the net longitudinal surface magnetic field of the resolution element limited by the stellar $v_e \sin i$, see also Chapter 2.3.2. The magnetic field structures of opposite polarities cancel each other within the resolution element, so that ZDI is blind to the small-scale field, e.g., the bipolar active regions emerging on the Sun. This issue is especially relevant for slow rotators like the Sun or stars with complex large-scale magnetic fields.

- The inclination between the line-of-sight and stellar rotation axis causes several limitation. For stars with low inclination angles (i.e. more pole-on view) the magnetic field of the southern hemisphere is mostly obscured and the field reconstruction of the low latitudes is affect by cross-talk between the radial and meridional component, (Donati & Brown, 1997). For stars with high inclination angles $i > 85^\circ$ (i.e. more equator-on view) the Doppler-shift of the northern and southern hemisphere is identical, which causes mirroring effects about the equator.

- The variable quality and S/N of the observed Stokes profiles affect the reconstructed maps. This is especally relevant by comparing maps of the same star that have an activity cycle, e.g. for τ Boo, (Mengel et al., 2016). Here a robust stopping criterion would help as proposed by Alvarado-Gómez et al. (2015a).

- An uneven phase coverage and phase gaps widely affect the reconstructed maps. Also the comparison between maps having a different amount of phase coverage needs to done carefully.

- ZDI assumes that the surface magnetic field is stable along one stellar rotation. This is not as much an issue for fast rotating stars as for slow rotating ones. We know from the Sun that changes in the magnetic field distributions can happen on significantly smaller time scales than the rotation period of the Sun.

1.4 Origin of the stellar magnetic field

The question of the origin of stellar magnetic fields seems to be answered for cool stars with outer convection zones although there are still many open questions. Observational and theoretical evidences strongly favour that the magnetic fields of cool stars are generated by dynamo processes via inductive processes in the stellar interior. Chabrier & Küker (2006) showed that

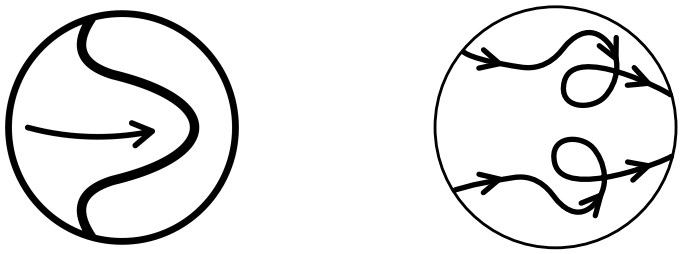

a. **b.**

Figure 1.5: The illustration of the α- and Ω-effect. **a.** The Ω-effect converts poloidal fields into toroidal as the differential rotation furls the field lines around the star. **b.** The α-effect converts the toroidal field lines back to poloidal ones by twisting the toroidal field lines due to the cyclonic turbulence.

fossil fields[11] would dissipate by convection within 1000 years for all stars with spectral types later than mid-F. Due to the high turbulence in the outer convection zone of these stars the field would diffuse very quickly. However, we observe highly variable global and local fields on timescales from seconds to decades on stars, which were formed billions of years before, for example on our own Sun. Also the observational result, that the magnetic flux increases with rotation or inverse Rossby number[12] (R_o^{-1}) until it saturates (Reiners, 2012), goes hand in hand with the predictions of conventional dynamo theories. The theory of fossil field origin seems to be refuted for cool stars. However, for hot stars, which have an outer radiative zone and show predominantly stable and simple magnetic fields, the fossil field origin is a possible explanation, see also the review of Donati & Landstreet (2009).

Larmor (1919) first suggested that the solar magnetic field is induced by plasma motions. Later, Parker (1955) introduced the $\alpha\Omega$-dynamo: a weak poloidal field is wound around the star by differential rotation[13] forming a strong toroidal band (Ω-effect), while the cyclonic turbulence restores a poloidal field of opposite polarity by twisting the toroidal field (α-effect), see Fig. 1.5. Further dynamo models were developed, but for this thesis the flux transport model by Babcock (1961) and Leighton (1969) plays a important role in connection with a non-potential coronal evolution, e.g., see review of Mackay & Yeates (2012).

The flux transport model determines the surface magnetic flux from bipolar sunspot pair injections which undergo shearing and diffusion effects, (Wang et al., 1989; van Ballegooijen

[11] Fossil fields describe here stellar magnetic fields, that are remainder of the initial magnetic field of the molecular cloud from which the star was born.

[12] The Rossby number is defined as the ratio between rotation period and turnover time in the convection cell, $R_o = \frac{P_{\rm rot}}{\tau_{\rm conv}}$, (Noyes et al., 1984).

[13] The differential rotation describes the latitude dependent rotation of stars. For example our Sun rotates faster at the equator ($P_{\rm rot} = 25.6$ days) than at the poles ($P_{\rm rot} = 33.5$ days), so that the equator overtakes the pole every ≈ 120 days, (Phillips, 1995).

et al., 2000; Baumann et al., 2004; Mackay et al., 2004; Jiang et al., 2013b). The shearing effects are driven by the differential rotation and the meridional flow. The meridional flow describes a poleward motion that drags the field from the equatorial and mid latitudes towards the pole, (Babcock, 1961; DeVore et al., 1985). It weakens with higher latitudes and the Sun shows a maximum speed of $11\,\mathrm{m\,s^{-1}}$, while Mackay et al. (2004) showed that faster rotating stars must have higher meridional flows to simulate the observed polar spot configurations, see also Schrijver & Title (2001). The diffusion processes are mainly driven by the granulation and supergranulation that breaks up magnetic field distributions, (Leighton, 1964). Greater details about flux transport models can be found in Chapter 2.2.

The flux transport models are usually combined with further approaches: e.g. (1) with 3D models, where the emerging bipoles are directly included as source of poloidal field, (Miesch & Teweldebirhan, 2016; Karak & Miesch, 2017) or (2) a thin-layer $\alpha\Omega$-dynamo is combined with buoyancy instabilities for 3D flux tube rises and horizontal flux transport at the surface, (Işık et al., 2011), or (3) in connection with a non-potential coronal evolution model using the magnetofrictional technique, (Mackay & Yeates, 2012; Gibb et al., 2016) as used in this thesis. The review of Wiegelmann et al. (2017) nicely summarises the non-potential coronal magnetic field models.

1.5 Appearance of the stellar magnetic field

Stellar magnetic activity has many different faces. They are best observable at our own Sun. In Section 1.5.1 I introduce solar and stellar activity phenomena by giving special attention to solar and stellar activity cycles. Section 1.5.2 focusses on the current knowledge about the stellar large-scale magnetic field topologies.

1.5.1 Solar and stellar activity

Our Sun shows a number of activity phenomena, e.g. sunspots, prominences, coronal holes, flares, stellar winds, etc. They are driven by the solar magnetic field and show a cyclic behaviour. The solar activity cycle has a period of ≈ 11 years (Schwabe cycle, Schwabe 1849). The large-scale field evolves from an axisymmetric dipole at activity minimum, see e.g. Ossendrijver (2003), to a chaotic small-scale structured field distribution at activity maximum back to a reversed dipolar field. The magnetic cycle (seeing the same polarity at the poles) is therefore ≈ 22 years long, (Hale et al., 1919).

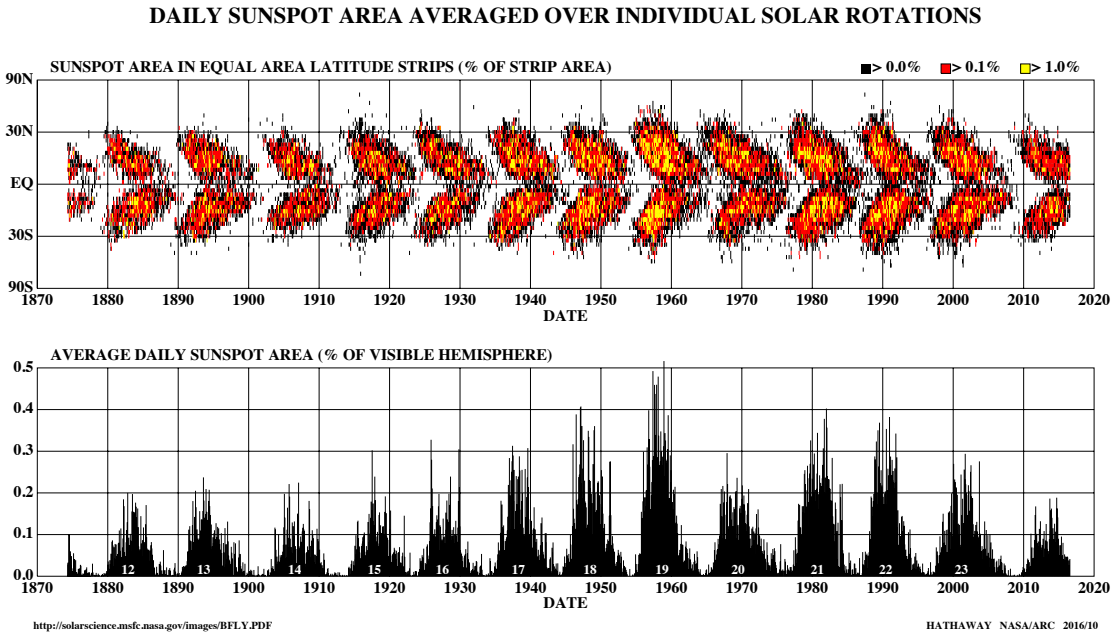

Figure 1.6: The record of sunspots of the Royal Greenwich Observatory since 1874. Top: The latitudinal position of sunspots as function of time. The sun spots emerge in two bands at the two hemispheres and their latitude of emergence shifts towards the equator as the 11-yr solar cycle progresses. Bottom: The percentage of the visible solar surface that is covered by sunspots with time. The white number indicates the solar cycle number. Image used from NASA in accordance to their media usage guidelines.

Sunspots are the most obvious tracer of solar activity in photospheric observations and mark the emergence of magnetic flux ($5 \cdot 10^{21}\,\mathrm{Mx} - 3 \cdot 10^{22}\,\mathrm{Mx}$) through the solar surface, (Schrijver & Zwaan, 2000). They appear as dark spots often divided into umbra (dark central region, pre-dominantly radial field) and penumbra (outer brighter region, pre-dominantly azimuthal and meridional field). With the beginning of a new solar cycle (at activity minimum) the sunspots emerge at mid latitude $\pm 35°$ until the latitude of emergence decreases down to $\pm 8°$ at the end of the activity cycle, (Carrington, 1858; Spörer, 1879). The top panel of Fig. 1.6 displays the latitudinal position of sunspots since 1874 and the bottom panel the percentage of the visible solar surface covered by sun spots. The range of latitudes where active regions emerge is also known as active latitudes. The number of sunspots increases rapidly during the increasing phase of the activity cycle until the activity maximum and shows a longer and shallower decrease towards the activity minima, see Fig. 1.7. The maximum number of sunspots per cycle varies as seen for the last three cycles in Fig. 1.7. The sunspots or active regions appear usually as bipoles: two magnetic field regions or spots of opposite polarity, while the leading spot emerges at lower latitudes and shows the same polarity as the polar region of the corresponding hemisphere (Joy's law). The bipoles show therefore opposite polarities at the

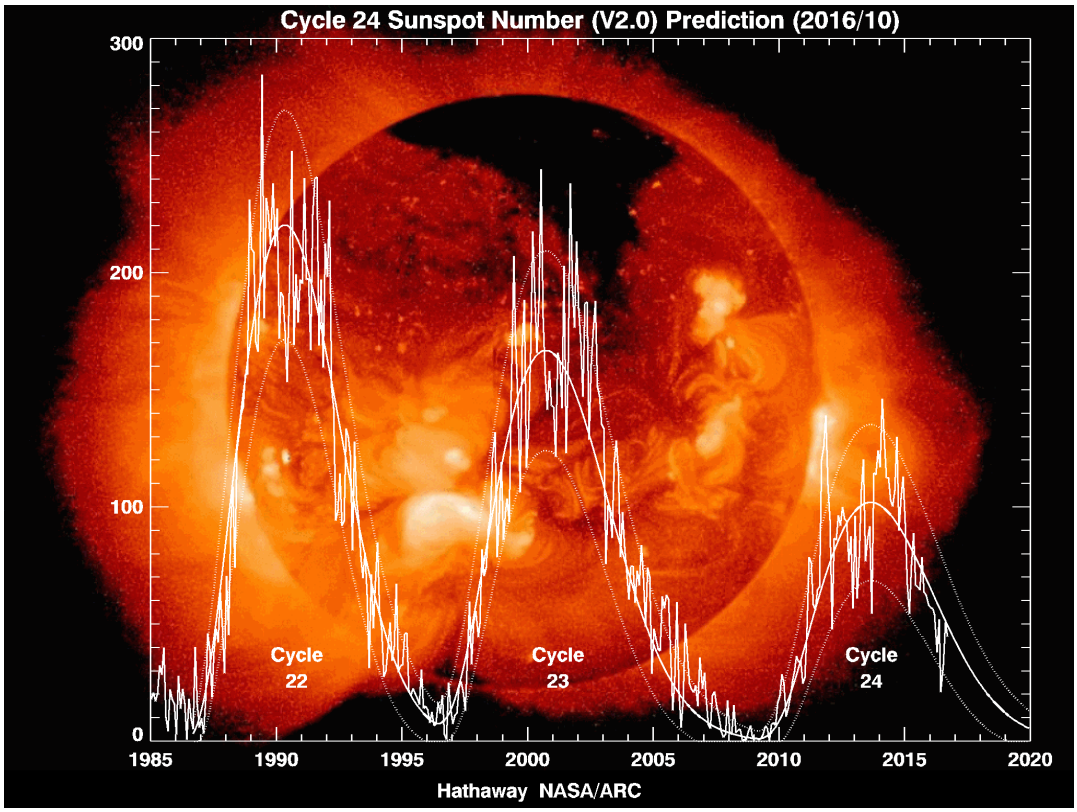

Figure 1.7: The Sunspot number prediction after David Hathaway (NASA/MSFC) for the last three cycles. Image used from NASA in accordance to their media usage guidelines.

different hemispheres (Hale's law). Sunspots host magnetic flux densities of several thousand Gauss, see e.g. Moon et al. (2007). In contrast, the global field displays flux densities of only a few Gauss, (Babcock & Babcock, 1955; Mancuso & Garzelli, 2007).

Further, the chromosphere shows a cyclic behaviour as well. The chromospheric activity cycle is determined by the S-Index based on Ca II H&K measurements. The Mount Wilson Observatory Survey (Wilson, 1968) unveiled chromospheric activity cycles with periods between 3–21 yrs on several stars other than the Sun, (Baliunas et al., 1995; Frick et al., 2004; Lockwood et al., 2007). Phillips & Hartmann (1978) detected also stellar photospheric cycles and Lockwood et al. (2004, 2007) found evidence for the relation of both cycles. The Sun is photospherically bright during the chromospheric activity maximum due to plages as well as other older stars. For younger stars the photospheric and chromospheric cycle are often in anti-phase. This could be a hint that they are highly covered by dark star spots during the activity maximum, (Strassmeier, 2009).

The first magnetic activity cycle of a star other than our Sun was detected at τ Boo, (Donati et al., 2008a; Fares et al., 2009, 2013; Mengel et al., 2016; Jeffers et al., 2018). The large-

scale field reverses its polarity every ∼120 days during the maximum of its chromospheric cycle and inferred X-ray activity cycle, (Jeffers et al., 2018). Further, the K5 dwarf 61 Cyg A shows cyclic behaviour in their large-scale field polarity, (Boro Saikia et al., 2016; Jeffers et al., 2014), where 61 Cyg A chromospheric activity cycle is in phase with its photospheric magnetic cycle similar to the Sun. Also other stars are observed with multi-epochs show polarity flips, e.g. Petit et al. (2009); Morgenthaler et al. (2011); Fares et al. (2009); Mengel et al. (2016). However, there are also cool stars that show little variation or more or less stable large-scale fields, which is likely to be related to their low differential rotation, (Morin et al., 2008a).

See et al. (2016) combined the results of ZDI observed polarity reversals with chromospheric cycles. Plotting the chromospherically determined cycle period over rotation period or Rossby number[14], cool stars lie mainly on an active or inactive branch, (Brandenburg et al., 1998; Böhm-Vitense, 2007; Lehtinen et al., 2016). See et al. (2016) found that stars on the inactive branch show predominantly poloidal fields through their entire cycle, while the stars on the active branch show large temporal variations and significant toroidal fields. A possible explanation could be that the stellar magnetic field is formed by two different dynamos: the active branch stars may obtain a near surface shear layer dynamo, while the inactive branch stars host a shear layer dynamo at the tachocline (layer between the inner radiative core and outer convection zone) similar to the Sun, (Böhm-Vitense, 2007).

The Sun displays next to the strong Schwabe cycle also other cycles, see e.g. Gleissberg (1958). The different cycles modulate each other which seems to be common on spotted stars, (Oláh et al., 2007, 2009). Some stars show active longitudes as well, which were first observed on FK Com (Jetsu et al., 1991). They appear as two active longitudes usually 180° apart from each and are characterised by increased spot activity following a cyclic behaviour, (Korhonen et al., 2001). There are also hints of active longitudes on the Sun, (Berdyugina & Usoskin, 2003).

The stellar activity shows dependancies on various parameters. Skumanich (1972) found that chromospheric activity and stellar rotation rates decrease with age and related this to an increased magnetic activity with faster rotating stars. Other tracers of magnetic activity scale up with rotation as well as with later spectral type, (Hartmann & Noyes, 1987; Güdel, 2007;

[14]The Rossby number is again defined as the ratio between rotation period and turnover time in the convection cell, see page 19.

Reiners, 2012)[15]. Stars owning the same rotation period show an increased activity with lower mass and cooler effective temperature, (Donati & Landstreet, 2009; Marsden et al., 2014). Vidotto et al. (2014) analysed a large sample of cool stars and how different magnetic activity tracers evolve with age, rotation period, Rossby number and X-ray luminosity. Folsom et al. (2016); Folsom et al. (2018) enlarged this analysis by young solar-type objects. They confirmed the results of Saar (1996) and Reiners (2012) that the averaged field strength detected by ZB increases with Rossby number until it saturates for $R_o < 0.1$, which is also seen in X-ray luminosity, (Wright et al., 2011). Vidotto et al. (2014) also showed that the averaged large-scale field detected by ZDI follows the same trend, where the M dwarfs seem to be separated into two groups in the saturated regime. This was suggested by Donati et al. (2008b), who determined the maps of the early M Dwarfs, and might be caused by a different efficiencies in producing large- and small-scale fields. See et al. (2017) reports that the averaged unsigned magnetic field strength of the dipolar component follows the trend with inverse Rossby number as well.

1.5.2 Stellar magnetic field topology

The large ZDI surveys (MagIcS, BCool, MaTYSSE and Toupies) explored a wide range of cool stars and unveiled their magnetic field and further properties, e.g. Donati et al. (2006a); Marsden et al. (2006b); Petit et al. (2008); Morin et al. (2010); Fares et al. (2013); Jeffers et al. (2014); Folsom et al. (2016); Hébrard et al. (2016); Hill et al. (2017); Folsom et al. (2018). The large-scale field properties are summarised by Donati et al. (2011) in a very compact format, see Fig. 1.8:

- Stars with Rossby numbers $R_o > 1$ show generally weak fields, that are poloidal and axisymmetric, e.g. the Sun, 61 Cyg A.
- Stars with $R_o \lesssim 1$ and masses $M > 0.5\,\mathrm{M}_\odot$ obtain stronger fields, which are strongly or even dominantly toroidal with a mostly non-axisymmetric poloidal component, e.g. EK Dra, DS Leo
- Stars with $M < 0.5\,\mathrm{M}_\odot$ show two kinds of topologies: either strong, poloidal and axisymmetric fields or weaker, dominantly toroidal and non-axisymmetric fields,

[15] Further examples for magnetic activity tracers are the X-ray luminosity (Pallavicini et al., 1981; Walter & Bowyer, 1981), the chromospheric emission (Middelkoop, 1981; Mekkaden, 1985; Noyes et al., 1984) and the mean magnetic field (Vidotto et al., 2014; Folsom et al., 2016).

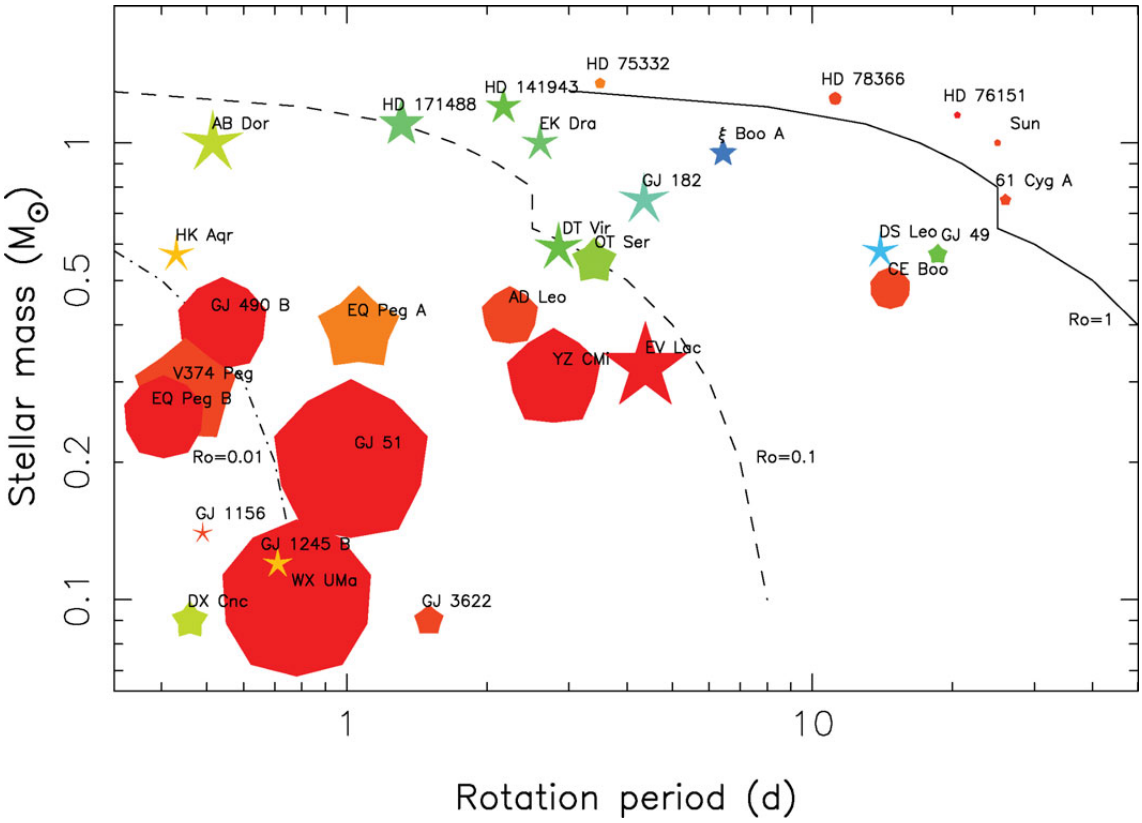

Figure 1.8: The large-scale magnetic field topology properties of cool stars as function of stellar mass and rotation rate. Symbol size relates to the relative magnetic energy densities from 1.5 kG to 3 G. The symbol colour indicates the poloidal/toroidal fraction with blue and red for purely toroidal and purely poloidal fields, respectively. The symbol shape illustrates the axisymmetry of the poloidal field component with decagons for purely axisymmetric and star-shapes for purely non-axisymmetric poloidal fields, respectively. The Rossby numbers $R_o = 1, 0.1$ and 0.01 are indicated by the solid, dashed and dash-dot line. Figure reproduced from Donati (2010, fig. 1) with permission.

e.g. WX Uma, DX Cnc

The M dwarfs (lower part of Fig. 1.8) are split in three subregimes by their magnetic topology: early M dwarfs, which are partly convective, show complex and weak fields that are toroidal and non-axisymmetric, (Donati et al., 2008b). Mid M dwarfs, which are fully convective, display simple and strong fields that are poloidal and axisymmetric, (Morin et al., 2008a). Late M dwarfs, which are fully convective as well, could obtain both topologies, (Morin et al., 2010). Vidotto et al. (2013) showed that the different large-scale magnetic field topologies of the early, mid and late M dwarfs widely affect the magnetosphere of potentially habitable planets. In contrast, the ZB measurements of the averaged unsigned magnetic field show no change in behaviour over the fully convective threshold for M dwarfs, (Reiners, 2012).

Reiners & Basri (2009) used the magnetic field measurements from Stokes V and I to determine the fraction of magnetic energy stored in the large-scale field compared to the total field for M dwarfs. They showed that the large-scale field detected with Stokes V hosts only $\approx 6\,\%$ of the total field for early M dwarfs having more complex field topologies and $\approx 14\,\%$ for mid M dwarfs having simple field topologies. Recently, we determined the fraction of magnetic flux recovered by ZDI compared to the measurements done with the ZB (See et al., 2019). We could confirm that ZDI detects only up to 20 % of the ZB measurements and found that both magnetic fluxes are related by a power law. The majority of the magnetic energy is hidden in the small-scale field and not detectable with ZDI.

Petit et al. (2008) found that for solar-like stars the energy fraction of the toroidal field increases with rotation. For rotation periods shorter than 12 days the toroidal component dominates. Also See et al. (2015) analysed the magnetic field topology of a large sample of 55 stars. They found that the toroidal field rises with inverse Rossby number steeper than the poloidal field. The poloidal and toroidal magnetic energy show two power law dependences: one for stars with masses above $0.5\,\mathrm{M}_\odot$ with $\langle B_{\mathrm{tor}}^2 \rangle \propto \langle B_{\mathrm{tor}}^2 \rangle^{1.25\pm0.06}$ and one for stars with masses below $0.5\,\mathrm{M}_\odot$ with $\langle B_{\mathrm{tor}}^2 \rangle \propto \langle B_{\mathrm{tor}}^2 \rangle^{0.72\pm0.08}$, see Fig. 1.9.

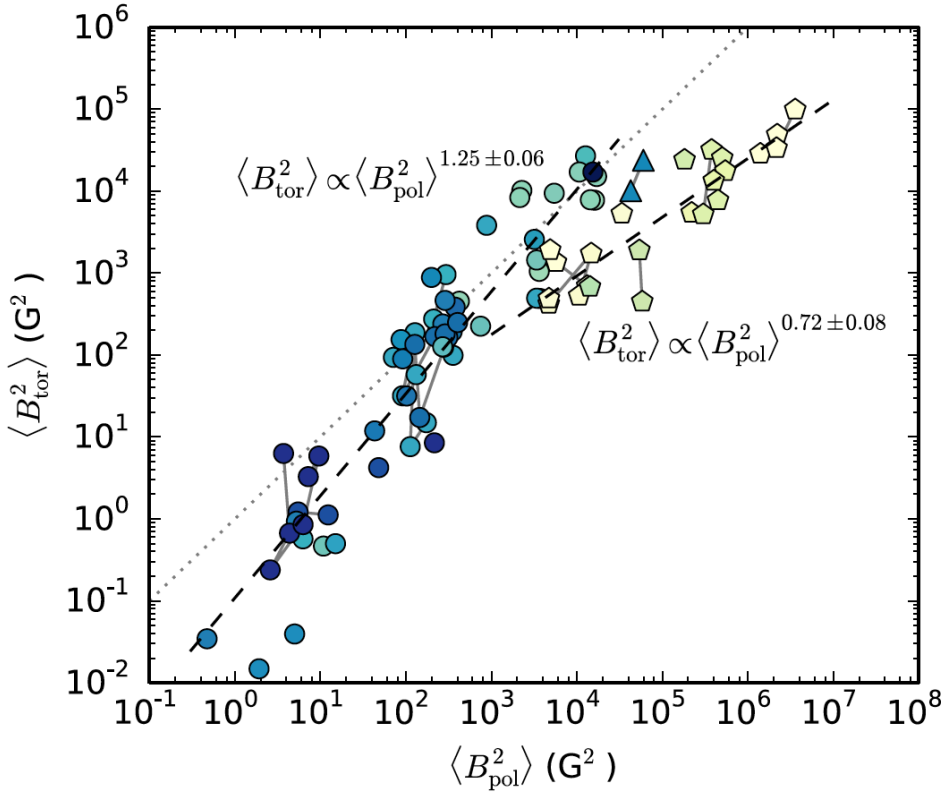

Figure 1.9: The toroidal against poloidal magnetic energy for 55 cool stars colour-coded by mass. The colours get lighter with decreasing mass from 1.5−0.1 $M_\odot$. Stars with multiple epochs are connected by grey lines. The dashed lines indicate the best fits for stars with masses above 0.5 $M_\odot$ and for stars with masses below 0.5 $M_\odot$. The dotted line displays equal toroidal and poloidal energies. Figure reproduced from See et al. (2015, fig. 2 top) with permission.

2

Basics

In this Chapter, I present the basics of my thesis projects. I start with the spherical harmonic decomposition method, which allows, e.g., the extraction of the large-scale magnetic field topology, followed by the definitions of the most used magnetic field parameters, see Section 2.1. The base of my projects are the 3D non-potential flux transport simulations, which are introduced in Section 2.2. Further, I present the modulation of the Stokes IV profiles, see Section 2.3, which are the input for the Zeeman-Doppler-Imaging (ZDI) code, see Section 2.4. Furthermore, I present two tests: one about the line profile sensitivity to different length scales of magnetic structures under varying projected equatorial rotation velocities, see Section 2.3.2 and one test about the usage of the different magnetic field descriptions for solar-like stars, see Section 2.4.1.

2.1 Definitions and decomposition method

A major analysis tool of my thesis is the spherical harmonic decomposition after Vidotto (2016). The method decomposes the surface vector magnetic field of, e.g., highly resolved simu-

lated maps into their single harmonic modes and returns the coefficients $\alpha_{\ell m}, \beta_{\ell m}$ and $\gamma_{\ell m}$ of Eq. 1.26. This inversion of the magnetic field equations allows the analysis of the input magnetic field map in terms of every length scale of the magnetic field structures given by the modes ℓ and m[1], see also Chapter 3.

For my PhD thesis I wrote a spherical harmonic decomposition code based on Vidotto (2016). In the following, I briefly report the inversion of the magnetic field equations for the determination of the coefficients $\alpha_{\ell m}, \beta_{\ell m}$ and $\gamma_{\ell m}$. This derivation is based on Vidotto (2016, section 2), where all details can be found.

Eq. 1.26 can be rewritten as

$$B_r(\theta,\phi) = \sum_{\ell m} \alpha_{\ell m} Y_{\ell m}(\theta,\phi), \tag{2.1}$$

$$B_\theta(\theta,\phi) = \sum_{\ell m} \beta_{\ell m} Z_{\ell m}(\theta,\phi) + \gamma_{\ell m} X_{\ell m}(\theta,\phi), \tag{2.2}$$

$$B_\phi(\theta,\phi) = -\sum_{\ell m} \beta_{\ell m} X_{\ell m}(\theta,\phi) - \gamma_{\ell m} Z_{\ell m}(\theta,\phi), \tag{2.3}$$

where

$$Y_{\ell m}(\theta,\phi) = P_{\ell m} e^{im\phi}, \tag{2.4}$$

$$X_{\ell m}(\theta,\phi) = \frac{1}{(\ell+1)\sin\theta} \frac{\partial Y_{\ell m}(\theta,\phi)}{\partial \phi} = \frac{imP_{\ell m} e^{im\phi}}{(\ell+1)\sin\theta}, \tag{2.5}$$

$$Z_{\ell m}(\theta,\phi) = \frac{1}{\ell+1} \frac{\partial Y_{\ell m}(\theta,\phi)}{\partial \theta} = \frac{1}{\ell+1} \frac{\mathrm{d}P_{\ell m}}{\mathrm{d}\theta} e^{im\phi}. \tag{2.6}$$

The vector spherical harmonics $\mathbf{Y}_{\ell m} = Y_{\ell m}(\theta,\phi)\hat{\mathbf{r}}$ and

$$\mathbf{\Psi}_{\ell m} = \nabla Y_{\ell m}(\theta,\phi) = \frac{\partial Y_{\ell m}}{\partial \theta}\hat{\boldsymbol{\theta}} + \frac{1}{\sin\theta}\frac{\partial Y_{\ell m}}{\partial \phi}\hat{\boldsymbol{\phi}} = (\ell+1) Z_{\ell m}\hat{\boldsymbol{\theta}} + (\ell+1) X_{\ell m}\hat{\boldsymbol{\phi}}. \tag{2.7}$$

show the following orthogonal properties (Barrera et al., 1985; Carrascal et al., 1991): The surface integral $\left(\int \mathrm{d}\Omega = \int \sin\theta \mathrm{d}\theta \mathrm{d}\phi\right)$ over the vector spherical harmonic modes and their

[1]The angular size of the magnetic structures ϑ is approximately given by $\vartheta = \frac{180^\circ}{\ell}$.

complex conjugated modes (indicated by '$*$') is only non-zero for $\ell = \ell'$ and $m = m'$,

$$\int \mathbf{Y}_{\ell m} \cdot \mathbf{Y}^*_{\ell' m'} \mathrm{d}\Omega = \int Y_{\ell m} Y^*_{\ell' m'} \mathrm{d}\Omega = \delta_{\ell' \ell} \delta_{m' m}, \tag{2.8}$$

$$\int \mathbf{\Psi}_{\ell m} \cdot \mathbf{\Psi}^*_{\ell' m'} \mathrm{d}\Omega = \ell(\ell+1) \delta_{\ell' \ell} \delta_{m' m}. \tag{2.9}$$

Combining Eq. 2.7 and 2.9 results in:

$$\int \left(Z_{\ell m} Z^*_{\ell' m'} + X_{\ell m} X^*_{\ell' m'} \right) \mathrm{d}\Omega = \frac{\ell}{\ell+1} \delta_{\ell' \ell} \delta_{m' m}. \tag{2.10}$$

To derive the coefficients $\alpha_{\ell m}, \beta_{\ell m}$ and $\gamma_{\ell m}$, one multiplies the Eqs. 2.1-2.3 with the matching complex conjugated modes and integrates over the stellar surface. The coefficients $\alpha_{\ell m}, \beta_{\ell m}$ and $\gamma_{\ell m}$ are complex numbers, e.g., $\alpha_{\ell m} = \Re(\alpha_{\ell m}) + i\Im(\alpha_{\ell m})$.

To compute $\alpha_{\ell m}$, Eq. 2.1 is multiplied with $Y^*_{\ell' m'}$ and integrated over the stellar surface, while the orthogonal property (Eq. 2.8) is used:

$$\int B_r(\theta, \phi) Y^*_{\ell' m'} \mathrm{d}\Omega = \int \sum_{\ell m} \alpha_{\ell m} Y_{\ell m} Y^*_{\ell' m'} \mathrm{d}\Omega = \sum_{\ell m} \alpha_{\ell m} \delta_{\ell' \ell} \delta_{m' m} = \alpha_{\ell' m'}. \tag{2.11}$$

This results in the following equations for the real and imaginary part of $\alpha_{\ell m}$ using that

$$Y^*_{\ell' m'} = P_{\ell' m'} \left(e^{i m' \phi} \right)^* = P_{\ell' m'} \left(\cos(m'\phi) + i \sin(m'\phi) \right)^* = P_{\ell' m'} \left(\cos(m'\phi) - i \sin(m'\phi) \right) \tag{2.12}$$

and by dropping the prime symbols $'$:

$$\begin{aligned} \Re(\alpha_{\ell m}) &= \int B_r(\theta, \phi) P_{\ell m} \cos(m\phi) \mathrm{d}\Omega, \\ \Im(\alpha_{\ell m}) &= -\int B_r(\theta, \phi) P_{\ell m} \sin(m\phi) \mathrm{d}\Omega. \end{aligned} \tag{2.13}$$

To compute $\beta_{\ell m}$ one needs to multiply Eq. 2.2 by $Z^*_{\ell' m'}$ and Eq. 2.3 by $-X^*_{\ell' m'}$ and integrate

the summed result over the stellar surface:

$$\begin{aligned}
&\int \left[B_\theta(\theta,\phi)Z^*_{\ell'm'} - B_\phi(\theta,\phi)X^*_{\ell'm'}\right]\mathrm{d}\Omega \\
&= \int \sum_{\ell m}\beta_{\ell m}\left[Z^*_{\ell'm'}Z_{\ell m} + X^*_{\ell'm'}X_{\ell m}\right]\mathrm{d}\Omega + \int \sum_{\ell m}\gamma_{\ell m}\left[Z^*_{\ell'm'}X_{\ell m} - X^*_{\ell'm'}Z_{\ell m}\right]\mathrm{d}\Omega \\
&= \sum_{\ell m}\beta_{\ell m}\frac{\ell}{\ell+1}\delta_{\ell'\ell}\delta_{m'm} = \beta_{\ell'm'}\frac{\ell'}{\ell'+1}.
\end{aligned} \tag{2.14}$$

The orthogonal property (Eq. 2.9) was used, so that the integral $\int \sum_{\ell m}\gamma_{\ell m}[Z^*_{\ell'm'}X_{\ell m} - X^*_{\ell'm'}Z_{\ell m}]\mathrm{d}\Omega$ cancels to zero after some algebraic manipulation, which can be seen in Vidotto (2016, appendix A). The real and imaginary part of $\beta_{\ell m}$ is then:

$$\begin{aligned}
\Re(\beta_{\ell m}) &= \frac{1}{\ell}\int\left[B_\theta(\theta,\phi)\frac{\mathrm{d}P_{\ell m}}{\mathrm{d}\theta}\cos(m\phi) + B_\phi(\theta,\phi)\frac{mP_{\ell m}}{\sin\theta}\sin(m\phi)\right]\mathrm{d}\Omega, \\
\Im(\beta_{\ell m}) &= -\frac{1}{\ell}\int\left[B_\theta(\theta,\phi)\frac{\mathrm{d}P_{\ell m}}{\mathrm{d}\theta}\sin(m\phi) - B_\phi(\theta,\phi)\frac{mP_{\ell m}}{\sin\theta}\cos(m\phi)\right]\mathrm{d}\Omega.
\end{aligned} \tag{2.15}$$

The computation of $\gamma_{\ell m}$ is comparable to the computation of $\beta_{\ell m}$. Now the Eq. 2.2 is multiplied by $X^*_{\ell'm'}$ and Eq. 2.3 by $Z^*_{\ell'm'}$. The summed result is again integrated over the stellar surface, while the orthogonal property (Eq. 2.9) is applied:

$$\begin{aligned}
&\int \left[B_\theta(\theta,\phi)X^*_{\ell'm'} + B_\phi(\theta,\phi)Z^*_{\ell'm'}\right]\mathrm{d}\Omega \\
&= \int \sum_{\ell m}\beta_{\ell m}\left[X^*_{\ell'm'}Z_{\ell m} - Z^*_{\ell'm'}X_{\ell m}\right]\mathrm{d}\Omega + \int \sum_{\ell m}\gamma_{\ell m}\left[X^*_{\ell'm'}X_{\ell m} + Z^*_{\ell'm'}Z_{\ell m}\right]\mathrm{d}\Omega \\
&= \sum_{\ell m}\gamma_{\ell m}\frac{\ell}{\ell+1}\delta_{\ell'\ell}\delta_{m'm} = \gamma_{\ell'm'}\frac{\ell'}{\ell'+1}.
\end{aligned} \tag{2.16}$$

Vidotto (2016, appendix A) proves that the integral $\int \sum_{\ell m}\beta_{\ell m}\left[X^*_{\ell'm'}Z_{\ell m} - Z^*_{\ell'm'}X_{\ell m}\right]\mathrm{d}\Omega$ cancels to zero, so that the real and imaginary part of $\gamma_{\ell m}$ are:

$$\begin{aligned}
\Re(\gamma_{\ell m}) &= -\frac{1}{\ell}\int\left[B_\theta(\theta,\phi)\frac{mP_{\ell m}}{\sin\theta}\sin(m\phi) - B_\phi(\theta,\phi)\frac{\mathrm{d}P_{\ell m}}{\mathrm{d}\theta}\cos(m\phi)\right]\mathrm{d}\Omega, \\
\Im(\gamma_{\ell m}) &= -\frac{1}{\ell}\int\left[B_\theta(\theta,\phi)\frac{mP_{\ell m}}{\sin\theta}\cos(m\phi) + B_\phi(\theta,\phi)\frac{\mathrm{d}P_{\ell m}}{\mathrm{d}\theta}\sin(m\phi)\right]\mathrm{d}\Omega.
\end{aligned} \tag{2.17}$$

To calculate the spherical harmonics coefficients, only the surface vector magnetic field

(B_r, B_θ, B_ϕ) is now needed. The radial, azimuthal and meridional magnetic field maps are usually provided as bi-dimensional discrete arrays (latitude versus longitude). In my case, I used 180 latitudinal grid points and 360 longitudinal grid points and interpolate to this grid resolution if necessary by applying the CONGRID function of the programming language IDL. Vidotto (2016) provided a discrete form of the Eq. 2.13, 2.15 and 2.17 in the appendix B of her paper. The integral of the equations become discrete sums and the arrays of the magnetic field components are inserted straight forward to determine the real and imaginary part of the coefficients for certain ℓ and m modes. For the calculation, I used the programming language IDL, which is optimized to run matrices operations. The mathematical operations are applied to the different arrays directly without running through every single matrix element by, e.g., FOR loops, which drastically fastens the code.

By only entering the surface vector magnetic field (B_r, B_θ and B_ϕ) of all kind of simulations or observations I can determine the coefficients $\alpha_{\ell m}, \beta_{\ell m}$ and $\gamma_{\ell m}$ and analyse the magnetic field regarding different length scales of the magnetic structures given by the ℓ-mode. The resolution of the map is determined by the maximum $\ell_{\max}$-mode. The coefficients with ℓ or m modes higher than $\ell_{\max}$ are zero or contain noise.

I determine the averaged magnetic field or further parameters of the magnetic field topology either for specific length scales identified by the single ℓ-modes or for sub-structures, e.g., the large-scale field, identified by the cumulative ℓ_Σ-modes. The cumulative ℓ_Σ-modes include all lower ℓ-modes. For example the large-scale field of $\ell_\Sigma = 5$ contains all ℓ-modes $\ell = 1$ to $\ell = 5$.

My analysis of the magnetic field topology is mainly parameter based. For that, I mostly use the mean squared flux density over the stellar surface ($\mathrm{d}\Omega = \sin\theta \mathrm{d}\theta \mathrm{d}\phi$) ,

$$\langle B_k^2 \rangle = \frac{1}{4\pi} \int B_k^2(\theta, \phi) \mathrm{d}\Omega, \quad k \in (r, \theta, \phi) \text{ or } k \in (\mathrm{pol}, \mathrm{tor}), \tag{2.18}$$

$$\langle B_{\mathrm{tot}}^2 \rangle = \frac{1}{4\pi} \int \sum_k B_k^2(\theta, \phi) \mathrm{d}\Omega, \quad k \in (r, \theta, \phi), \tag{2.19}$$

which is also called the magnetic energy, e.g., see review from Reiners (2012). For the simulated maps, $\langle B^2 \rangle \left[G^2\right]$ is a very good proxy for the magnetic energy but not equivalent. To get the magnetic energy density the factor $\frac{1}{2\mu}$ is missing, where μ is the permeability. For the observed and ZDI reconstructed maps, $\langle B^2 \rangle \left[G^2\right]$ is restricted to the net magnetic flux energy

per resolution element. Nevertheless, I call $\langle B^2 \rangle \left[G^2\right]$ in the following magnetic energy to be consistent with the literature and my publications. Additionally, I compute the total surface average field,

$$\langle B_{\rm tot} \rangle = \frac{1}{4\pi} \int \sqrt{\sum_k B_k^2(\theta,\phi)} {\rm d}\Omega, \quad k \in (r,\theta,\phi). \tag{2.20}$$

Further, I calculate the fraction of certain field components, e.g., for spherical polar or the poloidal and toroidal coordinates, dividing the magnetic energy of the field component by the total magnetic energy,

$$f_k = \frac{\langle B_k^2 \rangle}{\langle B_{\rm tot}^2 \rangle}, \quad k \in (r,\theta,\phi) \text{ or } k \in ({\rm pol}, {\rm tor}). \tag{2.21}$$

The determination of the magnetic energy and its fractions is often done for specific ℓ-modes, e.g. $\langle B_{\ell=2}^2 \rangle, f_{\ell=2}$, or for cumulative ℓ_Σ-modes, e.g. $\langle B_{\ell_\Sigma=5}^2 \rangle, f_{\ell_\Sigma=5}$. For the axisymmetric fraction I divide the magnetic energy of the axisymmetric modes $(m=0,\ell)$ or $(m=0,\ell_\Sigma)$ by the magnetic energy of all m-modes $(\sum m,\ell)$ or $(\sum m,\ell_\Sigma)$,

$$f_{{\rm axi},\ell} = \frac{\langle B_{m=0,\ell}^2 \rangle}{\sum_m \langle B_{m,\ell}^2 \rangle} \quad \text{or} \quad f_{{\rm axi},\ell_\Sigma} = \frac{\langle B_{m=0,\ell_\Sigma}^2 \rangle}{\sum_m \langle B_{m,\ell_\Sigma}^2 \rangle}. \tag{2.22}$$

For the non-axisymmetric fraction, the magnetic energy of all non-axisymmetric modes $(m \neq 0,\ell)$ or $(m \neq 0,\ell_\Sigma)$ is accordingly divided by the magnetic energy of all m-modes $(\sum m,\ell)$ or $(\sum m,\ell_\Sigma)$.

2.2 The 3D non-potential flux transport simulations

My thesis projects are grounded on the solar-based 3D non-potential flux transport simulations, which were provided by our collaborator Duncan Mackay. I am using the surface vector magnetic field maps of two simulation sets:

1. the simulated Sun at activity maximum and further simulated stars that are scaled to the solar activity level, see Chapter 3 and 4, and

2. long time solar simulations covering 15 years including the solar cycle 23 and the beginning of solar cycle 24, see Chapter 5.

Both sets are based on the non-potential model of van Ballegooijen et al. (2000) and its further developments by Gibb et al. (2016) and Yeates & Mackay (2012). In the following, I describe the flux transport model and the shared properties of the simulations. The unique details of the different simulation sets can be found in the corresponding chapters (3.2, 4.2, and 5.2.1).

The non-potential flux transport model connects the photospheric magnetic field evolution with the coronal field evolution above via the magnetofricational technique (van Ballegooijen et al., 2000). The magnetic field at the photosphere evolves under the emergence of buoyant flux tubes[2], the advection of flux by the large-scale surface flux motions of differential rotation and meridional flow and the diffusion of flux due to small-scale motions of convective cells or flux cancellation across the polarity inversion line. The coronal field response to the flux emergence and the changing photospheric field is through a mixture of twisting, shearing and reconnecting coronal field lines. The model simulates the non-potential 3D vector magnetic field from the stellar surface to the outer boundary at source surface ($r = 2.5\,\mathrm{R}_\odot$). At the source surface the magnetic field lines are forced to be completely open meaning the magnetic field is purely radial, assuming that the thermal pressure is strong enough to open up all field lines, see Altschuler & Newkirk (1969). The properties of the emerging flux are based on solar synoptic maps observed by the National Solar Observatory (NSO), Kitt Peak (KP).

It starts with the evolution of the photospheric radial field

$$B_r = \frac{1}{\mathrm{R}_\odot \sin\theta}\left[\frac{\partial}{\partial\theta}(\sin\theta A_\phi) - \frac{\partial A_\theta}{\partial\phi}\right] \tag{2.23}$$

by solving the two dimensional flux transport equations of the vector potential A_θ and A_ϕ in spherical coordinates, see e.g. Yeates (2014); Gibb et al. (2014):

$$\begin{aligned}\frac{\partial A_\theta}{\partial t} &= u_\phi B_r - \frac{D}{\mathrm{R}_\odot \sin\theta}\frac{\partial B_r}{\partial\phi} + S_\theta(\theta,\phi,t),\\ \frac{\partial A_\phi}{\partial t} &= -u_\theta B_r + \frac{D}{\mathrm{R}_\odot}\frac{\partial B_r}{\partial\theta} + S_\phi(\theta,\phi,t).\end{aligned} \tag{2.24}$$

The diffusion constant $D = 450\,\mathrm{km^2 s^{-1}}$ models the diffusion process of granulation and supergranulation (Leighton, 1964). The source terms S_θ and S_ϕ allow the injection of new magnetic

[2]It should be mentioned that the non-potential flux transport models used here simulate the emergence of flux tubes in an ad hoc fashion and does not model the flux emergence process itself.

flux. The azimuthal velocity u_ϕ is determined via the differential rotation profile $\Omega(\theta)$, so that

$$u_\phi = \Omega(\theta) \mathrm{R}_\odot \sin\theta. \tag{2.25}$$

The differential rotation profile, $\Omega(\theta)$, is different for the two sets of simulations. The first set (Chapter 3 and 4) obtains a scalable simplified version of the solar differential rotation profile,

$$\Omega(\theta) = K(\Omega_0 - \mathrm{d}\Omega_\odot \cos^2\theta)\,\mathrm{deg\,d^{-1}}, \tag{2.26}$$

where $\Omega_0 = 0.9215\,\mathrm{deg\,d^{-1}}$, $\mathrm{d}\Omega_\odot = 3.65\,\mathrm{deg\,d^{-1}}$ and the scaling factor $K = 0.3 - 5$. The second set (Chapter 5) uses the differential rotation profile based on the solar observations by Snodgrass (1983),

$$\Omega(\theta) = (0.18 - 2.30\cos^2\theta - 1.62\cos^4\theta)\,\mathrm{deg\,d^{-1}}. \tag{2.27}$$

The meridional velocity u_θ is given by the meridional flow profile after Schüssler & Baumann (2006),

$$u_\theta = C\frac{16}{110}\sin(2\lambda)\exp(\pi - 2|\lambda|), \tag{2.28}$$

where $\lambda = \pi/2 - \theta$ is the latitude and $C = 11\,\mathrm{m\,s^{-1}}$ the peak solar flow[3]. Both differential rotation profiles and the meridional flow profile are displayed in Fig. 2.1.

The source terms S_θ and S_ϕ in Eq. 2.24 allow the emergence of new magnetic flux. This is done by inserting individual twisted bipoles mimicking active regions rather than using functional source terms (Mackay & van Ballegooijen, 2001; Mackay & van Ballegooijen, 2006). The 3D bipoles are modelled as idealised twisted flux tubes with two footpoints of opposite polarity breaking through the solar surface (Yeates et al., 2008). The bipole model of Yeates et al. (2008) is used for both sets of simulations, where several properties (e.g. peak field strength, spot separation, tilt angle, etc.) are determined from the solar synoptic maps observed by NSO/KP using a semi-automated technique to identify bipoles with fluxes over 50 G (Yeates, 2014). However, the individual bipole properties are different for the two sets of simulations and can be found in the Sections 3.2 and 5.2.1. The steps of inserting the bipoles into the running simulation are reported in Yeates et al. (2008) and Gibb et al. (2016).

[3] In Chapter 3 I also use simulations where the meridional flow is enhanced by a factor of ten, so that $C = 110\,\mathrm{m\,s^{-1}}$, see Section 3.2, page 56.

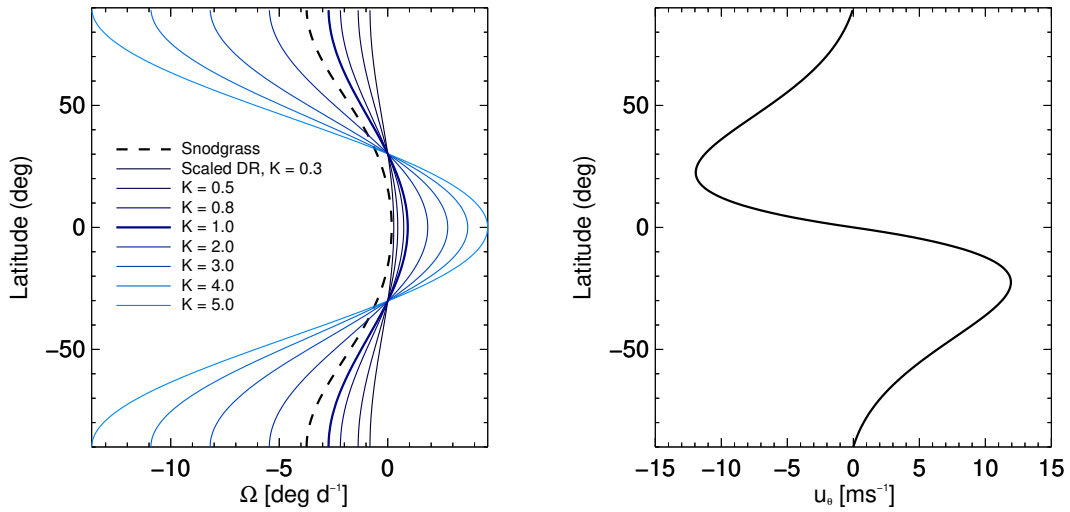

Figure 2.1: Left: The differential rotation profiles $\Omega(\theta)$. The solid lines plot the scalable solar differential profile of Eq. 2.26 for different scale factors K indicated by colour, see legend. The dashed line displays the differential profile of Snodgrass (1983), Eq. 2.27. Right: The meridional flow profile u_θ is displayed where negative values describe the flow towards the northern pole and positive values towards the southern pole.

The simulations run on a non-uniform spherical grid whose resolution reduces from 384 or 192 grid points in longitude at the equator for set 1 or 2 to 12 grid points at the polar grid boundary (±89.5° latitude)[4]. For further detail see Yeates (2014, appendix A). The initialisation of the coronal field in the simulations is done via the potential field extrapolation of a synoptic map from NSO/KP. Each set uses a different initialisation map, see Section 3.2 and 5.2.1.

The evolution of the photospheric magnetic field determines the evolution of the coronal field. The magnetofrictional technique (Yang et al., 1986) enables this link by introducing a velocity parallel to the Lorentz force in the induction equation. The changing magnetic field is therefore advected from the photosphere through a series of non-linear force-free equilibria. The introduction of a further radial outflow velocity forces the coronal magnetic field to be purely radial at the outer boundary ($r = 2.5\,\mathrm{R}_\odot$) (Mackay & van Ballegooijen, 2006). The coronal field evolution influences the evolution of the photosphere. I am only using the photospheric magnetic field maps from the simulations. Further details on the evolution of the coronal field of the simulations can be found in Yeates & Mackay (2012); Gibb et al. (2016).

[4]This corresponds to an angular resolution of 0.9375° or 1.875° at the equator for set 1 or 2 and 30° at the poles.

2.3 The modulation of the line profiles

In Chapter 4 and 5, I use the ZDI technique to 'observe' the simulations. To do so, I need to model the polarimetric line profiles of the simulations first. I describe the modulation of the line profiles in Section 2.3.1 and analyse the effect of the equatorial projected rotational velocity $v_e \sin i$ on the resolution of the Stokes V profiles in Section 2.3.2. These sections are based on section 3.1 and 3.2 of my paper Lehmann et al. (2019).

2.3.1 The modulation of the Stokes I and V profiles

For the modulation of the line profiles I used a code provided by our collaborator Gaitee Hussain, which is based on Hussain et al. (2016).

The local Stokes I profiles are modelled as Gaussian, based on a Milne Eddington line profile, whose parameters are fine-tuned to match the Least Squares Deconvolution (LSD, see page 17) like mean profile of the solar twin 18 Sco[5] as described in Alvarado-Gómez et al. (2015b). I use the linear limb darkening relation published by Sing (2010) and apply a slope of $u \approx 0.65$ for solar-type stars. The local Stokes V profiles $V(v)$ are modelled as the derivative of the local Stokes I profiles $I(v)$ by applying the weak-field approximation,

$$V(v) \propto g B_{\rm los} \frac{\partial I(v)}{\partial v}, \tag{2.29}$$

where g is the Landé factor of a spectral line and $B_{\rm los}$ the line-of-sight magnetic field, (Reiners, 2012). The weak-field approximation (Unno, 1956; Stenflo, 1994) holds if the Zeeman splitting is much smaller than the Doppler width of the spectral line, which is the case for stellar fields less than 1 kG. The large-scale solar field is only a few Gauss, so the weak-field approximation should be more than safe to use for solar-like stars. I assume an effective Landé factor of $g \approx 1.2$, which is typical for LSD profiles of G-type stars.

The stellar surface is divided into pixels. The grid size is determined by the number of latitudes ($n_{\rm lat} = 180$). The calculation of the relative contribution of the stellar pixel to the intensity profile is determined by the foreshortening angle of that pixel, which includes the check if that particular stellar pixel is visible or not. The velocity associated with that particular pixel is also calculated and used to shift the contribution of the local line profile. Simultaneously,

[5]The G2 dwarf 18 Sco is a slowly rotating ($P_{\rm rot} = 22.7 \pm 0.5$ d) solar twin with a $v_e \sin i = 2.1 \pm 0.5\,{\rm km\,s^{-1}}$ and often named as one of the best solar twins, (Petit et al., 2008; Marsden et al., 2014).

the limb angle is determined and used to adjust the pixels intensity according to the linear limb darkening law. Finally, the local Stokes profiles are binned to 30 velocity bins across the stellar disc ranging from $-20\,\mathrm{km\ s^{-1}}$ to $20\,\mathrm{km\ s^{-1}}$, which corresponds to a spectral resolution of similar to HARPS.

The disc-integrated Stokes I and V profiles are always modelled from the fully resolved simulated surface field map using the rotation period and $v_e \sin i$ of the modelled star. For the simulations representing the Sun a rotation period of $P_{\mathrm{rot}} = 27.0\,\mathrm{d}$ and a $v_e \sin i = 0.64\,\mathrm{km\,s^{-1}}$ or $1.62\,\mathrm{km\,s^{-1}}$ is assumed corresponding to an inclination of $i = 20°$ and $i = 60°$. For the simulations representing stars less or more active as the Sun the rotation periods and $v_e \sin i$ values can be found in the Tables 3.1 and 4.1. Each time series consists of 25 sets of Stokes IV profiles, which are equally spaced in observational phase (every 14.4°). The brightness distribution cannot be reconstructed for the slowly rotating and relatively low activity stars that were simulated. A uniform brightness is therefore assumed for the generation of the disc-integrated Stokes IV profiles. Further, Gaussian noise is added to the line profiles. The level of noise is different for each set of simulations and can be found next to further details of line profile modulation in the Sections 4.2 and 5.2.2.

2.3.2 The effect of the projected equatorial velocity $v_e \sin i$ on the resolution of the Stokes V profiles

One of the main aims of my PhD thesis is to understand the limitations of ZDI. ZDI can only detect or observe what is captured in the Stokes profiles. I started therefore a small analysis of what effect $v_e \sin i$ has on the resolution of the line profiles[6].

The highly resolved simulated magnetic field maps in combination with the spherical harmonic decomposition enables me to investigate the influence of magnetic structures of different length scales on the Stokes V profiles. First, I want to estimate at which length scale magnetic structures no longer contribute to the observed Stokes V profiles. I modelled the Stokes V profiles of two magnetic maps including an increasing number of ℓ_Σ-modes to determine the length-scale beyond which the Stokes V profiles do not change significantly. The Stokes V profiles are than "blind" to magnetic structures smaller than the length-scale given

[6]It is widely known that the resolution of stellar magnetic field structures dependences on $v_e \sin i$, see e.g. Morin et al. (2008b, 2010). However, until the publication of Lehmann et al. (2019) there has not been a comprehensive exploration of the limited spatial resolution effects on a large set of input maps including structures from $\ell_\Sigma = 1-28$ for slow rotators with $v_e \sin i = 1.6-24\,\mathrm{km\,s^{-1}}$.

Table 2.1: The artificially increased rotation periods and the corresponding velocities v_e and $v_e \sin i$ for investigating the effect of $v_e \sin i$ on the resolution of the Stokes V profiles.

$P_{\rm rot}$ [d]	v_e [km/s]	$v_e \sin i$ [km/s] $i = 20°$	$v_e \sin i$ [km/s] $i = 60°$
10.95	4.62	1.58	4.00
5.48	9.24	3.16	8.00
3.65	13.86	4.74	12.00
2.74	18.48	6.32	16.00
2.19	23.10	7.90	20.00
1.83	27.70	9.48	24.00
0.49	104.00	35.54	90.00

by this threshold ℓ-mode. The equatorial projected rotational velocity $v_e \sin i$ of the star shows the strongest influence on the result and has a direct impact on the spatial resolution that Doppler Imaging can cover. Morin et al. (2010) present a rule of thumb for determining the spatial resolution in terms of ℓ-modes,

$$\ell_{\rm max} \simeq \max\left(\frac{2\pi v_e \sin i}{\rm FWHM}, \ell_{\rm min}\right), \tag{2.30}$$

where FWHM is the full-width half-maximum of the Stokes I profile and $\ell_{\rm min}$ the assumed minimal resolution for very slow rotators typically $\ell_{\rm min} = 4-8$.

I modelled the Stokes V profiles for three stars of the simulation set introduced in Chapter 4, representing the Sun, a three and a five times more active star in terms of differential rotation and flux emergence rate. I used the method described in the previous section without applying any noise. I selected 10 maps per star covering the timeframe of one year and computed the line profiles for the input maps including the modes $\ell_\Sigma = 1, 2, \ldots, 28$. The stars are spun up to artificially high rotation periods from $P_{\rm rot} \approx 11$ days to ≈ 0.5 days corresponding to $v_e \sin i = 4 - 90\,{\rm km\,s^{-1}}$ for $i = 60°$. I analysed the effect of inclination as well by modelling the profiles for an inclination angle of 20° and 60°. Table 2.1 lists the applied rotation periods and velocities.

Fig. 2.2 shows the Stokes V profiles for an example solar map observed with an inclination of 20° (near pole-on) at the top row and for an example map for a five times more active star observed with an inclination of 60° (near equator-on) at the bottom row. Their Stokes V profiles are presented for three different rotation periods decreasing from left to right. The colour of the line profiles indicates the number of included ℓ_Σ-modes, see also colour bar on the right. For the low $v_e \sin i \leq 5\,{\rm km\,s^{-1}}$ the Stokes V profiles remain unchanged after including

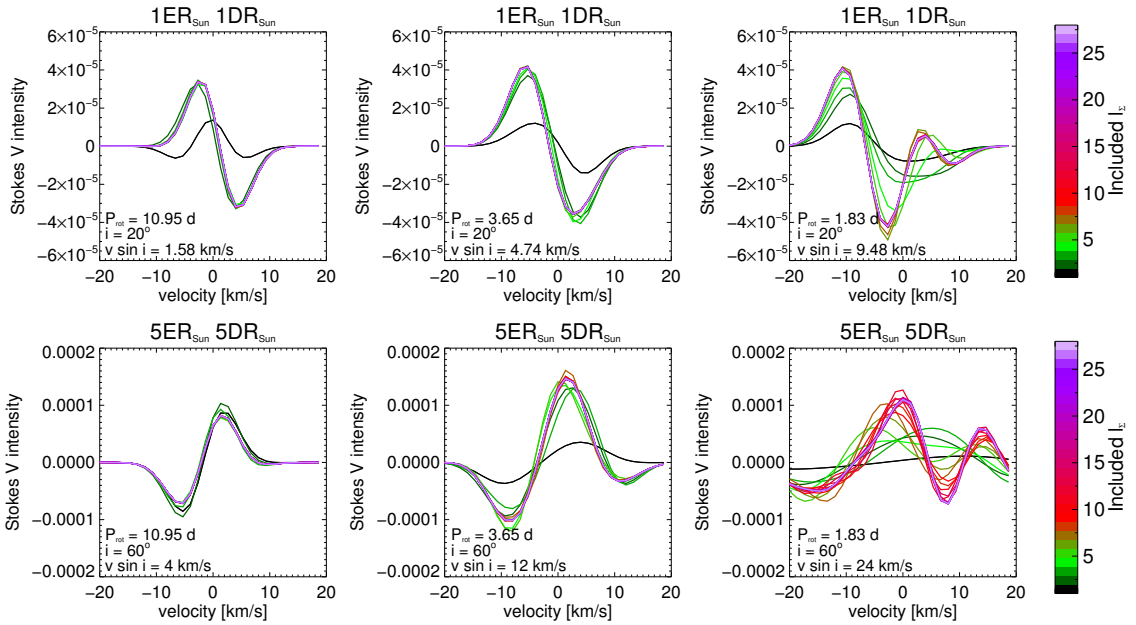

Figure 2.2: The Stokes V profiles of an example phase modelled from a map of the solar-like star observed at $i = 20°$(top row) and from a map of the most active star (five times more active than the Sun) observed at $i = 60°$ (bottom row). These are representative of the changes seen over the entire time-series in each case. The rotation periods are artificially increased (from left to right) and the Stokes V profiles are generated by including more and more ℓ_Σ-modes, i.e. smaller scale structures, of the input map (see colour bar on the left).

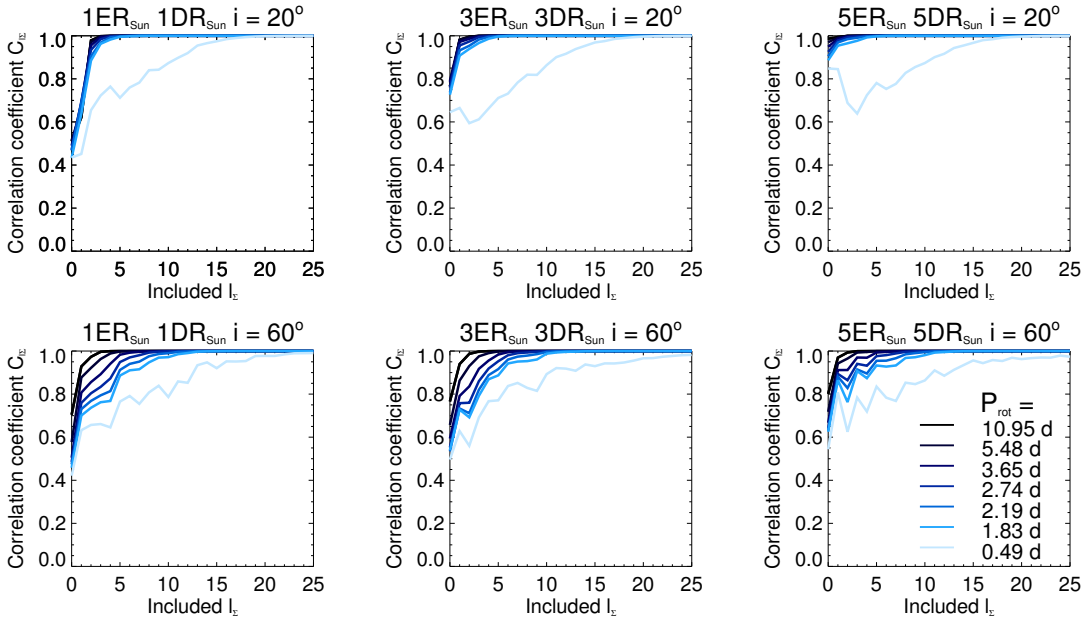

Figure 2.3: The correlation coefficient C_{ℓ_Σ} between two successive ℓ_Σ-modes for the three different stars (left to right) and the lower inclination $i = 20°$ (top row) and the higher inclination $i = 60°$ (bottom row). The colour of the curves indicates the applied rotation period.

modes higher than $\ell_\Sigma = 5$. The threshold ℓ_Σ increases with increasing $v_e \sin i$, e.g., $\ell_\Sigma = 15$ for $v_e \sin i = 24\,\mathrm{km\,s^{-1}}$. The inclination angle influences the structure of the Stokes V profiles for solar-like stars, too. For low inclinations only the polar region is visible, which produces fewer and simpler magnetic field structures. For high inclinations the more magnetically structured equatorial region becomes detectable.

To quantify the influence of the included ℓ_Σ-modes, I determined the correlation coefficient between two Stokes V profiles (V_{ℓ_Σ}) of successive ℓ_Σ-modes and averaged them over the ten maps per star ($n_{\mathrm{map}} = 10$),

$$C_{\ell_\Sigma,\mathrm{map}} = \texttt{correlate}\left(V_{\ell_\Sigma,\mathrm{map}}, V_{\ell_\Sigma+1,\mathrm{map}}\right), \tag{2.31}$$

$$C_{\ell_\Sigma} = \frac{\sum_{\mathrm{Map}=1}^{n_{\mathrm{map}}} C_{\ell_\Sigma,\mathrm{map}}}{n_{\mathrm{map}}}. \tag{2.32}$$

The correlation coefficient C_{ℓ_Σ} is calculated for all P_{rot} in Table 2.1. Figure 2.3 shows C_{ℓ_Σ} against ℓ_Σ for each star (left to right) and both inclination angles 20° and 60° (top and bottom row). The different P_{rot} are indicated by the colour, while the colour gets lighter with decreasing P_{rot} (i.e. more rapid rotation). If $C_{\ell_\Sigma} = 1$ than the Stokes V profiles of ℓ_Σ and $\ell_\Sigma + 1$ are identical, so that the Stokes V profiles are blind for magnetic structures of the corresponding length scale and smaller. The correlation coefficients are higher for lower inclination due to the lower $v_e \sin i$ and the less complex structures at the poles. An observer is only able to observe magnetic structures of $\ell \leq 5-7$ corresponding to an angular resolution of $\vartheta \gtrapprox 36° - 25.7°$ for slow rotators ($P_{\mathrm{rot}} \geq 3.6\,\mathrm{days}$) with high inclination angles ($i = 60°$). The same resolution is achieved for faster rotating stars ($P_{\mathrm{rot}} \geq 1.8\,\mathrm{days}$) with lower inclination angles ($i = 20°$). For faster rotators with $P_{\mathrm{rot}} \leq 1.8\,\mathrm{days}$ an observer can resolve structures down to $\ell = 15$ corresponding to $\theta \approx 12°$ and for the very fast rotating stars, structures down to a few degree sizes. The correlation coefficients for the most active star (five times more active than the Sun), $i = 60°$, display a zig-zag pattern for the lower rotation periods, see Fig. 2.3 bottom right. This star's large-scale field structure is dominated by two toroidal bands of opposite polarity, which is best captured by the even ℓ-modes, see Chapter 3. The inclusion of even ℓ_Σ-modes causes a larger difference to the Stokes V profiles and therefore a lower C_{ℓ_Σ} than the inclusion of odd ℓ_Σ. In addition, the high correlation coefficients for $\ell_\Sigma \geq 5$ indicate that the large-scale field should be well approximated by including $\ell_\Sigma = 5$.

2.4 The implementation of the Zeeman-Doppler-Imaging technique

This section reports the details of the Zeeman-Doppler-Imaging (ZDI) code, that was used in Chapter 4 and 5. Section 2.4.1 compares four different magnetic field descriptions used for ZDI reconstructions and presents conclusions about their advantages and disadvantages. Section 2.4.2 presents the implementation details of the ZDI code used here. Theses sections are based on section 2.3.2 and 2.3.3 of my paper Lehmann et al. (2019).

2.4.1 Comparison of four magnetic field descriptions for ZDI

Different descriptions of the magnetic field are used for the ZDI technique. Several descriptions have been tested and compared for simple magnetic field or single spot configurations (see e.g. Donati & Brown 1997; Hussain et al. 2001) or by fitting the observed Stokes V profiles (see e.g. Hussain et al. 2002; Donati et al. 2006a; Kochukhov et al. 2017).

I compared four different magnetic field descriptions using the simulated magnetic field maps as input data. At this point I do not produce ZDI reconstructions. I rather tested the reconstruction abilities of the different field descriptions. This allowed me to examine which description is the most effective one when reconstructing the magnetic field morphology of the different surface vector magnetic field simulations, without considering any other aspect of the ZDI.

I compared four different descriptions based on spherical harmonics, including two potential and two non-potential models. I do not take into account the direct ZDI approach that fits independent magnetic structures directly to the Stokes profiles. This approach could cause non-physical div $\mathbf{B} \neq 0$ field configurations, as the different field components are not related to each other. I tested therefore only the descriptions based on the spherical harmonic decomposition, where the magnetic field components are related to each other and follow Gauß's law for magnetism ($\nabla \cdot \mathbf{B} = 0$). The spherical harmonic magnetic field description, see Eq. 1.26, specifies a magnetic field with the help of the coefficients $\alpha_{\ell m}, \beta_{\ell m}$ and $\gamma_{\ell m}$. Restricting one or more coefficients results in the four different field descriptions, that are here compared. The potential model[7] requires $\gamma_{\ell m} = 0$, that leads to a purely poloidal field configuration as the

[7]For a potential field the curl of the field has be zero ($\nabla \times \mathbf{B} = 0$). Both potential models fulfil this requirement at large distances ($r \gg R_\star$). A magnetic field following the potential $\alpha_{\ell m} = \beta_{\ell m}$ model is curl free straight away without further requirements, see Eq. 1.26. The azimuthal and meridional component of the curl of the potential $\alpha_{\ell m} \neq \beta_{\ell m}$ model becomes zero at large distances ($r \gg R_\star$), see also Donati et al. (2006b, section 5.1).

toroidal field is zero ($\mathbf{B}_{\rm tor} = 0$), see Eq. 1.32. The non-potential models $\gamma_{\ell m} \neq 0$ can use $\gamma_{\ell m}$ to fit the field structures and $\mathbf{B}_{\rm tor} \neq 0$. A further description forces $\alpha_{\ell m} = \beta_{\ell m}$, which allows the extrapolation of the magnetic field from the stellar surface up to the corona, (Hussain et al., 2002; Jardine et al., 2013). However, this approach reduces the degree of freedom as well as the potential model.

The following four descriptions of the magnetic field are compared:

- **potential** $\alpha_{\ell m} = \beta_{\ell m}$: This model has the fewest degrees of freedom as $\alpha_{\ell m} = \beta_{\ell m}$ and $\gamma_{\ell m} = 0$.
- **potential** $\alpha_{\ell m} \neq \beta_{\ell m}$: This model gains one degree of freedom by allowing $\alpha_{\ell m} \neq \beta_{\ell m}$ but still requires $\gamma_{\ell m} = 0$. It should be able to better fit the meridional and azimuthal field components (see Hussain et al. 2001).
- **non-potential** $\alpha_{\ell m} = \beta_{\ell m}$: This model allows $\gamma_{\ell m} \neq 0$ and therefore a toroidal field component by providing the possibility to extrapolate the field structure from the stellar surface to higher atmospheres (see Hussain et al. 2002).
- **non-potential** $\alpha_{\ell m} \neq \beta_{\ell m}$: This model has the maximum number of degrees of freedom by allowing $\alpha_{\ell m} \neq \beta_{\ell m}$ and $\gamma_{\ell m} \neq 0$ and should perfectly reconstruct the magnetic field structure at the surface (see e.g. Donati et al. 2006a).

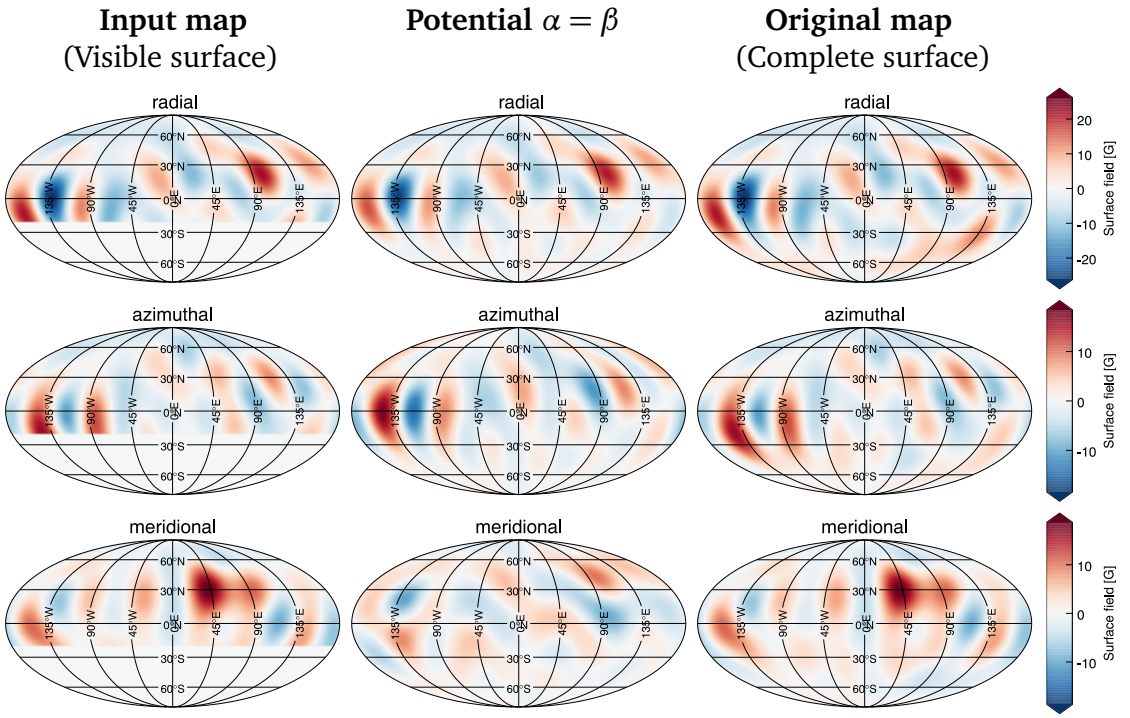

Figure 2.4: The Mollweide projected magnetic field maps of the different descriptions of the magnetic field for the solar-like star (ER = 1 $ER_\odot$ and DR = 1 $DR_\odot$). The radial component is displayed in the top row, the azimuthal in the middle row and the meridional component at the bottom row. From left to right: the input map with a restricted large-scale field to $\ell_\Sigma = 7$ and truncated latitudes corresponding to an inclination of $i = 20°$, the potential ($\alpha_{\ell m} = \beta_{\ell m}$) reconstruction and the original simulated maps for $\ell_\Sigma = 7$.

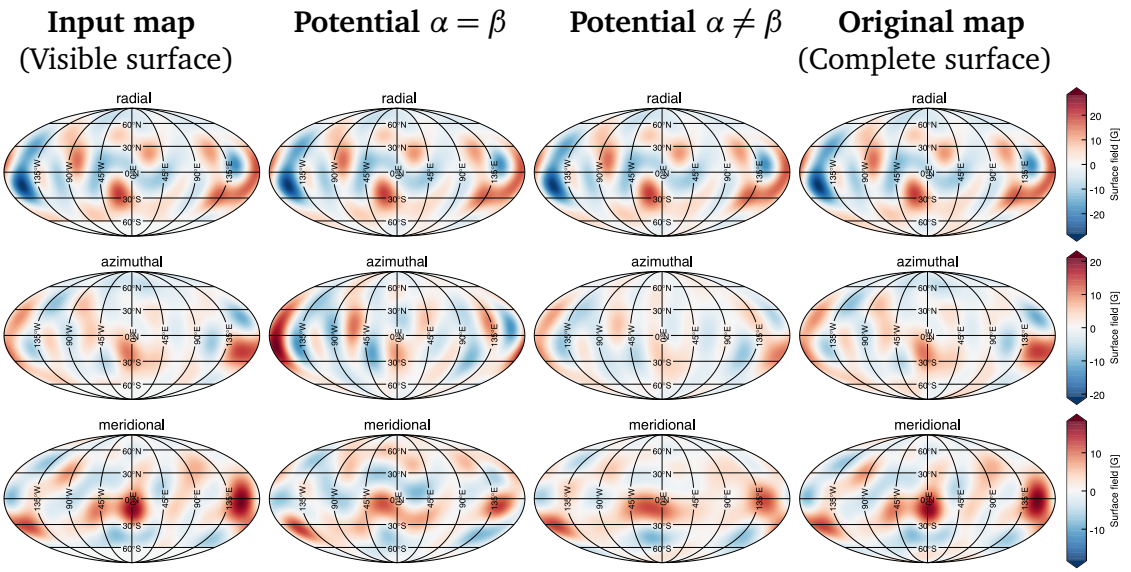

Figure 2.5: The Mollweide projected magnetic field maps of the different descriptions of the magnetic field for the solar-like star (ER = 1 $ER_\odot$ and DR = 1 $DR_\odot$). Form left to right: the input map including $\ell_\Sigma = 7$ and truncated latitudes corresponding to an inclination of $i = 60°$, the potential ($\alpha_{\ell m} = \beta_{\ell m}$) reconstruction, the potential ($\alpha_{\ell m} \neq \beta_{\ell m}$) reconstruction and the original simulated maps for $\ell_\Sigma = 7$. The same format as the Fig. 2.4 is used.

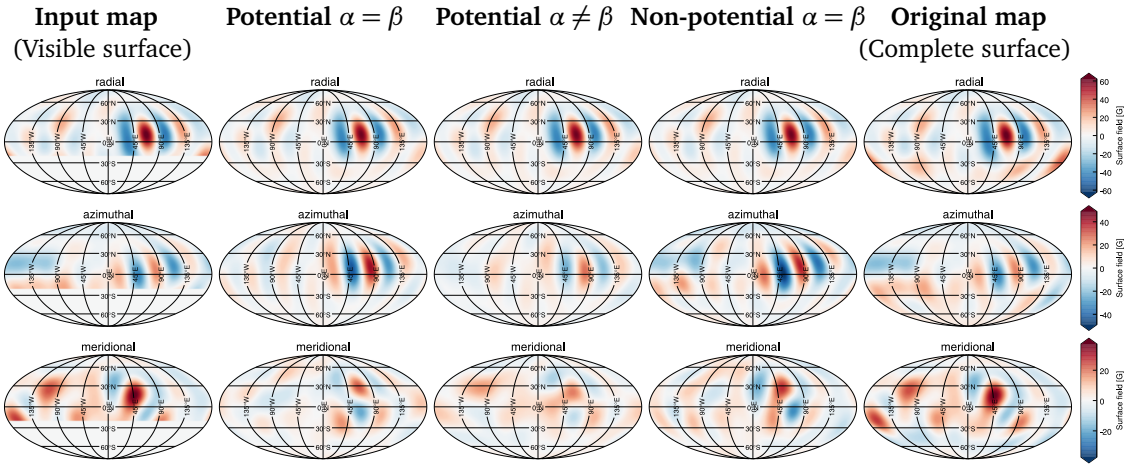

Figure 2.6: The Mollweide projected magnetic field maps of the different descriptions of the magnetic field for the more active star ($\mathrm{ER} = 3\,\mathrm{ER}_\odot$ and $\mathrm{DR} = 3\,\mathrm{DR}_\odot$). Form left to right: the input map including $\ell_\Sigma = 7$ and truncated latitudes corresponding to an inclination of $i = 20°$, the potential ($\alpha_{\ell m} = \beta_{\ell m}$) reconstruction, the potential ($\alpha_{\ell m} \neq \beta_{\ell m}$) reconstruction, the non-potential ($\alpha_{\ell m} = \beta_{\ell m}$) reconstruction and the original simulated maps for $\ell_\Sigma = 7$. The same format as the Fig. 2.4 is used.

Figure 2.7: The Mollweide projected magnetic field maps of the different descriptions of the magnetic field for the most active star ($\mathrm{ER} = 5\,\mathrm{ER}_\odot$ and $\mathrm{DR} = 5\,\mathrm{DR}_\odot$, $i = 20°$). From left to right: the input map including $\ell_\Sigma = 7$ and truncated latitudes corresponding to an inclination of $i = 20°$, the potential ($\alpha_{\ell m} = \beta_{\ell m}$), the potential ($\alpha_{\ell m} \neq \beta_{\ell m}$), the non-potential ($\alpha_{\ell m} = \beta_{\ell m}$), the non-potential ($\alpha_{\ell m} \neq \beta_{\ell m}$) reconstruction and the original simulated maps for $\ell_\Sigma = 7$. The same format as the Fig. 2.4 is used.

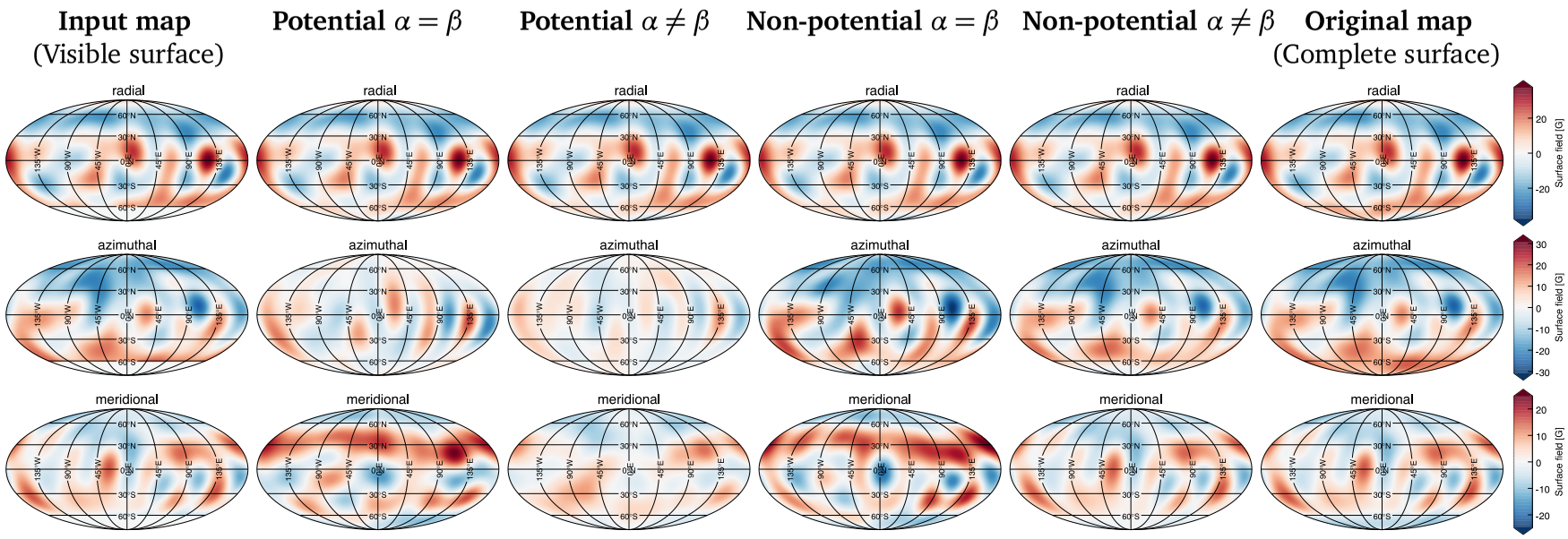

Figure 2.8: Mollweide projected magnetic field maps of the different descriptions of the magnetic field for the same star and map as in Fig. 2.7 but for a higher inclination angle $i = 60°$ ($\mathrm{ER} = 5\,\mathrm{ER}_\odot$ and $\mathrm{DR} = 5\,\mathrm{DR}_\odot$, $i = 60°$). The same format as the Fig. 2.7 is used.

I examine the simulated large-scale field ($\ell_\Sigma = 7$) of 3 stars 10 stellar maps each presented in Chapter 4.2 for both inclination angles $i = 20°$ and $i = 60°$. They include a solar model, a star three times and five times more active than the Sun in terms of differential rotation and flux emergence rate. The latitudes that are obscured due to the inclination effect are truncated, see Fig. 2.4-2.8, left column. The input map represents therefore the maximum possible field that is observable with ZDI. I reconstructed the magnetic field map using the decomposition method described in Section 2.1 by altering the coefficients depending on the model, see Fig. 2.4-2.8, middle columns. I compared the reconstructed magnetic field of the different models with the original map (simulated large-scale field $\ell_\Sigma = 7$ without truncated latitudes), see Fig. 2.4-2.8, right column. Additionally, I determined the correlation coefficient between the reconstructed and the original maps.

In general, I found that the non-potential $\alpha_{\ell m} \neq \beta_{\ell m}$ model is always able to reconstruct the original map to a satisfactory level, i.e., showing the highest correlation coefficients. The spherical harmonics description reconstructs even the obscured magnetic field of the southern hemisphere to a certain extent, which leads to a higher agreement between the reconstructed and original maps than between the input and original maps. The other three models often miss essential field structures. The potential $\alpha_{\ell m} = \beta_{\ell m}$ is the worst model as expected from the low number of degrees of freedom. From a mathematical point of view, the first three models are not able to reconstruct the full range of the input magnetic field distributions. The limitation of the coefficients $\alpha_{\ell m}, \beta_{\ell m}$ and $\gamma_{\ell m}$ prevents the reconstruction of essential structures of the input magnetic field morphology. No ZDI code using these descriptions will be able to fully reconstruct the correct field morphology. Nevertheless, I found that some of the simulated magnetic field morphologies are able to be reconstructed to a convincing level using the more restricted models.

Specifically, the radial component (Fig. 2.4-2.8, top row) is the same for all models as it only depends on the $\alpha_{\ell m}$ coefficient, see Eq. 1.26. The radial field is therefore equally well reconstructed regardless of the model and reached correlation coefficients higher than 0.98 for inclination $i = 60°$ and 0.9 for $i = 20°$. The azimuthal component can be reconstructed with the potential model for some of the solar case simulations. Fig. 2.4 displays such an example, where the azimuthal field reconstruction (middle row) of the potential $\alpha_{\ell m} = \beta_{\ell m}$ model is acceptable. Fig. 2.5 shows an example where the potential $\alpha_{\ell m} = \beta_{\ell m}$ model is no longer able to fit the azimuthal field, but the potential $\alpha_{\ell m} \neq \beta_{\ell m}$ model is. The potential models became

increasingly inadequate if the stars become more active. With the activity level of the stars the correlation coefficients of the potential models decreases while the correlation coefficients of the non-potential modes increases. Fig. 2.6 shows an example of a three times more active star than the Sun, where the potential models are insufficient but the non-potential $\alpha_{\ell m} = \beta_{\ell m}$ model is acceptable. For the five times more active stars, only the non-potential $\alpha_{\ell m} \neq \beta_{\ell m}$ can fit the azimuthal input map, see Fig. 2.7. The reconstruction of the meridional component is often only possible by using the non-potential $\alpha_{\ell m} \neq \beta_{\ell m}$ model but benefits in general from allowing $\alpha_{\ell m} \neq \beta_{\ell m}$, see Fig. 2.7 bottom row. Additionally, I found that the correlation coefficients decrease by $10-20\,\%$ per degree of freedom, independent of the activity level of the star.

Furthermore, the inclination angle also affects the reconstruction quality. The correlation coefficients increase by $10-20\,\%$ from inclination angle $i = 20^\circ$ to $i = 60^\circ$. The field reconstruction of the more active stars is more strongly affected by the inclination. The large-scale field of the more active stars mainly consists of two azimuthal band-like structures at mid latitudes showing the opposite polarity, see Fig. 2.7 and 2.8. For low inclination angles the structure of the southern band is missing, so that the true large-scale morphology is hidden from the observer, see Fig. 2.7.

Summarising, the non-potential $\alpha_{\ell m} \neq \beta_{\ell m}$ model is the only model that guaranties the correct reconstruction without artefacts or missing structures. This model is therefore used for all ZDI applications in this thesis. The other models have advantages, e.g. for the reconstruction of the coronal field, but one needs to be aware that the quality of the reconstruction (here determined via a correlation coefficients) decreases by $10-20\,\%$ per degree of freedom. Especially, if one is interested in the reconstruction of the meridional or azimuthal field should use all three coefficients without restrictions. The more active the star, the more strongly is the reconstruction affected by the restriction of the coefficients. Further, the inclination angle affects the large-scale field reconstruction, in particular the more active stars with solar flux emergence pattern.

2.4.2 ZDI setup and implementation

I applied the ZDI code provided by our collaborator Gaitee Hussain. The code is based on the spherical harmonic description (see Chapter 1.2.2), uses a Least Squares Deconvolution (LSD) like mean profile fine tuned to fit the solar twin 18 Sco (see Chapter 1.3.2) and applies the

maximum entropy ansatz to overcome the uniqueless problem.

First, I generated time-series consisting of 25 Stokes profiles from the fully resolved maps of the simulated stars using the method described in Section 2.3.1, before I used them as input for the ZDI code. The Stokes profiles are equally spaced over a full stellar rotation, so that I do not investigate the effects of phase gaps or coverage. Further, I assume that the large-scale field does not change significantly over one stellar rotation. However, I investigate the effects of missing flux from the obscured hemisphere by considering two stellar inclination angles in Chapter 4. An inclination angle of $i = 60°$ and $i = 20°$ is applied. For the high inclination of $i = 60°$ the large-scale field down to $\approx 30°$ latitude should contribute to the Stokes profiles, whereby for the low inclinations the signal should be dominated by the polar region.

For the ZDI reconstructions the non-potential $\alpha_{\ell m} \neq \beta_{\ell m}$ model for the magnetic field description is used as here the correct reconstruction of the magnetic field is secured, see Section 2.4.1. All three coefficients $\alpha_{\ell m}, \beta_{\ell,m}$ and $\gamma_{\ell,m}$ are free to fit the Stokes profiles and are not restricted.

Furthermore, all spherical harmonic modes are equally weighted to investigate the effect of the maximum entropy regularisation onto the spherical harmonic based ZDI code. Neither axisymmetric nor non-axisymmetric modes are preferred and neither the toroidal or non-potential field is enhanced or rejected. I allow ℓ_Σ-modes up to $\ell_\Sigma = 7$. Most of the time the ℓ_Σ-modes up to $\ell_\Sigma = 5$ contain significant magnetic energy but sometime also $\ell = 6, 7$ store noticeable magnetic energy, so that $\ell_\Sigma = 7$ guaranties that I get all the information out of the Stokes profiles that are there. For slow rotators like the Sun the Stokes V profiles are blind for higher ℓ_Σ-modes as shown in Fig. 2.2, see Section 2.3.2.

Further, I use a maximum entropy regularisation in this thesis. For the maximum entropy approach, the field configuration containing the least amount of information required to fit the observations to a specific χ^2 is chosen. The amount of the information is determined via the entropy S, where different entropy functions for the minimisation can be implemented, see e.g. Donati & Brown (1997); Hussain et al. (2001); Hébrard et al. (2016). I am using the form developed by J.-F. Donati presented in Hussain et al. (2000, eq. 3):

$$S(f) = \sum \phi_i - m_i - f_i \log \frac{\phi_i + f_i}{2m_i}, \tag{2.33}$$

where $\phi_i = \sqrt{f_i^2 + 4m_i^2}$ and f_i is the magnetic field of each image pixel i. The equation can be adjusted by the value of the default image m_i, which is set to $m_i = 10\,\mathrm{G}$ in this thesis. Such low m_i gives a higher penalty to each field value in terms of entropy, which favourites stronger magnetic features at smaller areas. I tested also higher values of m_i, e.g. $m_i = 100$, and the entropy function of Hussain et al. (2001, eq. 5), but both showed a lower fitting performance. I was always able to fit the Stokes V profiles with a reduced $\chi^2 \leq 5$ with an exception of four maps. Often the fit was better than $\chi^2 \leq 2$. Further details of the ZDI code can be found in Hussain et al. (2016).

3

The magnetic field topology of solar-based non-potential simulations

3.1 Introduction

To understand the observed cool star magnetic field topology[1], I start with the analysis of the large and small-scale field of 3D non-potential flux transport simulations based on the Sun.

We can observe the solar magnetic field in great detail in both resolution and time. However, the direct comparison of the high resolution solar with the relatively low resolution stellar magnetic field maps is not possible due to the huge resolution difference. Vidotto (2016) introduced a spherical harmonic decomposition method to determine the large-scale magnetic field from a solar synoptic map observed with the Synoptic Optical Long-term Investigations of the Sun facility (SOLIS; Keller et al. 2003). This vector magnetic field of the Sun-as-a-star

[1]The term topology refers here to the spatial vector magnetic field structures at the stellar surface as is common in the literature of this research field.

can be directly compared with other cool stars observations[2].

The surface magnetic field of cool stars can be observed with the Zeeman-Doppler-Imaging technique but is limited to the large-scale field as it suffers from small-scale field cancellations. See et al. (2015) analysed and summarised the magnetic field properties of 55 stars spanning F, G, K and M dwarfs. They discovered that the toroidal magnetic energy scales more steeply with inverse Rossby number then the poloidal energy does. The stars follow two power law dependencies between the toroidal and poloidal energy. Stars with masses above $0.5\,\mathrm{M}_\odot$ display a steeper dependence of $\langle B^2_{\mathrm{tor}}\rangle \propto \langle B^2_{\mathrm{pol}}\rangle^{1.25\pm0.06}$ compared to lower mass stars with $\langle B^2_{\mathrm{tor}}\rangle \propto \langle B^2_{\mathrm{pol}}\rangle^{0.72\pm0.08}$, see Fig. 1.9. Further, they found that highly toroidal magnetic field topologies are also highly axisymmetric.

My aim is now to relate the small with the large-scale field using the 3D non-potential flux transport simulations of Gibb et al. (2016) to understand the observed magnetic field topologies and their dependencies. The simulations represent solar-like stars whose parameters differ in flux emergence, differential rotation and meridional flow rate. I analysed the impact of these three parameters onto the large-scale field topology detectable with ZDI and determined if it is possible to derive conclusions about the small-scale field distribution from the observable large-scale field.

Very little is known about flux emergence patterns or rates of stars other than the Sun. Mackay et al. (2004) speculated about the nature of stellar emergence profiles for faster rotating stars with polar magnetic field caps. However, methods have been devolped for future detections, see e.g. Berdyugina (2005) for a review. One promising method is to use exoplanet transits as probes for star spots at the host star's surface, see e.g. Llama et al. (2012) or Morris et al. (2017).

Also the meridional flow is unknown for cool stars other than the Sun. It can be estimated by the Hale cycle (Baklanova & Plachinda, 2015)[3]. In contrast, the differential rotation is widely detectable via the modulation of chromospheric emission lines (Donahue et al., 1996)

[2]We compare the large-scale field topology of the Sun-as-a-star with the observed magnetic field topologies analysed by See et al. (2015) for a good fraction of the solar cycle 24 in Vidotto et al. (2018). However, this was done and published after the work and publications (Lehmann et al., 2017; Lehmann et al., 2018) presented in this chapter.

[3]The mean meridional flow velocity is estimate by assuming that the magnetic dipole moment does not vanish completely but migrates during one Hale cycle (P_{Hale}, time span of two polar polarity reversals, to see the same polarity at poles) once along the circumference of the star, $\langle v_{\mathrm{mer}}\rangle = \frac{2\pi R_\star}{P_{\mathrm{Hale}}}$, (Livshits & Obridko, 2006; Moss et al., 2013; DeRosa et al., 2012). This results in $\langle v_{\mathrm{mer}}\rangle = 6.29\,\mathrm{m\,s^{-1}}$ for the Sun by assuming $P_{\mathrm{Hale}} = 22\,\mathrm{yr}$, which reasonably fits the observations, (Plachinda et al., 2011).

or more precisely via ZDI (Donati & Brown, 1997; Petit et al., 2002; Marsden et al., 2006b; Waite et al., 2011; Marsden et al., 2011). The differential rotation increases with effective temperature and stellar mass (Barnes et al., 2005; Collier Cameron, 2007; Küker & Rüdiger, 2011).

Gibb et al. (2016) analysed the influence of the flux emergence rate and differential rotation onto the non-potential coronal magnetic field. They used a flux transport model based on solar observations in connection with a non-potential coronal evolution model, (Mackay & van Ballegooijen, 2006; Yeates & Mackay, 2012). They discovered that an increased flux emergence rate adds more flux into the corona but the global coronal structure stays unchanged. An increase in the differential rotation opens the corona up and makes its field more non-potential.

In this chapter, I use self-consistent simulations based on Gibb et al. (2016) and investigate their photospheric magnetic field in respect of the magnetic structure for different length scales. I am not re-analysing the results of Gibb et al. (2016), which focus on the coronal response to the changing stellar parameters. I concentrate at the photosphere as the magnetic field topology is observed in this layer. In addition, I want to improve the accessibility of the simulations to the observers by extracting the large-scale field for the radial, azimuthal and meridional component next to the toroidal and poloidal component.

This chapter is based on the letter Lehmann et al. (2017) and the paper Lehmann et al. (2018). In the letter I analysed the magnetic field topology of 17 stellar models (one map per model), which are a snapshot of the simulations in Gibb et al. (2016). Motivated by the results, we enlarged the simulation set by extending the parameter range to lower differential rotation rates and by accessing/changing a further parameter: the meridional flow. Additionally, I analysed all 390 maps per stellar model in Lehmann et al. (2018) to derive statistical secured results. In this thesis chapter, I present the results of both publications focusing predominantly on the enlarged data set published in Lehmann et al. (2018).

The chapter starts with the introduction of the simulations and the modelling techniques in Section 3.2 and 3.3. The results are presented in Section 3.4, followed by their discussion in Section 3.5. The chapter ends with a summary in Section 3.6.

3.2 Simulations

I am using a large set of 3D non-potential flux transport simulations, which model the magnetic field of several stars using the Sun as a guide. I kindly received the simulations from our collaborator Duncan Mackay. Most of the simulations were published by Gibb et al. (2016). Due to the results of our surface magnetic field topology analysis in Lehmann et al. (2017), Duncan Mackay enlarged the parameter range of the stellar models, which are presented and analysed in Lehmann et al. (2018).

The general description of the simulations and the applied flux transport model in connection with a non-potential coronal evolution model is provided in Chapter 2.2. More details of the simulation set can be found in sections 2 and 3 of Gibb et al. (2016)[4].

The simulations include 390 maps per stellar model, that vary in the flux emergence, differential rotation and meridional flow parameters. The fixed point is a stellar model of our own Sun to which the other parameters are scaled. The flux emergence rate was determined for the solar activity maximum with 0.62 bipolar active regions per day and is scaled by the factor $D = 1, 3, 5$, see also page 57. The differential rotation is scaled by the factor $K = 0.3, 0.5, 0.8, 1, 3, 5$ using a solar differential rotation profile

$$\Omega(\theta) = K(\Omega_0 - \mathrm{d}\Omega_\odot \cos^2\theta)\,\mathrm{deg\,d^{-1}}, \tag{3.1}$$

where $\Omega_0 = 0.9215\,\mathrm{deg\,d^{-1}}$, $\mathrm{d}\Omega_\odot = 3.65\,\mathrm{deg\,d^{-1}}$, as described in Chapter 2.2. The meridional flow is defined after Schüssler & Baumann (2006),

$$u_\theta = C\frac{16}{110}\sin(2\lambda)\exp(\pi - 2|\lambda|), \tag{3.2}$$

as described in Chapter 2.2. The peak solar flow C is set to be $C = 11\,\mathrm{m\,s^{-1}}$ for the solar case and $C = 110\,\mathrm{m\,s^{-1}}$ for the stellar models with ten times higher meridional flow[5]. The study by Gibb et al. (2016) includes the scaling of the differential rotation rate ($K = 1, 2, 3, 4, 5$) and of the flux emergence rate ($D = 1, 2, 3, 4, 5$), from which I mainly use a sub set including $K = 1, 3, 5$ and $D = 1, 3, 5$. The expansion to lower rates of the differential rotation ($K =$

[4]Further, I want to refer to the paper of Gibb et al. (2014), where the authors investigate the effects of the differential rotation and the supergranulation using related simulations of single isolated bipolar active regions on coronal time-scales.

[5]Figure 2.1 in Chapter 2 displays the differential and meridional flow profiles.

0.3, 0.5, 0.8) and to higher rates of the meridional flow was provided by Duncan Mackay (priv. communication, 2016).

The bipoles[6] emerge as vector potentials (see section 2.3 of Gibb et al. 2016) based on the model of Yeates et al. (2008). To overcome the problem that the flux emergence profile is unknown for stars other than the Sun, Gibb et al. (2016) determined the statistical flux emergence properties from solar synoptic magnetograms observed by National Solar Observatory/Kitt Peak (NSO/KP). To ensure that the emerging bipoles were not affected by the long-term solar cycle variation of the flux emergence, they considered the solar flux emergence between 2000 January and 2001 January around the solar activity maximum of solar cycle 23. The properties of 227 emerged bipoles (emergence time, latitude, longitude, flux, tilt angle and half separations) were determined by Yeates (2014) to fit the observed emerged fluxes, see also Yeates et al. (2007). Gibb et al. (2016) developed a model, which allows the variation of several properties of the emerged bipoles, based on the results of Yeates (2014), see section 3 of Gibb et al. (2016). For example: They found that the time interval t between two single flux emergences follows a certain exponential distribution. The probability distribution function (PDF) [7] is given by

$$P(t) = -\frac{1}{\tau} \exp\left(\frac{-t}{\tau}\right), \tag{3.3}$$

where $\tau = 1.61\,\mathrm{d}$. To determine the time of the next bipole emergence, Gibb et al. (2016) used a random number generator for an exponential distribution $E[\tau]$ with the expected value $\tau = 1.61\,\mathrm{d}$. To scale the flux emergence rate they included the scaling factor D into the exponential distribution $E[1.61/D\mathrm{d}]$. The other properties of the emerged bipoles follow further empirical relations and are modelled with the help of uniform, normal and exponential distribution number generators, see section 3 of Gibb et al. (2016).

The simulations start with an initial map that is based on the smoothed synoptic magnetogram for CR1970[8], see Gibb et al. (2016, fig. 2), and run on grid of 384 grid points at the equator to 12 grid points at the polar boundary. The corresponding initial coronal field was extrapolated from the observed photospheric field using a potential field model. After

[6] Bipoles describe two star spots of opposite polarity within an active region. They are the footpoints of a lifted flux tube breaking through the stellar photosphere.

[7] The exponential distribution describes the distribution of the time values t indicating the time between two events that occur independently at a constant rate τ, e.g., raindrops hitting the ground or in this case the emergence of bipoles at the solar surface. The probability distribution function $P(t)$ returns the probability to obtain a certain value for t, where $t > 0$.

[8] Carrington Rotation (CR) 1970: 2000 November 24 to 2000 December 21.

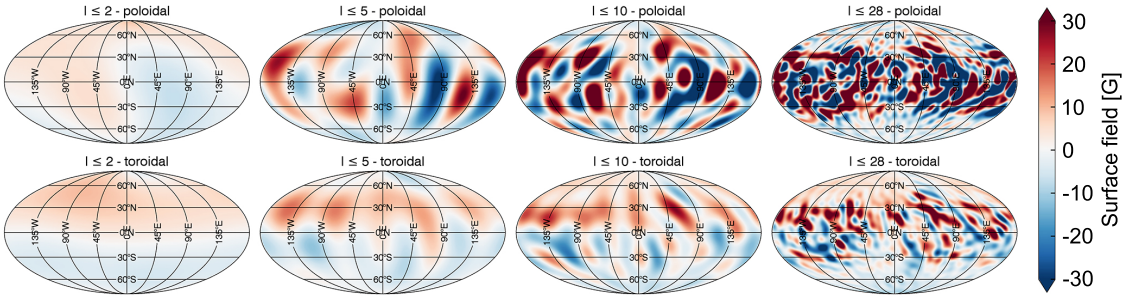

Figure 3.1: The surface magnetic field for a simulated star with three times the solar flux emergence rate and three times the solar differential rotation modulated with a flux transport model (Gibb et al., 2016) restricted to spherical harmonic ℓ_Σ-modes of $\ell_\Sigma = 2$ (left), $\ell_\Sigma = 5$ (middle left), $\ell_\Sigma = 10$ (middle right), and for $\ell_\Sigma = 28$ (right). The top row displays the poloidal and the bottom row the toroidal field component. The main polarity pattern of the toroidal field of the emerging bipoles, i.e., the polarity reversal across the equator, can be detected through all ℓ_Σ-modes down to $\ell_\Sigma = 2$. The colourbar saturates at ±30 G.

$100 - 200$ days the simulations reach a steady state, see Gibb et al. (2016, fig. 3). I analyse only the photospheric ($r = \mathrm{R}_\odot$) vector magnetic field maps. An analysis of the coronal magnetic field and further coronal properties is presented by Gibb et al. (2014, 2016).

3.3 Modelling techniques

Essential for this work is the spherical harmonic decomposition method published by Vidotto (2016), which I introduced in Chapter 2.1. It allows us to express the vector magnetic field as spherical harmonics of different ℓ degree. The higher the ℓ-mode, the higher the order of the multipole and therefore the smaller the selected magnetic structure.

Fig. 3.1 shows one example of the simulated vector magnetic field maps. On the right the fully resolved map for the poloidal (top) and toroidal field (bottom) is displayed. Moving to the left, the number of included ℓ-modes is reduced. The small-scale field structures are filtered out and only the large-scale field becomes visible.

The highest ℓ-mode ($\ell_{\max}$) relates to the spatial resolution of the magnetic field. High-resolution solar synoptic maps reach $\ell_{\max} = 192$ (DeRosa et al., 2012), while stellar synoptic maps show often resolutions of $\ell_{\max} = 5 - 10$ (Morin et al., 2010; Johnstone et al., 2014; Yadav et al., 2015; Folsom et al., 2016). In this study I analyse the magnetic field topology using $\ell = 1 - 28$ corresponding to angular length scales of $\vartheta = 180°$ to $\approx 4.7°$, where the simulated maps are as good as fully-resolved.

The spherical harmonic decomposition is completely consistent with the descriptions used in several ZDI studies (Donati et al., 2006a; Fares et al., 2012; Hussain et al., 2002; Morgen-

Table 3.1: The rotation period in days for the simulations. The simulations vary in flux emergence rate (ER), differential rotation rate (DR) and meridional flow rate (MF), which are displayed in terms of the solar values.

a. For solar meridional flow $\mathrm{MF} = \mathrm{MF}_\odot$:

ER\DR	$0.3\,\mathrm{DR}_\odot$	$0.5\,\mathrm{DR}_\odot$	$0.8\,\mathrm{DR}_\odot$	$1\,\mathrm{DR}_\odot$	$3\,\mathrm{DR}_\odot$	$5\,\mathrm{DR}_\odot$
$1\,\mathrm{ER}_\odot$	25.2	25.8	26.2	27.0	30.4	32.0
$3\,\mathrm{ER}_\odot$	16.5	16.6	17.0	17.4	19.0	20.2
$5\,\mathrm{ER}_\odot$	13.9	14.1	14.2	14.3	15.9	17.0

b. For higher meridional flow $\mathrm{MF} = 10\,\mathrm{MF}_\odot$:

ER\DR	$1\,\mathrm{DR}_\odot$	$3\,\mathrm{DR}_\odot$	$5\,\mathrm{DR}_\odot$
$1\,\mathrm{ER}_\odot$	26.8	30.7	33.4
$3\,\mathrm{ER}_\odot$	16.7	19.5	20.6
$5\,\mathrm{ER}_\odot$	14.0	15.7	16.4

thaler et al., 2012; Kochukhov, 2015). It allows a fair order of magnitude comparison of any vector field map (resulting from the Sun or synthetic maps from numerical dynamo simulations or flux transport studies) to observed magnetic field maps by selecting the corresponding resolution.

Other studies used also the low order spherical harmonics to filter the large-scale field, see e.g. Morin et al. (2010); Johnstone et al. (2014); Folsom et al. (2016). For example, Yadav et al. (2015) filtered the large-scale field for $\ell_{\max} = 10$ from a fully convective M dwarf simulations[9] and compared them further with the ZDI reconstruction from synthetic spectropolarimetric data. They found that the $\ell_\Sigma = 10$ large-scale field fits well the synthetic ZDI reconstructions. I apply now the spherical harmonic decomposition to 3D non-potential flux transport simulations focusing on solar-like stars[10].

The different stellar models of the simulations from Gibb et al. (2016) are not exactly related to rotation periods. Several parameters are related or scaled to the Sun. I defined that the solar model ($\mathrm{ER} = 1\,\mathrm{ER}_\odot$, $\mathrm{DR} = 1\,\mathrm{DR}_\odot$, $\mathrm{MF} = 1\,\mathrm{MF}_\odot$) shall have a rotation period of $P_{\mathrm{rot}} = 27\,\mathrm{d}$. I used the result found by Saar (1996), that the mean flux density is related to the stellar rotation:

$$\langle |B_I| \rangle \propto P_{\mathrm{rot}}^{-1.7}, \tag{3.4}$$

[9] They applied the open-source MagIC code based on anelastic magnetohydrodynamic equations, (Gastine & Wicht, 2012).

[10] In Chapter 4 I apply a full ZDI routine to the simulations and compared the results with the filtering of the spherical harmonic decomposition method.

where $\langle|B_I|\rangle$ is the total mean unsigned flux density from Zeeman-Broadening measurements[11]. As the simulated magnetic field maps are fully resolved, I can use the relation from Saar (1996). I calculated $\langle|B_I|\rangle$ of each map and averaged them to one mean value per stellar model. For the solar case $\langle|B_I|\rangle = 14.7\,\mathrm{G}$ and is set to $P_{\mathrm{rot}} = 27\,\mathrm{d}$. Using Eq. 3.4 allows then the estimation of the rotation periods of the other stellar models, which range from 13.9 d to 33.4 d, see Table 3.1. An increase in the flux emergence rate causes an increase in $\langle|B_I|\rangle$ and therefore to shorter rotation periods. An increase in the differential rotation or meridional flow leads to a decrease of $\langle|B_I|\rangle$ due to flux cancellations in the small-scale field and therefore to longer rotation periods. The influence of the differential rotation is greater compared to the meridional flow.

My analysis of the large-scale field properties is based on an optimal average algorithm, that mimics the observational limitations. The simulations contain over $n_{\mathrm{obs}} = 390$ magnetic maps per stellar model for every day $j(i,m)$,

$$j(i,m) = i + m \cdot P_{\mathrm{rot}}, \tag{3.5}$$

where $i \in [0, n_i]$ is the start date and $m \in [0, n_m]$ is defined as the counter for the multiple of the rotation period P_{rot}, while $n_i = P_{\mathrm{rot}} - 1$ and $n_m = \mathrm{mod}\left(\frac{n_{\mathrm{obs}}}{P_{\mathrm{rot}}}\right)$. One needs a full stellar rotation to detect the magnetic field of the whole stellar surface. For any magnetic field parameter $F(j(i,m))$, I determine the arithmetic mean $\mu(i)$ by averaging over the multiple m of the rotation period P_{rot} in respect of a certain start date i,

$$\mu(i) = \frac{\sum_{m=1}^{n_m} F\left(j(i,m)\right)}{n_m}, \tag{3.6}$$

which is equivalent to an arithmetic mean over n_m subsequently observed stellar magnetic field maps. I have the advantage of obtaining surface magnetic field maps of every day for the simulations and not only every mP_{rot} days (one snapshot per stellar rotation). I can compute therefore the optimal average $\sigma_{\mathrm{opt\ avg}}$ over all arithmetic means $\mu(i)$ of the different start dates i,

$$\sigma_{\mathrm{opt\ avg}} = \frac{\sum_{i=1}^{n_i} \mu(i)}{n_i}. \tag{3.7}$$

Furthermore, I calculated the corresponding 1-σ standard derivation using the same concept.

[11] Also the averaged large-scale field strength $\langle|B_V|\rangle$ from ZDI measurements increases with rotation period following a power law relation ($\langle|B_V|\rangle \propto P_{\mathrm{rot}}^{-1.32\pm0.14}$, Vidotto et al. 2014).

3.4 The magnetic field topologies of the simulated stars

I investigated the magnetic field properties of the simulated surface magnetic field maps regarding the poloidal and toroidal magnetic energy (Section 3.4.1-3.4.3), the energy distribution across the ℓ-modes (Section 3.4.4) and the axisymmetry of the field (Section 3.4.5). The results are compared to the observational results of See et al. (2015), where possible. The impact of the stellar parameters flux emergence rate (ER), differential rotation rate (DR) and meridional flow rate (MF) is best seen in Section 3.4.2 and 3.4.3.

3.4.1 Comparing the simulations with observations

First, I analyse the magnetic energy budgets of the poloidal and toroidal field component motivated by fig. 2 (top) of See et al. (2015) (reproduced in Fig. 1.9). In Lehmann et al. (2017, fig. 2)[12] I presented only one map per stellar model in contrast to Lehmann et al. (2018, fig. 1) which displays the optimal average over 390 maps per stellar model, see Fig. 3.2. In Fig. 3.2 I present the results for nine stellar models covering the flux emergence rates $\mathrm{ER} = 1, 3, 5\,\mathrm{ER}_\odot$ and differential rotation rates $\mathrm{DR} = 1, 3, 5\,\mathrm{DR}_\odot$ modeled with a solar meridional flow. The same parameter range as in Lehmann et al. (2017, fig. 2) is covered and allows a direct comparison. Further, Fig. 3.13b in the chapter appendix includes the full parameter range study including all 27 stellar models available in Lehmann et al. (2018) by using the same format as Fig. 3.2.

The observational results[13] of See et al. (2015) are displayed by grey symbols. Stars with masses lower than or equal to $0.5\,\mathrm{M}_\odot$ are displayed as triangles and stars with higher masses as squares. Fig. 3.2 shows the toroidal against the poloidal mean squared flux density $\langle B^2 \rangle$, which is called magnetic energy in the following to be consistent with the literature (see discussion in Chapter 2.1 at page 33). The dashed line represents the unity line, where both components show equal energies.

The top panel includes only the cumulative ℓ_Σ-modes[14] $\ell_\Sigma = 5$ and 10 (dark and light green circles), which are two typical resolutions for observed slowly and moderately rotating stars. A

[12] Fig. 2 of Lehmann et al. (2017) is displayed as Fig. 3.13a in the chapter appendix.

[13] The observations were done in the framework of the Bcool and Toupies survey and were published by Petit (in prep.); Boro Saikia et al. (2015); do Nascimento et al. (2014); Donati et al. (2003, 2008b); Fares et al. (2009, 2010, 2012, 2013); Folsom et al. (2016); Morin et al. (2008a,b, 2010); Jeffers et al. (2014); Petit et al. (2008); Waite et al. (2011).

[14] The cumulative ℓ_Σ-modes include all lower ℓ-modes and can describe whole substructures like the large-scale field, see also Chapter 2.1 at page 33.

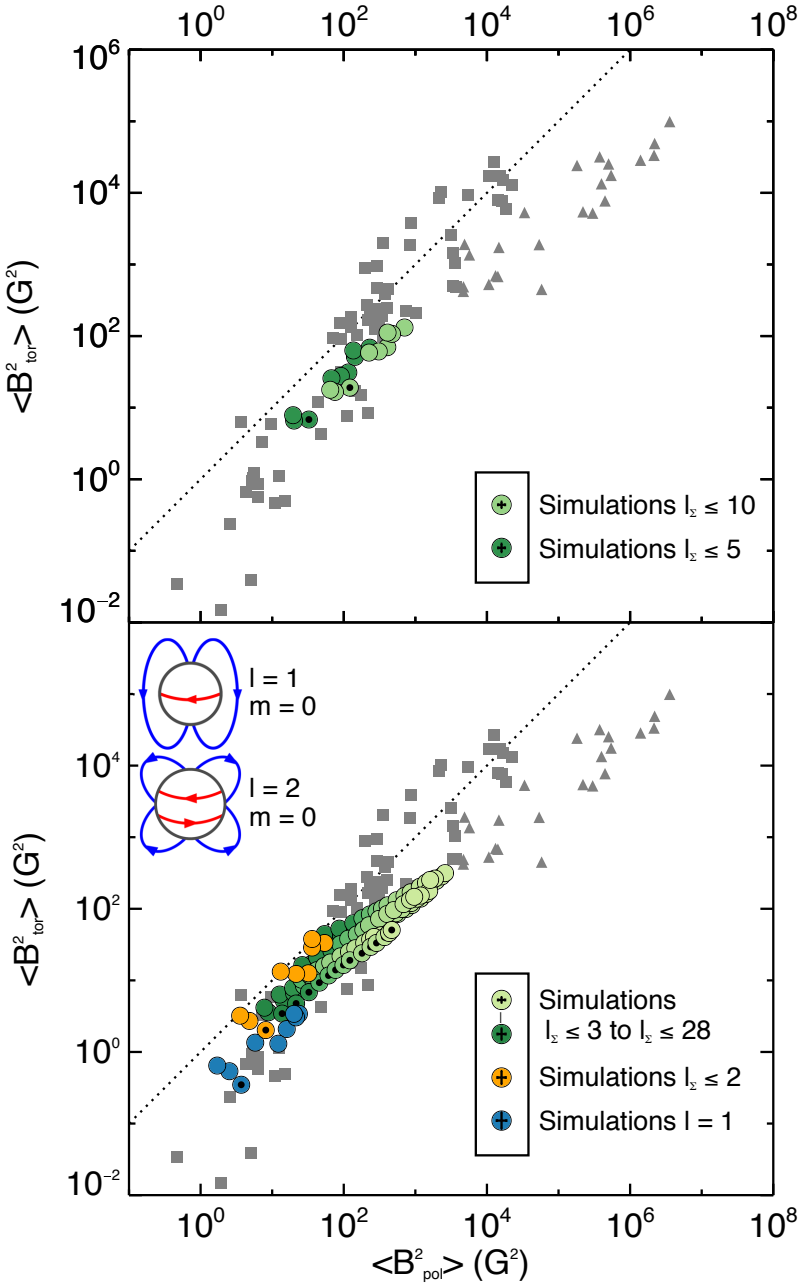

Figure 3.2: The magnetic energy stored in the poloidal $\langle B^2_{\rm pol}\rangle$ and the toroidal component $\langle B^2_{\rm tor}\rangle$. The observations are displayed by grey symbols, where stars with stellar masses $M_\star \geq 0.5\,{\rm M}_\odot$ are plotted as squares and stars with masses $M_\star < 0.5\,{\rm M}_\odot$ as triangles. The simulations covering flux emergence rates of ER $= 1, 3, 5\,{\rm ER}_\odot$ and a differential rotation of DR $= 1, 3, 5\,{\rm DR}_\odot$ are shown as coloured circles. The simulated Sun is indicated by the solar symbol $\odot$ and the dashed line indicates equal poloidal and toroidal energies. Top: For a direct comparison between the simulations and observations the simulations are restricted to the large-scale field by spherical harmonics up to $\ell_\Sigma = 5$ (dark green circles) or $\ell_\Sigma = 10$ (light green circles). Bottom: Including all surface scale sizes for the simulations: the dipolar mode $\ell = 1$ (blue circles), the cumulative quadrupolar mode $\ell_\Sigma = 2$ (orange circles), and the higher cumulative ℓ_Σ-modes $\ell_\Sigma = 3$ to $\ell_\Sigma = 28$ (greenish circles), where the colour gets lighter with increasing ℓ_Σ-modes. The higher ℓ_Σ-modes follow the powerlaw $\langle B^2_{\rm tor}\rangle \propto \langle B^2_{\rm pol}\rangle^{0.77\pm0.02}$. The inserts show the poloidal (blue) and toroidal (red) field lines for the axisymmetric dipole and quadrupole mode.

direct comparison between the observations and simulation is now possible. The simulations representing the Sun are indicated by the solar symbol ⊙. All stellar models (coloured circles) lie within the regime of the observations (grey symbols). They cover the same parameter range given by the solar-like stars, e.g., by HN Peg (Boro Saikia et al., 2015) or ε Eri (Jeffers et al., 2014).

In the bottom panel of Fig. 3.2, I display all ℓ_Σ-modes up to $\ell_\Sigma = 28$. Be aware that a direct comparison with the observations is now misleading due to resolution differences. I colour-coded the ℓ_Σ-modes in three regimes: blue for the dipolar modes, orange of the quadrupolar modes and greenish colours for the higher ℓ_Σ-modes, where the colour gets lighter with increasing ℓ_Σ-modes. The dipolar modes are poloidal dominated. The quadrupolar modes $\ell = 2$ obtain around one order of magnitude higher toroidal energy and show the highest toroidal energy of all ℓ-modes. The higher ℓ_Σ-modes follow a fixed ratio between the toroidal and poloidal energy of $\langle B^2_{\rm tor}\rangle \propto \langle B^2_{\rm pol}\rangle^{0.77\pm0.02}$. This power law relation is remarkably similar to the power law found for low mass M dwarfs by See et al. (2015), see also discussion in Section 3.5.

Furthermore, I calculated the 1-σ standard derivation of the optimal average and display the maximal errorbars for the shown ℓ_Σ-modes in the legend of Fig. 3.2. For most ℓ_Σ-modes the error is smaller than the plot symbol and decreases with increasing ℓ_Σ-modes on the log-log scale.

Comparing the optimal average of the 390 maps per stellar model in Fig. 3.2 with the snapshot single maps in Fig. 3.13a, I noticed that the optimal average reduces the spread and the trend with ℓ_Σ-modes become clearer, especially for the higher ℓ_Σ-modes. However, even in Fig. 3.13a the trend with ℓ_Σ-modes is well seen. The solar model is closer to the other stellar models in Fig. 3.2 compared to Fig. 3.13a. The single analysed solar map in Fig. 3.13a shows a generally lower toroidal energy than the average of the solar-case simulations as suggested by Lehmann et al. (2017).

To sum up, the large-scale field of the flux transport simulations matches well the solar-like star observations regarding the poloidal and toroidal energy. The ℓ_Σ-modes show three behaviours: a mainly poloidal dipolar mode, a quadrupolar mode obtaining the highest toroidal energy fraction and higher ℓ_Σ-modes that follow the power law $\langle B^2_{\rm tor}\rangle \propto \langle B^2_{\rm pol}\rangle^{0.77\pm0.02}$.

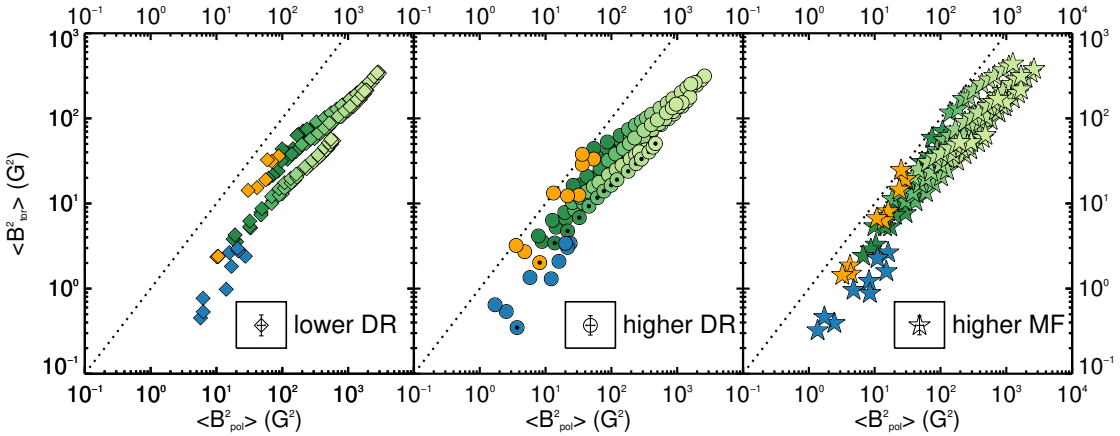

Figure 3.3: The poloidal $\langle B^2_{\rm pol}\rangle$ and toroidal energies $\langle B^2_{\rm tor}\rangle$ for the simulations split in three groups. All three groups cover flux emergence rates of ER $= 1, 3, 5\,{\rm ER}_\odot$. The same format as in Fig. 3.2 bottom is used. Left: The lower DR simulations (diamonds) with differential rotation of DR $= 0.3, 0.5, 0.8\,{\rm DR}_\odot$. Middle: The higher DR simulations (circles) with DR $= 1, 3, 5\,{\rm DR}_\odot$ (the same simulations as plotted in Fig. 3.2 bottom). Right: The higher MF simulations (stars) owning the same differential rotation as the higher DR simulation but a higher meridional flow of MF $= 10\,{\rm MF}_\odot$.

3.4.2 The impact of differential rotation and meridional flow

I analysed the effect of the differential rotation and meridional flow onto the magnetic field properties of different length scales. I split the sample into three groups:

- **lower DR** includes the simulations with sub-solar differential rotation of DR $= 0.3, 0.5,$ $0.8\,{\rm DR}_\odot$,
- **higher DR** includes the simulations with differential rotation of DR $= 1, 3, 5\,{\rm DR}_\odot$ and
- **higher MF** includes the simulations with the same differential rotation as the higher DR group, but having a meridional flow ten times higher than our Sun with MF $= 10\,{\rm MF}_\odot$.

All three groups consider the flux emergence rates of ER $= 1, 3, 5\,{\rm ER}_\odot$. Fig. 3.3 compares the three groups in respect of the toroidal and poloidal energy using the same format as Fig. 3.2 (bottom panel).

The higher DR simulations are closer to the dashed unity line than the lower DR simulations, see left and middle panel of Fig. 3.3. The poloidal energy $\langle B^2_{\rm pol}\rangle$ decreases with higher differential rotation. For the higher DR some of the ℓ_Σ-modes, especially the $\ell_\Sigma = 2$ modes (orange circles), become toroidal dominated as the toroidal energy stays constant while the poloidal energy decreases. This is reflected in the shallower slope of the higher ℓ_Σ-modes

(greenish symbols) for the higher DR $\left(\langle B^2_{\rm tor}\rangle \propto \langle B^2_{\rm pol}\rangle^{0.77\pm0.02}\right)$ compared to the lower DR $\left(\langle B^2_{\rm tor}\rangle \propto \langle B^2_{\rm pol}\rangle^{0.87\pm0.02}\right)$ simulations.

The higher meridional flow affects the middle ℓ_Σ-modes most strongly, see middle and right panel of Fig. 3.3. Next to the $\ell_\Sigma = 2$ mode also other low ℓ_Σ-modes are closer to the unity line and show an increase of the toroidal energy by losing slightly poloidal energy. This results in the more curved appearance of the $\ell_\Sigma \geq 3$ modes. Further, the dipolar $\ell = 1$ modes display a slightly lower $\langle B^2_{\rm tor}\rangle$. The higher ℓ_Σ-modes follow a power law relation as well $\left(\langle B^2_{\rm tor}\rangle \propto \langle B^2_{\rm pol}\rangle^{0.80\pm0.02}\right)$.

Summarising, the differential rotation seems to lower the poloidal energy while the toroidal energy remains unchanged. The meridional flow changes the large-scale field topology of the lower to mid ℓ_Σ-modes by slightly decreasing the poloidal energy and increasing the toroidal energy.

3.4.3 The impact of emergence rate

Fig. 3.4 plots the poloidal $\langle B^2_{\rm pol}\rangle$ (top panel) and toroidal energy $\langle B^2_{\rm pol}\rangle$ (bottom panel) logarithmically over all differential rotation rates ($0.3 - 5\,{\rm DR}_\odot$) and ℓ_Σ-modes. The background colour indicates the flux emergence rate (ER) and gets darker with increasing ER. The differential rotation increases from left to right for each flux emergence rate. The error bars are similar or smaller than the plot symbol.

Both magnetic energies, $\langle B^2_{\rm pol}\rangle$ and $\langle B^2_{\rm tor}\rangle$, increase with flux emergence rate, see Fig. 3.4. The differential rotation causes a widely linear decrease of $\log(\langle B^2_{\rm pol}\rangle)$, where this trend is best seen for lower flux emergence rates, Fig. 3.4 top. In Fig. 3.4 bottom I see a weak decrease of $\langle B^2_{\rm tor}\rangle$ for the higher ℓ_Σ-modes. The lower ℓ_Σ-modes increase with differential rotation (especially the solar flux emergence rate) or stay constant. The toroidal energy $\langle B^2_{\rm tor}\rangle$ increases by around one order of magnitude from $\ell = 1$ to $\ell_\Sigma = 2$. This increase gets stronger with flux emergence rate.

The next figure, Fig. 3.5, compares the logarithmically poloidal (top) and toroidal energy (bottom) for the solar (left) and higher meridional flow (right) simulations using a similar format then Fig, 3.4.

The poloidal energy is mostly unaffected by the meridional flow. Only the lowest ℓ_Σ-modes

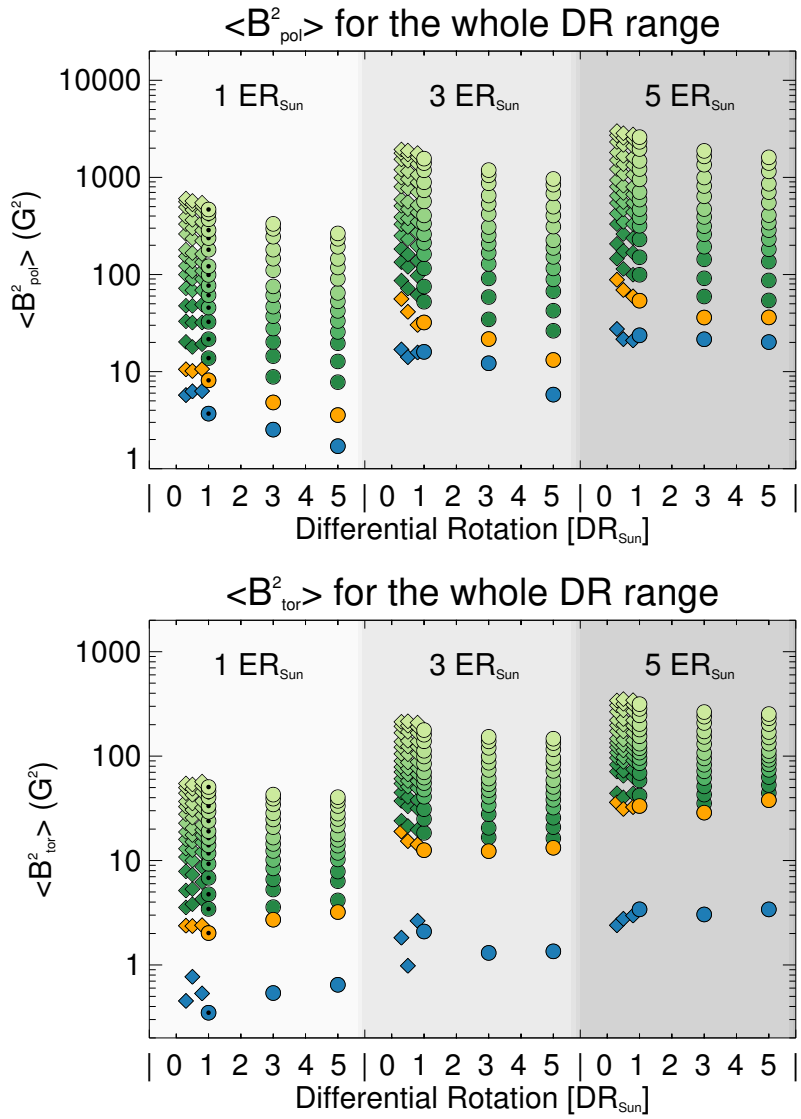

Figure 3.4: The poloidal $\langle B^2_{\rm pol}\rangle$ (top) and toroidal magnetic energy $\langle B^2_{\rm tor}\rangle$ (bottom) over the whole range of differential rotation accessible from the simulations for the cumulative ℓ_Σ-modes. The differential rotation increases to the right for each flux emergence rate, which is indicated by the background shade. The background shade becomes darker with increasing flux emergence rate. The lower DR simulations are displayed as diamonds and the higher DR simulations as circles and the simulated Sun is marked by the solar symbol $\odot$. The same colour scheme is used as in Fig. 3.2.

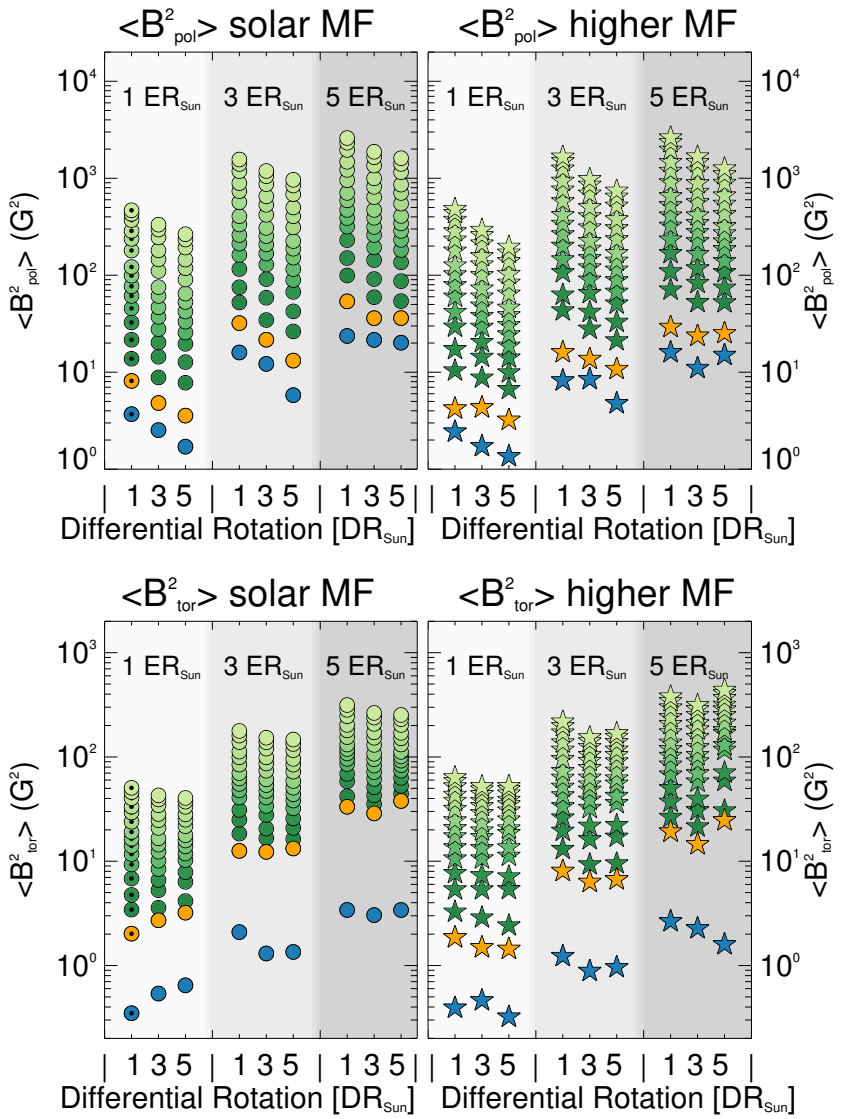

Figure 3.5: The poloidal $\langle B^2_{\rm pol}\rangle$ (top) and toroidal energy $\langle B^2_{\rm tor}\rangle$ (bottom) over the higher differential rotation range for the cumulative ℓ_Σ-modes comparing the solar meridional flow simulations (left, circles) with the higher meridional flow simulations (right, stars). Beside that the same format as in Fig. 3.4 is used.

show slightly lower $\langle B^2_{\rm pol}\rangle$. However, the $\langle B^2_{\rm tor}\rangle$ changes with increasing meridional flow: in general, $\langle B^2_{\rm tor}\rangle$ becomes stronger for high ℓ_Σ-modes but weaker for low ℓ_Σ-modes. The even low ℓ_Σ-modes increase stronger than the odd low ℓ_Σ-modes but the gap between $\ell = 1$ and $\ell_\Sigma = 2$ is smaller with higher MF.

Furthermore, I analysed the quadrupole/dipole $\frac{\langle B^2_{l=2}\rangle}{\langle B^2_{l=1}\rangle}$ and octopole/dipole ratio $\frac{\langle B^2_{l=3}\rangle}{\langle B^2_{l=1}\rangle}$ of the total magnetic energy. Both show no clear dependencies on differential rotation or meridional flow. For solar flux emergence rates the octopole/dipole ratio is larger than the quadrupole/dipole ratio, while for higher flux emergence rates it is reversed.

To sum up: With higher flux emergence rates the energy of the toroidal and poloidal field increases for all ℓ_Σ-modes. The toroidal energy increases by approximately one order of magnitude from the dipolar to the cumulative quadrupolar mode. This increase gets stronger with rising flux emergence rate. Higher differential rotation decreases the poloidal energy for all ℓ_Σ-modes, while the toroidal energy shows a weaker decrease for high ℓ_Σ-modes but remains widely constant for the low ℓ_Σ-modes. With higher meridional flow a weak decrease of the poloidal and toroidal energy for the low ℓ_Σ-modes occur, while the toroidal energy gets stronger for the high ℓ_Σ-modes. The rise of the toroidal energy is stronger for the low even ℓ_Σ-modes than for the odd ℓ_Σ-modes.

3.4.4 The distribution of magnetic energy across ℓ-modes

The previous figures suggested that the differential rotation, flux emergence and meridional flow differently affect the single ℓ-modes. I investigate therefore the energy distribution $\langle B^2\rangle(\ell)$ across the single ℓ-modes.

Figure 3.6 displays the energy distribution of the radial (green), azimuthal (red) and meridional component (blue) over the ℓ-modes $\ell = 1 - 28$[15]. The flux emergence and differential rotation rate of each stellar model is indicated by the title of each barplot. Fig. 3.6 includes only solar meridional flow rates. The left column of Fig. 3.15 in the chapter appendix shows the meridional flow equivalent to the middle column of Fig. 3.6.

I noticed the following by analysing the individual values of the energy distributions: The maximum energy per ℓ-mode increases with flux emergence rate, see vertical direction of Fig. 3.6, and decreases with differential rotation rate, see horizontal direction of Fig. 3.6,

[15] In addition, Fig. 3.14 in the chapter appendix presents a detailed view on the first ten ℓ-modes.

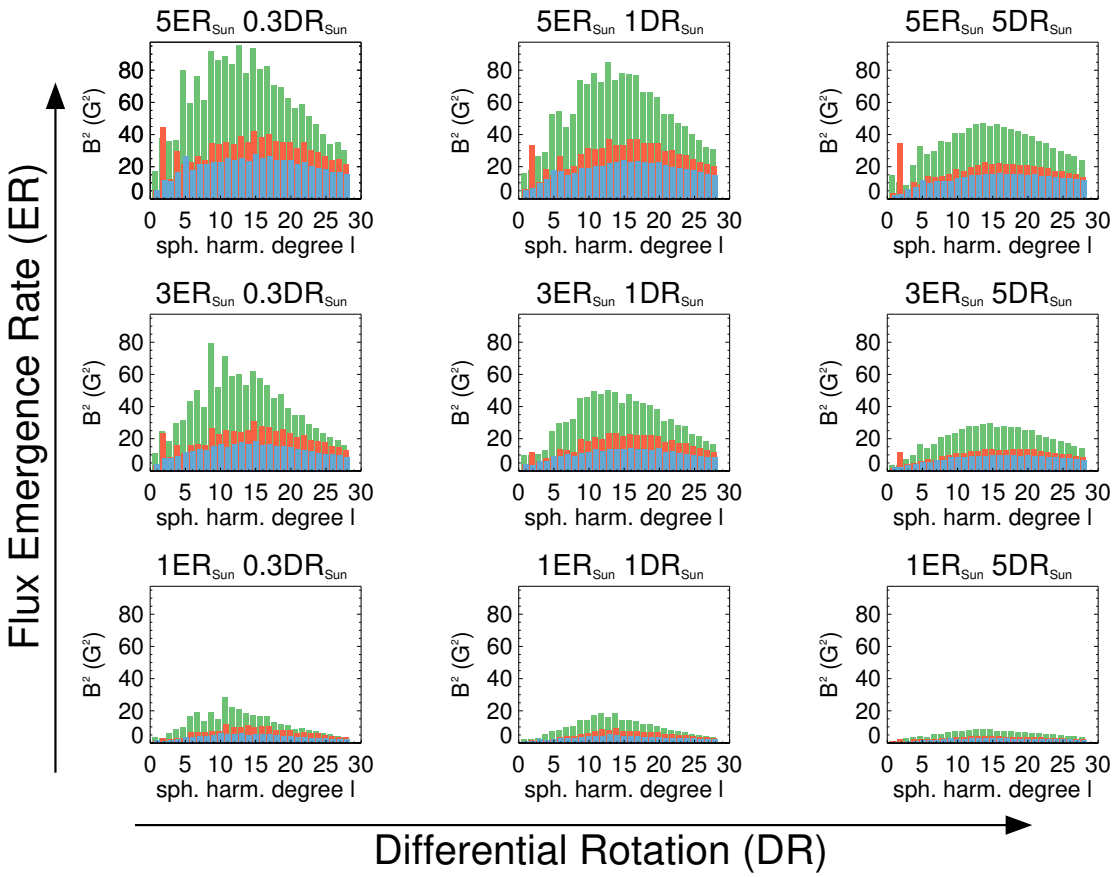

Figure 3.6: The magnetic energy distribution for the radial $\langle B^2_{\rm rad}\rangle(l)$ (green bars), azimuthal $\langle B^2_{\rm azi}\rangle(l)$ (red bars) and meridional component $\langle B^2_{\rm mer}\rangle(l)$ (blue bars). The title above each barplot indicates the flux emergence rate and differential rotation. The differential rotation increases horizontally and the flux emergence rate vertically. All here shown simulations have a solar meridional flow. For a comparison with the higher meridional flow simulations, see Figure 3.15 left column.

where the flux emergence rate displays the greater effect.

The differential rotation (DR) produces in general a decrease of $\langle B^2_{\rm rad}\rangle$, $\langle B^2_{\rm azi}\rangle$ and $\langle B^2_{\rm mer}\rangle$ for most of the ℓ-modes[16]. The only exception is the azimuthal quardupolar mode that remains constant. The meridional and the radial quadrupolar mode decrease even more strongly than the dipolar mode for high DR. See also Fig. 3.14 in the chapter appendix for a detailed view on the first ten ℓ-modes. The higher meridional flow (MF) causes an increase of $\langle B^2_{\rm mer}\rangle$ at the cost of $\langle B^2_{\rm rad}\rangle$ for the low ℓ-modes, see Fig. 3.15 left column. Higher MF simulations show a lower $\langle B^2_{\rm azi}\rangle$ for the quadrupolar mode.

In addition, the stellar parameters influence the shape of the energy distributions. The azimuthal $\ell = 2$ mode becomes more and more dominant over the other azimuthal modes until it stores the highest $\langle B^2_{\rm azi}\rangle$ with increasing flux emergence rate (ER). The ER enhances also the following trends with DR. With increasing DR the peak of the radial distribution becomes broader and shifts to slightly higher ℓ-modes. In general, the radial component peaks before the azimuthal and meridional component for solar MF. With higher MF, see Fig. 3.15 left column, the peak of the meridional components shifts to lower ℓ-modes and peaks than before the radial and azimuthal component. A higher MF flattens also the azimuthal $\ell = 2$ mode compared to the peak of the azimuthal component at mid ℓ-modes and broadens the peak distribution of the radial component.

A rather simpler pictures occurs in Fig. 3.7, which plots the poloidal $\langle B^2_{\rm pol}\rangle(\ell)$ and toroidal energy distributions $\langle B^2_{\rm rad}\rangle(\ell)$. The peak values for both components increase as well with ER and decrease with DR, where ER has a stronger effect. In general, the toroidal distribution (without $\ell = 2$) peaks at lower ℓ_Σ-modes than the poloidal distribution.

The toroidal $\ell = 2$ mode increases relatively to the peak of the toroidal distribution at mid ℓ-modes with increasing ER similar to the azimuthal distribution. A higher DR causes a decrease of the poloidal energy for all ℓ-modes. The quadrupolar mode stands out again: with increasing DR the toroidal $\ell = 2$ is widely constant or shows a slight increase while the poloidal $\ell = 2$ mode even stronger decreases compared to the other modes. For high ER and low DR next to the $\ell = 2$ further even ℓ-modes can be enhanced. For DR $\geq 3\,\mathrm{DR}_\odot$ the toroidal quadrupolar mode becomes the strongest toroidal mode. Furthermore, with increasing DR the poloidal peak distribution becomes broadener and shifts to slightly higher ℓ-modes.

[16] At the first glance this seems counter-intuitive to the prediction of the dynamo theory but I discuss this result extensively in Section 3.5.

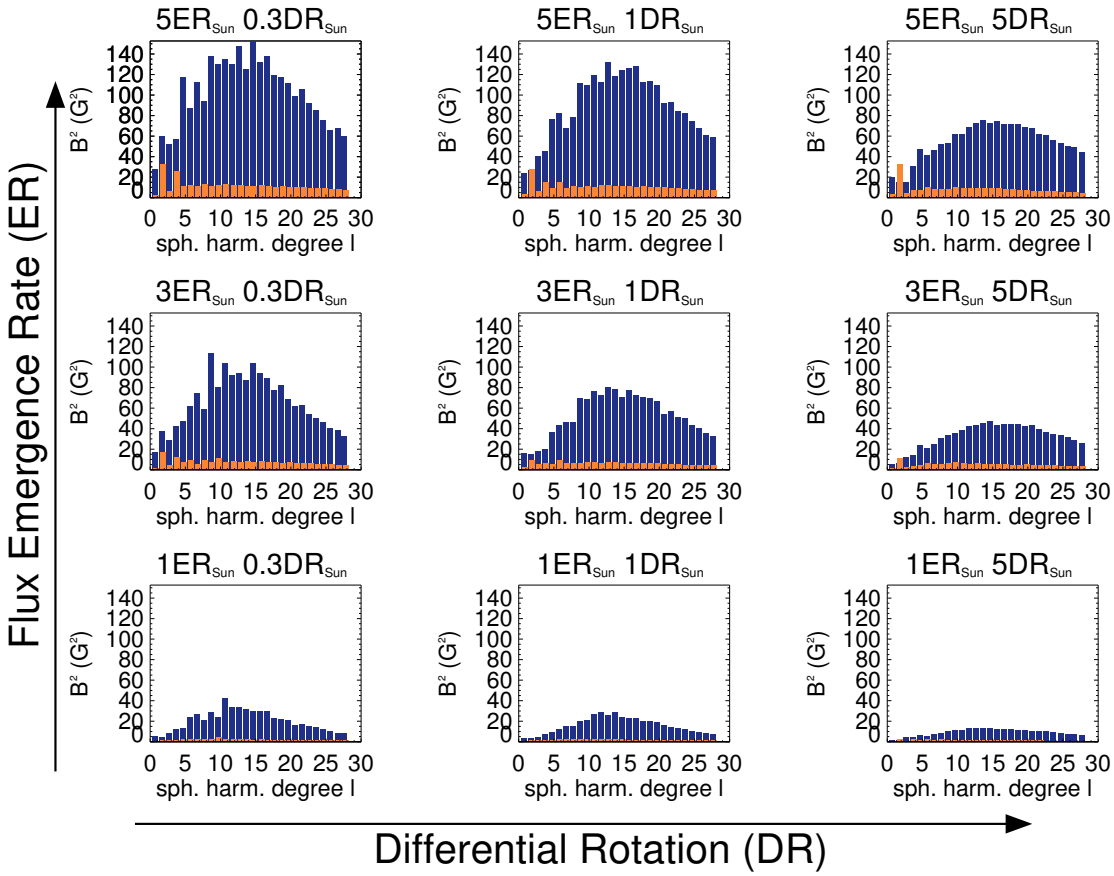

Figure 3.7: The magnetic energy distribution for the poloidal $\langle B^2_{\rm pol}\rangle(\ell)$ (plum bars) and toroidal component $\langle B^2_{\rm tor}\rangle(\ell)$ (orange bars). The same format as for Fig. 3.6 is used. For a comparison with the higher meridional flow simulations, see Figure 3.15 right column.

With higher MF, see Fig. 3.15 right column, all low toroidal modes ($\ell \approx 2-16$) are enhanced, so that the strongest toroidal mode is always at mid ℓ-modes. Especially, the low even ℓ-modes are stronger for higher MF in connection with higher ER and DR as seen in the top row of Fig. 3.9. However, there is no preference to enhance only the $\ell = 2$ mode, see Fig. 3.9 top row. For higher MF the poloidal peak distributions becomes again broadener.

Summarising, the stellar parameters affect the magnetic energy distributions. With an increased flux emergence rate, $\langle B^2 \rangle$ increases for all ℓ-modes. The azimuthal and toroidal $\ell = 2$ mode is enhanced relative to the peak values in the mid ℓ-modes and could become the dominant azimuthal or toroidal mode. With an increased differential rotation, $\langle B^2 \rangle$ decreases for most ℓ-modes, where the azimuthal and toroidal $\ell = 2$ are exceptions as they stay widely constant. Next to this, the radial and poloidal peak distributions broaden and their peaks shift to lower ℓ-modes. With an increased meridional flow, $\langle B^2_{\rm mer} \rangle$ increases at the cost of $\langle B^2_{\rm rad} \rangle$, while the peak of the $\langle B^2_{\rm mer} \rangle(\ell)$ distribution shifts to lower ℓ-modes. Further, the lower toroidal ℓ-modes increase with meridional flow especially the even ℓ-modes. The azimuthal and toroidal $\ell = 2$ becomes weaker relatively to the peak values at mid ℓ-modes.

The $\ell = 2$ mode seems to react differently to changes in ER and DR compared to the other ℓ-modes. This becomes even more clear by analysing the fractions of the different field components $f(\ell)$, see Fig. 3.8. The top row displays the cumulative total $C_I(\ell)$ of the radial, azimuthal and meridional fraction of the total energy distribution per ℓ-mode:

$$C_I(\ell) = \sum_i f_i(\ell), \tag{3.8}$$

$$f_i(\ell) = \frac{\langle B^2_{\rm i} \rangle(\ell)}{\langle B^2_{\rm tot} \rangle(\ell)}, i \in ({\rm rad}, {\rm azi}, {\rm mer}), \tag{3.9}$$

$$\langle B^2_{\rm tot} \rangle(\ell) = \langle B^2_{\rm rad} \rangle(\ell) + \langle B^2_{\rm azi} \rangle(\ell) + \langle B^2_{\rm mer} \rangle(\ell). \tag{3.10}$$

The second row of Fig. 3.8 plots the cumulative total $C_J(\ell)$ of the poloidal and toroidal fraction:

$$C_J(\ell) = \sum_j f_j(\ell), \tag{3.11}$$

$$f_j(\ell) = \frac{\langle B^2_{\rm j} \rangle(\ell)}{\langle B^2_{\rm tot} \rangle(\ell)}, j \in ({\rm pol}, {\rm tor}), \tag{3.12}$$

$$\langle B^2_{\rm tot} \rangle(\ell) = \langle B^2_{\rm pol} \rangle(\ell) + \langle B^2_{\rm tor} \rangle(\ell). \tag{3.13}$$

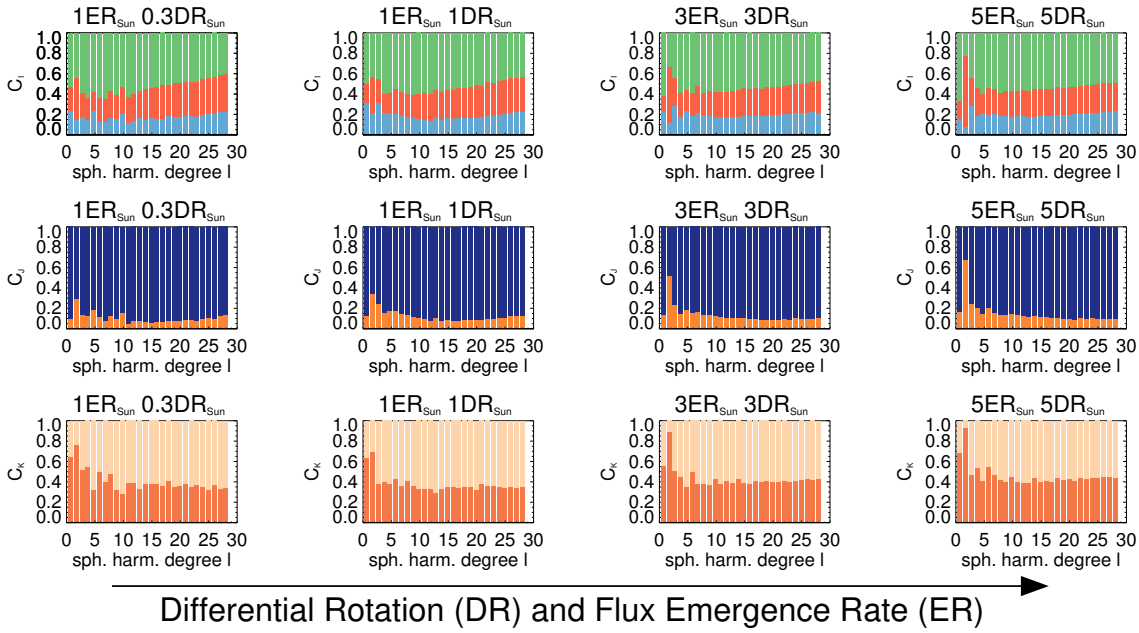

Figure 3.8: The cumulative total $C(\ell) = \sum f(\ell)$ of the fractions for the different field components over ℓ-modes for the solar meridional flow simulations. The top row shows the cumulative total $C_I(\ell) = f_{\mathrm{mer}}(\ell) + f_{\mathrm{azi}}(\ell) + f_{\mathrm{rad}}(\ell)$ of the meridional (blue), azimuthal (red) and radial (green) fraction. The middle row the cumulative total $C_J(\ell) = f_{\mathrm{tor}}(\ell) + f_{\mathrm{pol}}(\ell)$ of the toroidal (orange) and poloidal (plum) fraction. The bottom row displays the cumulative total $C_K(\ell) = f_{\mathrm{azi,tor}}(\ell) + f_{\mathrm{mer,tor}}(\ell)$ of the azimuthal toroidal (red orange) and the meridional toroidal (light orange) fraction, that build up the toroidal component. The title of each barplot indicates the flux emergence rate and differential rotation. Both parameters increase horizontally. For a comparison with the higher meridional flow simulations see Figure 3.16.

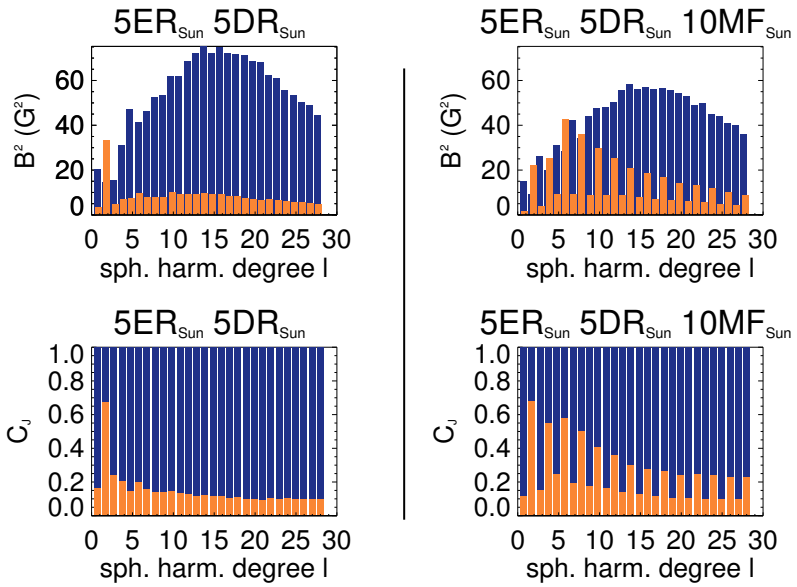

Figure 3.9: The simulations of an active star (DR $= 5\,\mathrm{DR}_\odot$ and ER $= 5\,\mathrm{ER}_\odot$) with solar meridional flow, left column, and higher meridional flow MF $= 10\,\mathrm{MF}_\odot$, right column. The top row displays the magnetic energy distribution for the poloidal $\langle B^2_{\mathrm{pol}}\rangle(\ell)$ (plum bars) and toroidal component $\langle B^2_{\mathrm{tor}}\rangle(\ell)$ (orange bars) and the bottom row the cumulative total $C_J(\ell) = f_{\mathrm{tor}}(\ell) + f_{\mathrm{pol}}(\ell)$ of the toroidal (orange) and poloidal (plum) fraction.

and the bottom row presents the cumulative total $C_K(\ell)$ of the azimuthal toroidal and meridional toroidal fraction of the toroidal energy $\langle B^2_{\rm tor}\rangle$, see also Eq. 1.32,

$$C_K(\ell) = \sum_k f_k(\ell), \tag{3.14}$$

$$f_k(\ell) = \frac{\langle B^2_{\rm k}\rangle(\ell)}{\langle B^2_{\rm tor}\rangle(\ell)}, k \in (\text{azi, tor; mer, tor}), \tag{3.15}$$

$$\langle B^2_{\rm tor}\rangle(\ell) = \langle B^2_{\rm azi,tor}\rangle(\ell) + \langle B^2_{\rm mer,tor}\rangle(\ell). \tag{3.16}$$

The colour schema is the same as in the previous Figures 3.6 and 3.7 and azimuthal toroidal fraction is coloured in red orange and the meridional toroidal fraction in light orange. Fig. 3.8 shows only the results for the solar MF simulations with increasing flux emergence rate and differential rotation. For the higher MF results, see Fig. 3.16 in the chapter appendix.

For the high ℓ-modes the radial $f_{\rm rad}$, azimuthal $f_{\rm azi}$ and meridional component $f_{\rm mer}$ are widely constant, see Fig. 3.8 top row. The largest fraction with $f_{\rm rad} \approx 0.5$ is given by the radial field. The azimuthal and meridional components display similar fractions with $f_{\rm rad} \approx f_{\rm azi} \approx 0.25$ widely unaffected by changes in ER or DR. I found only a small increase in $f_{\rm rad}$ while $f_{\rm azi}$ and $f_{\rm mer}$ slightly decrease for more active stellar models. The stellar parameters influence the large-scale magnetic energy stored in the low ℓ-modes much more strongly. With increasing DR, $f_{\rm azi}$ increases for the quadrupolar $\ell = 2$ mode and for some neighbouring ℓ-modes, too. Next to this, the radial $\ell = 1$ mode becomes stronger. An increasing ER enhances these effects. Comparing the solar with higher MF, see Fig. 3.16 top, I found that $f_{\rm mer}$ increases for the low ℓ-modes mainly at the cost of $f_{\rm rad}$ as seen for the energy distributions.

Also the poloidal $f_{\rm pol}$ and toroidal fraction $f_{\rm tor}$ remains unchanged for the high ℓ-modes with $f_{\rm pol} \approx 0.9$ and $f_{\rm tor} \approx 0.1$, see Fig. 3.8 middle row. For the large-scale field $f_{\rm tor}$ increases with increasing DR, especially the quadrupolar $\ell = 2$ mode. This reflects the strong decrease of $\langle B^2_{\rm pol}\rangle$ while $\langle B^2_{\rm tor}\rangle$ remains constant. The dipolar $\ell = 1$ mode is strongly poloidal, whereas the quadrupolar $\ell = 2$ mode is dominantly toroidal for DR $\geq 3\,\mathrm{DR}_\odot$. For the higher MF simulations, see Fig. 3.16 middle, $f_{\rm tor}$ increases for the low ℓ-modes as well, but the even ℓ-modes are especially enhanced. This effect is best seen for the more active stellar models, see Fig. 3.9 bottom row. For higher MF the $\ell = 2$ mode is often stronger but not always the strongest toroidal mode. The highest $f_{\rm tor}$ occurs also in the $\ell = 4$ or $\ell = 6$ mode for high DR and MF stellar models, (not shown).

In order to better understand the behaviour of the toroidal field, I analysed the relative contributions of its azimuthal and meridional parts. The higher ℓ-modes show roughly equal fractions for the meridional toroidal $f_{\mathrm{mer,tor}}$ (light orange bars) and azimuthal toroidal field $f_{\mathrm{azi,tor}}$ (red orange bars), whereas the lowest ℓ-modes are highly azimuthal toroidal. The quadrupolar $\ell = 2$ mode shows the highest $f_{\mathrm{azi,tor}}$ for the stellar models with solar MF. With increasing DR, $f_{\mathrm{azi,tor}}$ increases as well for both the quadrupolar $\ell = 2$ mode and the highest ℓ-modes. An increasing ER enhances these effects again. With increasing MF, $f_{\mathrm{mer,tor}}$ increases for the lowest ℓ-modes and $f_{\mathrm{azi,tor}}$ for the highest ℓ-modes, see Fig. 3.16 bottom. The increased meridional toroidal field can even suppress the strong azimuthal toroidal $\ell = 2$ mode, see Fig. 3.16 bottom. However, with stronger DR the $\ell = 2$ and further even ℓ-modes become dominant $f_{\mathrm{azi,tor}}$ again, (not shown).

Furthermore, I investigated the average of the large-scale field ($\ell = 1-5$) and the average over all ℓ-modes for the toroidal and azimuthal fraction, (not shown). The toroidal fraction f_{tor} doubles for the averaged large-scale field from ≈ 0.15 to ≈ 0.3 with increasing DR. Even the average over all ℓ-modes including the large and small-scale field shows a small increase of 0.05 in f_{tor}. The increase for f_{azi} of the large-scale field average is smaller (≈ 0.25 to ≈ 0.35). This confirms that the differential rotation is changing the field topology to more toroidal and slightly more azimuthal field topologies.

Summing up: The following effects of the differential rotation are enhanced by an increasing flux emergence rate. The toroidal f_{tor} and azimuthal f_{azi} fraction increase for the lower ℓ-modes representing the large-scale field. The azimuthal and toroidal $\ell = 2$ modes rise the most. In addition, the azimuthal toroidal fraction $f_{\mathrm{azi,tor}}$ increases for $\ell = 2$ and for the higher ℓ-modes. An increased meridional flow rate increases f_{mer} by decreasing f_{rad} for the low ℓ-modes. The rise of the toroidal fraction f_{tor} for the even ℓ-modes is most obvious. With higher MF, $f_{\mathrm{mer,tor}}$ increases for the low ℓ-modes while $f_{\mathrm{azi,tor}}$ rises for the high ℓ-modes.

3.4.5 The axisymmetry of different modes

The next point I discuss is the axisymmetry of the surface magnetic field simulations. Motivated by the results of See et al. (2015), I plot the fraction of the axisymmetric energy f_{axi} (see Eq. 2.22) versus the fraction of the toroidal energy f_{tor}, see Fig. 3.10a. The results of the optimal average are displayed as diamonds for the lower DR sample, as circles for the higher DR sample and as stars for the higher MF sample, otherwise the same format as for Fig. 3.2 is

used. The errorbars, indicating the standard derivation for the optimal average, are attached to each symbol but are not visible if the error is smaller than the plot symbol.

I can confirm the trend found by See et al. (2015) that toroidal dominated topologies are also highly axisymmetric topologies. Next to this, a clear trend with ℓ_Σ-modes is visible. This ℓ_Σ-mode trend was also visible using the smaller set of simulations including only 17 maps presented in Lehmann et al. (2017, fig. 3), see also Figure 3.17 in the chapter appendix. The dipolar $\ell = 1$ modes (blue) are mainly poloidal, while the cumulative quadrupolar modes $\ell_\Sigma = 2$ (orange) are strongly toroidal. Both modes show a high axisymmetric fraction. With increasing ℓ_Σ-modes (greenish symbols) both the fractions $f_{\rm axi}$ and $f_{\rm tor}$ decrease as well as the errors. A direct comparison between the simulations and the observations is possible by focusing on the greenish symbols for the $\ell_\Sigma = 5, 10$ modes. The simulations cover the same parameter range as the solar-like star observations. I find only very weak trends with differential rotation and meridional flow: the lower DR models own smaller fractions of $f_{\rm tor}$ and $f_{\rm axi}$, whereas the higher MF models show higher $f_{\rm tor}$ but similar $f_{\rm axi}$ compared to the higher DR models.

The axisymmetry of the field is underpinned by the axisymmetry of the poloidal and toroidal field, which can be seen in Figure 3.10b, motivated by See et al. (2015, fig. 7). The dipolar $\ell = 1$ modes (blue) show a high axisymmetric poloidal field, whereby the axisymmetry of the quadrupolar $\ell_\Sigma = 2$ (orange) and of the other low ℓ_Σ-modes (dark green) is mainly given by the axisymmetric toroidal field. The high ℓ_Σ-modes display only a low axisymmetric fraction. The fraction of poloidal field is larger than the fraction of toroidal field for the majority of the ℓ_Σ-modes, which explains that the errors for $f_{\rm axi,tor}$ are often larger than for $f_{\rm axi,pol}$. An increasing DR increases $f_{\rm axi,pol}$ and $f_{\rm axi,tor}$ for all ℓ_Σ-modes with exception of the dipolar modes. For the higher MF stellar models the dipolar modes strikingly display a lack of axisymmetric toroidal field while owning the same percentage of axisymmetric poloidal field as the solar MF stellar models.

To further investigate this lack of axisymmetric toroidal fraction with increasing MF, I plot the fraction of the axisymmetric poloidal $f_{\rm axi,pol}$ and axisymmetric toroidal field $f_{\rm axi,tor}$ for the solar and higher MF stellar models in Fig. 3.11 by using a similar format to Fig. 3.5. The top panel shows $f_{\rm axi,pol}$ and the bottom panel $f_{\rm axi,tor}$ for the solar MF (left) and for the higher MF models (right). With a fraction higher than 0.5 a field component becomes dominant,

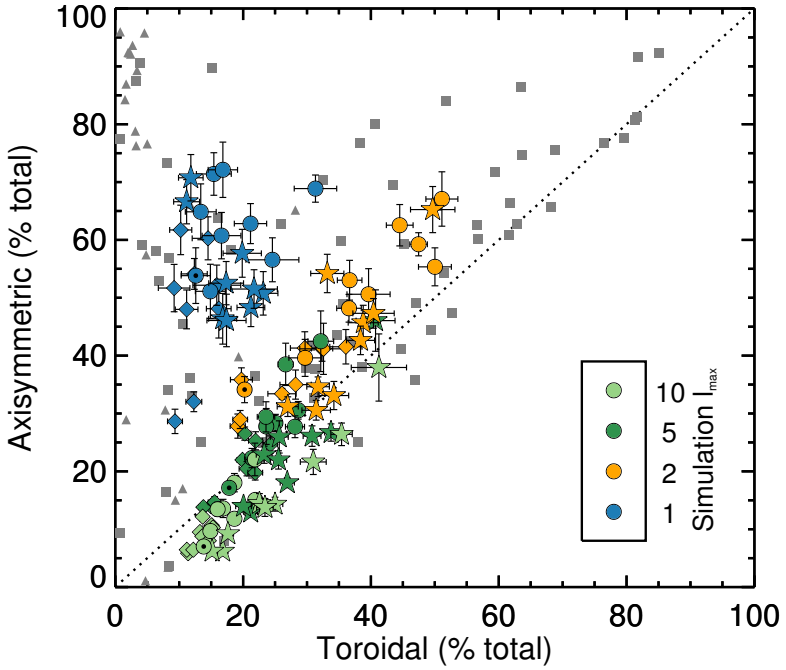

a.

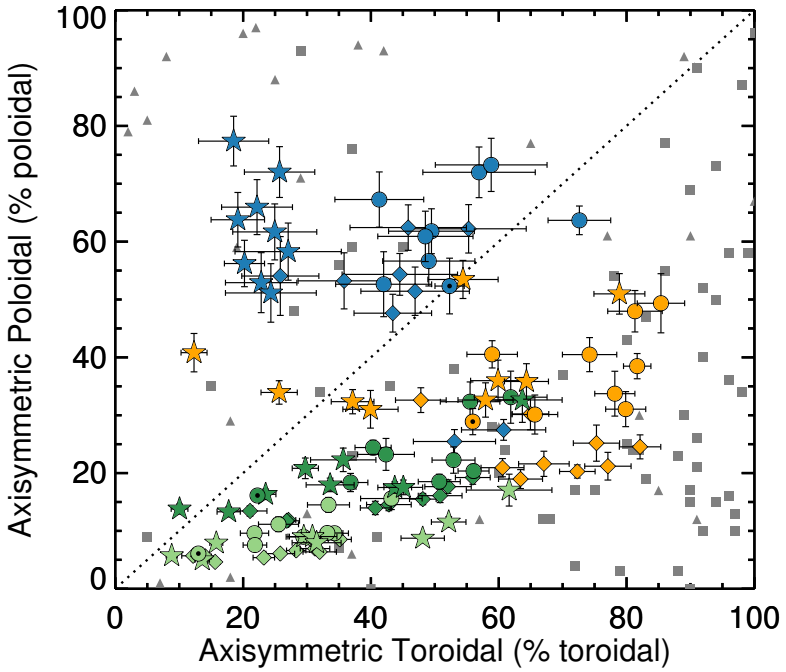

b.

Figure 3.10: The percentages of the axisymmetric and toroidal energies of the total magnetic energy (**a.**) and the percentages of the axisymmetric poloidal and the axisymmetric toroidal fraction (**b.**) for the simulations (coloured symbols) and for the observations (grey symbols). The figures presents the cumulative ℓ_Σ-modes $\ell_\Sigma = \ell_{\max} = 1, 2, 5, 10$, for the simulations. The lower DR simulations are plotted as diamonds, the higher DR simulations as circles and the higher MF simulations as stars. The same format as in Fig. 3.2 is used and the top figure is comparable to Lehmann et al. (2017), fig. 3.

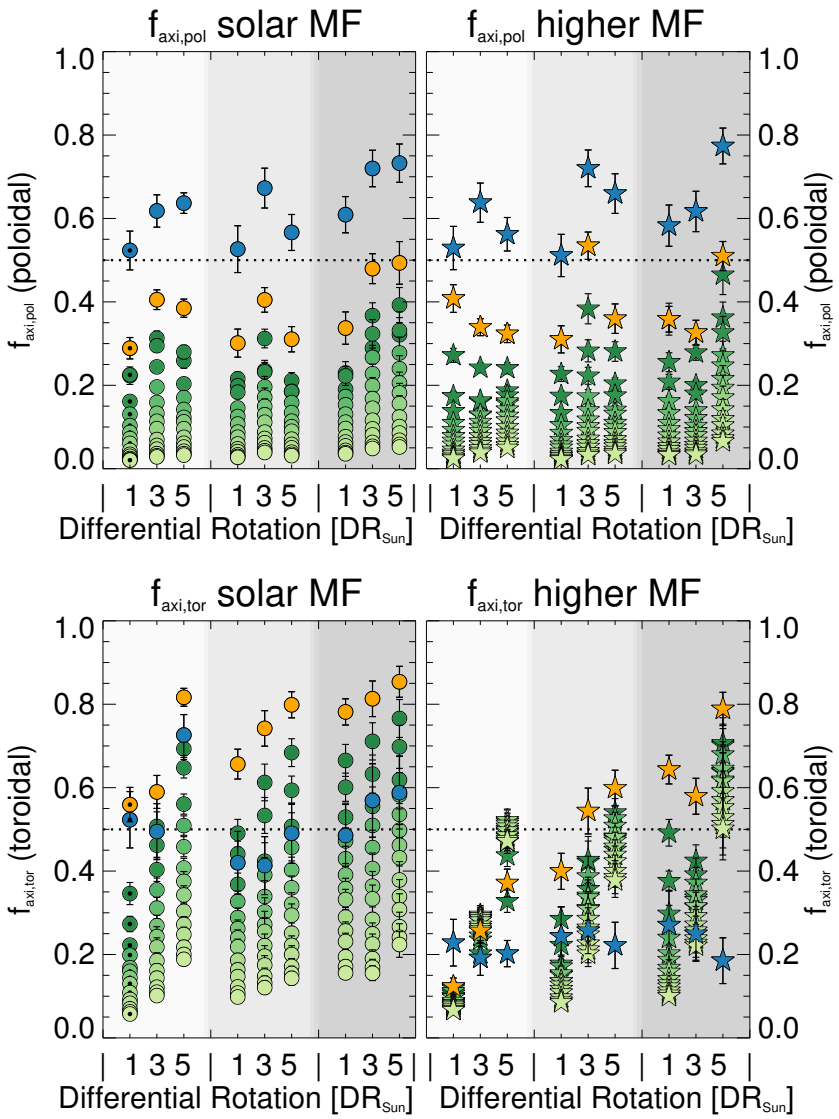

Figure 3.11: The fractions of the axisymmetric poloidal $f_{\mathrm{axi,pol}}$ energy (top) and of the axisymmetric toroidal $f_{\mathrm{axi,tor}}$ energy (bottom) for the cumulative ℓ_{Σ}-modes comparing the solar meridional flow simulations (left) with the higher meridional flow simulations (right). The same format as in Fig. 3.5 is used.

which is indicated by the dashed line. I find that the axisymmetric poloidal fraction $f_{\rm axi,pol}$ decreases with increasing ℓ_Σ-modes, see Fig. 3.11 top. The dipolar mode shows by far the highest $f_{\rm axi,pol}$ for the simulations with solar and higher MF. In general, there are no to little differences between the solar MF (left) and higher MF (right) models for $f_{\rm axi,pol}$.

For the solar MF simulations the $\ell_\Sigma = 2$ mode has the highest fraction of axisymmetric toroidal field $f_{\rm axi,tor}$, see Fig. 3.11 bottom left. With increasing ℓ_Σ-modes $f_{\rm axi,tor}$ decreases similar to $f_{\rm axi,pol}$, see top panel. The dipolar mode displays lower $f_{\rm axi,tor}$ than the $\ell_\Sigma = 2$ mode and for high ER even lower values than $\ell_\Sigma = 4$. However, with increasing DR, I see an increase of $f_{\rm axi,tor}$ for all ℓ_Σ-modes higher than $\ell_\Sigma = 2$. For the higher MF $f_{\rm axi,tor}$ behaves differently compared to the solar MF results, see Fig. 3.11 bottom right. First of all, $f_{\rm axi,tor}$ is in general lower and the ℓ_Σ-modes are closer together. With increasing ER the quadrupolar $\ell_\Sigma = 2$ has the highest $f_{\rm axi,tor}$ and decreases with increasing ℓ_Σ-modes. For the solar ER, I see a different, non-consistent and nearly opposite trend with ℓ_Σ-modes. Most important the dipolar modes display $f_{\rm axi,tor} \approx 0.2$ for all higher MF simulations independent of differential rotation or flux emergence rate, which explains the clear offset for the dipolar modes to lower $f_{\rm axi,tor}$ in Fig. 3.10b.

In a nutshell: I can confirm that the higher the toroidal field fraction, the higher the axisymmetry fraction. The most axisymmetric modes are the dipolar and cumulative quadrupolar modes. The axisymmetry of the dipolar modes is underpinned by the axisymmetric poloidal field while the axisymmetry of $\ell_\Sigma = 2$ and the higher ℓ_Σ-modes is based on the toroidal axisymmetric field. The $f_{\rm axi,pol}$ and $f_{\rm axi,tor}$ for all ℓ_Σ-modes higher than the dipolar mode is enhanced by the differential rotation although $f_{\rm axi,tor} > f_{\rm axi,pol}$ for all solar MF models. The higher meridional flow causes a lack of $f_{\rm axi,tor}$ especially for the dipolar modes but shows no effect on the $f_{\rm axi,pol}$.

3.4.6 Summarising the large-scale magnetic field topology

The magnetic field topologies are often summarised using the format of Fig. 1.8, (Donati et al., 2008b; Morin et al., 2008b, 2010; Jeffers et al., 2014; Folsom et al., 2016; Hébrard et al., 2016). In Fig. 3.12 I summarise the basic properties of the dipolar (left) and cumulative quadrupolar mode (right) using a similar format. As I only show $\ell = 1$ and $\ell_\Sigma = 2$ a direct comparison to the observation is not adequate. The observations include various numbers of ℓ_Σ-modes and observation constraints, which makes a comparison of stellar magnetic field

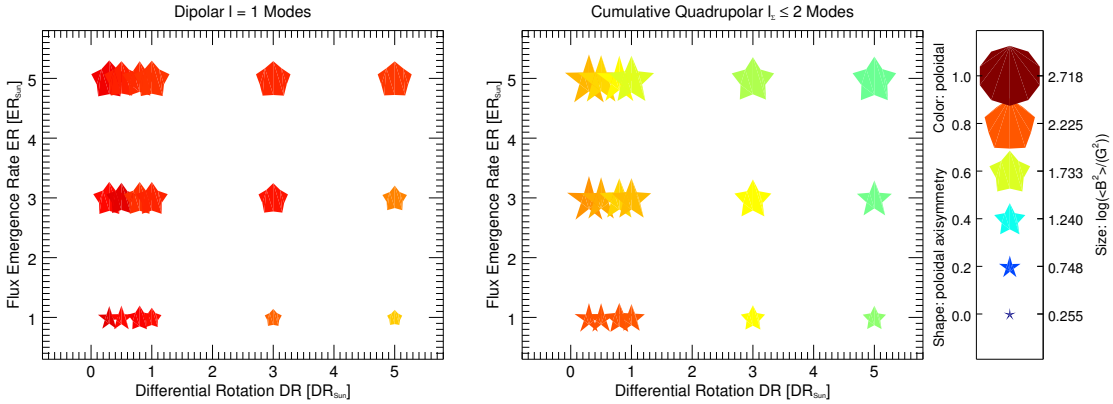

Figure 3.12: Summarising the properties of the dipolar $\ell = 1$ (left) and cumulative quadrupolar $\ell_\Sigma \leq 2$ mode (right) for the solar meridional flow simulations. The higher meridional flow simulations are not shown. The flux emergence rate is plotted versus the differential rotation. The symbol size indicates the logarithmic magnetic energy $\log\langle B^2\rangle$, the symbol shape the fraction of poloidal axisymmetric field $f_{\mathrm{pol,axi}}$ and the symbol color the fraction of the poloidal field f_{pol}.

topologies difficult anyway. The logarithmic magnetic energy $\log(\langle B^2\rangle)$, indicated by the symbol size, increases with ER for both modes and decrease slightly with DR (best seen for $\ell = 1$). The poloidal axisymmetric fraction $f_{\mathrm{pol,axi}}$, displayed by symbol shape, is generally higher for $\ell = 1$ than for $\ell_\Sigma = 2$ but shows no clear trend with ER or DR. The poloidal field fraction f_{pol}, indicated by symbol colour, is dominant for the dipolar mode but for $\ell_\Sigma = 2$ the picture is more diverse. With increasing DR the poloidal fraction decreases and therefore the toroidal fraction ($f_{\mathrm{tor}} = 1 - f_{\mathrm{pol}}$) increases. The toroidal fraction increases with ER as well but less strongly as with DR. The $f_{\mathrm{pol,axi}}$ and f_{tor} decreases by including higher ℓ_Σ-modes, while the trends with DR and ER remain visible.

3.5 Discussion

My aim is to better understand the observed magnetic field topologies, which are restricted to the large-scale field. With the analysis of the large- and small-scale magnetic field topology of several non-potential flux transport simulations, I could derive some conclusions about how the small and large-scale field influence each other and how the different stellar parameters affect the topology.

I find that the large-scale field of the simulated solar-based stellar models fit very well the observed solar-like stars. The magnetic field of the simulations responds to changes of the stellar parameter flux emergence, differential rotation and meridional flow rate, especially the large-scale field topology. I conclude that the magnetic field topology is determined mainly by the global dipolar field and the small-scale flux pattern at the photosphere. The flux pattern

is formed by the surface flux transport processes and the underlying flux emergences pattern.

For the large-scale field the first two spherical harmonic modes are the most important ones: the poloidal dominated dipolar $\ell = 1$ modes and the quadrupolar $\ell = 2$ modes, which often show the highest fraction of toroidal field. The dipolar modes are given by the global dipole field of the stellar models, which is poloidal dominated and highly (poloidal) axisymmetric. The toroidal quadrupolar modes are driven by the large-scale properties of the solar flux emergence pattern: the active regions emerge at mid to low latitudes with opposite polarities on the different hemispheres. This pattern is best characterised by the axisymmetric toroidal quadrupolar mode ($\ell = 2, m = 0$) of the spherical harmonics on global scale, see also insert in Fig. 3.2. The discovered increase of one order of magnitude for the toroidal field from the dipolar to the cumulative quadrupolar mode results from that. If one emerges a different flux pattern another spherical harmonic mode of the large-scale field would capture this pattern. For example bipoles emerging with the same polarity around the equator would be best captured by the axisymmetric toroidal dipolar mode ($\ell = 1, m = 0$). The best evidence for this hypothesis is that for higher MF the $f_{\rm tor}$ of further even ℓ-modes increases to capture the higher latitude position of the active regions. I conclude that the lower spherical harmonic modes can be sensitive to the large-scale properties of the small-scale flux emergence, i.e., to the preferable emergence region and the polarity pattern of the active regions.

Furthermore, the outstanding quadrupolar mode could be connected to a specific signature of a certain solar cycle phase. The flux emergence pattern for the simulations is captured during the activity maximum of the activity cycle 23. At that time the dipolar field was still detectable and the sunspots appeared mainly at mid-latitudes. The behaviour of the dipolar and quadrupolar modes and the large-scale magnetic field topology probably change by using the flux emergence pattern at the activity minimum or at the increasing or decreasing phase[17].

The small-scale field, captured by the higher spherical harmonic modes, is characterised by the size and shape of the bipoles. These modes are less axisymmetric and display a widely fixed ratio between the different field components (toroidal/poloidal and radial/azimuthal/meridional) mostly unaffected by the stellar parameters. As the bipoles obtain a larger area of radial field than of the azimuthal and meridional field, the radial energy distribution $\langle B^2_{\rm rad}\rangle(\ell)$ peaks at lower ℓ-modes than the azimuthal $\langle B^2_{\rm azi}\rangle(\ell)$ and the meridional $\langle B^2_{\rm mer}\rangle(\ell)$ one.

[17] In Chapter 5 I provide a detailed analysis of the solar magnetic field topology along the solar activity cycle 23. Among others I show that and how the dipolar and quadrupolar mode change with time.

Next to this, I found that the small-scale magnetic field topology shows a powerlaw behaviour, $\langle B^2_{\rm tor}\rangle \propto \langle B^2_{\rm pol}\rangle^{0.77\pm0.02}$, that is remarkably similar to the powerlaw $\langle B^2_{\rm tor}\rangle \propto \langle B^2_{\rm pol}\rangle^{0.72\pm0.08}$ found for the low-mass M-dwarfs ($M_\star < 0.5\,{\rm M}_\odot$) by See et al. (2015), see also Fig. 1.9. This might be a hint that M dwarfs are covered randomly by small-scale field structures that show a similar ratio between the poloidal and toroidal energy to the emerging bipoles in our flux transport simulations. Essential is that the small-scale field emerges randomly all over the stellar surface or for a good fraction of it but is not organised on a larger scale.

The more massive stars (including the solar-like stars) follow a different power law $\langle B^2_{\rm tor}\rangle \propto \langle B^2_{\rm pol}\rangle^{1.25\pm0.06}$, (See et al., 2015), see also Fig. 1.9. The large-scale field of the solar-based simulation restricted to $\ell_\Sigma \leq 5$ or 10 seems to follow this steeper power law with increasing flux emergence rate. This might be a hint that the observed topologies for more massive F, G, and K stars are also influenced by globally organised flux emergence patterns similar to our simulations.

However, these conclusions are only grounded on the similar power law behaviour. To derive more secure conclusions, I need to extend the parameter range of the simulations to reproduce the more active, faster rotating and toroidal dominated stars and the low mass M dwarfs. The simulations analysed here only recover the solar-like stars in a relatively narrow parameter space.

3.5.1 The effects of the stellar parameters on the magnetic topology

I find that the stellar properties flux emergence, differential rotation and meridional flow rate affect the surface magnetic field topology.

The flux emergence rate (ER) widely influences the surface magnetic field topology. The ER indicates the time rate at which new bipoles and magnetic features emerge. The stellar surface is occupied by a higher number of bipoles for a higher ER, which causes the increase of the magnetic energy $\langle B^2\rangle$ for all field components as seen by Gibb et al. (2016). Further, the toroidal and azimuthal quadrupolar mode is enhanced relative to the peak at mid and higher ℓ-modes for an increased ER. The bipoles follow the flux emergence pattern and emerge with opposite polarities on the two hemispheres at a relatively small latitude range, see Fig. 3.1 right. The global properties of the small-scale flux emergence pattern is best captured by the toroidal quadrupolar mode, which is well seen in Fig. 3.1 bottom left. A higher ER consolidates

these large-scale properties of the solar flux emergence pattern.

The mid and higher ℓ-modes capture the single bipoles themselves and increase moderately compared to the toroidal quadrupolar mode. The broadening of the peak distribution at mid ℓ-modes for the poloidal and radial energy distributions $\langle B^2 \rangle(\ell)$ results from the higher probability of seeing bipoles of different size and shape when the number of emerged bipoles rises.

The differential rotation rate (DR) affects the magnetic field topology, too. Most dominant is that the poloidal energy $\langle B^2_{\rm pol} \rangle$ decreases with increasing DR while the toroidal energy $\langle B^2_{\rm tor} \rangle$ remains widely constant. This results in a strong increase of the toroidal field fraction $f_{\rm tor}$. With higher DR the equator rotates faster than the poles and the bipoles become stretched and elongated. The polarity inversion line increases in length, which enlarges the area where the opposite polarities of the radial field cancel within the bipole. The radial and poloidal field decreases therefore. The toroidal and azimuthal toroidal field remains widely constant as there is no cancellation for these field components. I rather find a small increase in the toroidal energy $\langle B^2_{\rm tor} \rangle$ for the high ℓ-modes due to the presence of bipoles stretched in the toroidal direction. My results agree with Gibb et al. (2016), who found a more sheared and non-potential corona with increasing DR.

Next to this, a higher DR leads to more variability in the size and shape of the bipoles and causes the broadening of the poloidal and radial peak distribution $\langle B^2 \rangle(\ell)$. The differential rotation is a process highly aligned with the rotation axis, so that the axisymmetry of the topology increases with higher DR as well.

The last stellar parameter I analysed is the meridional flow rate (MF). An increased MF transports the bipoles and magnetic features more rapidly to higher latitudes where the shear of the differential rotation is stronger. This stretches the bipoles and they become more tilted. The bipoles form elongated structures that furl around the star and cause a mixed polarity pattern at higher latitudes. They cancel the old polarity of the global dipole and transport the new polarity more quickly to the poles. Due to these effects the poloidal energy $\langle B^2_{\rm pol} \rangle$ decreases for the low ℓ-modes.

Most interesting is that the higher MF pushes the bipoles to such high latitudes that, next to the quadrupolar, also other low to mid even ℓ-modes carry a high fraction of toroidal and azimuthal field. Only the even toroidal ℓ-modes are able to display the polarity switch across

the equator. Odd toroidal modes show the same polarity on both hemispheres. The higher latitude position of the bipoles is best represented by a combination of several even toroidal spherical harmonic modes, where the quadrupolar $\ell = 2$ mode is no longer necessarily the most toroidal one. The shearing effects of the differential rotation are stronger at the higher latitudes. The bipoles become stretched and tilted, which causes an increase of the toroidal energy $\langle B^2_{\rm tor}\rangle$ and of $f_{\rm azi,tor}$ for the higher ℓ-modes.

I found a strong decrease of the axisymmetric toroidal fraction $f_{\rm axi,tor}$ for the higher meridional flow simulations while the fraction of axisymmetric poloidal field $f_{\rm axi,pol}$ remains similar. This effect appears especially strong for the dipolar mode. The decreases of the dipolar axisymmetric toroidal field happens as all the bipoles and small-scale structures are dragged to higher latitudes. Nearly no flux is left near the equator to support the dipolar axisymmetric toroidal mode. For the solar MF simulations bipoles emerge and stay much closer to the equator and support the dipolar axisymmetric toroidal field. Moreover, the stretched mixed polarity structure at the higher latitude regions adds a global non-axisymmertric toroidal structure.

The stronger tilt of the bipoles and their stretch in the meridional direction increases the meridional energy $\langle B^2_{\rm mer}\rangle$ at the cost of the radial energy $\langle B^2_{\rm rad}\rangle$. The peak of the meridional energy distribution $\langle B^2_{\rm mer}\rangle(\ell)$ is also shifted to lower ℓ-modes and the fraction of meridional toroidal field $f_{\rm mer,tor}$ is increased. The higher MF causes again a higher variety of the sizes and shapes for the bipoles resulting again in the broadening of the poloidal $\langle B^2_{\rm pol}\rangle(\ell)$ and radial energy peak distribution $\langle B^2_{\rm rad}\rangle(\ell)$.

3.5.2 Connecting the simulations with the observations

Some of the trends for the large-scale field topology with the stellar parameters seem to agree with observational results or might be observable. The flux emergence rate shows a strong influence on the magnetic energy and is likely connected to the magnetic activity level of the stars.

For an increasing differential rotation I discovered that the poloidal energy decreases while the toroidal energy remains constant which results in an increase of the toroidal fraction with differential rotation. For the observations an increase of the toroidal field fraction was found with stellar mass (Donati & Landstreet, 2009, fig. 3). Furthermore, Kitchatinov & Olemskoy (2011) report an increase of the differential rotation with rising stellar mass and effective

temperature. The dependency of the differential rotation on the effective temperature is well studied from the theoretical side (Küker & Rüdiger, 2011; Kitchatinov & Olemskoy, 2011) and the observational (Barnes et al., 2005; Reiners, 2006; Collier Cameron, 2007). Comparing the large-scale magnetic field topology of the mid M dwarfs (Morin et al., 2008b) with the large-scale magnetic field topology of the more massive early M dwarfs (Donati et al., 2008b), one finds that the poloidal energy decreases with mass while the toroidal energy remains roughly the same. The toroidal fraction increases therefore with mass from the mid to the early M dwarfs. The differential rotation increases by one order of magnitude from the mid to the early M dwarfs as well, (Morin et al., 2008b; Donati et al., 2008b). The simulations analysed here display the same trends for an increasing differential rotation. However, the simulations are grounded on the Sun and do not represent M dwarfs.

The stellar meridional flow is not directly observable today. The strongest hint for a higher meridional flow is the decrease of the axisymmetric toroidal fraction while the axisymmetric poloidal fraction remains constant according to my results. It might be a hint of an increased MF if one of two solar-analogues shows a weaker toroidal axisymmetric field than the other. However, this would only be true if both stars host the same solar flux emergence pattern, flux emergence and differential rotation rate.

3.6 Summary

I analysed the large and small-scale magnetic field topology of simulations with varying stellar parameters. The simulations are based on a solar flux transport model, which is connected with a non-potential coronal evolution model. I examined trends of the large-scale field topology with three stellar parameters and compared them with the observed magnetic field topologies. The main results are summarised in the following:

- The large-scale magnetic field topology of the simulated solar-based stars fits the magnetic field topology of the observed solar-like stars.
- The large-scale field of the simulations mainly results from the global dipolar field and the global properties of the small-scale flux pattern. The global dipolar field is captured by the poloidal dominated dipolar mode of the spherical harmonics. The solar small-scale flux emerges at low to mid latitudes (active latitudes) with opposite polarities on the two hemispheres and is best recovered by the toroidal quadrupolar mode on large

scales. The large-scale field for the simulations is therefore mainly characterised by the poloidal dominanted dipolar modes and the quadrupolar modes, that often show the highest fraction of toroidal field. Both modes are highly axisymmetric.

- The magnetic field topology is affected by changes of the following stellar parameters:
  - An increasing flux emergence rate
    - ∗ increases the magnetic energy $\langle B^2 \rangle$ for all field components.
    - ∗ enhances the toroidal and azimuthal quadrupolar mode relative to the mid and higher ℓ-modes.
  - An increasing differential rotation
    - ∗ decreases the poloidal energy $\langle B^2_{\rm pol} \rangle$ and the toroidal energy $\langle B^2_{\rm tor} \rangle$ remains widely constant, which results in an increase of the toroidal field fraction $f_{\rm tor}$.
    - ∗ increases the axisymmetry.
  - An increasing meridional flow
    - ∗ enhances the low even toroidal spherical harmonic modes to mimic the higher latitude position of the magnetic features.
    - ∗ decreases the fraction of the axisymmetric toroidal field $f_{\rm axi,tor}$, especially for the dipolar mode, while the fraction of the axisymmetric poloidal field $f_{\rm axi,pol}$ is unchanged.
- The higher spherical harmonic modes are sensitive to the actually emerging bipoles and star spots. They are characterised by a low fraction of axisymmetric field and a widely fixed ratio between the different field components. In general, the small-scale field is less affected by the stellar parameters.
- However, an increase of the stellar parameters (flux emergence, differential rotation and meridional flow rate) cause a greater variation in the size and shape of the active regions at the stellar surface. The peak of poloidal $\langle B^2_{\rm pol} \rangle(\ell)$ and the radial energy distribution $\langle B^2_{\rm rad} \rangle(\ell)$ is therefore broadened.

My results show that simulations connecting photospheric flux transport models with non-potential coronal evolution models are an important tool to understand stellar magnetic field observations. I found that the observable large-scale magnetic field topology is sensitive to

the large-scale properties of the flux emergence pattern, i.e., preferable areas of emergence (e.g. active latitudes) and polarity pattern. The simulations are based on the observed solar flux emergence pattern during the activity maximum. The discovered dependencies with the stellar parameters are only evaluated for these types of stars. To derive more conclusive hints for observable trends, I recommend to do further examinations regarding the influence of the different flux emergence patterns and cycle phases. A wider parameter range of the analysed stellar parameters is advisable, too, to connect the discovered trends securely with the observational trends. The reader is reminded that the simulations cover only a small range of stellar parameters (e.g., in rotation period and Rossby number) compared to the observations. However, some general trends are most likely to be independent of the solar flux emergence pattern, e.g., the rising of magnetic flux with flux emergence rate and the decrease of poloidal energy and the resultant increase of the toroidal fraction with differential rotation rate. The observations display an increase of the toroidal field fraction with mass as well, looking similar to the trends I discovered with increasing differential rotation, that is believed to increase with stellar mass.

Appendix

3.A Additional figures

Fig. 3.13a displays the toroidal against poloidal energy for the sub-set of the 17 stellar models (one map per model) presented in Lehmann et al. (2017). Fig. 3.13b shows all analysed stellar models of Lehmann et al. (2018): the lower DR, higher DR and higher MF simulations. The exact same format as in Fig. 3.2 is used, where only the higher DR simulations are presented. By comparing both figures, I notice that the optimal average smooths the trend with ℓ_Σ-modes, especially for the higher ℓ_Σ-modes.

Figure 3.14 displays the first ten ℓ-modes of Fig. 3.6 for a more detailed view. For example, the strong azimuthal $\ell = 2$ mode is more obvious in this format. Be aware that the y-axis varies for all stellar models and is no longer fixed. The rotation period of the stellar models is mentioned in the top left corner of each barplot. Furthermore, Fig. 3.14 allows an easy comparison with observational results published in the literature.

Figure 3.15 shows the energy distributions $\langle B^2 \rangle(\ell)$ for stellar models with higher meridional flow. The left column displays the radial $\langle B^2_{\rm rad} \rangle(\ell)$ (green bars), azimuthal $\langle B^2_{\rm azi} \rangle(\ell)$ (red bars) and meridional $\langle B^2_{\rm mer} \rangle(\ell)$ (blue bars) energy distribution for a direct comparison with the middle column of Fig. 3.6. The right column shows the poloidal $\langle B^2_{\rm pol} \rangle(\ell)$ (plum bars) and toroidal $\langle B^2_{\rm tor} \rangle(\ell)$ energy distribution (orange bars) to be compared with the middle column of Fig. 3.7.

Figure 3.16 displays the cumulative total $C(\ell) = \sum f(\ell)$ of the different magnetic field fractions for the higher meridional flow stellar models with solar differential rotation and flux emergence rate for a direct comparison with the second column of Fig. 3.8 using the same format.

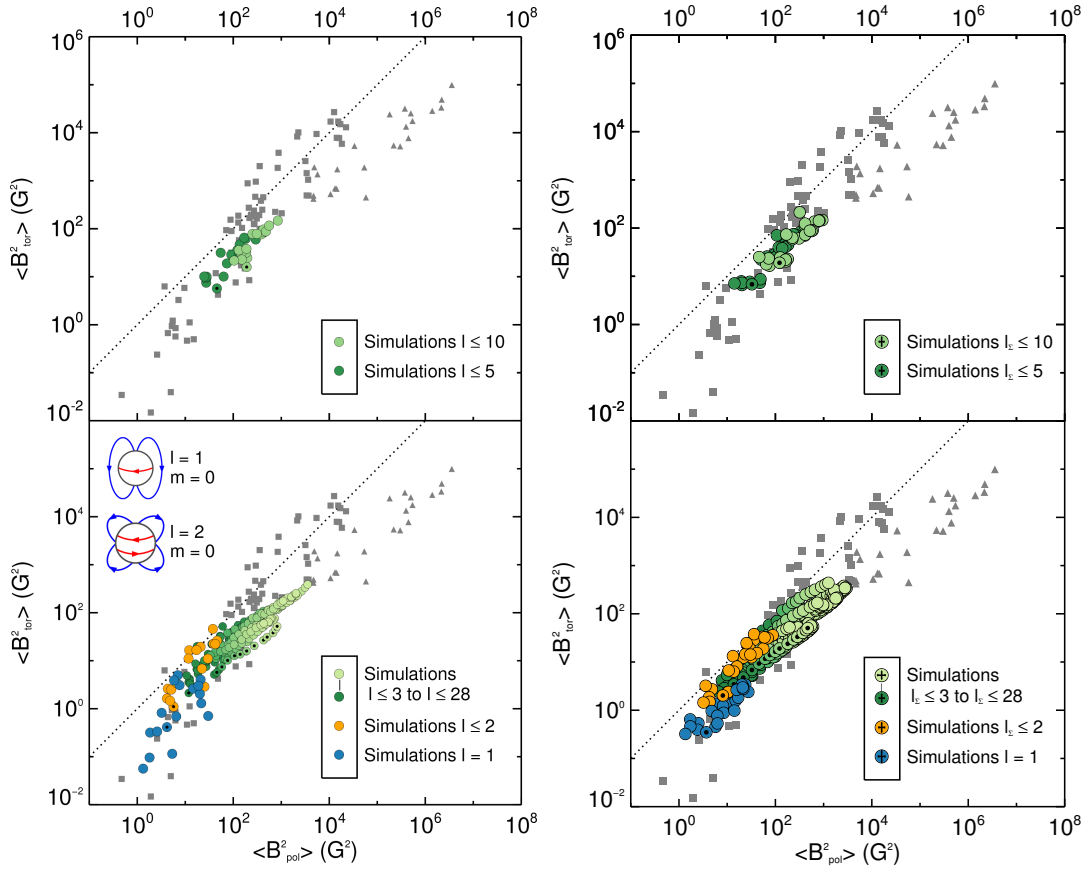

a. **b.**

Figure 3.13: Magnetic field energy stored in the toroidal $\langle B^2_{\rm tor}\rangle$ and poloidal fields $\langle B^2_{\rm pol}\rangle$ using the same format as in Fig. 3.2. **a.** For the 17 stellar models (one map per model) presented in Lehmann et al. (2017, fig. 2). **b.** For the complete set of simulations including the lower DR, higher DR and higher MF simulations, (Lehmann et al., 2018, fig. A1). The higher ℓ_Σ-modes follow the power law $\langle B^2_{\rm tor}\rangle \propto \langle B^2_{\rm pol}\rangle^{0.77\pm0.01}$.

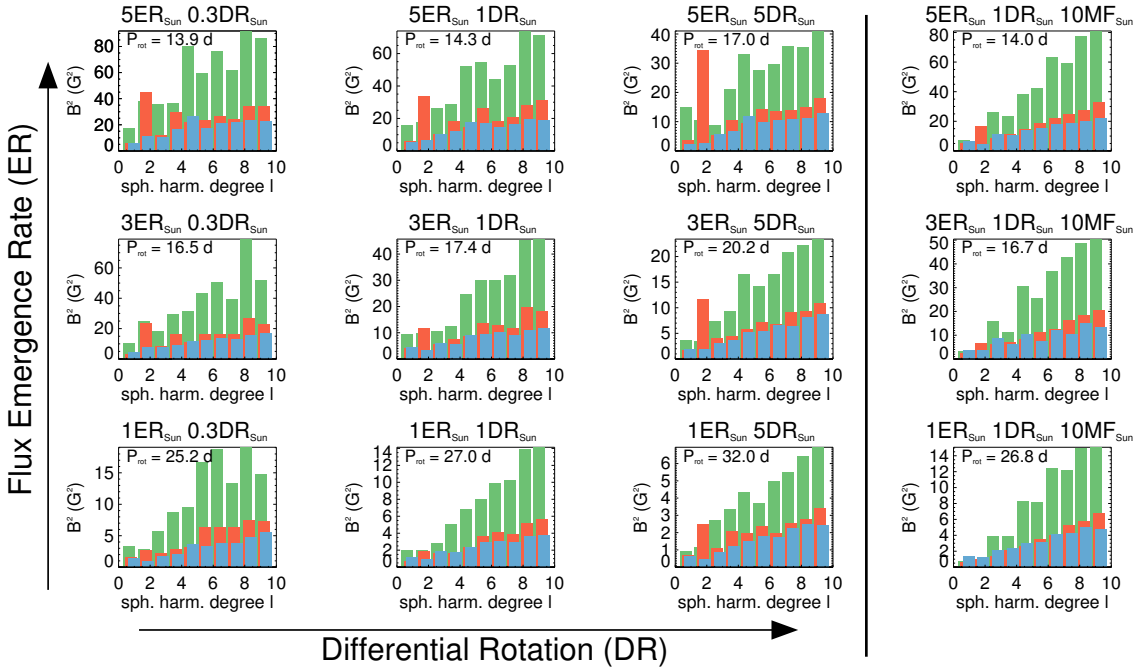

Figure 3.14: The first ten ℓ-modes of the energy distribution for the radial $\langle B^2_{\rm rad}\rangle(\ell)$ (green bars), azimuthal $\langle B^2_{\rm azi}\rangle(\ell)$ (red bars) and meridional component $\langle B^2_{\rm mer}\rangle(\ell)$ (blue bars). The y-axis varies for all stellar models and the rotation period of the simulated star is displayed in the top left corner of each barplot. The same format as in Fig. 3.6 is used and additionally three higher MF stellar models are displayed to the right of the vertical black line.

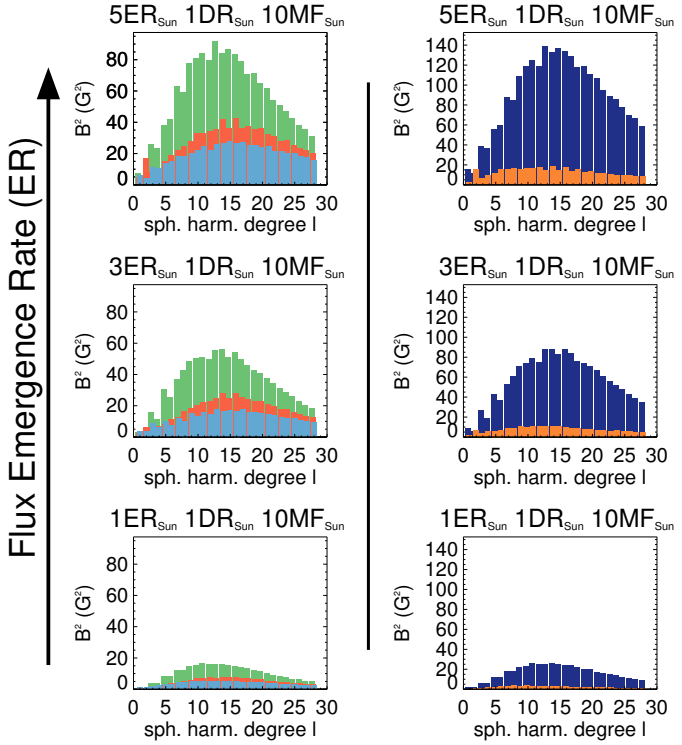

Figure 3.15: The magnetic energy distributions $\langle B^2\rangle(\ell)$ for the higher meridional flow simulations. The figure provides a direct comparison with the middle columns of Fig. 3.6 and 3.7, respectively. The same format as in Fig. 3.6 and 3.7 is used.

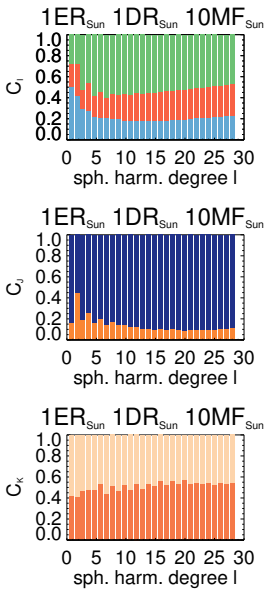

Figure 3.16: The cumulative total $C(\ell) = \sum f(\ell)$ of the fractions for the different field components for a higher meridional flow simulation. The figure provides a direct comparison with the simulated Sun, see Fig. 3.8 second column. The same format as in Fig. 3.8 is used.

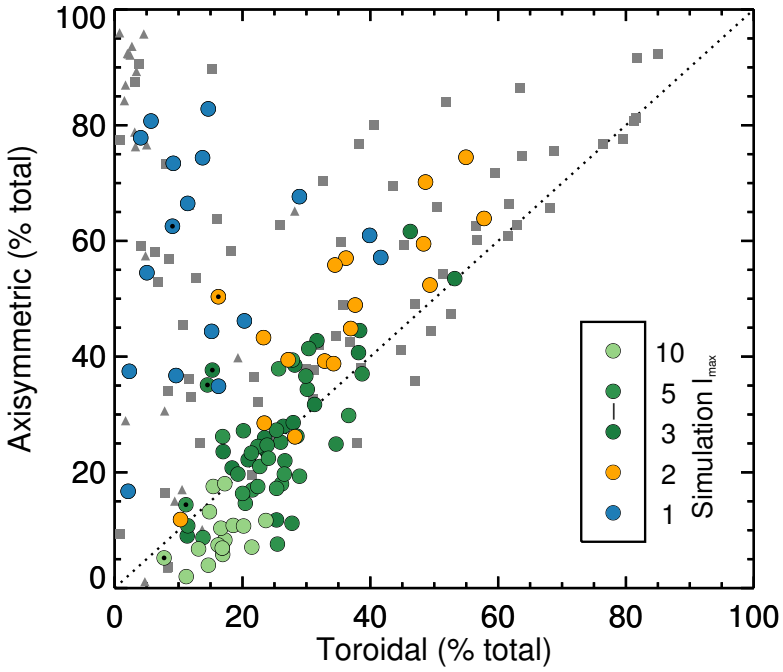

Figure 3.17: The percentage of axisymmetric and toroidal energy fraction for the 17 stellar models published in fig. 3 of Lehmann et al. (2017). For a direct comparison with Fig. 3.10a a similar format is used.

Fig. 3.17 displays the toroidal and axisymmetric fraction of the 17 stellar models published in Lehmann et al. (2017) for comparison with the complete sample and optimal average results in Fig. 3.10a. The same format as Fig. 3.2 is used.

4

Observing the simulations

4.1 Introduction

The Zeeman-Doppler-Imaging (ZDI) technique (Semel, 1989; Donati & Brown, 1997) enables us to map the stellar surface magnetic field. Due to flux cancellations within the resolution elements, we are only able to detect the large-scale field. Most of the magnetic flux (over 80 %) is hidden in the small-scale field (Reiners & Basri, 2009; Morin et al., 2010; See et al., 2019).

The observation of solar-like stars is even more challenging as these stars are typically slow rotators and relatively inactive. The spatial resolution of the ZDI reconstructed maps is limited by a combination of the stellar $v_e \sin i$, the instrumental spectral resolution, phase coverage and noise, see also Chapter 1.3.2. The spatial (angular) resolution of solar-like stars reaches typically only $\approx 40-20^\circ$ due to the low $v_e \sin i$ in the order of a few $\mathrm{km\,s^{-1}}$. Petit et al. (2002) showed that it is still possible to reconstruct the large-scale magnetic field topology[1] for slowly

[1]The terms topology and morphology describe here the spatial vector magnetic field structure and are used equally

rotating solar-like stars with $v_e \sin i < 15\,\mathrm{km\,s^{-1}}$. This is doubly challenging as next to the slow rotation also the Stokes V signals are very weak due to the relatively inactivity of solar-like stars. Further, a brightness map cannot be reconstructed with the Doppler Imaging technique. The low star spot activity (including dark spots and bright facular regions) is insufficient to show an impact on the narrow absorption lines in the unpolarised light (Stokes I).

A direct comparison between stellar and solar magnetic field maps is prevented by the huge resolution difference. With the help of the spherical harmonic decomposition method, (Vidotto, 2016), we were able to determined the large-scale field of the Sun and to directly compare it with solar-like star observations, (Vidotto et al., 2018). We showed that the large-scale field properties of the Sun fit the observational trends reported by See et al. (2015). The solar large-scale magnetic energy is poloidal dominated ($\gtrsim 70\,\%$) and lacks toroidal non-axisymmetric field similar to other solar-like stars.

Even if the comparison with the Sun is now possible, it is still challenging to derive the right conclusions from ZDI maps (especially for solar-like stars). In this Chapter, I want to determine how much of the large-scale field can be robustly reconstructed with ZDI for solar-like stars under the issue of flux cancellation and obscured hemisphere. Further, I want to determine how to interpret the reconstructed ZDI maps and what can be concluded from the large-scale field about the small-scale flux emergence.

I am using the 3D non-potential flux transport simulations of Gibb et al. (2016) as inputs to benchmark the ZDI technique. In the previous Chapter (Chapter 3), I analysed the simulations regarding their large and small-scale field topology and proved that they mimic the large-scale field properties of observed solar-like stars. They are the perfect data set to test the reliability of the ZDI technique and to determine what ZDI recovers from the solar-like magnetic field.

I would like to remind the reader about the results of the two studies in Chapter 2.3.2 and 2.4.1, which were done in the framework of the project presented here.

First, I analysed the dependence of the Stokes V profiles on $v_e \sin i$ and the spatial resolution of the input maps, see Chapter 2.3.2. For slow rotating solar-like stars with $v_e \sin i \leq 5\,\mathrm{km\,s^{-1}}$ the Stokes V profiles are insensitive to magnetic structures smaller than $\vartheta = 40 - 25°$, an angular size corresponding to $\ell_\Sigma = 5 - 7$. An observer is literally blind for smaller scale

as common in the literature of this research field. The mathematics distinguish between these two terms and defines both terms more strictly. For example, the topology describes the study of objects that are preserved under certain kind of deformations.

magnetic structures.

Second, I compared four different magnetic field descriptions based on the spherical harmonics, see Chapter 2.4.1. I showed that only certain magnetic field morphologies can be fitted by restricting the magnetic field coefficients $\alpha_{\ell,m}, \beta_{\ell,m}, \gamma_{\ell,m}$, see Eq. 1.26. For example, it was possible to fit a few maps of the solar-like star with a potential model ($\gamma_{\ell,m} = 0$). To ensure that the reconstructed magnetic field is as correct as possible, one should allow $\alpha_{\ell,m} \neq \beta_{\ell,m}$ and $\gamma_{\ell,m} \neq 0$. This is especially recommended if one is interested in the toroidal or azimuthal and meridional field component. Kochukhov et al. (2017) showed that the Stokes profiles of τ Sco (B0 V) can be equally well fitted with three of the here analysed descriptors, but resulting in three different vector magnetic field morphologies. It is therefore often impossible to discard single descriptions from fitting the observed Stokes V time series.

Section 4.2 introduces the applied data set of simulations, the synthetic Stokes V profile modelling and the details of the ZDI implementation and fitting. The results can be found in Section 4.3, where I present the comparison between the input and ZDI maps in Section 4.3.1. How the large-scale field properties, the energy distributions and surface averaged field are recovered can be seen in Section 4.3.2, 4.3.3 and 4.3.4. The chapter closes with a discussion and summary in Section 4.4 and 4.5.

The whole chapter is based on my paper Lehmann et al. (2019).

4.2 Simulations, techniques and ZDI fitting

To benchmark the ZDI technique, I use a subsample of the 3D non-potential flux transport simulations introduced in Chapter 3.2. The simulations were kindly provided by Duncan Mackay and are published in Gibb et al. (2016).

The details of this simulation set can be found in Chapter 3.2 and in sections 2 and 3 of Gibb et al. (2016). Further, a general description of the simulation and the surface flux motions can be found in Chapter 2.2. Here I only repeat the key properties.

The simulations are modelled with a flux transport model that is connected to a non-potential coronal evolution model via the magnetofrictional technique reaching from the stellar surface up to $2.5\,\mathrm{R}_\star$ (van Ballegooijen et al., 2000). The stellar flux emergence pattern is based on the solar flux emergence properties observed during the activity maximum from Jan-

uary 2000 to January 2001 (Yeates, 2014). The flux emergence (ER) and differential rotation rate (DR) are scalable (Gibb et al., 2016).

I selected three stellar models from the simulations presented in Chapter 3.2: the solar-like star ($\mathrm{ER} = 1\,\mathrm{ER}_\odot$, $\mathrm{DR} = 1\,\mathrm{DR}_\odot$)[2], a three times more active star ($\mathrm{ER} = 3\,\mathrm{ER}_\odot$, $\mathrm{DR} = 3\,\mathrm{DR}_\odot$) and the most active star ($\mathrm{ER} = 5\,\mathrm{ER}_\odot$, $\mathrm{DR} = 5\,\mathrm{DR}_\odot$). All three are simulated with a solar meridional flow rate. For each star 390 vector magnetic maps are available ranging over a timespan of one year. I selected 10 maps per stellar model, which are more or less equally distributed in time. I ensured that the 10 maps show the same averaged large and small-scale magnetic field properties as the optimal average over the 390 maps presented in Chapter 3.2.

I modelled the Stokes IV profiles for the three stellar models, ten maps each, as described in Chapter 2.3.1. I applied an inclination angle of $i = 20°$ and $60°$, which leads to a total of 60 time series in Stokes IV. Just repeating the key properties: each time series contains 25 equally spaced observations detected with 30 velocity bins ranging from $-20\,\mathrm{km\,s^{-1}}$ to $20\,\mathrm{km\,s^{-1}}$. The local Stokes profiles are fine tuned to match the solar twin 18 Sco. As mentioned in the introduction, a brightness distribution cannot be reconstructed for such slowly rotating and inactive stars. A uniform brightness is assumed for the generation of the disc-integrated Stokes IV profiles.

I add Gaussian noise to the synthetic line profiles. The amplitudes of the Stokes V profiles vary over two orders of magnitude for the three stellar models ($5.20 \cdot 10^{-6}\,\mathrm{V/I_C} - 1.85 \cdot 10^{-4}\,\mathrm{V/I_C}$). Each time series of Stokes V profiles shall be equally affected by noise, so that I scaled the S/N to the maximum amplitude of each time series. I choose a noise level corresponding to 3 % of the maximum Stokes V signature per data set. Looking at the noisy Stokes V profiles, they are by eye comparable with several observational datasets of similarly active stars, e.g., ε Eri (Jeffers et al., 2014) or 61 Cyg A (Boro Saikia et al., 2016). However, the resulting continuum S/N of the synthetic Stokes V profiles ranges from 3 560 000 to 100 000 from our least to most active set of models. These particularly high S/N values are reached as they are based on simulation. Even our most active model has therefore a S/N that is $\simeq 25\,\%$ higher than normally found in datasets for solar-activity stars. Table 4.1 lists the rotation periods and rotational velocities next to the S/N averaged over the ten maps per stellar model.

[2]The definitions of the solar flux emergence and differential rotation rate ($\mathrm{ER}_\odot$and $\mathrm{DR}_\odot$) can be found in Chapter 3.2 at page 56.

Table 4.1: The rotation periods, $v_e \sin i$ and averaged S/N for the analysed stellar models for both inclinations. The stars are characterised by their flux emergences rate (ER) and their differential rotation rate (DR) in solar terms.

ER [$ER_\odot$]	DR [$DR_\odot$]	P_{rot} [d]	$v_e \sin i$ [km/s] $i = 20°$	$v_e \sin i$ [km/s] $i = 60°$	S/N $i = 20°$	S/N $i = 60°$
1	1	27.00	0.64	1.62	1 550 000	550 000
3	3	19.00	0.91	2.31	370 000	340 000
5	5	17.00	1.02	2.58	160 000	200 000

In the next step, I used the modelled 60 Stokes IV time series as inputs for the ZDI code described in Chapter 2.4.2. Just as reminder: the ZDI code is based on spherical harmonics and uses the maximum entropy regularisation, (Hussain et al., 2016). The non-potential $\alpha \neq \beta$ model is applied to guarantee the correct field reconstruction, see Chapter 2.4.1. The maximum spatial resolution is given with the maximum ℓ-mode $\ell_{max} = 7$, which corresponds to an angular resolution of $\vartheta \approx 25°$. All ℓ and m modes are equally weighted, so that no a-priori assumptions are applied.

I applied the ZDI technique onto the synthetic line profiles and naturally try to find the best agreement with the inserted dataset. Figure 4.1 displays the ZDI fits to the Stokes V profiles for one example map per stellar model and inclination. The black lines indicate the noisy Stokes V profiles produced by using the fully resolved stimulated maps. The red lines show the best fits with ZDI. For comparison the blue lines, which are mostly hidden behind the red lines of the ZDI fits, present the noise-free Stokes V profiles. The observation phases are depicted on the right on the individual profiles. ZDI excellently fits the noisy Stokes V profiles. On average I reached a reduced $\chi^2 \approx 3$, while the best fit achieved $\chi^2 = 1.05$. Only four out of 60 maps had a $\chi^2 \geq 5$. My fitting degree is comparable to the fitting degree of solar-like star observations, e.g., for ε Eri (Jeffers et al., 2014). In most cases, the ZDI reconstructed profiles (red lines) match the noise-free simulated Stokes V profiles (blue lines), although I applied the ZDI fitting to the noisy Stokes V profiles (black lines). The two different inclinations have no significant effect on the fitting degree.

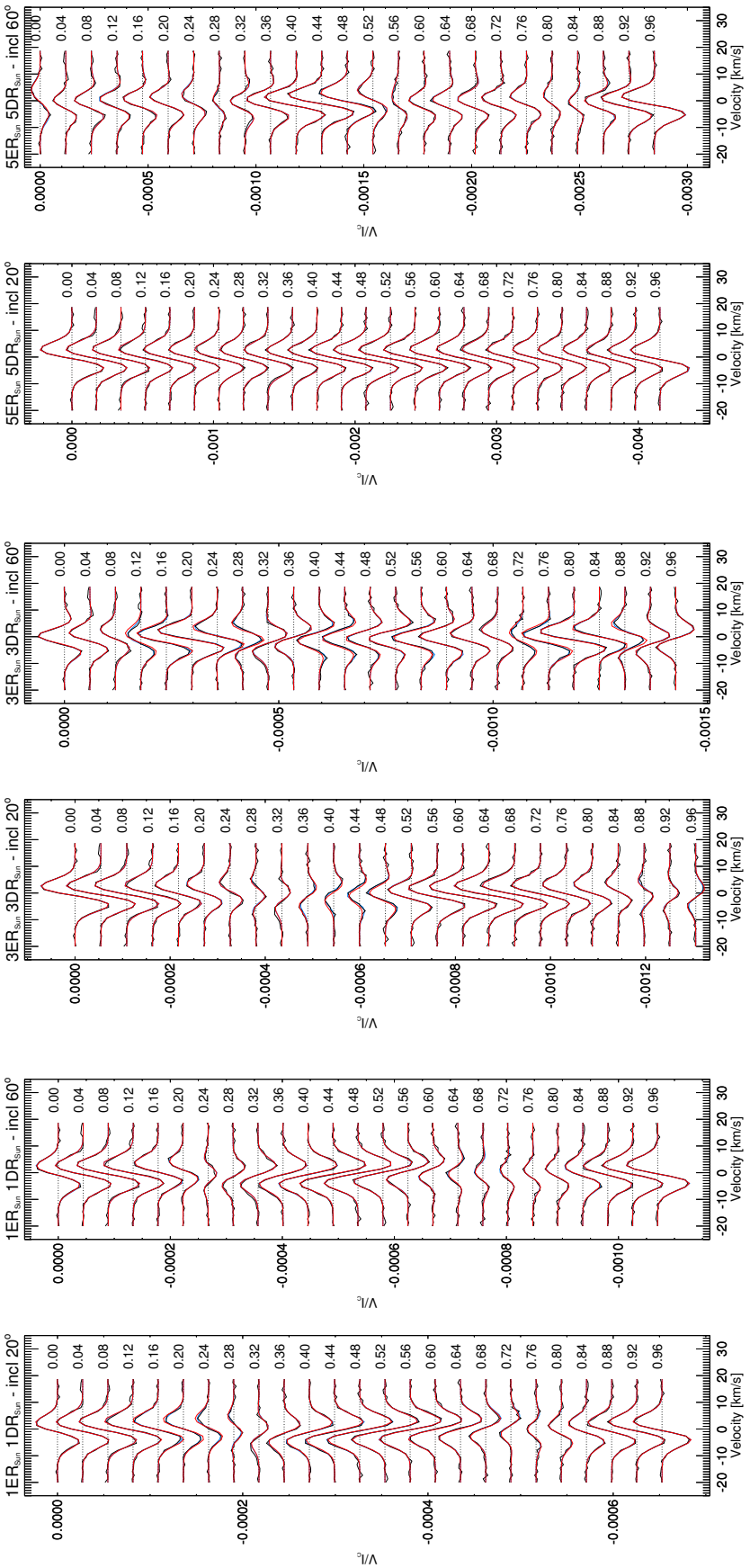

Figure 4.1: Six example sets of Stokes V profiles (one per inclination and stellar model) showing the fit of the Stokes V profiles modelled from the fully resolved input map with ZDI. In each case, the thick solid black line is the noisy Stokes V profile, that is fitted with ZDI. The red line is the resulting ZDI fit and the blue line (mostly behind the red line) is the noise-free Stokes V profile of the fully resolved input map. The dotted black line is the null-line. The phases are written to the right.

4.3 The observed field of the simulations

I compare the input with the ZDI reconstructed maps in Section 4.3.1 before I determine how much of the large-scale field is reconstructed in Section 4.3.2. Further, I examine how robust the magnetic energy distributions and the surface averaged magnetic fields per stellar model are recovered in Section 4.3.3 and 4.3.4.

4.3.1 Comparing the input maps with the ZDI reconstructions

Firstly, I compare the fully resolved input maps and their large-scale field extrapolations with their ZDI reconstructed maps. Figs. 4.2-4.4 present one example map per stellar model and inclination corresponding to the Stokes V profile fits presented in Fig. 4.1. I present typical fits for the lower and higher activity models and the best fits for the model with moderate activity. The Mollweide projected maps are shown for the radial (top row), azimuthal (middle row) and meridional field (bottom row). The first column presents the simulated input map from which the ZDI fitted Stokes V profiles are derived. The second and third columns show the large-scale of field of input map limited to $\ell_\Sigma = 7$ and 5, respectively. The last two columns demonstrate the reconstructed ZDI maps for an inclination of $i = 60°$ (4th column) and $i = 20°$ (5th column). Note that the maps are grouped by three different colour bars. It is more revealing to pay attention to the comparison of the morphology of the different maps rather than the magnetic field values indicated by the colour scale as the reconstructions recover much less field than their original input.

Generally, the ZDI restored maps significantly differ from the simulated input maps. The input maps (Figs. 4.2-4.4, 1st column) are dominated by small-scale field structures originating from active regions, whereas the ZDI reconstructed maps (Figs. 4.2-4.4, 4th and 5th column) show only large-scale field structures. As illustrated in Section 2.3.2 the Stokes V profiles exclusively provide information about the large-scale field and miss the small-scale field. This is especially true for slowly rotating stars. Hence it is necessary to compare the ZDI reconstructed maps with the large-scale field of the input maps (Fig. 4.2-4.4, 2nd and 3rd column). I allow the ZDI code to use ℓ-modes up to $\ell = 7$, but most of the information is accumulated in the ℓ-modes $\ell = 1 - 5$. I present therefore both large-scale field maps for $\ell_\Sigma = 7$ and $\ell_\Sigma = 5$ of the input maps. ZDI recovers significantly less magnetic field than the large-scale field of the input maps for all 60 fitted maps. Here, I compared the magnetic field

values averaged over the whole surface of the input maps. I do not take inclination effects into account. Considering inclination effects would decrease the magnetic field values of the input maps by a few percent.

For the solar-like star (ER = $1\,\mathrm{ER}_\odot$, DR = $1\,\mathrm{DR}_\odot$, Fig. 4.2) the morphology of the ZDI reconstructed maps show a significant difference depending on the inclination. The low inclination reconstructions display much less structure in all three vector components. The high inclination reconstructions reveal a much better agreement to the large-scale field of the input. The main features of the radial large-scale field $\ell_\Sigma = 5$ are recovered from the northern hemisphere down to the equatorial region but show in general larger structures than expected for $\ell_\Sigma = 5$. The reconstructed azimuthal field also recovers most of the main features of the northern hemisphere, however, with a higher uncertainty. The meridional field is affected by crosstalk with the radial field and illustrates the worst agreement as expected (Donati & Brown, 1997). The low inclination maps are limited to the polar view and a worse spatial resolution as the $v_e \sin i = 0.62\,\mathrm{km\,s^{-1}}$. With these ultra-low $v_e \sin i$ values, I am limited by the thermal width of the line profile as well as the spectral resolution of the instrumentation[3].

The ZDI reconstructed maps for the more active star (ER = $3\,\mathrm{ER}_\odot$, DR = $3\,\mathrm{DR}_\odot$, Fig. 4.3) demonstrate a higher agreement to the large-scale field of the input in comparison to the solar-like star. Especially, the radial map for the higher inclination star displays a good agreement with the large-scale field $\ell_\Sigma = 5$, Fig. 4.3 (top row, 3rd and 4th column). ZDI recovers here all features of the large-scale field down to south of the equatorial region. Be reminded of the two different colour scales by comparing the two maps. The main structures of the azimuthal and meridional field maps are also well recovered, though less accurately than the radial maps. The meridional field is in this case less affected by crosstalk compared to the map of the solar-like star as it is stronger. At this activity level the meridional field contributes more strongly to the Stokes V profiles and the resulting maps. The low inclination ZDI reconstruction (Fig. 4.3, 5th column) shows worse spatial resolution. At the same time it is more restricted to the structure of the northern hemisphere. However, there is still an acceptable agreement with the large-scale field in the input map.

The ZDI maps of the most active star (ER = $5\,\mathrm{ER}_\odot$, DR = $5\,\mathrm{DR}_\odot$, Fig. 4.4) generally display a good accordance with the large-scale field of input maps. The high inclination ZDI recon-

[3]The disc integrated Stokes V profile consists only of two local Stokes V profiles for such a low $v_e \sin i$ in connection with the assumed 30 velocity bins ranging from $-20\,\mathrm{km\,s^{-1}}$ to $20\,\mathrm{km\,s^{-1}}$.

structions display poorer spatial resolution than expected from the large-scale field $\ell_{\Sigma} = 5$ of the input maps. Even less structure is shown by the low inclination ZDI reconstructions. I want to highlight that the azimuthal field is especially well constrained. It dominates the global magnetic field and has the structure of a strong belt of negative polarity on the northern hemisphere. This azimuthal ring becomes more structured as the inclination increases. It also dominates the Stokes V profiles, especially at low inclination (refer to Fig. 4.1, 5th and 6th panel). The original input map (Fig. 4.4, 1st column) of this active star is characterised by many active regions, which predominantly have a negative azimuthal field at the northern hemisphere and a positive azimuthal field at the southern hemisphere. The global properties of this flux emergence pattern (two azimuthal bands of opposite polarity at mid-latitudes) shape the large-scale field and therefore dominate the ZDI reconstruction. For low inclination, where the star is seen nearly pole-on, ZDI is very sensitive this magnetic structure as the polar region contains a relatively low levels of magnetic flux.

All in all, I can conclude that ZDI recovers the visible structure of the large-scale field morphology of solar-like stars, but loses the magnetic field strengths. Restricting the original input maps to the large-scale field via the spherical harmonic decomposition (see Vidotto 2016; Lehmann et al. 2017; Lehmann et al. 2018) offers a great estimate of the magnetic field morphology structure that will be recovered by ZDI at best. ZDI recovers structures mostly less but at maximum down to $\ell = 5$ for solar-like slow rotators but observes significantly lower magnetic field strengths. Further, the inclination affects the ZDI reconstructions as lower inclinations (pole-on view) reduce the spatial resolution and further restrict the observations to the upper hemisphere.

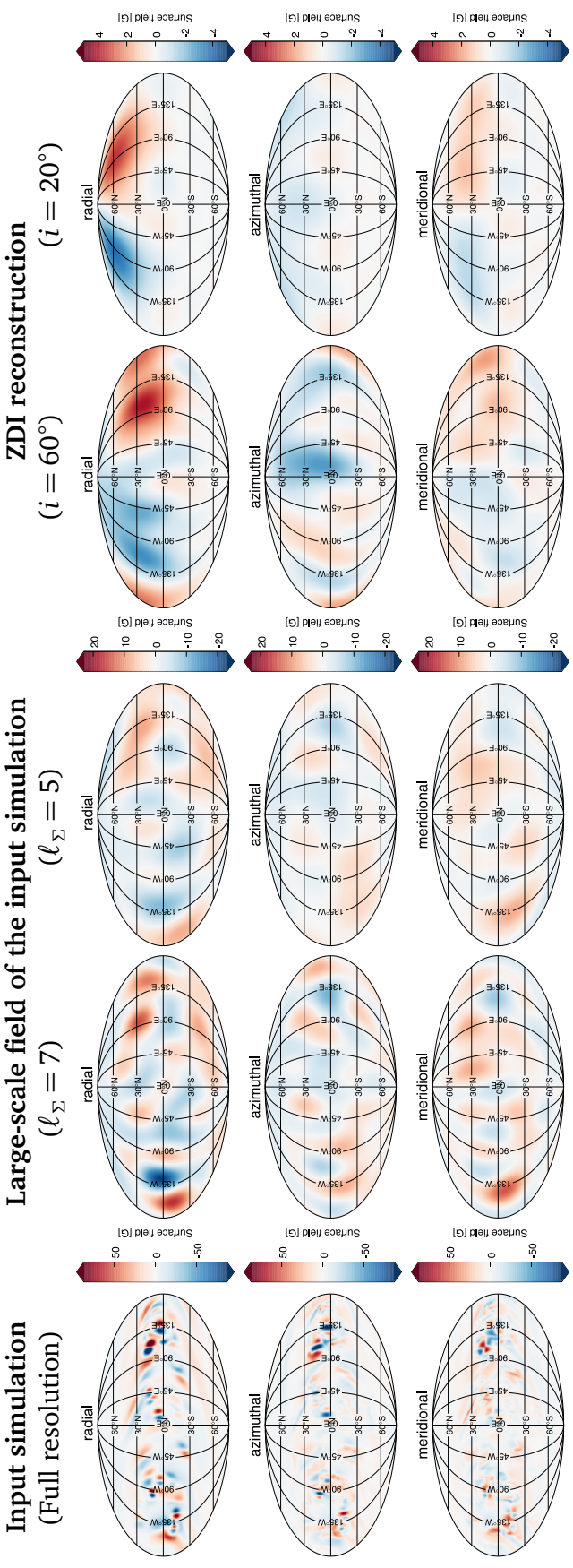

Figure 4.2: The Mollweide projected magnetic field maps for one example of the solar-like star ($\mathrm{ER} = 1\,\mathrm{ER}_\odot$ and $\mathrm{DR} = 1\,\mathrm{DR}_\odot$). From left to right: the simulated fully resolved simulated input map, the large-scale field of the simulated input map for $\ell_\Sigma = 7$ and 5 compared with the ZDI reconstructed maps applying an inclination of 60° and 20°. The radial component is displayed in the top row, the azimuthal in the middle row and the meridional component in the bottom row.

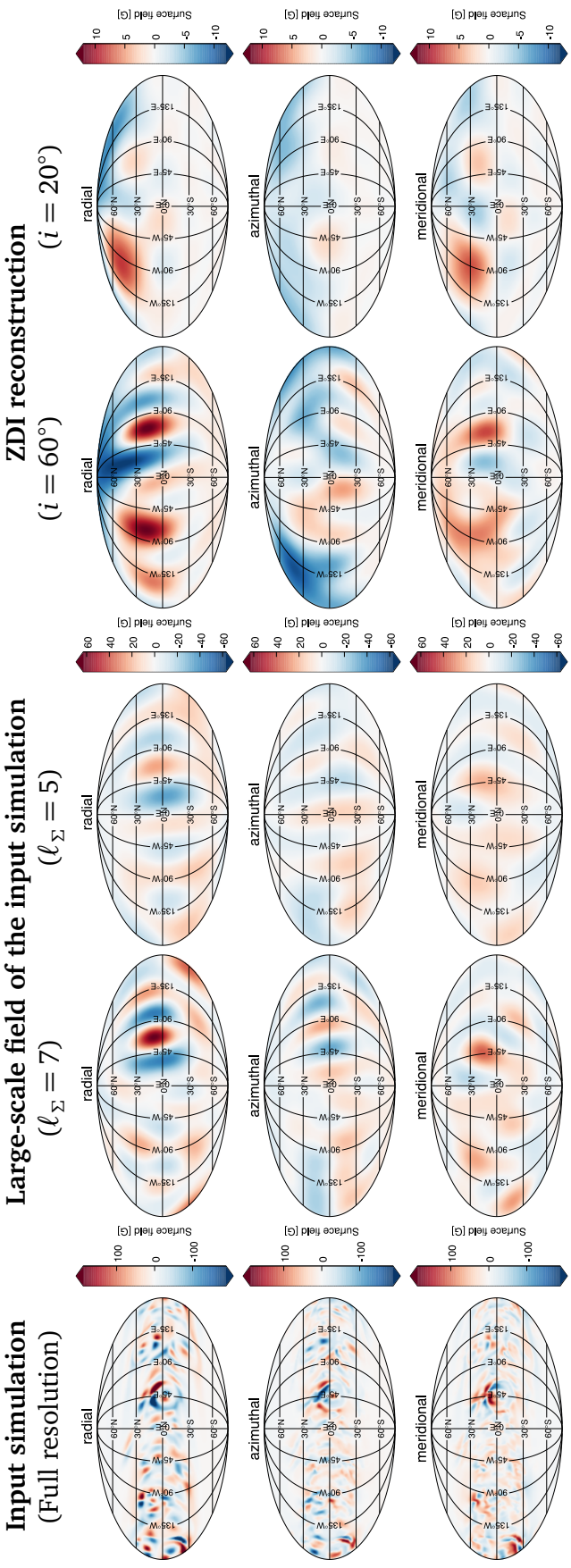

Figure 4.3: The Mollweide projected magnetic field maps for one example of the more active star ($\mathrm{ER} = 3\,\mathrm{ER}_\odot$ and $\mathrm{DR} = 3\,\mathrm{DR}_\odot$). The same format as in Fig. 4.2 is used.

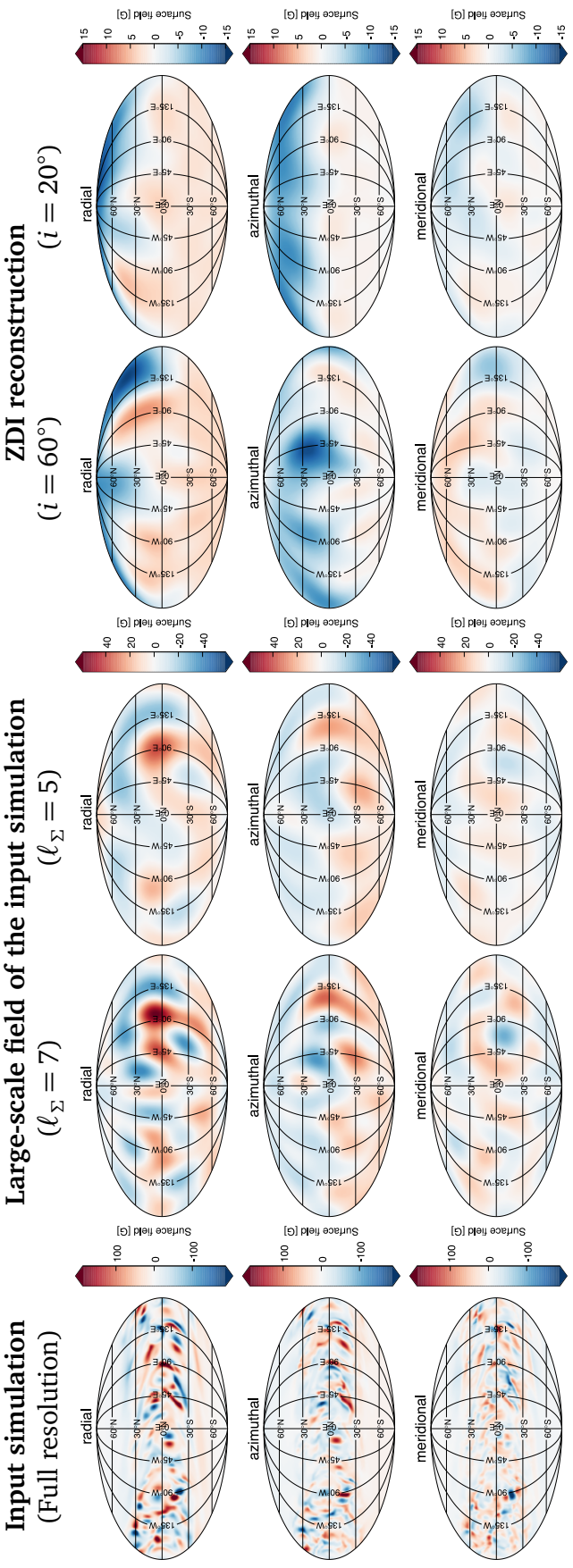

Figure 4.4: The Mollweide projected magnetic field maps for one example of the most active star ($\mathrm{ER} = 5\,\mathrm{ER}_\odot$ and $\mathrm{DR} = 5\,\mathrm{DR}_\odot$). The same format as in Fig. 4.2 is used.

4.3.2 Recovering the large-scale field properties

In the last section, I noticed that ZDI recovers less magnetic field than expected from the large-scale field extrapolation. I analysed this further, computing the mean-squared flux density (alias magnetic energy) $\langle B^2 \rangle [\mathrm{G}^2]$ of the poloidal and toroidal field, see Fig. 4.5. Fig. 4.5a shows the full range of energy values given by the cool stars observations[4] (grey symbols) analysed by See et al. (2015), see Fig. 1.9. They divided the sample by stellar mass: low mass stars with $M < 0.5\,\mathrm{M}_\odot$ are plotted as pentagons and higher mass stars as squares. Fig. 4.5b displays a more detailed view over the energy range defined by our models and maps (coloured symbols). The large-scale field input maps ($\ell_\Sigma = 7$) are indicated by circles and their corresponding ZDI maps by triangles, where the $i = 20°$ inclined ZDI maps are plotted using the up-side-down triangles (standing on their point) and the $i = 60°$ maps using the normal triangles (standing on their base). For the input maps I calculated the energy values for the whole surface not accounting for inclination effects. The activity level of the stellar model is given by the colour: blue for the solar-like stars, purple for the three times more active stars and red for the five times more active stars. I display the results for the ten maps per stellar model (fainter coloured symbols) and their average (stronger coloured and black bordered symbols), see legend in Fig. 4.5a. The dashed line represents the unity line, with equal poloidal and toroidal energies.

The large-scale field of the 30 simulated input maps show similar values to the observations of solar-like stars, see Chapter 3 or Lehmann et al. (2018) for the full analysis. Their ZDI recovered maps lie still within the spread given by the observations but show approximately one order of magnitude less magnetic energy in both components, see Fig. 4.5b. The ZDI reconstructions seem to follow the power law $\langle B^2_{\mathrm{tor}} \rangle \propto \langle B^2_{\mathrm{pol}} \rangle^{1.25 \pm 0.06}$ found by See et al. (2015) for stars with masses $M \geq 0.5\,\mathrm{M}_\odot$ independent of inclination. ZDI recovers therefore the trend with activity but with systematically lower magnetic energy values. The spread given by the ten maps per stellar model increases for the ZDI reconstructions compared to their input maps. ZDI reaches closer values to the large-scale field of the input maps for higher inclinations (more equator-on view). Additionally, I notice that with lower inclination, less poloidal energy tends to be reconstructed and that a slightly higher toroidal energy is recovered for the more active stars.

[4]The observations were published by Petit (in preparation); Boro Saikia et al. (2015); do Nascimento et al. (2014); Donati et al. (2003, 2008b); Fares et al. (2009, 2010, 2012, 2013); Folsom et al. (2016); Morin et al. (2008a,b, 2010); Jeffers et al. (2014); Petit et al. (2008); Waite et al. (2011).

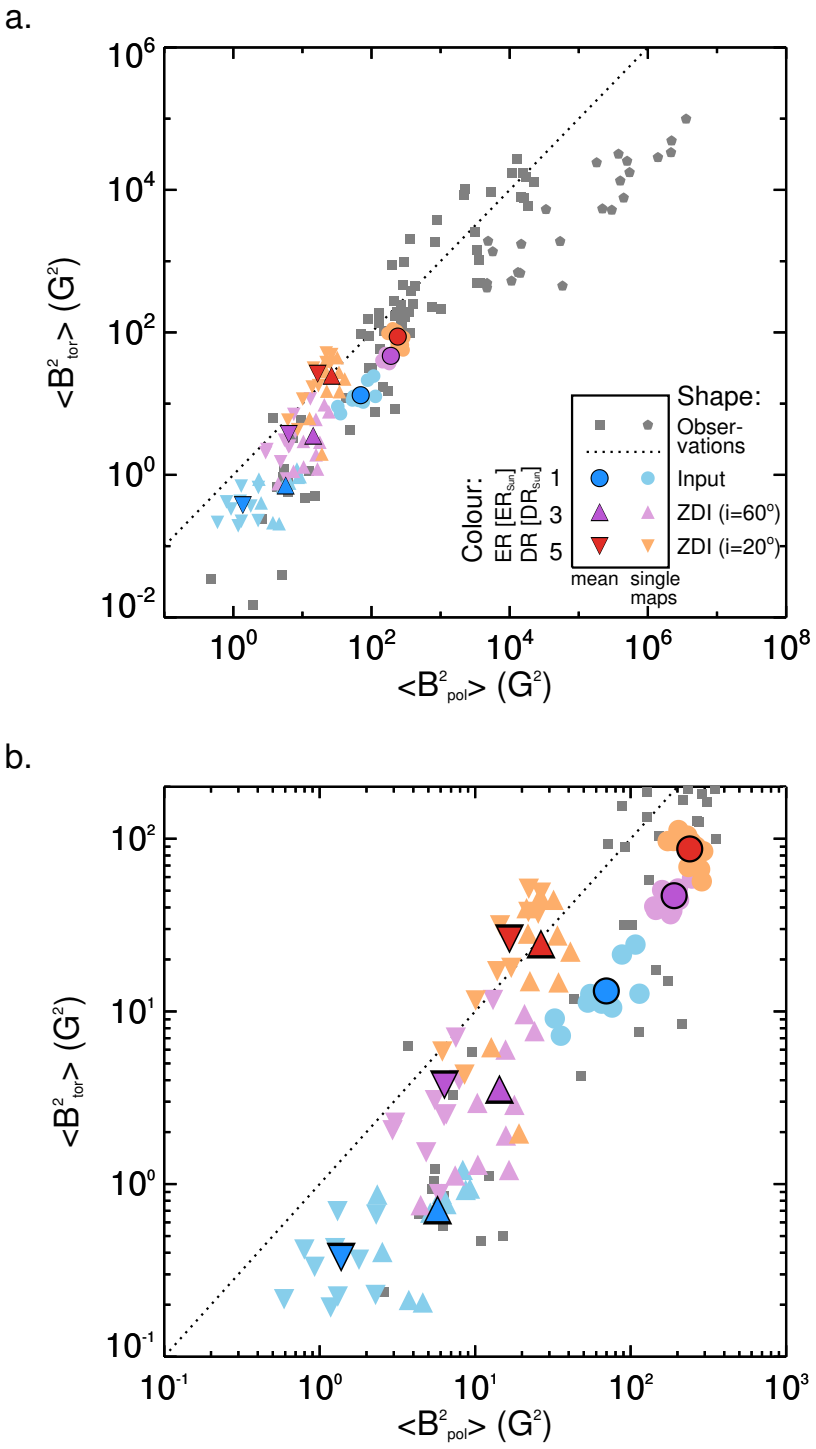

Figure 4.5: The toroidal against the poloidal magnetic energy for the observed cool stars (grey symboles), the simulated input stars with $\ell_\Sigma = 7$ (circles) and the ZDI reconstructed maps for inclination $i = 60°$ (triangle) and $i = 20°$ (upside down triangle). The colour indicates the activity of the star: blue for the solar-like star ($\mathrm{ER} = 1\,\mathrm{ER}_\odot$ and $\mathrm{DR} = 1\,\mathrm{DR}_\odot$), purple for the more active star ($\mathrm{ER} = 3\,\mathrm{ER}_\odot$ and $\mathrm{DR} = 3\,\mathrm{DR}_\odot$) and red for the most active star ($\mathrm{ER} = 5\,\mathrm{ER}_\odot$ and $\mathrm{DR} = 5\,\mathrm{DR}_\odot$). I plot all ten maps per star with a fainter colour and smaller symbol size and the average over the ten maps per star with the bolder colour and larger symbol size. The dashed line indicates the unity line. **a.** The full parameter range covered by the observations. **b.** A zoom in to the parameter range covered by the input and reconstructed maps.

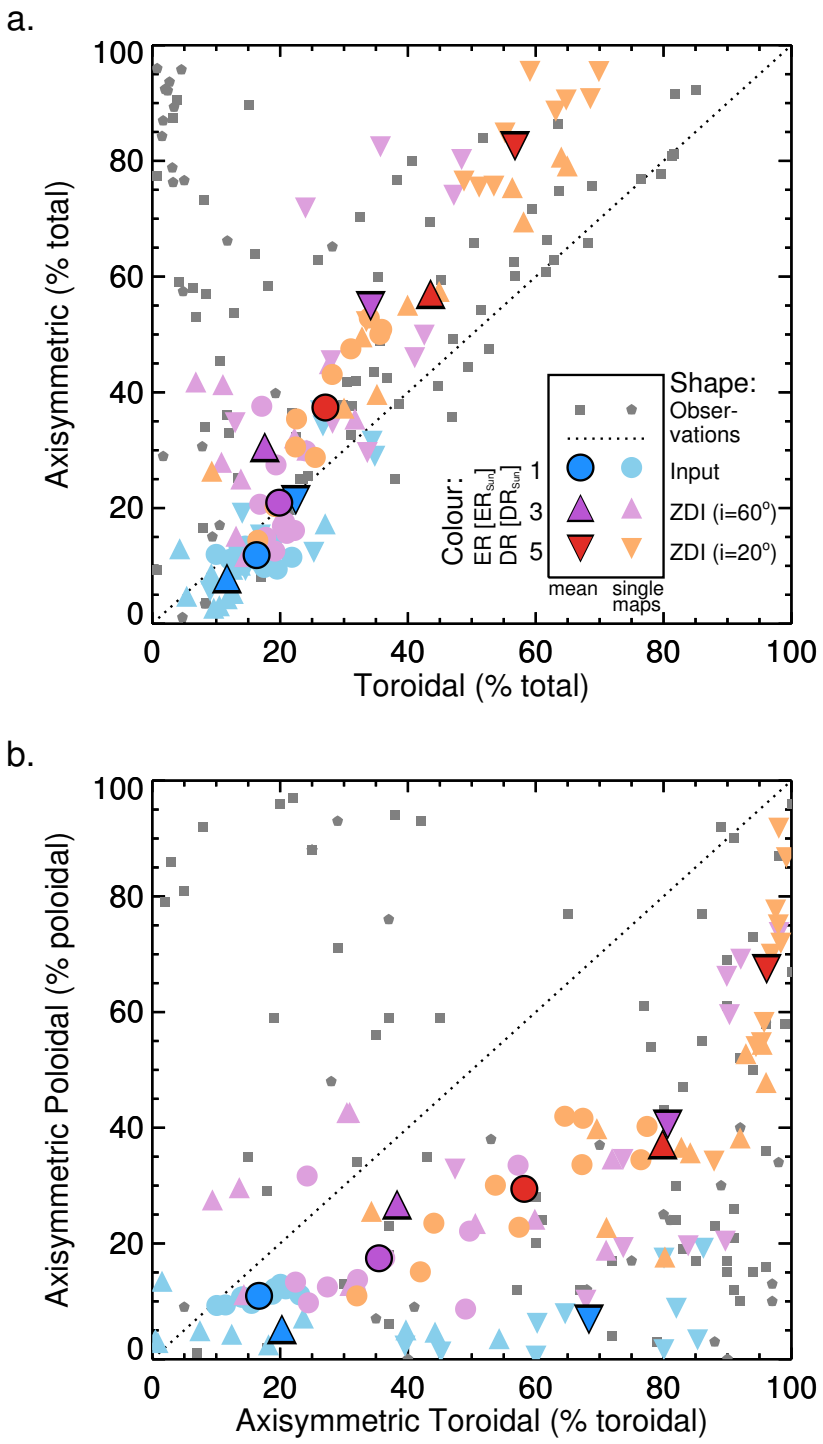

Figure 4.6: The percentage of axisymmetric fraction against the percentage of toroidal fraction (**a.**) and the percentage of the axisymmetric poloidal fraction against the percentage of the axisymmetric toroidal fraction (**b.**) for the observation, large-scale field input maps and ZDI reconstruction presented in Fig. 4.5. The same format as in Fig. 4.5 is used.

Fig. 4.6a plots the axisymmetric energy fraction against the toroidal energy fraction[5] using the same format as Fig. 4.5. All of my maps lie in the same parameter range given by the observations and they follow the trend found by See et al. (2015): the more toroidal the field morphology, the more axisymmetric it tends to be. The axisymmetric and toroidal fractions are well recovered within ±20 % for the solar-like stars (blue symbols). The more active the star, the more ZDI tends to overestimate the axisymmetric and toroidal fraction, which is enhanced by inclination.

Fig. 4.6b shows the axisymmetric poloidal fraction and the axisymmetric toroidal fraction using the same format as in Fig. 4.5. I found that the axisymmetry of the poloidal field is very well recovered by ZDI especially for low activity stars and higher inclinations. The more active the star, the more the axisymmetric poloidal field is overestimated but with less than 10 % error. This makes the axisymmetric poloidal fraction one of the best recovered properties, especially for low activity and higher inclined stars. The axisymmetry of the toroidal field is overestimated by ZDI as well but to a much higher extent. For low inclinations, the axisymmetric toroidal field is in general $40-50$ % higher than expected. The more active the star and the lower the inclination, the more the axisymmetric toroidal fraction is overestimated.

The energy values and fractions for the $\ell_\Sigma = 7$ input maps are computed over the whole surface. The inclination obscures parts of the visible hemisphere so that ZDI misses a fraction of the southern hemisphere. Taking only the visible surface of the input maps into account would reduce the mean values of the axisymmetric and toroidal fraction by at most 6 % and 2 % and the mean values of the axisymmetric poloidal and axisymmetric toroidal fraction by 5 % and 9 % for the lower inclination angle 20°. For higher inclination angles these corrections are even smaller.

The large-scale field properties are often summarised using the format of Donati et al. (2008b, fig. 14), see also Fig. 1.8. Fig. 4.7 displays the input and ZDI reconstructed maps for the large-scale field $\ell_\Sigma = 3$ (Fig. 4.7a) and for $\ell_\Sigma = 7$ (Fig. 4.7b) using a similar format. The input and ZDI reconstructed maps are most similar for $\ell_\Sigma = 3$, while the maximal possible ZDI resolution is $\ell_\Sigma = 7$ in this study. The thick line separates the three different stellar models. I plot the input and both ZDI reconstructions per stellar model from left to right. The average over the ten maps is plotted above and the individual ten maps below the dotted line. The

[5] See Chapter 2.1 for the definitions.

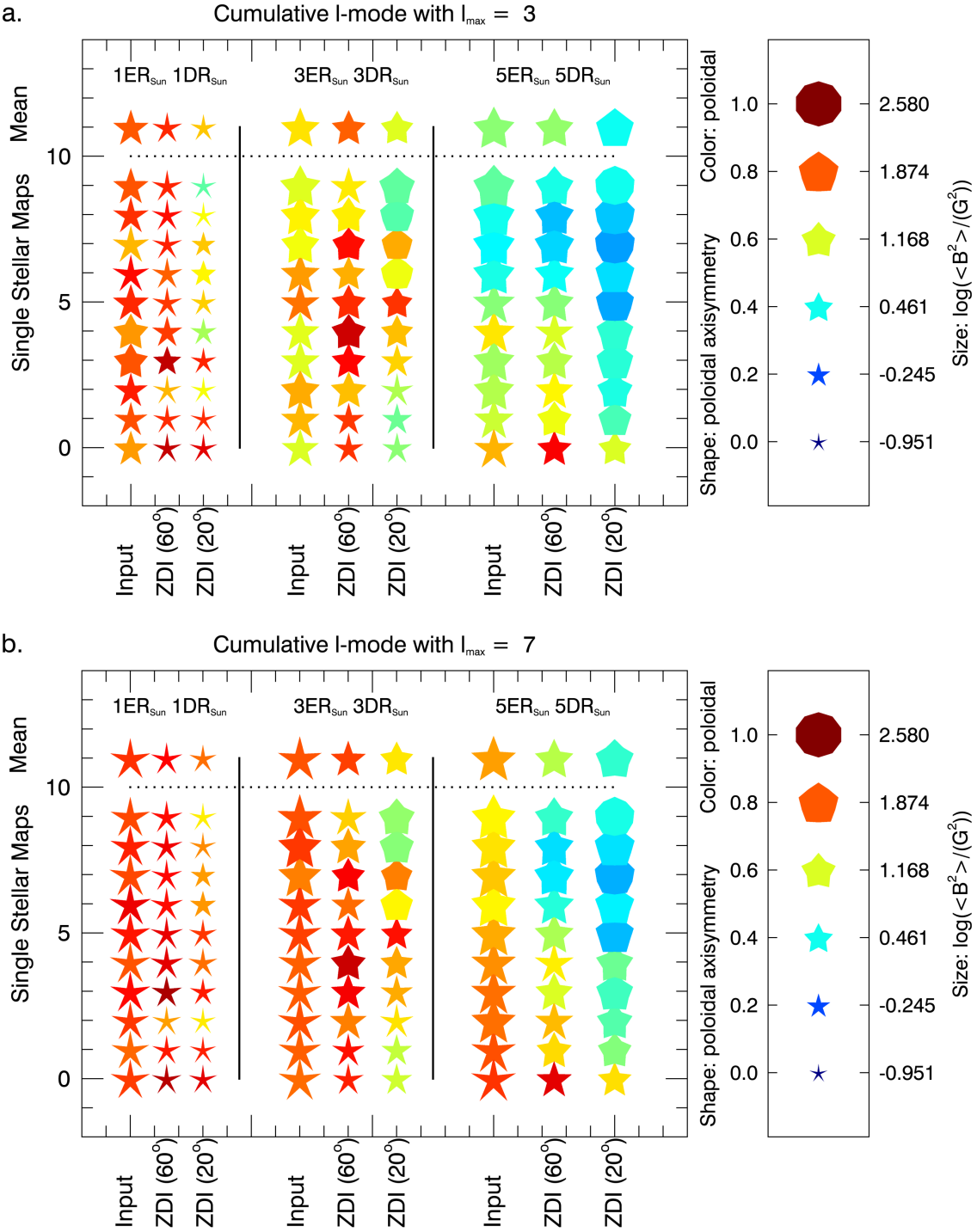

Figure 4.7: The properties of the large-scale field. The symbol size indicates the logarithmic magnetic energy $\log\left(\langle B^2\rangle\right)$. The symbol colour indicates the poloidal fraction $f_{\rm pol}$ and the shape the axisymmetry of the poloidal field $f_{\rm pol,axi}$. I plot all ten maps per star below the dashed line and the mean above the dashed line. The different stellar models are separated by a solid black line. I display for each stellar model from left to right the input map, the ZDI reconstructed map for $i = 60°$ and $i = 20°$. The best agreement between the input and the ZDI reconstruction can be find at $\ell_\Sigma = 3$ (**a.**). Additionally, I show the maximal ZDI resolution with $\ell_\Sigma = 7$ (**b.**).

symbol size indicates the logarithmic total magnetic energy $\log\left(\langle B^2 \rangle\right)$, the symbol colour the poloidal fraction $f_{\rm pol}$ and the symbol shape the axisymmetric poloidal field $f_{\rm pol,axi}$, see legend on the right.

The large-scale field morphology varies in the ten arbitrarily picked input maps for each stellar model, even on time scales much shorter than typical activity cycles lengths. Sometimes ZDI can recover these variations, e.g., for the five times more active star observed by $i = 60°$. However, this is not always the case and especially hard for low inclinations. ZDI fits the large-scale field properties for $\ell_\Sigma = 3$ much better than for $\ell_\Sigma = 7$, which is another hint that ZDI is restricted to the low order modes. The reconstructed field energy is lower. The more active the stellar model, the more the poloidal fraction tends to be underestimated and the axisymmetric fraction to be overestimated. These trends are enhanced by low inclination angles. Nevertheless, several single maps of all stellar models, and especially if observed with higher inclination angles, are in good agreement. ZDI is able to recover the large-scale field morphology for slowly rotating solar-like stars especially for higher inclinations but one should use the average values over several maps as the average is much better recovered by ZDI.

4.3.3 Recovering the energy distributions

I find that ZDI does not effectively recover the magnetic energy distributions across individual ℓ-modes. Fig. 4.8a displays the energy distributions for the first seven ℓ-modes for the poloidal (plum bars) and toroidal (orange bars) component. The activity of the stellar model rises from left to right, see column captions. The distributions for the original input map and for both ZDI reconstructions are plotted below each other. I present here the averaged results over the ten maps per stellar model and inclination.

The input maps and their ZDI reconstructions show opposite trends: for the input maps the magnetic energy increases and for the ZDI maps the magnetic energy mainly decreases with ℓ-mode. For the ZDI reconstructions the poloidal energy peaks at $\ell = 2$ or 3 for the solar-like star, while for the more active stars the poloidal energy peaks at $\ell = 1$. The more active the star, the more the toroidal energy at $\ell = 2$ becomes dominant for the input maps, see also Chapter 3. Most of the time, ZDI is able to recover the maximal toroidal energy at $\ell = 2$, but not always. The magnetic energy values are again much lower for the ZDI maps. The energy distributions of cool stars observations look similar to my ZDI results, see e.g. Jeffers et al. (2014); Rosén et al. (2016). I want to highlight that I neither push the solution towards

low ℓ-modes nor prefer any of the ℓ-modes. The maximum entropy implementation of ZDI naturally distributes energy over the allowed ℓ-modes by preferring that the energy decreases with increasing ℓ-mode as I could show here.

ZDI does a better job by recovering the relative fractions of the field components, see Fig. 4.8b. I plot the cumulative total $C_J(\ell)$ of the poloidal (plum) and toroidal (orange) fraction, where

$$C_J(\ell) = \sum_j f_j(\ell), \tag{4.1}$$

$$f_j(\ell) = \frac{\langle B_j^2 \rangle(\ell)}{\langle B_{\rm tot}^2 \rangle(\ell)}, j \in (\mathrm{pol}, \mathrm{tor}), \tag{4.2}$$

$$\langle B_{\rm tot}^2 \rangle(\ell) = \langle B_{\rm pol}^2 \rangle(\ell) + \langle B_{\rm tor}^2 \rangle(\ell). \tag{4.3}$$

ZDI recovers that the $\ell = 2$ mode has the highest fraction of toroidal energy for the more active stars. However, ZDI tends to overestimate the toroidal fraction for the dipolar $\ell = 1$ mode and to underestimate for $\ell = 4, 5$. The trend with ℓ-mode is similar for both ZDI reconstructions per stellar model, although the toroidal fraction is in general higher for lower inclination angles.

For an easier comparison, I calculated the residuals (subtracting the fraction of the ZDI maps from the fraction of the input maps), see Fig. 4.8c. Mismatches lower or higher than 20 % are divided by the dashed lines otherwise using the same format as before. Underestimations by ZDI are indicated by positive values, overestimations by negative values. The poloidal and toroidal fractions for $\ell \geq 4$ are recovered within a 20 % error. For higher inclinations ZDI underestimates the toroidal energy and overestimates the poloidal energy ($f_{\rm tor} = 1 - f_{\rm pol}$), accordingly, especially for less active stars. For lower inclinations, ZDI misses poloidal energy for the dipolar and octopolar mode ($\ell = 1, 3$) and adds toroidal energy, accordingly.

I analysed the other field components, too, and saw a similar picture: ZDI does not recover the magnetic energy distribution across ℓ-modes but does recover the fractions reasonably well. Only the axisymmetric/non-axisymmtric fractions and the azimuthal/meridional toroidal fractions show further systematic trends. Fig. 4.8d, plots the axisymmetric (dark violet) and the non-axisymmetric (rosa) residuals. For the highly inclined stars, ZDI tends to underestimate the axisymmetric energy and for low inclined stars to overestimate, especially for the more active ones. Checking the residuals for the azimuthal and meridional component

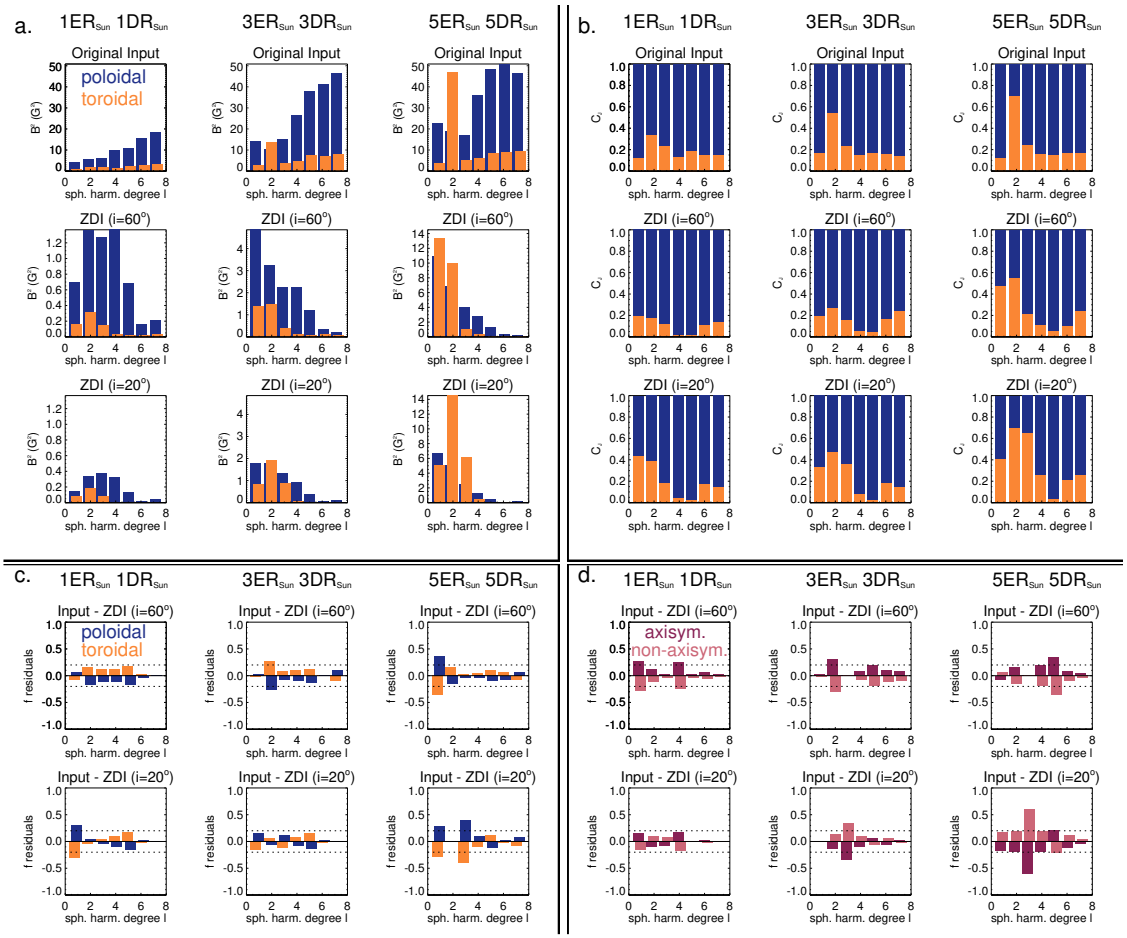

Figure 4.8: The energy distribution (**a.**) and the fractions (**b.**) for the first seven ℓ-modes of the toroidal (orange) and poloidal (plum) field component for the input maps (top row) and ZDI reconstructions for inclination 60° and 20° (2nd and 3rd row). On the bottom I plot the residuals (input - reconstruction) for both inclinations for the toroidal (orange) and poloidal (plum) fraction (**c.**) and for the axisymmetric (dark violet) and non-axisymmetric (rosa) field component (**d.**).

of the toroidal field (see Eq. 1.32), I find that ZDI underestimates the meridional toroidal energy by adding azimuthal toroidal energy for lower inclination angles but performs better at higher inclination angles, see Fig. 4.9.

4.3.4 Recovering the surface averaged field

In the previous sections and figures it was seen that ZDI recovers less magnetic energy or magnetic field strength than expected from the large-scale field extrapolation of the input maps. Reiners & Basri (2009) and Morin et al. (2010) showed for M dwarfs that the averaged magnetic field measured by ZDI $\langle B_V \rangle$ represents only $6-14\,\%$ of the total averaged magnetic field measured by Zeeman broadening $\langle B_I \rangle$. We enlarged the sample by F, G, and K dwarfs including further M dwarfs and showed that ZDI recovers from a few percent to at maximum $20\,\%$ of $\langle B_I \rangle$, (See et al., 2019). We report in Vidotto et al. (2018) that the large-scale field

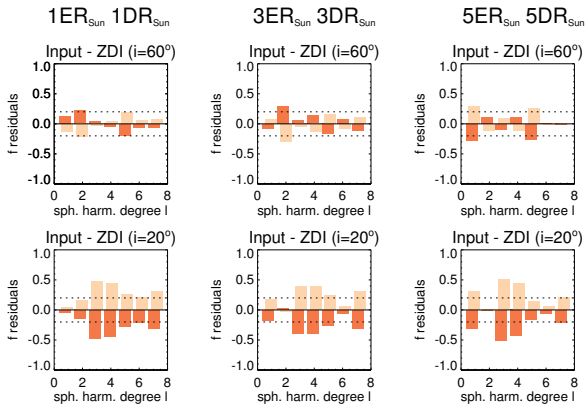

Figure 4.9: The residuals (input - reconstruction) for both inclinations for the azimuthal toroidal (dark orange) and meridional toroidal (light orange) fraction. The same format as in Fig. 4.8c is used.

($\ell_\Sigma = 5$) of 104 solar synoptic maps covering the current solar activity cycle 24 includes as well only $\approx 10-20\,\%$ of the total field most of the time.

Fig. 4.10 presents the analysis of $\langle B_V \rangle / \langle B_I \rangle$ for my three stellar models applying the same colour scheme as in Fig. 4.5. The averaged large-scale field $\langle B_V \rangle$ of the input maps is indicated by circles for $\ell_\Sigma = 7$ and pentagons for $\ell_\Sigma = 5$. Their ZDI reconstructions are plotted again using normal triangles for $i = 60°$ and up-side-down triangles for $i = 20°$. I calculated $\langle B_I \rangle$ from the fully resolved input map. The symbols in Fig. 4.10 display the mean over the ten maps per stellar model and the error bars represent the corresponding standard derivation.

I found that the large-scale field of the input maps mostly comprises $\approx 47\,\%$ for $\ell_\Sigma = 7$ and $\approx 37\,\%$ for $\ell_\Sigma = 5$ of the total average magnetic field, independent of the activity level of the star. ZDI recovers $\approx 12-17\,\%$ for the higher inclination and $\approx 6-13\,\%$ for the lower inclination. Next to the inclination trend, I also see a trend with stellar activity. The higher the stellar activity, the higher its $\langle B_V \rangle / \langle B_I \rangle$. Both trends result from the $v_e \sin i$ dependence of ZDI. The higher the stellar activity, and the higher the inclination angle, the higher the stellar $v_e \sin i$ and in accordance the resolution and field reconstruction by ZDI. If I consider the obscuration effect of the stellar inclination, the $\langle B_V \rangle / \langle B_I \rangle$ mean values reduce by less than $\approx 6\,\%$ for the input maps and less than $\approx 5\,\%$ for the ZDI reconstruction for low inclination angles and even less for higher ones. Even if I analyse here solar-like stars, it is remarkable that my $\langle B_V \rangle / \langle B_V \rangle$ values are similar to those M dwarf observations, where the stars are much more active and faster rotators, (Reiners & Basri, 2009; Morin et al., 2010; See et al., 2019).

Furthermore, I analysed the amount of average magnetic field that is underestimated by ZDI. I computed the average magnetic field of the ZDI reconstructed maps $\langle B_{\rm ZDI} \rangle$ and divided

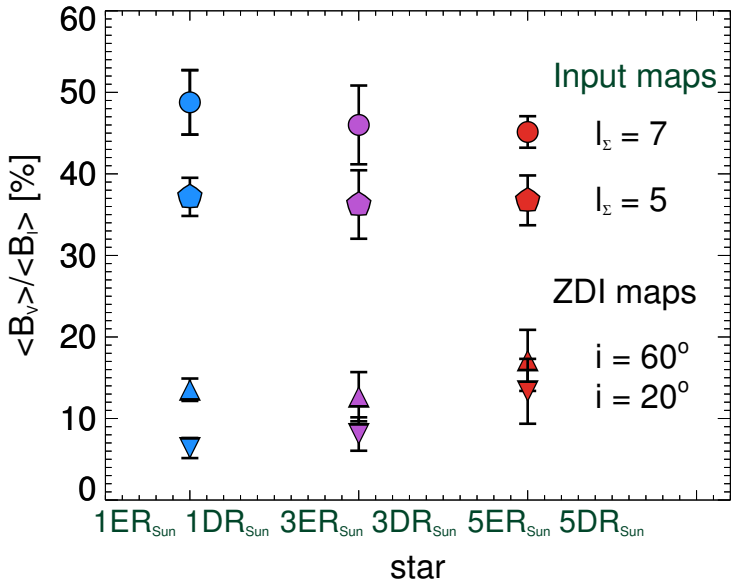

Figure 4.10: The fraction $\langle B_V \rangle / \langle B_I \rangle$ of the mean flux density that is recovered by the large-scale field of the input maps for $\ell_\Sigma = 5$ and 7 and the ZDI reconstructed maps for the three different stars. The denominator $\langle B_I \rangle$ is the unsigned mean magnetic flux density of the full resolved input map. For the circular and pentagon symbols $\langle B_V \rangle$ is equal to the large-scale field for $\ell_\Sigma = 7$ and 5 of the input maps. For the normal and up-side-down triangular symbols $\langle B_V \rangle$ is equal to the ZDI reconstructed maps for the inclination angles $i = 60°$ and $i = 20°$.

it by the average magnetic field of the input maps $\langle B_{\rm Inp} \rangle$ per ℓ-mode. I got a large range of $10 - 110\,\%$ across the individual maps depending on stellar activity, ℓ-mode and inclination. In general, the recovered percentage increases with stellar activity or better with $v_e \sin i$. For example for the dipolar $\ell = 1$ mode I got $\langle B_{\rm ZDI} \rangle / \langle B_{\rm Inp} \rangle = 0.40 \pm 0.11$ for the solar-like star and $\langle B_{\rm ZDI} \rangle / \langle B_{\rm Inp} \rangle = 0.58 \pm 0.12$ for the three times and $\langle B_{\rm ZDI} \rangle / \langle B_{\rm Inp} \rangle = 0.96 \pm 0.16$ for the five times more active star. The higher the ℓ-mode, the lower $\langle B_{\rm ZDI} \rangle / \langle B_{\rm Inp} \rangle$ tends to be but there are a number of exceptions. The large spread in combination with the high dependence on the individual maps and $v_e \sin i$ makes it impossible to provide a general correction factor for the underestimation by ZDI. This is especially true if one keeps in mind that the analysed sample of stellar models covers only a very small fraction of the observed cool stars.

4.4 Discussion and conclusion

To the begin, I want to highlight that the spherical harmonic decomposition method (Vidotto, 2016) provides an easy and fast routine to estimate the magnetic field topology detectable with ZDI of any vector magnetic field map. For rapidly-rotating, fully-convective stars with $v_e \sin i = 20\,{\rm km\,s^{-1}}$, Yadav et al. (2015) showed that the ZDI maps can be mimicked from

simulated maps using the spherical harmonic decomposition including $\ell_{\Sigma} = 10$. For the much slower-rotating solar-like stars with $v_e \sin i \leq 5\,\mathrm{km\,s^{-1}}$, I showed that the inclusion of $\ell_{\Sigma} \approx 3{-}5$ provides an adequate estimation of the large-scale field structure detectable with ZDI. With the help of the spherical harmonic decomposition one is able to determine the large-scale field of, e.g., solar-dynamo simulated maps or any other vector magnetic field map. This allows a direct comparison with other cool star ZDI observations, without running a ZDI routine. Caution is only needed by comparing the absolute magnetic field values or energies. It is better suited to the morphologies themselves.

In general, I found that ZDI is able to reconstruct the main structures of the large-scale field for slow rotating solar-like stars. The more active and inclined (i.e. more equator-on) the star, the better the ZDI reconstruction is, especially after averaging over several maps of the same target. The relatively inactive solar-like stars show variations in the large-scale magnetic field from one stellar rotation to another. Under good circumstances (more active stars, higher inclination) ZDI can often follow this variation.

One downside is that ZDI is not able to recover the correct level of field strengths and energies for solar-like slow rotators. The magnetic energy is underestimated by approximately one order of magnitude. Even by comparing the ZDI maps with the input maps considering the inclination effect, the result will not change by more than a few percent. This underestimation is mainly due to the fitting process of the Stokes profiles. The Stokes profiles can be fit by a range of magnetic field values for the same reduced χ^2 for slowly-rotating solar-like stars. The applied maximum entropy regularisation in ZDI favours the lowest energy solution. The actual magnetic field is likely to be underestimated, while still yielding an equally good fit of the Stokes V profiles (as defined by the reduced χ^2).

The underestimation of the surface magnetic field strengths and energies by ZDI for solar-like slow rotators has a direct impact on, e.g., the determination of the stellar angular momentum-loss rates or of the habitability of exoplanets. For example, Finley et al. (2019) find that their ZDI based angular momentum-loss rates are systematically lower by a factor of 3-30 compared to results from rotation evolution models by Matt et al. (2015). Just recently, we could show that the estimated angular momentum-loss for low mass stars with weak magnetic fields can be underestimated by up to a factor of ten using the here presented ZDI maps, see See et al. (2020). Furthermore, the underestimation of surface magnetic field of host stars in extraso-

lar planetary systems via ZDI affects, e.g., the estimations about the hability of exoplanets. The exoplanets are likely to be stronger affected by the stellar wind than determined from the ZDI maps and would need a stronger planetary magnetic field to be habitable. In addition, the distance enlarges where the stellar wind significantly affects or interacts with the planets. Recently, Farrish et al. (2019) explored the magnetic environment of extrasolar systems using flux transport models highlighting the dependency of the habitability from the host star's large-scale magnetic field.

I found that ZDI works better for higher inclination angles than for lower inclination angles (i.e. better for equator-on than pole-on views). Lower inclination observations show less magnetic energy and especially less poloidal energy. Accordingly, the relative toroidal fraction increases. Also the axisymmetry of the total field and of both components, the poloidal and toroidal, is enhanced for low inclined stars. In extrema, I found that the axisymmetric toroidal fraction was overestimated by $40-50\,\%$. Furthermore, I discovered trends with stellar activity and $v_e \sin i$ for the ZDI recovered maps. The higher the stellar activity, the higher the detected toroidal energy especially in connection with low inclination angles. Also the toroidal and axisymmetric fraction is higher, the more active the star. The stellar activity is here defined in respect of the solar flux emergence and differential rotation rate.

One needs to discuss both trends, inclination and activity, in the context of the solar flux emergence pattern. The solar flux emergence pattern is characterised by a strong quadrupolar $\ell = 2$ azimuthal toroidal mode on a global scale as the small-scale solar flux emerges in the range of the two active latitudes with opposite polarities on the hemispheres. This pattern is also highly axisymmetric on the global scale. The large-scale field toroidal $\ell = 2$ mode mimics therefore the emergence of the active regions in a sense. With an increasing flux emergence rate the number of active regions per time increases and the stronger the axisymmetric toroidal $\ell = 2$ mode becomes, see Figs. 4.2-4.4 and Fig. 4.8. With an increasing differential rotation, the poloidal field within the active regions decreases, see Chapter 3, which causes another increase of the toroidal fraction. The more the azimuthal toroidal ring dominates the Stokes V profiles (for more active and lower inclined stars), the more ZDI struggles to detect the details of the (relatively low contrast) smaller field structures on the top of the toroidal ring. The maximum entropy regularisation enhances this effect as it pushes to an image with the least amount of information in order to fit the Stokes profiles. The penalty for adding small scale field structures on top of the ring likely dominates over the much smaller improvement in the

Stokes V fit. An overestimation of the toroidal and axisymmetric fraction becomes likely for low inclined and more active stars with solar flux emergence pattern.

ZDI observations of stars with Rossby numbers $R_o \leq 0.1$ and stellar masses $M \geq 0.5\,\mathrm{M}_\odot$ show strong toroidal bands at mid to low latitudes, see Fig. 1.8 or Chapter 1.5.2. In respect of my results presented here, a possible explanation may be that these stars have well populated active latitudes, that cause the strong $\ell = 1$ or $\ell = 2$ toroidal modes. I also confirm that the toroidal and poloidal energy increases with stellar activity following the power law relation found by See et al. (2015) for stars with masses $M \geq 0.5\,\mathrm{M}_\odot$, see also Fig. 1.9. ZDI recovers this power law relation with activity very well. However, my simulations do not reach the stellar parameters in terms of $v_e \sin i$ and stellar activity to tests this theory properly. Anyway, I want to highlight that ZDI found indeed similar poloidal dominated topologies for slowly rotating solar-like stars as found in this study, e.g. HD 146233 (Petit et al., 2008) or HD 147513 (Hussain et al., 2016).

Another main results is that ZDI is not able to recover the magnetic energy distributions across individual ℓ-modes (neither in absolute values nor in relative trend). The energy distributions recovered by ZDI are controlled by the maximum entropy regularisation, which searches for the simplest field required to fit the Stokes profiles and tends to put magnetic structures into the lowest energy modes first. I do not put artificially weight on certain ℓ-modes, i.e. all ℓ-modes are equally weighted. The ZDI resulting energy distributions (mainly energy decreases with ℓ-mode) show the opposite trend than the input maps (mainly energy increases with ℓ-mode). An infinite number of energy distributions can reproduce a given magnetic field topology or Stokes IV time series. As this is an ill-posed problem, ZDI is unable to reconstruct the correct input distribution.

Nevertheless, I found that ZDI does a reasonable good job by recovering the fraction of the individual magnetic field components across the ℓ-modes. The fractions are mostly reliable within $\sim 20\,\%$ error for solar-like slow rotators. For lower inclinations I see again an overestimation of the (azimuthal) toroidal and axisymmetric field, due to same reasons as previously discussed. ZDI is able to recover the field fractions to a satisfying level, which is encouraging for the interpretation of cool stars observed magnetic field topologies.

To finally conclude, ZDI does a good job of recovering the large-scale field topologies for $\ell_\Sigma \leq 5$ (best for $\ell_\Sigma = 3$). Especially the main magnetic field structures and fractions of the

different field components are recovered. ZDI underestimates the field strength and energy and is not able to reconstruct the energy distribution with ℓ-modes for solar-like slow rotators. ZDI is limited by the fitting process of the Stokes profiles and the limitations or consequences of using the maximum entropy regularisation to overcome the ill-posed problem. Further, ZDI is affected by inclination effects and one needs to keep in mind by the interpretation of the large-scale field the global properties of the small-scale flux emergence pattern (if known like for the Sun).

4.5 Summary

I analysed the reliability of the ZDI technique using 3D non-potential magnetic field simulations as points of reference in the framework of slowly-rotating, solar-like stars. I found that ZDI is able to recover the main structures of the large-scale field morphology but underestimating the magnetic energy by approximately one order of magnitude. The ZDI reconstructed maps are compared with the whole surface input maps to provide realistic estimates of the reconstruction ability of ZDI. However, taking only the visible surface of the input maps into account would change the recovered properties only by a few percent.

My main conclusions are:

- ZDI recovers the main magnetic structures ($\ell_\Sigma = 3$—5) of the large-scale field for slow rotating solar-like stars. The large-scale field properties are reasonably well reconstructed but it is recommended to use the average over several maps.

- ZDI recovers the power law relation $\langle B^2_{\rm tor}\rangle \propto \langle B^2_{\rm tor}\rangle^{1.25\pm0.06}$ for stars with masses $M \geq 0.5\mathrm{M}_\odot$ (See et al., 2015) but with systematically lower magnetic field values.

- The large-scale field of solar-like stars can vary significantly from one stellar rotation to another even if one does not take activity cycles into account. ZDI can follow these variations to a certain extent for higher inclined, more active stars.

- The axisymmetric poloidal fraction is the best recovered parameter by ZDI.

- The inclination of the star affects ZDI: higher inclination angles (i.e. more equator-on view) provide better results. The lower the inclination angle, the higher the overestimation of the toroidal and axisymmetric fraction for slow rotators with solar flux emergence

patterns. The increase in the toroidal fraction is mainly caused by a lack of poloidal energy in the reconstructions.

- ZDI reacts to the rotation period and activity of the star. The faster the star rotates within my sample of stellar models, the higher the number of resolution elements across the Stokes profiles and therefore the more magnetic field is recovered. The higher the stellar activity for slow rotators with solar flux emergence pattern, the higher the toroidal and axisymmetric fraction.

- ZDI in connection with a maximum entropy ansatz is not able to recover the magnetic energy distribution across individual ℓ-modes. However, the fractions of the different field components per ℓ-mode are mostly correct within a 20 % error.

- The averaged magnetic field per ℓ-mode detected by ZDI varies between $10-110\,\%$ compared to the average magnetic field per ℓ-mode of the corresponding input map. It is not possible to apply a fixed correction factor for the ZDI maps due to this large variation, which depends on the individual ℓ-mode, stellar activity and stellar $v_e \sin i$.

- The total averaged field detected by ZDI is only $6-17\,\%$ of the total average magnetic field of the fully resolved input map for slow rotating solar-like stars. Higher $v_e \sin i$ increase the fraction.

I want to highlight once again that my focus for benchmarking ZDI lies in ZDI's ability to recover the large-scale field properties of slow rotating solar-like stars. The tests are performed under optimal conditions: assuming a high S/N, an evenly spaced, well sampled spectral time series and a static surface magnetic field over the course of one stellar rotation. Further tests are planned including varying level of S/N, phase coverage and evolving magnetic field maps.

5

The solar magnetic field topology along the activity cycle

5.1 Introduction

The fascinating magnetic activity phenomena on our Sun emerge on one hand randomly in time and position but on the other they follow certain periodic patterns. In this chapter I focus on the solar activity cycle and analyse surface vector magnetic field simulations and their ZDI reconstructions covering 15 years. This work is in preparation to be submitted to the MNRAS under the title "The magnetic field vector of the Sun-as-a-star – III. Evolution of the large-scale vector field of the 3D non-potential flux-transport simulated activity cycle 23 and its reconstruction with ZDI" by L. T. Lehmann, G. A. J. Hussain, A. A. Vidotto, M. M. Jardine and D. H. Mackay.

I introduce solar and stellar activity cycles and present the current state of research in Section 1.5.1. I will repeat some key information here and focus more on the solar activity

cycles of the recent years.

Our Sun reverses its global dipolar field every ≈ 11 years, which leads to a magnetic cycle (seeing the same polarity at the poles) of ≈ 22 years. With the beginning of a new activity cycle sunspots appear at mid latitude range (±35°) and the global dipole weakens. At activity maximum the global dipole and the axisymmetry of the solar magnetic field is at minimum while the sunspot number is at maximum. The sunspots emerge at lower and lower latitude during the following decreasing phase. Simultaneously the new global dipolar field gets stronger and stronger and shows the opposite polarity. The dipole strength becomes maximum at activity minimum when the number of sunspots is lowest. DeRosa et al. (2012) confirmed that the solar dipolar magnetic energy is in anti-phase with the sunspot number (SSN) while the ratio of the quadrupolar to the dipolar magnetic energy is in phase with SSN for solar cycle 21–23, see DeRosa et al. (2012, fig. 4).

The dipolar and total magnetic energy decrease with each activity maximum for the most recent solar cycles 21–23 (DeRosa et al., 2012; Kakad et al., 2019). The sunspot number decreases as well with each activity maximum for the last four cycles and each of them shows the double peak feature, see e.g. Fig. 1.7 or Kakad et al. (2019, fig. 1). DeRosa et al. (2012) report also that the axial dipole coefficient and the dipolar magnetic energy shows a longer decreasing phase between solar cycle 23 (SC23) and our current solar cycle 24 (SC24) compared to previous solar cycles. The solar minimum between SC23 and 24 (2008–2010) was unusually deep and long. Kakad et al. (2019) found a significant decrease in the integrated solar magnetic energy density for each solar cycle from SC21 to 24 but the strongest decrease with 51 % from SC23 to 24. Also the maximum speed of the solar wind decreased from 73 km s^{-1} to 57 km s^{-1} (Kakad et al., 2019). Janardhan et al. (2018) found an unusual hemispheric asymmetry in polar field reversal for SC24 following this strong minimum. They noticed that the northern hemisphere shows the reversal in June 2012 followed by near-zero field period until 2014 while the southern hemisphere shows the reversal one year later at mid 2013, see Fig. 5.1. This was followed by a rapid increase of the first three large-scale field components around 2015 (Finley et al., 2018). In a nutshell, the solar cycles 21–24 got weaker in magnetic energy and SSN, where an unusual long and deep minimum occurred in 2008–2010 between SC23 and 24. The current solar cycle 24 seems to be affected by this showing, e.g., an asymmetry in the polar field reversals.

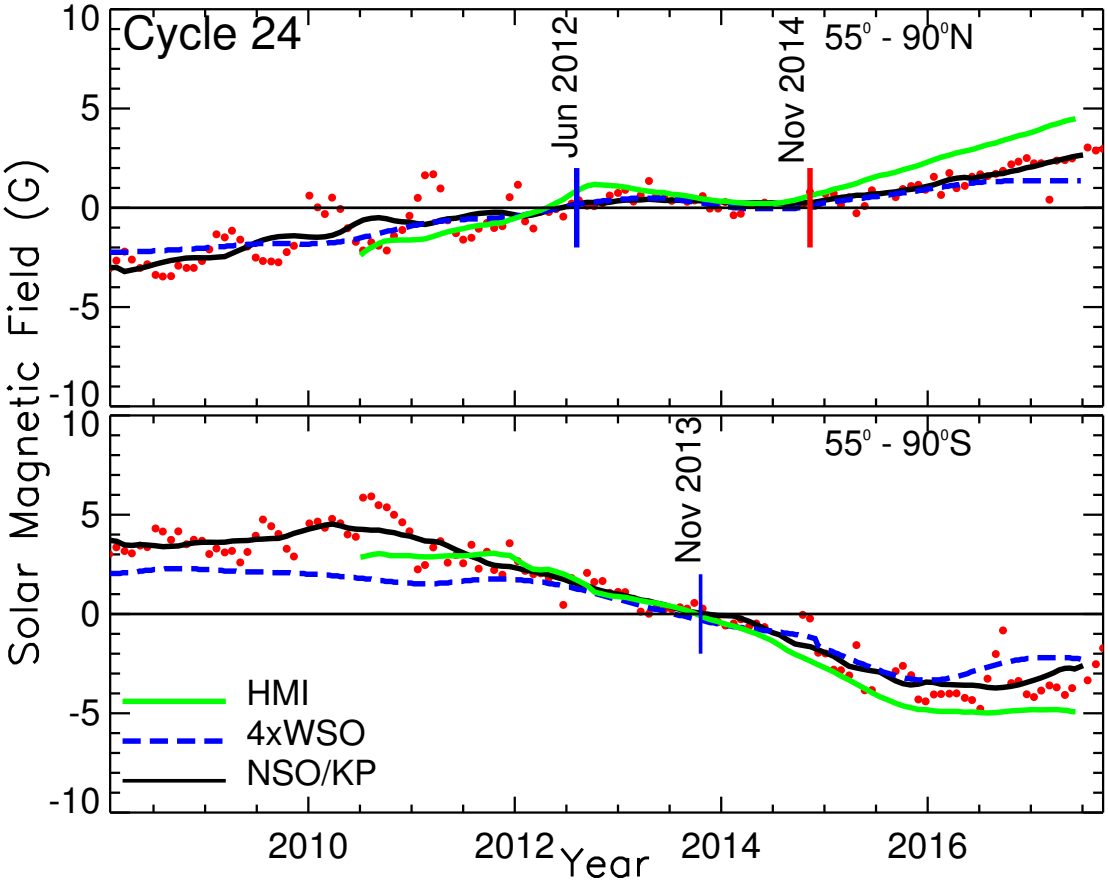

Figure 5.1: The signed values of polar field strengths (red dots) for the latitude range $55^\circ - 90^\circ$ from NSO/KP in the solar northern (top) and southern (bottom) hemispheres. The dashed blue curve shows the signed values of polar field strengths from WSO applying a 1.58 year (or 20nHz) low pass filter and the solid green curve displays the signed values of polar field strengths from SDO/HMI. The solid black curve indicates the smoothed line through the data points of the NSO/KP from which time of reversal is determined and marked by the little blue and red vertical line. The northern hemisphere shows an extended zero-field condition after the first reversal in June 2012 before the reversal is completed in November 2014. The southern hemisphere shows a normal reversal in November 2013 similar to previous cycles. Figure reproduced from Janardhan et al. (2018, fig. 1 bottom panel) with permission.

In Vidotto et al. (2018) we analysed the large-scale magnetic field of most part of the SC24 from January 2010 until April 2018. We used high-resolution full-disc vector magnetograms observed by SOLIS (Synoptic Optical Long-term Investigations of the Sun; Keller et al. 2003) at the NSO (National Solar Observatory) and by HMI (Helioseismic and Magnetic Imager; Pesnell et al. 2012; Hoeksema et al. 2014) at the SDO (Solar Dynamics Observatory). We found that the large-scale magnetic field is less axisymmetric during the increasing phase as during the decreasing phase for SC24. Further, we could confirm that sunspots must be a major contributor to the large-scale toroidal field and that the solar large-scale field is in line with the observational trends of the cool stars magnetic field topologies presented by See et al. (2015).

Next to the Sun also other cool stars show activity cycles. Several stars are observed showing chromospheric and/or photospheric activity cycles, which can be in phase like for our Sun or in anti-phase. ZDI unveiled global magnetic field reversals in phase with the chromospheric activity cycle similar to our Sun for two stars: the F7 dwarf τ Boo (Jeffers et al., 2018) and the K dwarf 61 Cyg A (Boro Saikia et al., 2016, 2018). Both show activity cycle periods shorter than the Sun with 120 days for τ Boo (Jeffers et al., 2018) and $\approx$ 7 years for 61 Cgy A (Boro Saikia et al., 2018). Furthermore, the ZDI observations show that stars owning high temporal variations have significant toroidal fields otherwise they are predominantly poloidal like our Sun (See et al., 2016).

The main question I want to answer in this Chapter is: Can a solar-like cycle be observed with ZDI and what would be the best strategy? The easiest way would be simply looking at the magnetic field maps for polar field reversals but observing sun-like stars is still challenging and the magnetic field maps can be misleading, e.g., through effects due to the inclination angle, see Section 4.3.1. My aim is to present a more reliable method for detecting solar-like cycles using a parameter based analysis of the magnetic field topology.

To answer this question I analyse 118 simulated surface vector magnetic field maps which cover the years 1996–2011 and therefore the SC23 (1996.37–2008.96) and the first part of the following SC24. Further, I reconstruct the magnetic field maps of 41 maps with ZDI. I compare the magnetic field topology of the simulations and their reconstructions with the observed cool star magnetic field topologies presented by See et al. (2015) and with the solar observations for SC24 analysed by Vidotto et al. (2018).

Section 5.2 introduces the simulations and the applied ZDI implementation. Section 5.3 presents the results, while Section 5.3.1 sets the simulations of SC23 in the context of cool star observations before I analyse their magnetic field topology evolving with time in Section 5.3.2 and compare them with the solar observations in Section 5.3.3. The results of ZDI reconstructed maps and their analysis are included. A summary and further conclusion can be find in Section 5.4.

5.2 Simulations and techniques

5.2.1 The solar cycle simulations

The simulations of solar cycle 23 (SC23) are kindly provided by Duncan Mackay and were published in Yeates & Mackay (2012). The details are presented in section 2 of Yeates & Mackay (2012). I also recommend reading Yeates et al. (2008) for further details. This section (5.2.1) is based on Yeates & Mackay (2012, section 2), and the references therein if not directly mentioned.

Yeates & Mackay (2012) simulate the evolution of the large-scale photospheric and coronal magnetic field for 15 years covering SC23 (1996–2011). The simulations are modelled with the non-potential flux transport model described in Chapter 2.2. A brief reminder: the non-potential model connects a surface flux transport model with the magnetofrictional relaxation in the corona above (van Ballegooijen et al., 2000). The large-scale mean field in the corona is determined using the induction equation, where the Ohmic diffusion is neglected. The unresolved small-scale fluctuations are included via the mean electromotive force. This was done using the hyperdiffusion ansatz after van Ballegooijen & Cranmer (2008) and tested with a constant diffusivity, which did not change the main results. The magnetofrictional technique (Yang et al., 1986) is used to determine the velocity, including a radial outflow (Mackay & van Ballegooijen, 2006).

The simulations were modeled using a non-uniform spherical grid. The grid resolution changes from 192 grid points at the equator to 12 grid points at the polar grid boundary at 89.5° latitude, see also appendix A or fig. 7 in Yeates (2014). The initialisation of the simulations was done with a potential field extrapolation based on the synoptic magnetogram for CR1910[1] from the US National Solar Observatory, Kitt Peak (NSO/KP) and was correct for

[1]Carrington Rotation (CR) 1910: 1996 June 01 to 1996 June 28.

differential rotation to represent 1996 May 15. The emergence of new active regions drives the evolution of the coronal field which is simultaneously sheared by photospheric motions. The photospheric motions are modelled using a standard surface flux transport model (Leighton, 1964; Sheeley, 2005), where the supergranular diffusivity is given with $D = 450\,\mathrm{km}^2\ \mathrm{s}^{-1}$, the meridional flow profile by Schüssler & Baumann (2006) using a peak speed of $11\,\mathrm{m\ s}^{-1}$ and the Snodgrass (1983) differential rotation profile. In Chapter 2.2 I describe the photospheric motions in greater detail and present the equations of the profiles used, see page 36.

The active regions are emerged as idealised 3D magnetic bipoles (two magnetic spots of opposite polarity) using the model of Yeates et al. (2008). Their properties (magnetic flux, location, size and tilt angle) are determined from NSO/KP synoptic maps[2]. The tilt angle is afterwards reduced by 20 % (Cameron et al., 2010; Jiang et al., 2013a) and an additional decay term for the photospheric magnetic field using a time-scale of 10 yr (Schrijver et al., 2002; Schrijver & Liu, 2008) is included to reproduce the observed polar field strength after reversal. In total 1838 bipoles with a magnetic flux between $2\cdot10^{20}\,\mathrm{Mx}-5.3\cdot10^{22}\,\mathrm{Mx}$ emerged between CR1911 (1996 June) and CR2110 (2011 May). There are three data periods (CR2015–16, CR2040–41, CR2091) where no bipoles are inserted. Figure 5.2 shows the butterfly diagram for the longitudinal average radial magnetic field for the observations from NSO/KP and the simulations.

I am using only the photospheric ($r = \mathrm{R}_\odot$) vector magnetic field maps of this non-potential 3D simulation reaching from the solar surface up to source surface[3] in the corona $R = 2.5\,\mathrm{R}_\odot$. In total I analysed 118 maps, which are listed in Table 5.1 in the appendix of this chapter with some of their key parameters and their SSN. The sunspot data are from the World Data Center SILSO, Royal Observatory of Belgium, Brussels. I use the monthly mean total sunspot number, which is the arithmetic mean of the daily total sunspot number over all days of each calendar month.

5.2.2 The map selection and applied ZDI implementation

First of all I run a quick test by selecting 10 maps out of the 118 simulated surface magnetic field maps for SC23. This corresponds roughly to one map per year. The modulation of their Stokes V profiles, their reconstructed maps and magnetic energy values looked promising so I

[2]After 2003 with the SOLIS telescope, before with the older vacuum telescope.
[3]The source surface is the outer boundary condition at which the magnetic field is forced to be purely radial in the assumption that the thermal pressure is high enough at this distance to open up the field lines.

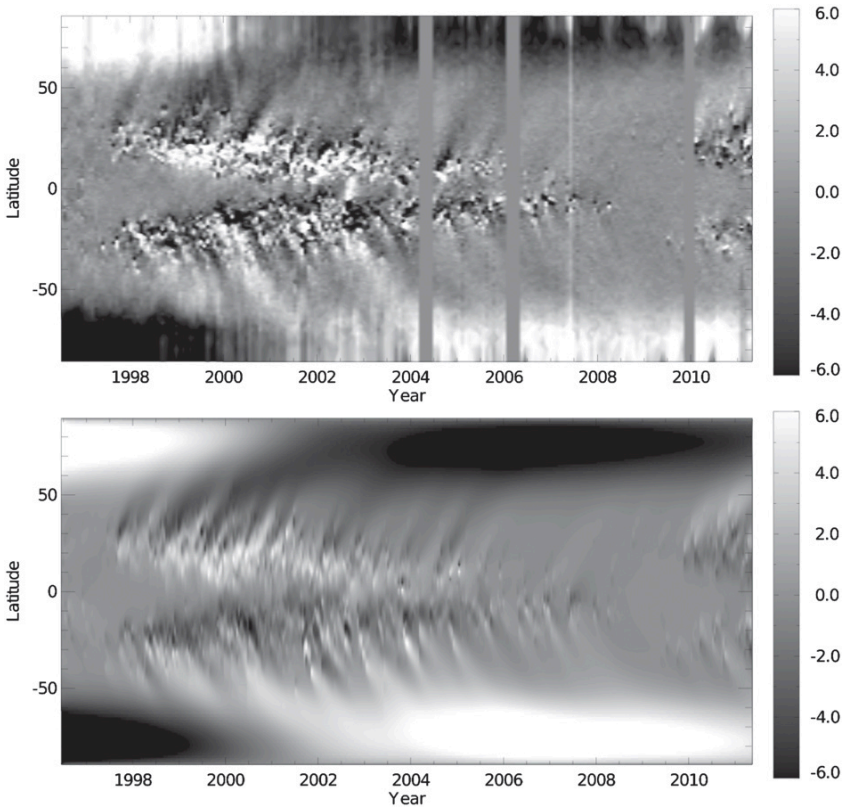

Figure 5.2: The longitudinal-averaged radial magnetic field against time (Butterfly diagram) for the NSO/KP synoptic maps including three data gaps (top) and for the simulations (bottom). Figure reproduced from Yeates & Mackay (2012, fig. 2) with permission.

continued the project by determining and analysing the ZDI reconstructions of further simulated maps. To run ZDI for all 118 maps would be out of proportion. Furthermore, it is unlikely that one would receive such a high amount of telescope time to cover a stellar magnetic cycle in that detail. I selected 41 maps out of the 118 simulated maps for the ZDI reconstruction. Half of them (21 maps) are equally spaced in time from mid 1996 until beginning 2011. Additionally, I selected 20 maps in between, especially around the activity maximum as the simulated maps show the highest variation in the magnetic topology there, e.g. see Fig. 5.12a. Table 5.2 in the appendix of this chapter lists the 41 selected maps and some of their key properties.

To apply ZDI to the solar cycle simulations I followed the methods and routines described in Chapter 4. I used the implementation of solar-like stars with solar flux emergence and differential rotation rate by applying a different noise level. In the following paragraphs I only repeat the main parameters of the modelling and describe the different S/N application. The details of the Stokes IV profile modelling are described in Section 2.3.1.

The Stokes profiles of the 118 simulated maps of the SC23 are modelled by assuming a rotation period of 27.0 days and an inclination angle of 60°, which leads to $v_e \sin i = 1.62\,\mathrm{km\ s^{-1}}$. I applied again a spectral resolution similar to HARPS corresponding to 30 velocity bins ranging from $-20\,\mathrm{km\ s^{-1}}$ to $20\,\mathrm{km\ s^{-1}}$ per Stokes profile. Each time-series of Stokes V profiles per solar cycle map consists of 25 observational phases, which are equally spaced in time. The noise level of the Stokes profiles is different compared to the Stokes profiles described in Chapter 4. In Section 4.2 the S/N relates to the maximum amplitude of each time series per map, so that all maps are equally affected by the noise. The S/N changes for each map, see Section 4.2, page 98, for further details. In this chapter I assumed a fixed S/N that corresponds to 10% of the maximum amplitude of all Stokes V profiles across the solar cycle. Each map is differently affected by the noise. The Stokes V amplitudes of the 118 maps range from $2.02 \cdot 10^{-5}\,\mathrm{V/I_C}$ to $7.83 \cdot 10^{-5}\,\mathrm{V/I_C}$. The continuum S/N corresponding to 10% of the maximum amplitude ($\mathrm{amplitude_{max}} = 7.83 \cdot 10^{-5}\,\mathrm{V/I_C}$) is:

$$\mathrm{S/N} = \frac{1}{10\,\%\ \mathrm{amplitude_{max}}} = \frac{1}{0.1 \cdot 7.834145 \cdot 10^{-5}} = 127\,646 \approx 130\,000. \qquad (5.1)$$

I used the fixed S/N = 130 000 for all maps of the solar cycle. Time series showing lower

Stokes V amplitudes are more strongly affected by the noise than time series showing higher Stokes V amplitudes. This allows us to determine if and how the detected large-scale magnetic field topology is influenced by noise along the magnetic cycle. In addition, I tested further fixed signal-to-noise-ratios of S/N = 30 000, 80 000 guided by typical and very good signal-to-noise-ratios of current observations, see e.g. Jeffers et al. (2014); Boro Saikia et al. (2018), and a S/N = 425 000 which corresponds to 3% of the maximum amplitude of all Stokes V profiles along the cycle. The Stokes V profiles become too noisy to extract reliable maps using S/N = 30 000 and 80 000. A S/N corresponding to 3% of the maximum amplitude leads of course to less noisy Stokes V profiles and more detailed maps, but obtaining a S/N = 425 000 for a solar-like star is not possible with current telescope facilities. Even a S/N of 130 000 is more than challenging today.

I used the ZDI routine described in Chapter 2.4.2 to reconstruct the magnetic field maps for the 41 selected maps of the simulated SC23. The ℓ_Σ-modes are weighted equally. Neither an axisymmetric nor a non-axisymmetric topology is preferred. All ℓ_Σ-modes contribute equally to the topology, so that no length scale is preferred. I allowed a maximum ℓ_Σ-mode of $\ell_{\Sigma,\max} = 7$ similar to the reconstructions in Chapter 4. For most maps only the ℓ_Σ-modes up to $\ell_\Sigma \leq 5$ show significant magnetic energy. Nevertheless there are some maps where $\ell_\Sigma = 6, 7$ store notable magnetic energy so that I chose a $\ell_{\Sigma,\max} = 7$.

Figure 5.3 shows the ZDI fitted Stokes V spectra for three example maps. I present one map for the increasing phase (map 0720 corresponds to the year 1997.97), the activity maximum (map 1620 = 2000.44) and minimum (map 4680 = 2008.82). See also Table 5.2 for further information about the single maps. The ZDI fits are indicated by the solid red line and the fitted Stokes V profiles by the black solid line. Additionally, I plotted the noise-free Stokes V profiles of the input map as blue dashed line. The three maps were fitted with a reduced $\chi^2 = 1.1 - 1.2$. The best fit with reduced $\chi^2 = 1.05$ was achieved for map 0945. The ZDI maps are fitted with $\chi^2 \leq 1.8$ with one exception: map 1665 was only able to fit with a reduced $\chi^2 = 2.7$. Map 1665 obtains also the highest number of sunspots. I noticed that the Stokes V amplitude decreases around activity maximum. These maps are therefore more strongly affected by the noise.

Figures 5.4–5.6 display the Mollweide projected maps for the radial (top), azimuthal (middle) and meridional field (bottom) for the three Stokes V timeseries in Fig. 5.3. The maps in

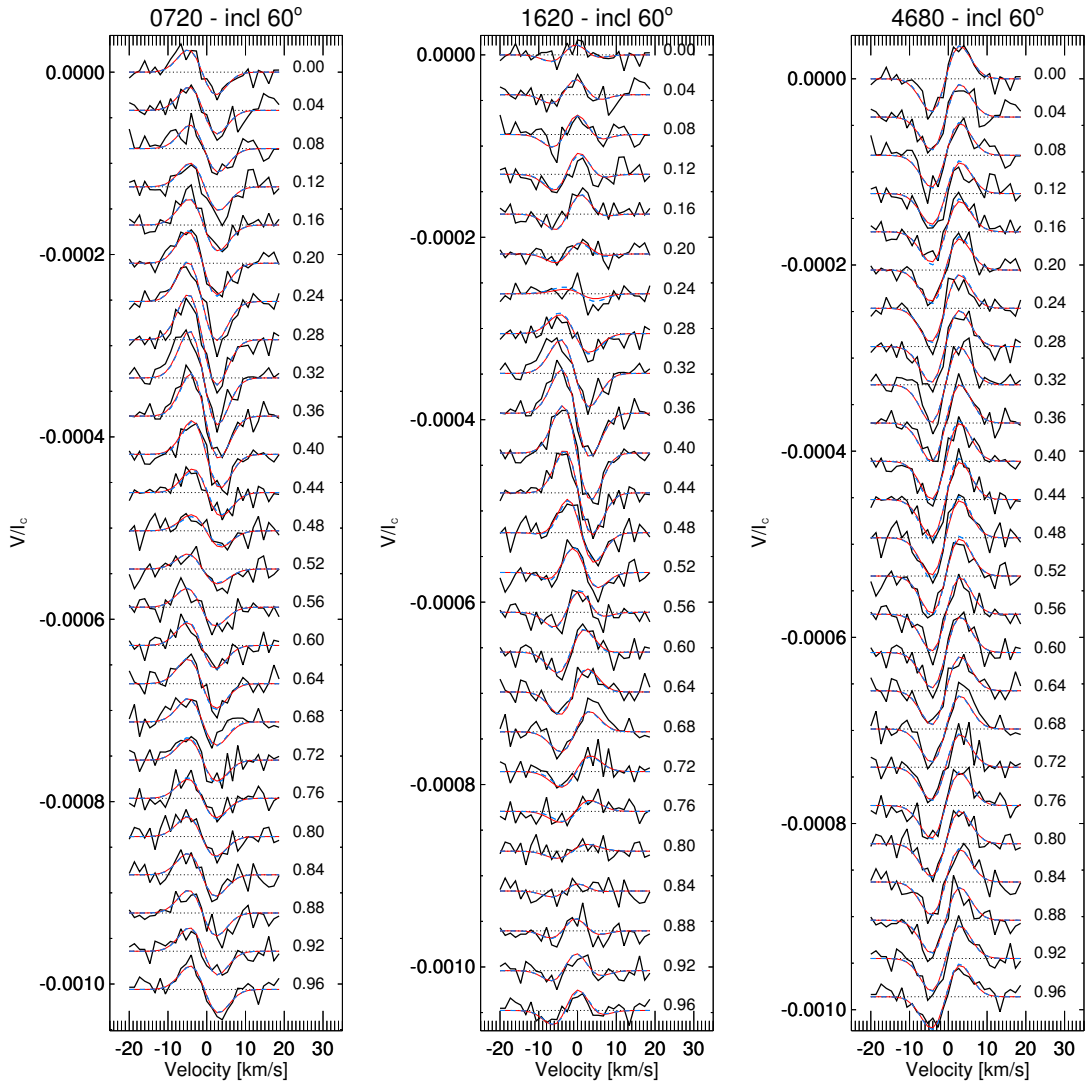

Figure 5.3: Three examples of Stokes V timeseries for the maps 0720 (this corresponds to year 1997.97), 1620 (2000.44) and 4680 (2008.82) from left to right. The ZDI fit (red solid line) of the noisy Stokes V profiles (black solid line), overplotted by the noise-free Stokes V profile (dashed blue line). The dashed black line is the null line and phases are written to the right.

the left column are the full resolved simulations from which I modelled Stokes V profiles. The next two columns show the large-scale field for $\ell_\Sigma = 7$ and 5 of the simulation. The last column shows the ZDI reconstructed maps. The ZDI reconstructed maps are most of the time in better agreement with $\ell_\Sigma = 5$. They are even a bit less structured, see e.g. Fig. 5.4. During the activity maximum with high SSN the ZDI maps are clearly less structured but capture the main features of the large-scale field, see e.g. Fig. 5.5. ZDI is restricted by an inclination angle of 60°, which prevents the complete detection of the southern hemisphere magnetic field. The maps show therefore very few structures below 30°S. ZDI reconstructs the dipole dominated field very well during the activity minimum, see Fig. 5.6. Fig. 5.6 shows also very well that the large-scale field and therefore also ZDI is mostly blind for single bipolar sunspots.

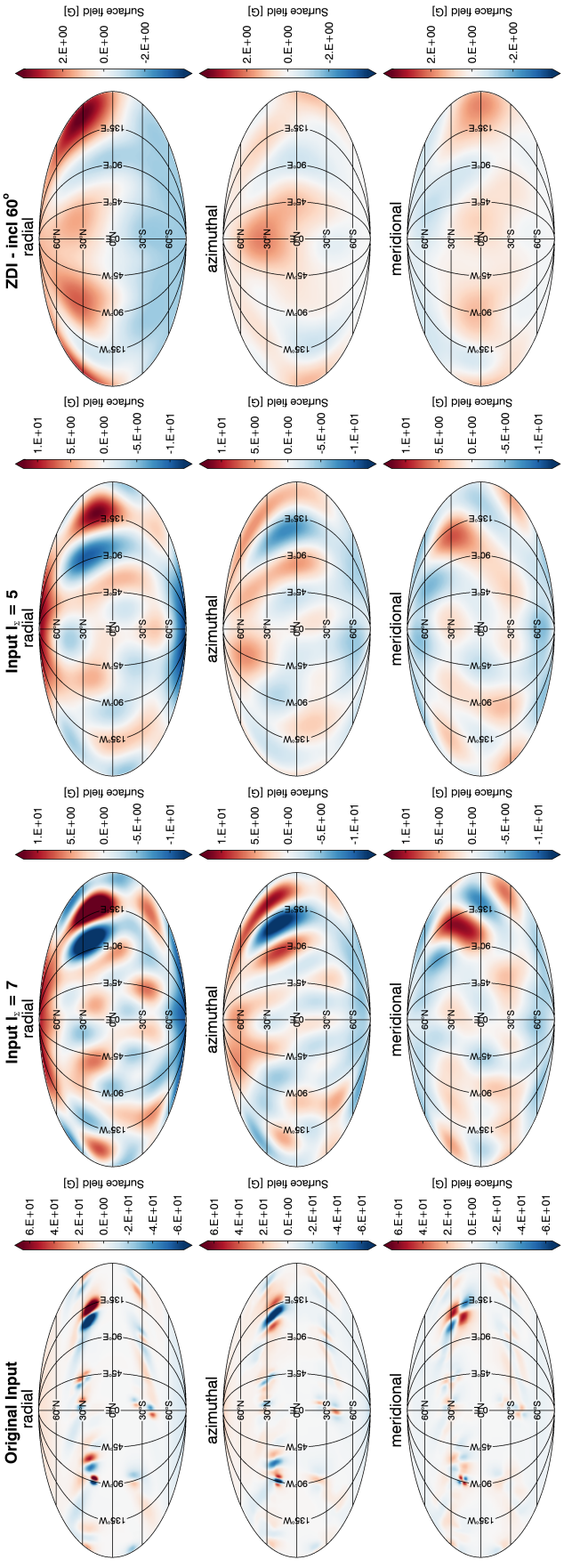

Figure 5.4: The Mollweide projected maps for 0720 = 1997.97. From left to right: Full resolved input map of the simulations, the large-scale field of the input map for $\ell_\Sigma = 7$ and 5 and the ZDI reconstructed map. From top to bottom: the radial, azimuthal and meridional surface magnetic field. Be aware of the different colour bars.

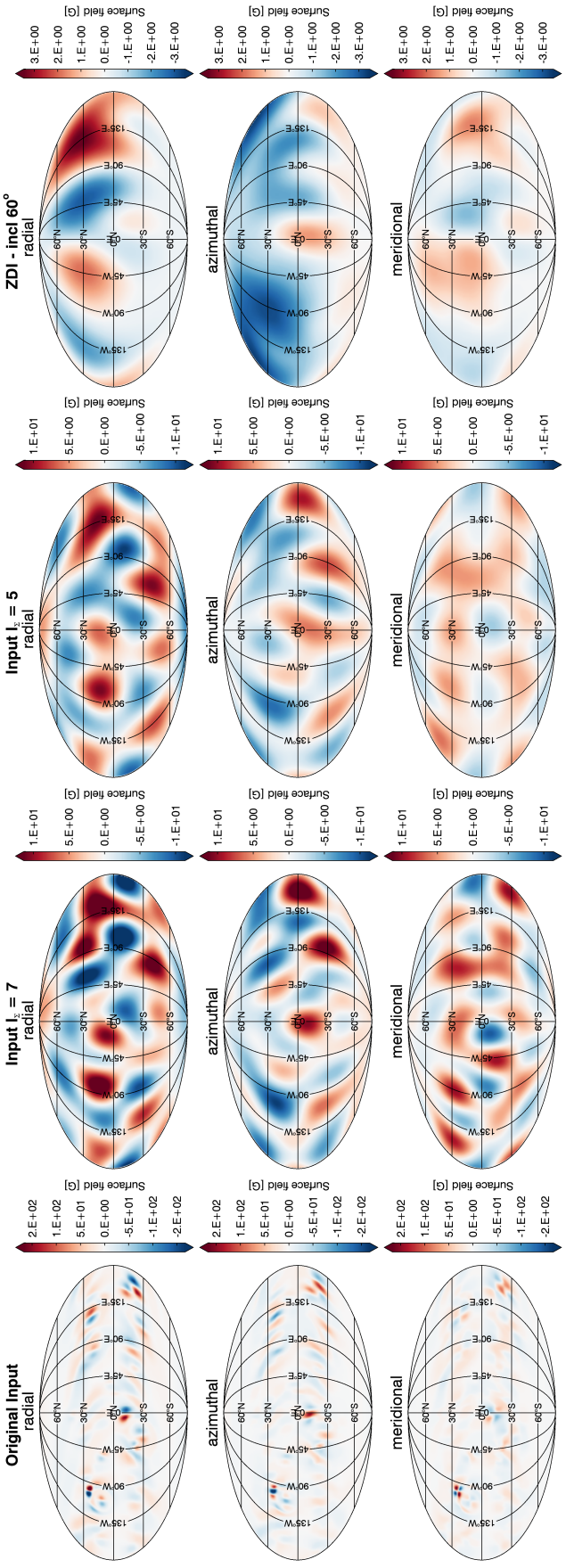

Figure 5.5: The Mollweide projected maps for 1620 = 2000.44. The same format as for Fig. 5.4 is used.

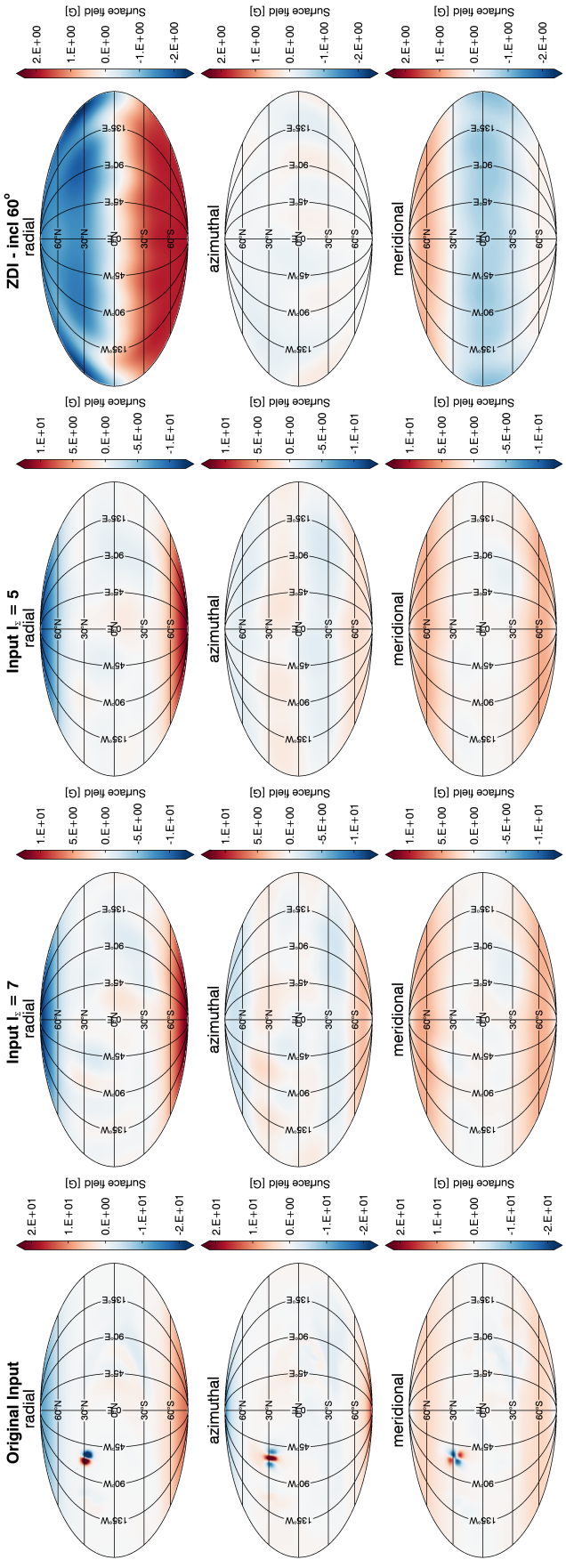

Figure 5.6: The Mollweide projected maps for 4680 = 2008.82. The same format as in Fig. 5.4 is used.

To observe a stellar magnetic cycle with 41 successful observations is also very unlikely even for the longer solar-like cycles. I developed a statistical analysis to mimic 8 observations per cycle. I divided the timescale of the simulated cycle into eight bins equally spaced in time. As the selected 41 maps are not equally spaced in time, it appears that some bins contain a higher number of maps than others. The sixth column in Table 5.2 refers to the bin number of each map. I randomly select one map per bin, which means that e.g. the three maps of bin number 7 are more often selected than the seven maps in bin number 1. This reflects the fact that I selected around half of the maps around the activity maximum, where the large-scale field topology of the simulated maps shows a higher variability, see Section 5.3.2 of further details. I repeated the draw of the 8 maps (one map per bin) 100 times and calculated the mean and standard derivation per bin for the different magnetic field parameters. This gives an estimation about the magnetic field parameter range per bin along the cycle.

5.3 The magnetic field topology along the activity cycle and its discussion

I present the results of the analysis of the 118 simulated surface magnetic field maps for the solar cycle 23 (SC23) and of their 41 ZDI reconstructed maps. The simulated maps of SC23 and their ZDI reconstructions are compared with other cool stars observations in Section 5.3.1. How the magnetic field parameters evolve along the magnetic cycle is analysed in Section 5.3.2. Furthermore, I compare the simulations of SC23 with the observations of SC24 in Section 5.3.3.

5.3.1 The solar cycle in context of cool stars observations

To compare the large-scale field topology of the simulations with their ZDI reconstructions I used the so called “confusogram” (based on Donati et al. 2008b, fig. 14). Figure 5.7 presents the total magnetic energy $\langle B^2_{\rm tot} \rangle$ by symbol size, the fraction of the poloidal field by symbol colour and the axisymmetric poloidal fraction by symbol shape (see Chapter 2.1 for the definitions) for the 41 simulations (Fig. 5.7a,b) and their ZDI reconstructions (Fig. 5.7c,d). All four plots use the same scale, see legend on the right. The mean squared flux density is often referred as magnetic energy $\langle B^2 \rangle [\mathrm{G}^2]$, see Section 2.1, page 33. For the ZDI reconstructed maps $\langle B^2 \rangle [\mathrm{G}^2]$ is restricted to the net magnetic flux of the resolution elements. To be consistent with my previous paper and for an easier reading, I will refer to the mean squared flux

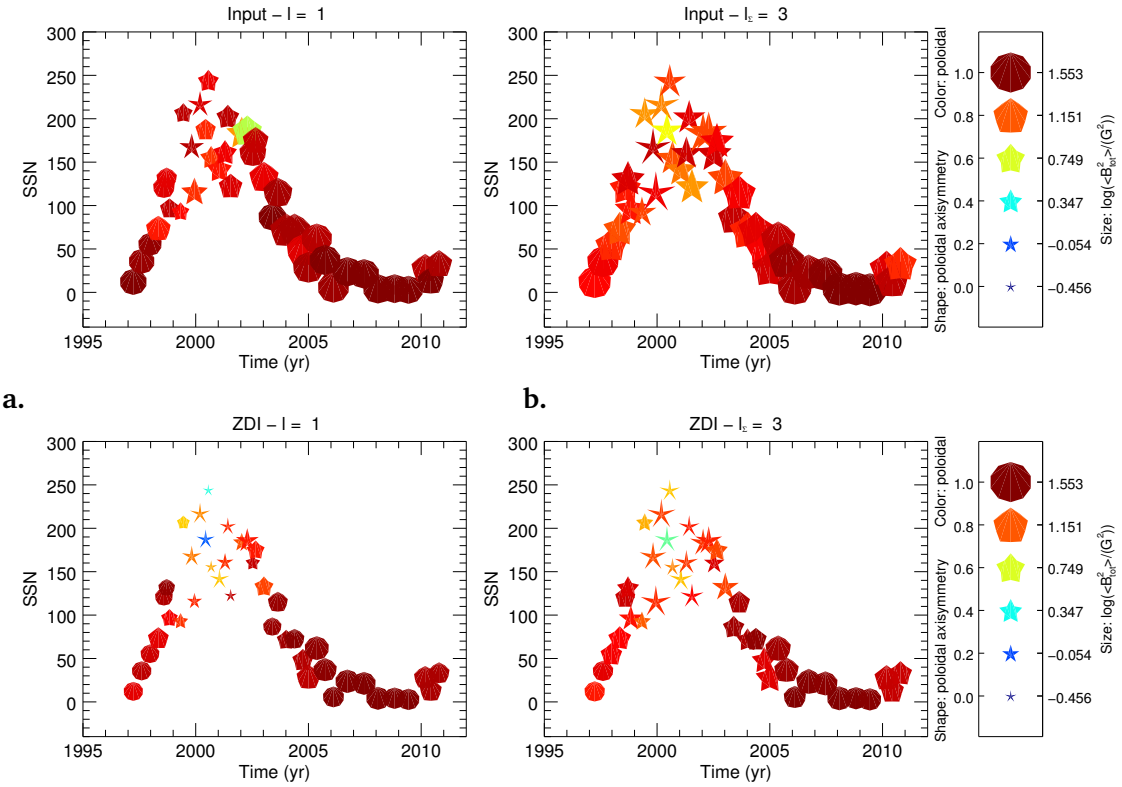

Figure 5.7: The large-scale magnetic field topology for the 41 simulated maps (**a.**, **b.**) and their ZDI reconstructed maps (**c.**, **d.**). The dipolar mode $\ell = 1$ (**a.**, **c.**) and the cumulative $\ell_\Sigma = 3$ mode (**b.**, **d.**) are presented. The y-axis indicates the sunspot number (SSN) and the x-axis the time in years. The symbol size displays the logarithmic total magnetic energy $\langle B^2_{\rm tot} \rangle$. The symbol colour the fraction of the poloidal field $f_{\rm pol}$ and the symbol shape the fraction of the axisymmetric poloidal field $f_{\rm axi,pol}$. See also legend on the right.

density as magnetic energy. I present the dipolar and cumulative $\ell_\Sigma = 3$ mode, see Fig. 5.7a,c and b,d. The simulations show the expected evolution with SSN (compare with Fig. 1.7). The topology and SSN change rapidly during the activity maximum around 2001, see Fig. 5.7a. The dipolar mode shows a varying, but in general lower, $f_{\rm pol}$ and $f_{\rm axi,pol}$ in that phase. During the minimum phase between 2008–2010 the dipole is strongly poloidal and axisymmetric poloidal. The cumulative $\ell_\Sigma = 3$ mode shows higher magnetic energies than the dipolar mode as expected. The $\ell_\Sigma = 3$ mode displays a lower $f_{\rm pol}$ as the quadrupolar mode is included, which shows the lowest $f_{\rm pol}$, see Fig. 5.7b. The $f_{\rm axi,pol}$ is lower compared to the dipolar mode during the activity maximum and $f_{\rm axi,pol}$ decreases with increasing SSN. At activity maximum the topologies are less poloidal and less axisymmetric poloidal, and additionally huge changes happen on short time scales. This is all known from solar observations (see Section 1.5.1) and the simulations represent them very well. The unique features of the SC23 like the extended decreasing phase and the long minimum are well captured by the simulations.

The large-scale magnetic field energy $\langle B^2_{\rm tot}\rangle$ recovered by ZDI is lower for every map in all ℓ_Σ-modes, see Fig. 5.7c,d. During the activity maximum ZDI maps show lower poloidal and axisymmetric poloidal fractions than the input maps. The topology of the activity minimum is very well recovered. The best agreement between the simulated input maps and their ZDI reconstructed maps is achieved for $\ell_\Sigma = 3$, see Fig. 5.7b,d. In general, ZDI seems to recover the large-scale field topology very well for SSN < 100 with the exception of the lower total magnetic energy. The simpler the field topologies with lower SSN become, the easier ZDI recovers the large-scale topology.

Figure 5.8 displays the surface averaged magnetic field $\langle B_{\ell_\Sigma=5}\rangle$ including ℓ_Σ-modes up to $\ell_\Sigma = 5$ against sunspot number (SSN), where the symbols are also colour-coded by the SSN. This will allow an easier comparison with further figures in this chapter. The circles indicate the simulations. The 41 maps that have a ZDI reconstructed map are plotted with a black border. The ZDI reconstructed maps are displayed as triangles. For the simulated maps $\langle B_{\ell_\Sigma=5}\rangle$ increases linearly with SSN by showing a relatively wide spread. The slope determined via a least-squares best fit is

$$\langle B_{\ell_\Sigma=5}\rangle = 3.0026\,\mathrm{G} + 0.0165\,\mathrm{G}\cdot\mathrm{SSN}. \tag{5.2}$$

The large-scale field of the simulations increases with an enhanced amount of the small-

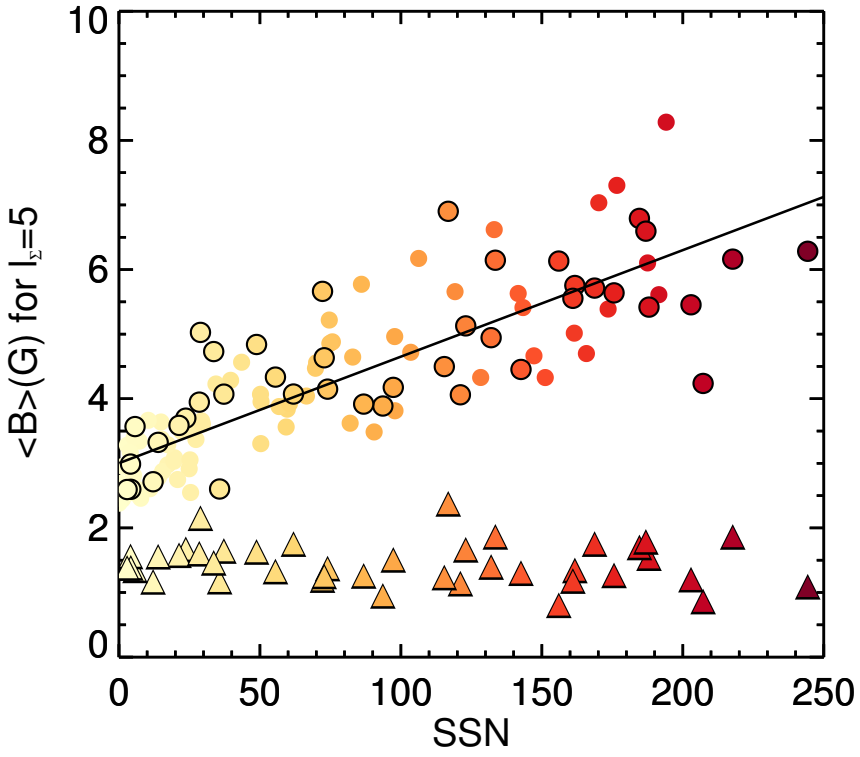

Figure 5.8: The surface averaged large-scale magnetic field $\langle B \rangle$ including $\ell_\Sigma = 5$ plotted against sunspot number (SSN). The simulated input maps are displayed as circles, where the 41 maps that have a ZDI reconstructed map are ringed with a black border. The ZDI reconstructed maps are plotted as triangles. The black line indicates the linear fit through the simulations. Additionally, the symbols are colour-coded by SSN (x-axis) for an easier comparison with further figures in this Chapter.

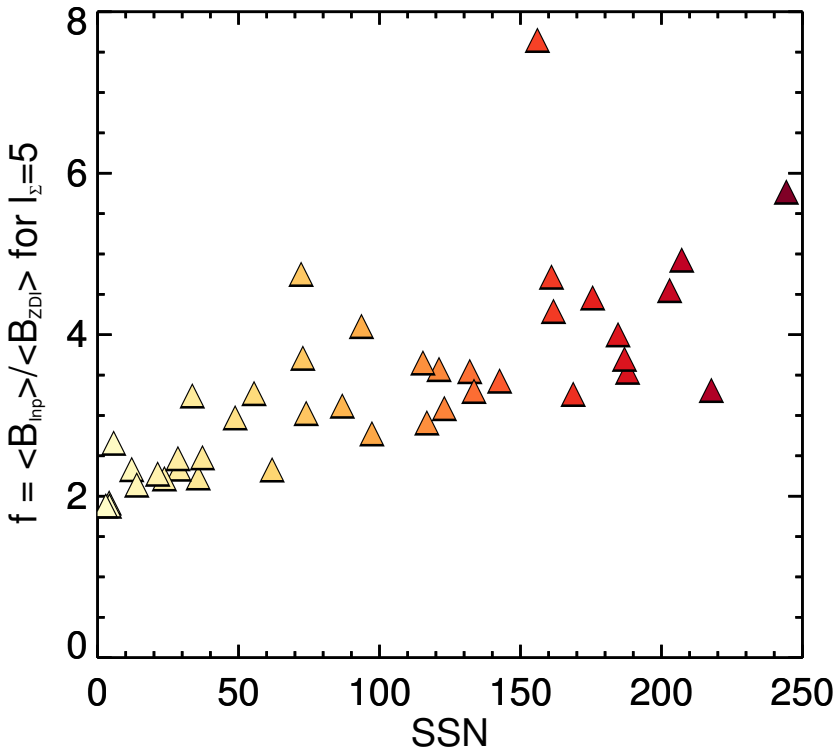

Figure 5.9: The surface averaged magnetic field of the large-scale field including $\ell_\Sigma = 5$ of the simulated maps divided by their ZDI reconstructed maps $f = \frac{\langle B_{\ell_\Sigma=5,\mathrm{Inp}}\rangle}{\langle B_{\ell_\Sigma=5,\mathrm{ZDI}}\rangle}$ against SSN. The symbols are colour-coded by SSN.

scale field structures like star spots. This allows only a rough estimation of the star spot coverage due to the large spread and shallow slope. Far more interesting is if ZDI recovers this trend. This is not the case. The surface averaged large-scale magnetic field $\langle B_{\ell_\Sigma=5}\rangle$ is constant with SSN and shows values between $\langle B_{\ell_\Sigma=5}\rangle = 0.8 - 2.4\,\mathrm{G}$. The large-scale field recovered by ZDI is again lower than the field of the input maps. That $\langle B_{\ell_\Sigma=5}\rangle$ is independent of SSN indicates that surface averaged magnetic field reconstructed by ZDI is blind for the small-scale field in star spots. The ZDI determined $\langle B_{\ell_\Sigma=5}\rangle$ allows therefore no estimation about the spot coverage.

Figure 5.9 shows the ratio f of the surface averaged large-scale field of the simulated input maps $\langle B_{\ell_\Sigma=5,\mathrm{Inp}}\rangle$ divided by $\langle B_{\ell_\Sigma=5,\mathrm{ZDI}}\rangle$ of the ZDI reconstructed maps, $f = \frac{\langle B_{\ell_\Sigma=5,\mathrm{Inp}}\rangle}{\langle B_{\ell_\Sigma=5,\mathrm{ZDI}}\rangle}$, against SSN. There is a more or less linear increase but it has a wide spread. I would therefore not recommend to use f as correction factor for ZDI maps especially as the equivalent of the SSN of observed stars other than the Sun is unknown. Further this is an estimation based on the Sun and we do not know if this relation is also true for other cool stars.

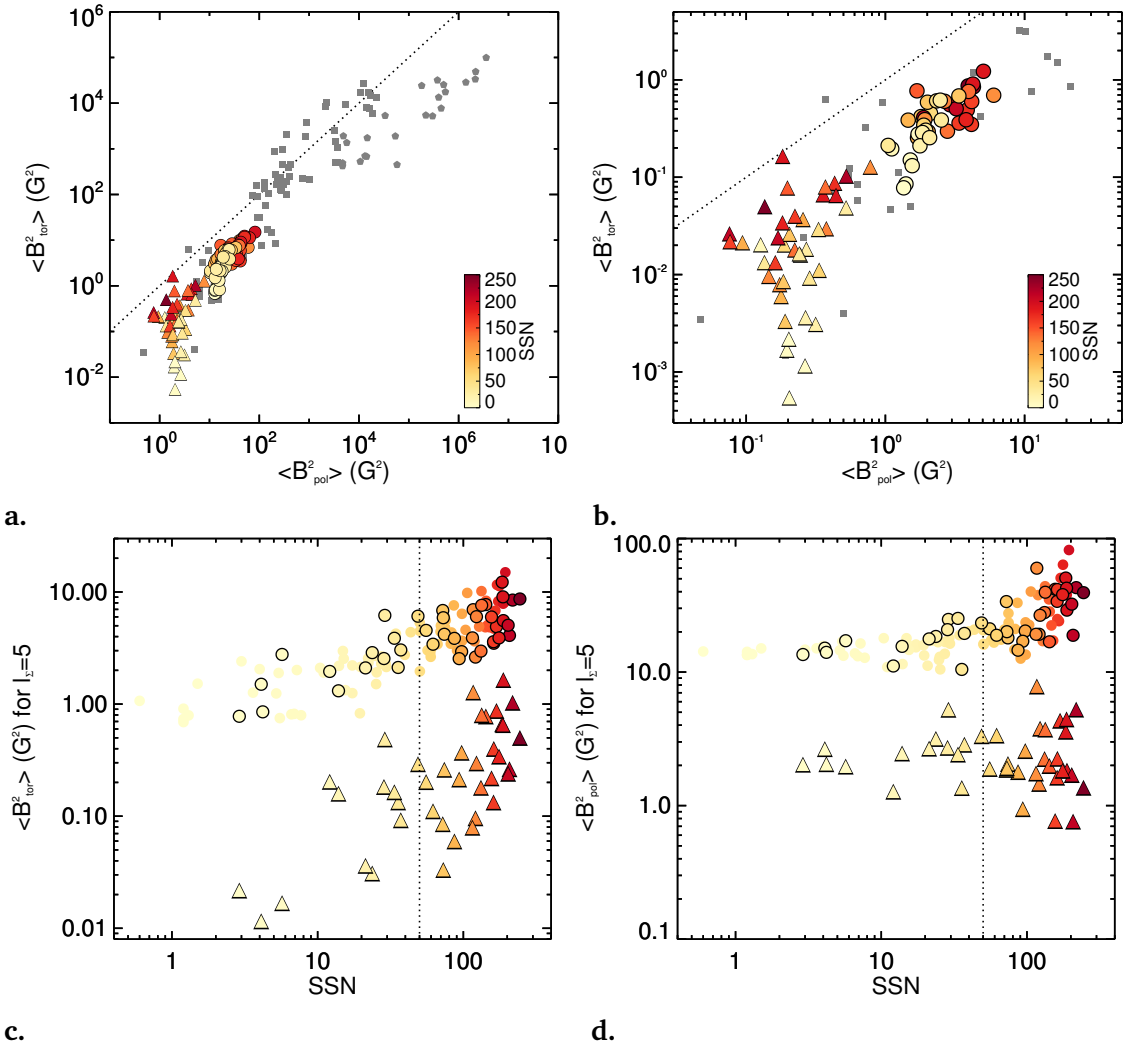

Figure 5.10: Top row: The magnetic energy of the toroidal field $\langle B^2_{\rm tor}\rangle$ against the poloidal field $\langle B^2_{\rm pol}\rangle$. The observed stars are displayed by grey symbols, where stars with masses equal or higher than $0.5\,M_\odot$ are plotted as squares otherwise as pentagons. The simulated maps of solar cycle 23 (circles) and their ZDI reconstructed maps (triangles) are colour-coded by sunspot number (SSN) and displayed for $\ell_\Sigma = 5$, see legend on the right. **a.** Shows the whole range given by the cool stars observation. All 118 maps of the simulated solar cycle are plotted (circles) and the 41 ZDI maps (triangles). **b.** Only the 41 simulated maps and their ZDI reconstructions are displayed. Bottom row: The toroidal $\langle B^2_{\rm tor}\rangle$ **(c.)** and poloidal $\langle B^2_{\rm pol}\rangle$ **(d.)** magnetic energy against SSN for the cumulative $\ell_\Sigma = 5$. The dashed line indicates SSN = 50.

To compare the large-scale field of the solar cycle simulations with the cool star observations I used again the format of the toroidal $\langle B^2_{\rm tor}\rangle$ against the poloidal magnetic energy $\langle B^2_{\rm pol}\rangle$, see Fig. 5.10a. The solar cycle simulations with a higher SSN are at the same parameter range as the simulated Sun of Chapter 3 and 4. They were expected to be consistent with the solar maps in Chapter 3 and 4 which are based on solar observations around the activity maximum showing a high SSN. The ZDI reconstructions are again offset by a bit more than one order of magnitude in the toroidal and poloidal energy. Maps with low SSN show an even higher offset for $\langle B^2_{\rm tor}\rangle$. This can be best seen in Figure 5.10b. For SSN below $\approx$ 50 the toroidal magnetic energy drops suddenly while the poloidal energy is constant, see Fig. 5.10c,d. This trend is recovered by ZDI. In other words: for SSN $>$ 50 $\langle B^2_{\rm tor}\rangle$ and $\langle B^2_{\rm pol}\rangle$ follow the power law relation $\langle B^2_{\rm tor}\rangle \propto \langle B^2_{\rm pol}\rangle^{0.8\pm0.3}$. Below this limit $\langle B^2_{\rm pol}\rangle$ stays constant and only $\langle B^2_{\rm tor}\rangle$ decreases further with SSN. The higher the SSN, the higher $\langle B^2_{\rm tor}\rangle$, which underlines that the large-scale toroidal field energy is driven to a significant degree by the magnetic energy of small-scale field structures like sunspots. Small-scale field structures can contribute to the large-scale poloidal field $\langle B^2_{\rm pol}\rangle$ for SSN $>$ 50 but do not have to, see Fig. 5.10d. The lower limit of the large-scale poloidal energy $\langle B^2_{\rm pol}\rangle$ ($\approx 10\,{\rm G}^2$) is most likely given by the global dipolar field. For high SSN the global dipolar field is near zero, so that the power law relation might be mainly given by small-scale field emergences. The ZDI reconstructed maps show again a wider spread than the input maps but be aware of the log-log scale. The trends with SSN are reasonably well recovered by ZDI.

Furthermore, I plot the fraction of the axisymmetric field against the fraction of the toroidal field similar to Fig. 3.10a and 4.6a in Chapter 3 and 4 using the same definitions, see Eqs. 2.21 and 2.22. The axisymmetry decreases with SSN. ZDI recovers this trend but tends to underestimate the toroidal fraction for lower SSN. For higher SSN the toroidal fraction is overestimated for a few maps. The simulations with high SSN cover again the same region as the solar simulations in the previous Chapters 3 and 4.

To summarise ZDI recovers the magnetic field topology best for SSN below 100. For low SSN, the toroidal energy drops while the poloidal energy stays constant and with increasing SSN the axisymmetric fraction decreases. Both trends are recovered by ZDI but the ZDI reconstructed maps show more than one order of magnitude less toroidal and poloidal energy. ZDI is also blind for the increase of the large-scale surface averaged magnetic field $\langle B_{\ell_\Sigma=5}\rangle$ with SSN and shows only constant values for $\langle B_{\ell_\Sigma=5}\rangle$ independent of SSN.

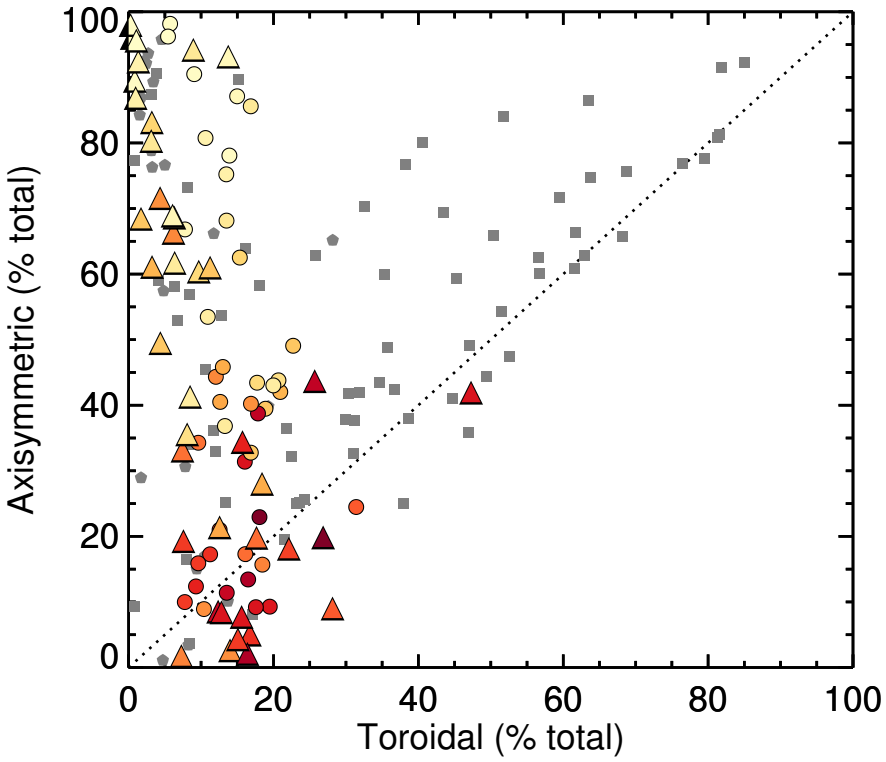

Figure 5.11: The fraction of the axisymmetric $f_{\rm axi}$ against the fraction of the toroidal field $f_{\rm tor}$ for the 41 maps of the simulated solar cycle and their ZDI reconstructed maps for $\ell_\Sigma = 5$. The same format as in Fig. 5.10b is used. The dashed line indicates the unity line.

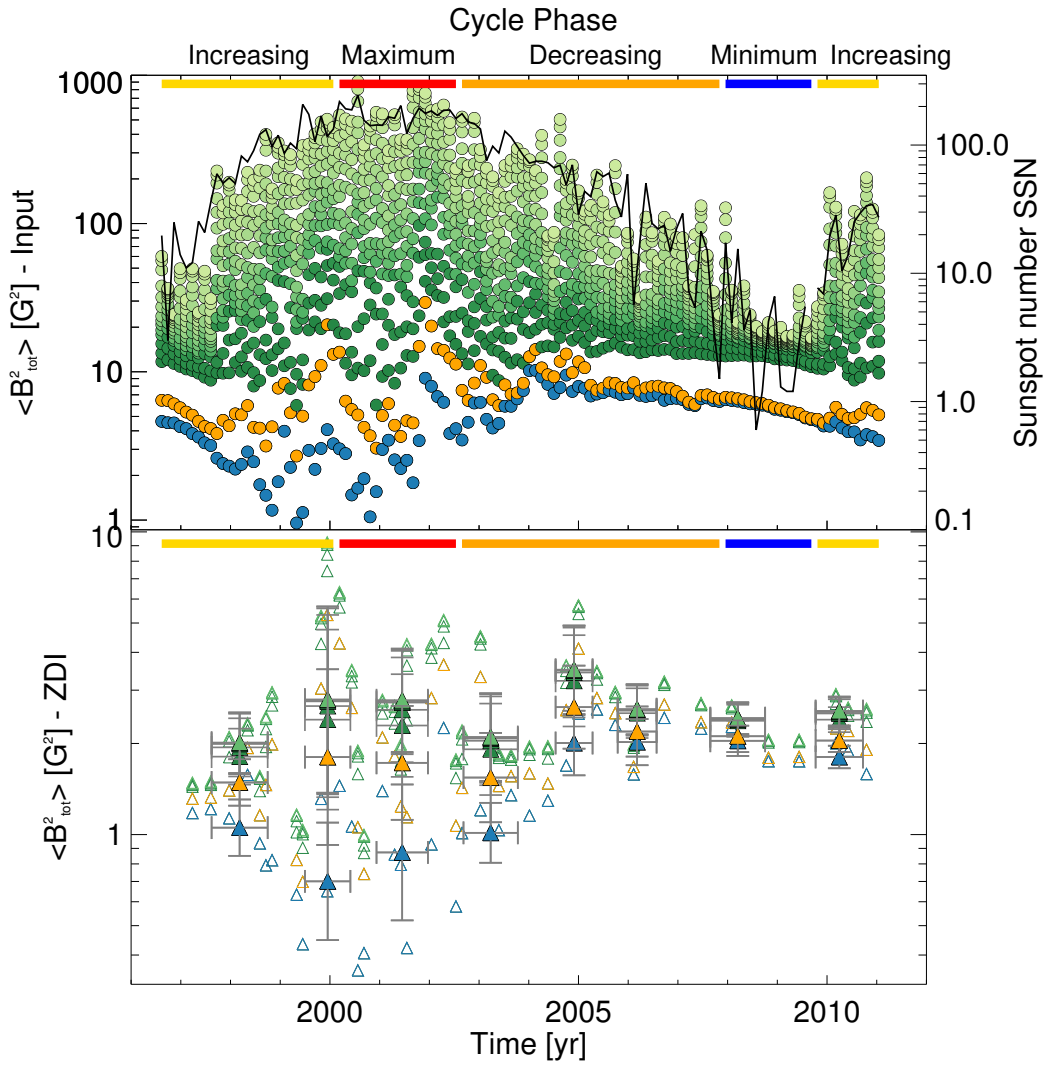

Figure 5.12: The total magnetic energy $\langle B^2_{\rm tot}\rangle$ against time for the cumulative ℓ_Σ-modes. The corresponding cycle phases are indicated by the coloured thick lines at the top of each plot. Top: All 118 simulated maps of solar cycle 23. The dipole mode $\ell = 1$ is blue, the quadrupolar mode $\ell_\Sigma = 2$ is orange and all higher cumulative modes $\ell_\Sigma = 3-28$ are plotted as greenish circles, where the colour lightens with ℓ_Σ–mode. The sunspot number is overplotted as black line, see y-axis on the right. Bottom: All 41 ZDI reconstructed maps (open triangles) and their binned mean (filled triangles) and standard derivation (error bars) for $\ell_\Sigma = 1-7$. The same colour schema as the top panel is used.

5.3.2 The variation of the magnetic field properties along the cycle

In this section I examine how certain magnetic field properties evolve along the solar cycle and if ZDI is able to recover these trends.

First, I analyse the total magnetic energy $\langle B^2_{\rm tot}\rangle$. Figure 5.12 top shows $\langle B^2_{\rm tot}\rangle$ against time for the 118 simulations for the cumulative ℓ_Σ–modes $\ell_\Sigma = 1-28$ using the same colour scheme as previous figures, e.g. see Fig. 3.2. The SSN is overplotted as the black line. The

total magnetic energy of the high cumulative ℓ_Σ-modes $\ell_\Sigma \approx 28$ follow the SSN distribution. They contain the magnetic energy of the large and small-scale field. The low ℓ_Σ–modes, which are only sensitive to the large-scale field, show a discrepancy with the SSN trend. The dipolar mode $\ell = 1$ (blue circles) decreases during the increasing cycle phase, is minimum at activity maximum and rises rapidly at the beginning of the decreasing phase before a slow decrease starts. The dipolar mode of the simulations follows therefore the trend of the observations published by DeRosa et al. (2012). The solar dipolar field weakens during the increasing phase until it vanishes at the beginning of the activity maximum. After that the dipolar field rises again showing the opposite polarity with the beginning of the decreasing phase. The quadrupolar field follows the SSN trend: it increases during the increasing phase, is maximum at activity maximum and decreases until activity minimum. This is similar to the result based on solar observations by DeRosa et al. (2012). The $\ell_\Sigma = 2$ shows also the double peak feature during the maximum phase, which is hard to see for the SSN on the log-scale, see alternatively Fig. 1.7. The large-scale field of the simulations and also the total field including the small-scale structures behave as expected from the solar observations, see e.g. DeRosa et al. (2012); Kakad et al. (2019).

Fig. 5.12 bottom displays the 41 ZDI reconstructed maps (empty triangles). The mean and standard derivation of the statistical analysis for the 8 bins[4] are plotted as filled triangles. Be aware of the different range of the $\langle B^2_{\rm tot}\rangle$-axes for the top and bottom panel. The ZDI maps are only sensitive to the large-scale field, so that only the first seven ℓ_Σ-modes are plotted using the same colour-scheme as on the top panel. The total magnetic energy $\langle B^2_{\rm tot}\rangle$ of the ZDI maps is approximately one order of magnitude lower compared to the input maps as seen in Fig. 5.10a. They show a large spread during the activity maximum. I do not recommend to use $\langle B^2_{\rm tot}\rangle$ to estimate the cycle phase or even to detect activity cycles on stars similar to our Sun. If necessary the best tracer would be the dipolar mode as this mode shows the largest variability along time. All higher modes are, on average over several maps, more or less constant along the cycle.

Figure 5.13 shows three examples of 8 randomly selected maps (one map per bin). In Fig. 5.13a one would detect the solar-like cycle correctly, in Fig. 5.13b no cycle at all and in Fig. 5.13c a solar-like cycle but offset in phase or in anti-phase.

[4]Details were described in Section 5.2.2 at page 137.

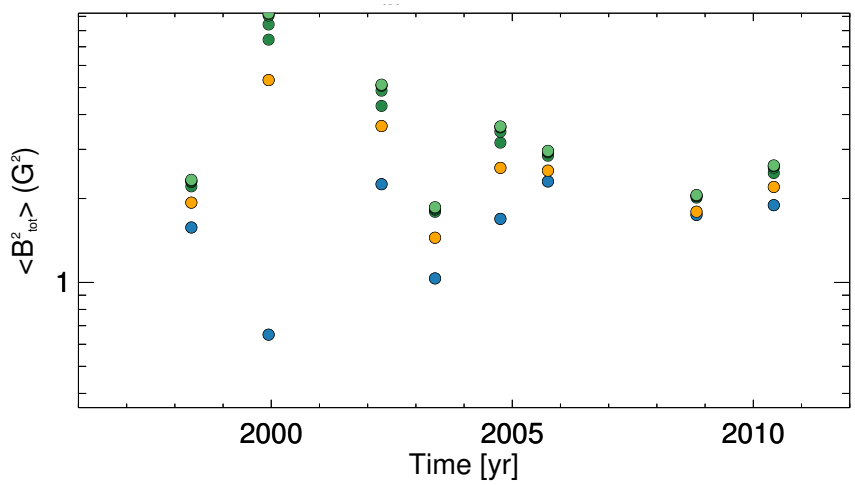

a.

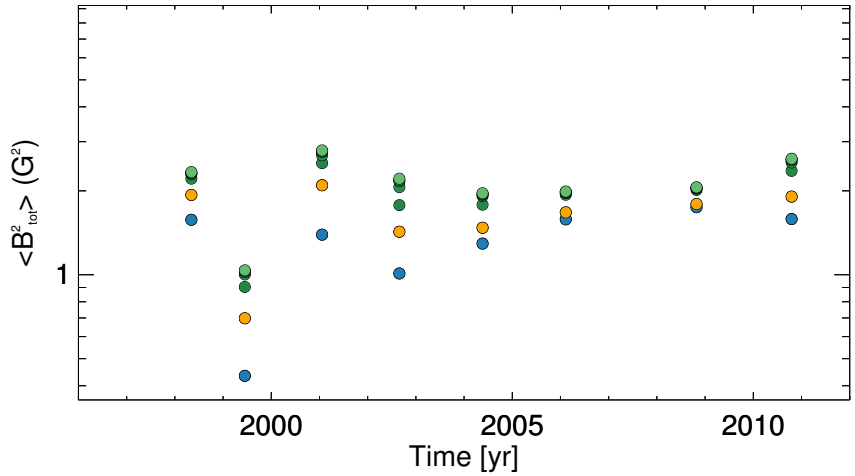

b.

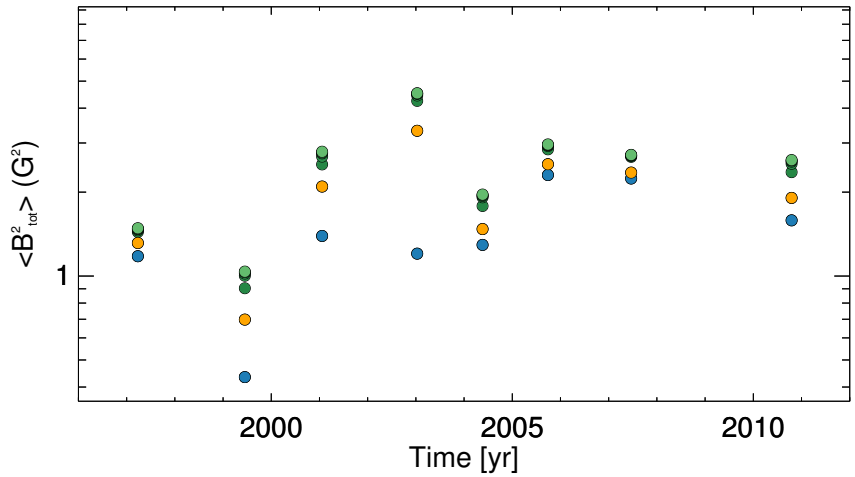

c.

Figure 5.13: The draw of 8 ZDI reconstructed maps (one map per bin) and their total magnetic energy $\langle B^2_{\rm tot} \rangle$ against time. The same colour-scheme is used as in Fig. 5.12. An example for the interpretation of the solar cycle correct in phase is shown in **a.** for no cycle in **b.** and for a cycle in anti-phase or offset in phase in **c.**

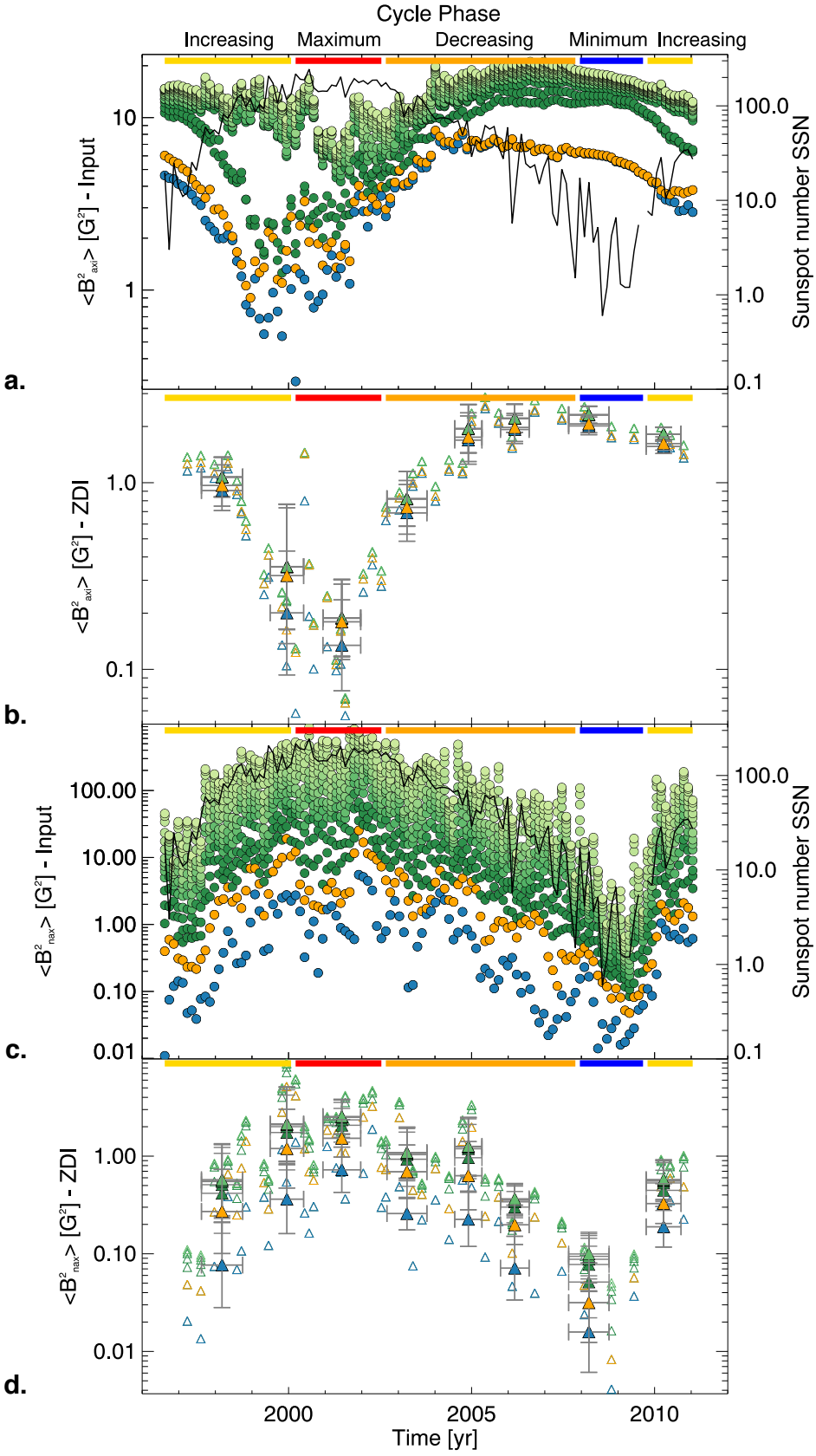

Figure 5.14: The axisymmetric $\langle B^2_{\rm axi}\rangle$ (**a.**, **b.**) and the non-axisymmetric $\langle B^2_{\rm nax}\rangle$ magnetic energy (**c.**, **d.**) for all 118 simulations (**a.**, **c.**) and the 41 ZDI reconstructed maps (**b.**, **d.**). The same format as in Fig. 5.12 is used.

To find solar cycles or to estimate the cycle phase for solar-like stars from ZDI observations one needs to determine and analyse the different components of the magnetic field. I found that the analysis of the axisymmetric and non-axisymmetric component are most promising. Figure 5.14 shows the axisymmetric $\langle B^2_{\rm axi}\rangle$ (Fig. 5.14a,b) and non-axisymmetric $\langle B^2_{\rm nax}\rangle$ magnetic energy (Fig. 5.14c,d) against time using the same format as in Fig. 5.12. The low ℓ_Σ-modes of the simulations show a clear minimum during the activity maximum and a broad maximum at the end of the decreasing and during the minimum phase for the axisymmetric energy $\langle B^2_{\rm axi}\rangle$, see Fig. 5.14a. The ZDI reconstructed maps recover this trend of the large-scale field very well, see Fig. 5.14b. The non-axisymmetric energy $\langle B^2_{\rm nax}\rangle$ shows the opposite trend with a broader maximum around the activity maximum and sharp minimum during the minimum phase. All ℓ_Σ-modes of the simulations follow this trend, which shows also an excellent agreement with the SSN evolution, see Fig. 5.14c. The large-scale field captured by the ZDI reconstructed maps recovers this trend of the $\langle B^2_{\rm nax}\rangle$ very well, see Fig. 5.14d. The determination of the $\langle B^2_{\rm axi}\rangle$ and $\langle B^2_{\rm nax}\rangle$ for the ZDI reconstructed maps looks more than promising to be a good tracer to discover solar-like cycle. Both parameters show easily distinguishable trends that are well recovered by ZDI. This is supported by the far smaller error bars in Fig. 5.14b,d.

Another magnetic field parameter that allows a very good detection of solar-like cycles is the fraction of the axisymmetric poloidal field,

$$f_{\rm axi,pol,\ell_\Sigma} = \frac{\langle B^2_{m=0,\ell_\Sigma,{\rm pol}}\rangle}{\sum_m \langle B^2_{m,\ell_\Sigma,{\rm pol}}\rangle}. \tag{5.3}$$

Figure 5.15 shows $f_{\rm axi,pol,\ell_\Sigma=7}$ against time for the cumulative $\ell_\Sigma = 7$ for the simulations (top) and ZDI reconstructions (bottom) using the same format as Fig. 5.12. The fraction $f_{\rm axi,pol}$ covers nearly the full range from 0.0 to 1.0 from activity maximum to minimum, which is well recovered by ZDI. The simulations show a rapid decrease during the increasing phase in connection with a broad minimum during the maximum activity phase and a slow nearly linear increase during the decreasing phase, see Fig. 5.15 top. ZDI sees less details of the increasing and decreasing phase but catches clearly the maximum and minimum phase, see Figure 5.15 bottom. In fact $f_{\rm axi,pol}$ is the parameter that is best recovered by ZDI, see Section 4.3.2, which makes $f_{\rm axi,pol}$ to one of the best or the best tracer for solar-like cycles of other observed cool stars. Alternatively, $f_{\rm axi}$ looks nearly the same as it is mostly driven by the axisymmetric poloidal field. The fraction $f_{\rm axi}$ shows a bit more spread and slightly lower/higher

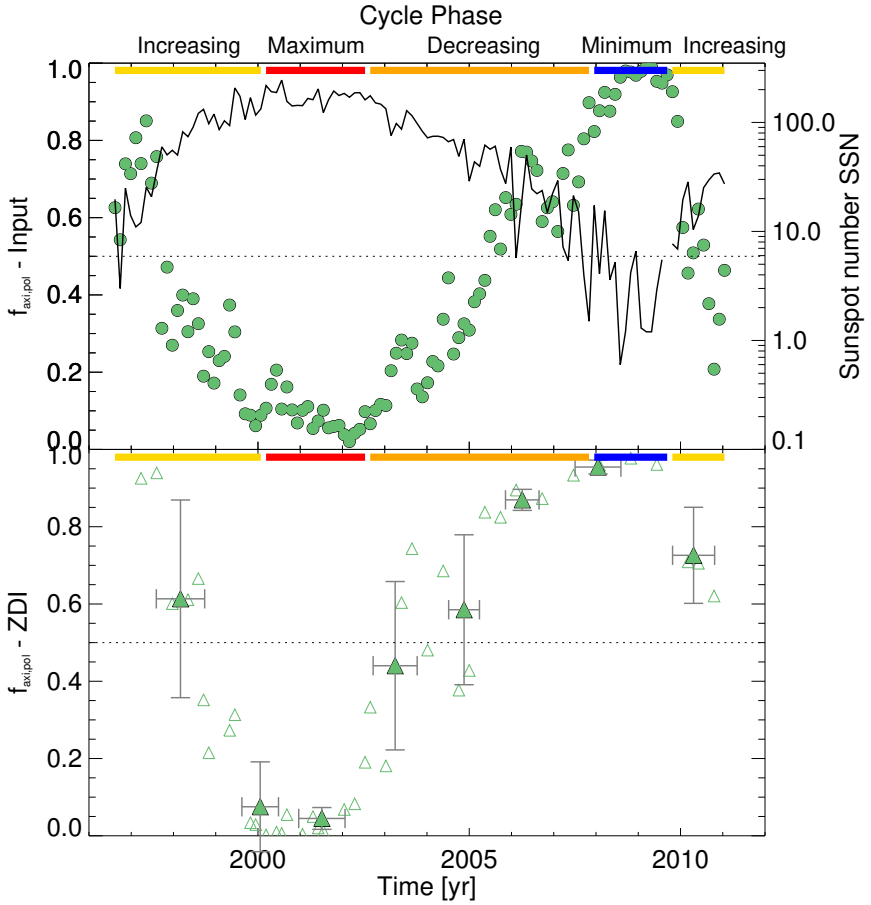

Figure 5.15: The fraction of the axisymmetric poloidal field $f_{\rm axi,pol}$ for the cumulative ℓ_Σ-mode $\ell_\Sigma = 7$. The same format as in Fig. 5.12 is used but only $\ell_\Sigma = 7$ is plotted.

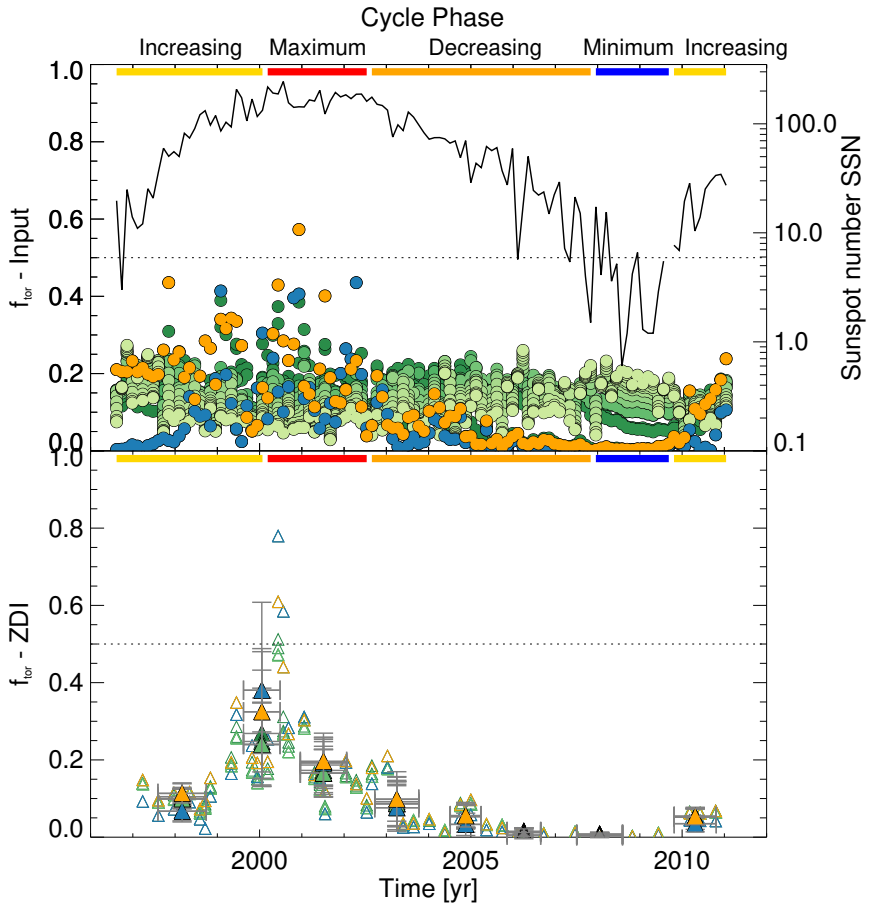

Figure 5.16: The toroidal fraction $f_{\rm tor}$ for the whole range of $\ell_\Sigma = 1-28$ for the simulations and $\ell_\Sigma = 1-7$ for the ZDI reconstructions. The same format as in Fig. 5.12 is used.

maxima/minima due to the contribution of $f_{\rm axi,tor}$ which is less well recovered by ZDI. However, $f_{\rm axi}$ is a very good tracer as well.

The fraction of the toroidal field $f_{\rm tor}$, see Eq. 2.21, is not a suitable tracer for solar-like cycle. Figure 5.16 top shows $f_{\rm tor}$ against time for the cumulative $\ell_\Sigma = 1-28$ of the simulations using the same format as Fig. 5.12. The higher ℓ_Σ-modes ($\ell_\Sigma > 3$) show a mostly flat distribution with time. The dipolar mode (blue circles) and quadrupolar mode (orange circles) show a scattered peak around activity maximum. The values are widely scattered from 0.05 to 0.6 for $\ell_\Sigma = 2$ during that time. The ZDI reconstructed maps follow with all $\ell_\Sigma \leq 7$ modes the trend of the quadrupolar mode but showing less spread and partly lower values. Estimating the cycle phase is therefore difficult as one needs to find the peak around activity maximum which appears in a small time window and obtains only a small amplitude. The Sun is too inactive to use $f_{\rm tor}$ as cycle tracer but the analysis of $f_{\rm tor}$ can be used as additional check to

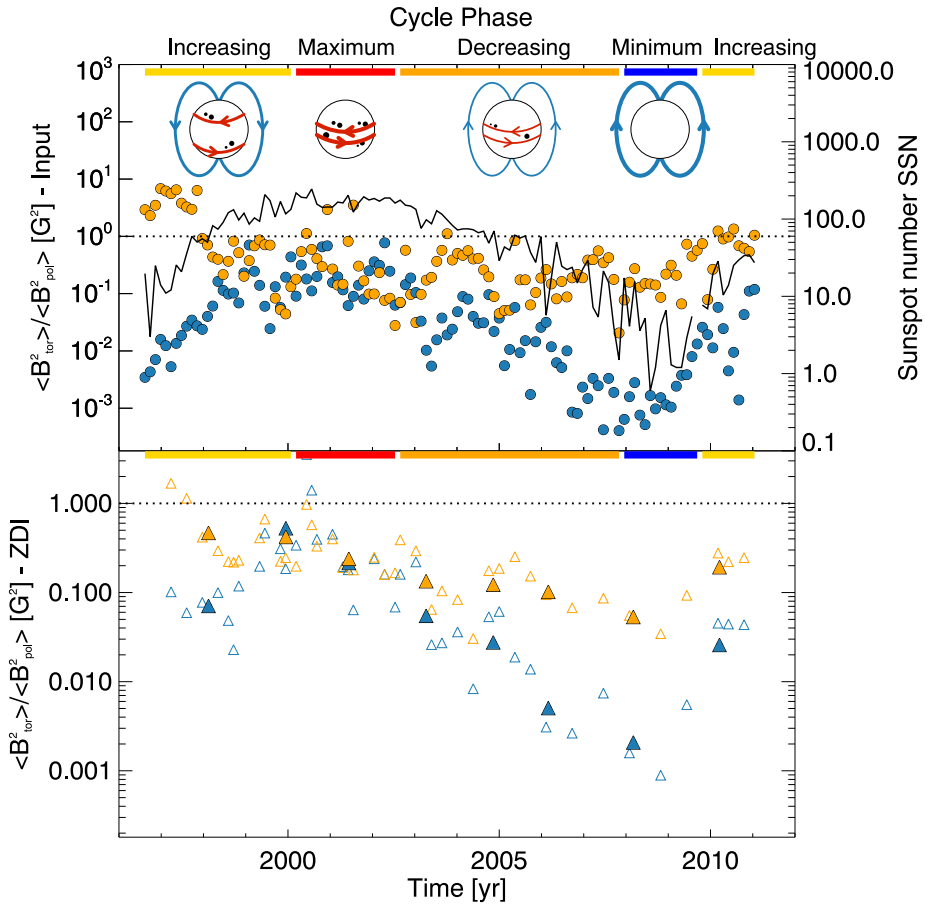

Figure 5.17: The ratio of the toroidal and poloidal magnetic energy $\frac{\langle B^2_{\rm tor}\rangle}{\langle B^2_{\rm pol}\rangle}$ for the dipolar $\ell = 1$ and quadrupolar $\ell = 2$ mode. The four little inserts at the top illustrate how the poloidal dipolar (blue) and toroidal quadrupolar mode (red) vary along the solar cycle. The quadrupolar mode responds to the global properties of the small-scale flux emergence (black dots). The same format as in Fig. 5.12 is used but presenting only the first two single ℓ-modes.

confirm the detection of the activity maximum for the solar-like cycle.

After finding good tracers to detect solar-like cycles I want to focus once more on the analysis of the large-scale field and what it might tell us about the small-scale field distribution for the specific case of our Sun. Figure 5.17 displays the ratio of the toroidal and poloidal magnetic energy $\frac{\langle B^2_{\rm tor}\rangle}{\langle B^2_{\rm pol}\rangle}$ for the single ℓ-modes $\ell = 1$ and 2 using the same format as Fig. 5.12. The dashed line indicates when the toroidal energy dominates. The $\frac{\langle B^2_{\rm tor}\rangle}{\langle B^2_{\rm pol}\rangle}$ of the dipolar and quadrupolar mode reflects the evolution of the global dipole (mainly poloidal) and of global properties of the small-scale flux emergence pattern (possible sources of toroidal field) with time. The four little inserts at the top of Fig. 5.17 illustrate the behaviour of the dipole (blue arrows) and of the global properties of the small-scale flux emergence (red arrows) during the

four phases of the solar cycle. The top panel of Fig. 5.17 displays the result for the simulations. During the increasing phase the global dipole is still strongly poloidal but weakens while the sunspots appear at mid latitudes. The sunspots or active regions in general are best captured by the toroidal quadrupolar mode, see also Chapter 3. This is reflected by a low $\frac{\langle B^2_{\rm tor}\rangle}{\langle B^2_{\rm pol}\rangle}$ for the dipolar mode that increases as the dipole weakens towards the activity maximum and by a very strong quadrupolar $\frac{\langle B^2_{\rm tor}\rangle}{\langle B^2_{\rm pol}\rangle}$ that decreases as the latitude of sunspots emergence migrates towards the equator. When the latitude of sunspots emergence migrates towards the equator during the maximum and decreasing phase, the toroidal quadrupolar mode decreases while the toroidal dipolar mode becomes stronger[5]. The ratio $\frac{\langle B^2_{\rm tor}\rangle}{\langle B^2_{\rm pol}\rangle}$ for $\ell = 2$ is now mostly poloidal dominated. As the poloidal dipole is weak during the activity maximum $\frac{\langle B^2_{\rm tor}\rangle}{\langle B^2_{\rm pol}\rangle}$ for $\ell = 1$ shows its maximum. During the decreasing phase the dipolar mode becomes more and more poloidal dominated as the reversed global dipole establishes and becomes stronger until $\frac{\langle B^2_{\rm tor}\rangle}{\langle B^2_{\rm pol}\rangle}$ $\ell = 1$ reaches its minimum. At the same time the sunspot number decreases which causes a small decrease of $\frac{\langle B^2_{\rm tor}\rangle}{\langle B^2_{\rm pol}\rangle}$ $\ell = 2$ but $\frac{\langle B^2_{\rm tor}\rangle}{\langle B^2_{\rm pol}\rangle}$ shows a large spread as single active regions can have a strong influence on $\frac{\langle B^2_{\rm tor}\rangle}{\langle B^2_{\rm pol}\rangle}$ $\ell = 2$. After the minimum $\frac{\langle B^2_{\rm tor}\rangle}{\langle B^2_{\rm pol}\rangle}$ increases again for $\ell = 2$ as expected but also $\frac{\langle B^2_{\rm tor}\rangle}{\langle B^2_{\rm pol}\rangle}$ for $\ell = 1$ increases. This is caused by an unusual early and rapid increase of the dipolar toroidal energy for SC24 after the long activity minimum 2008–2010. Perhaps the active regions emerged earlier at lower latitudes but this couldn't be confirmed by comparing single maps by eye for the two increasing phases. It might be that there is a connection to the asymmetric polar field reversal reported by Janardhan et al. (2018) after the unusually quiet and long minimum phase. To draw more reliable conclusions further simulations of the increasing phase until the maximum phase and beyond of SC24 are needed.

ZDI is likely to recover the solar evolution of $\frac{\langle B^2_{\rm tor}\rangle}{\langle B^2_{\rm pol}\rangle}$ for $\ell = 1$ and 2 as seen in Fig. 5.17 bottom. Especially, the different characteristics of $\frac{\langle B^2_{\rm tor}\rangle}{\langle B^2_{\rm pol}\rangle}$ $\ell = 1$ and 2 during the maximum and minimum phase are well recovered. However, ZDI recovers less toroidal magnetic energy for the quadrupolar mode, so that the toroidal energy is not dominant during the increasing phase.

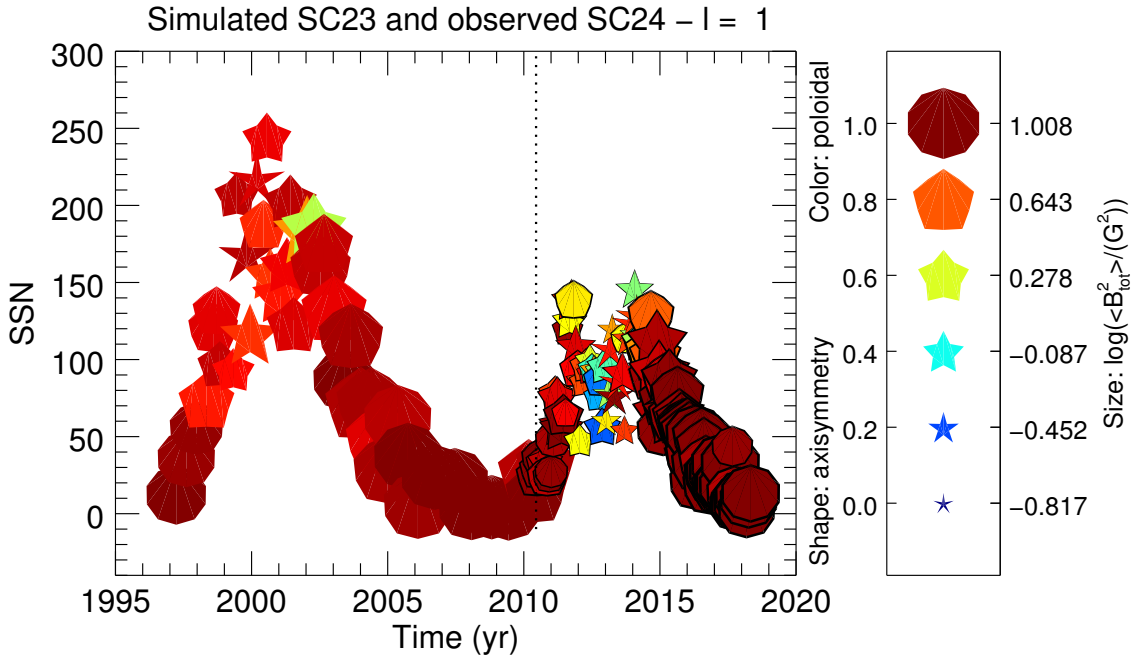

a.

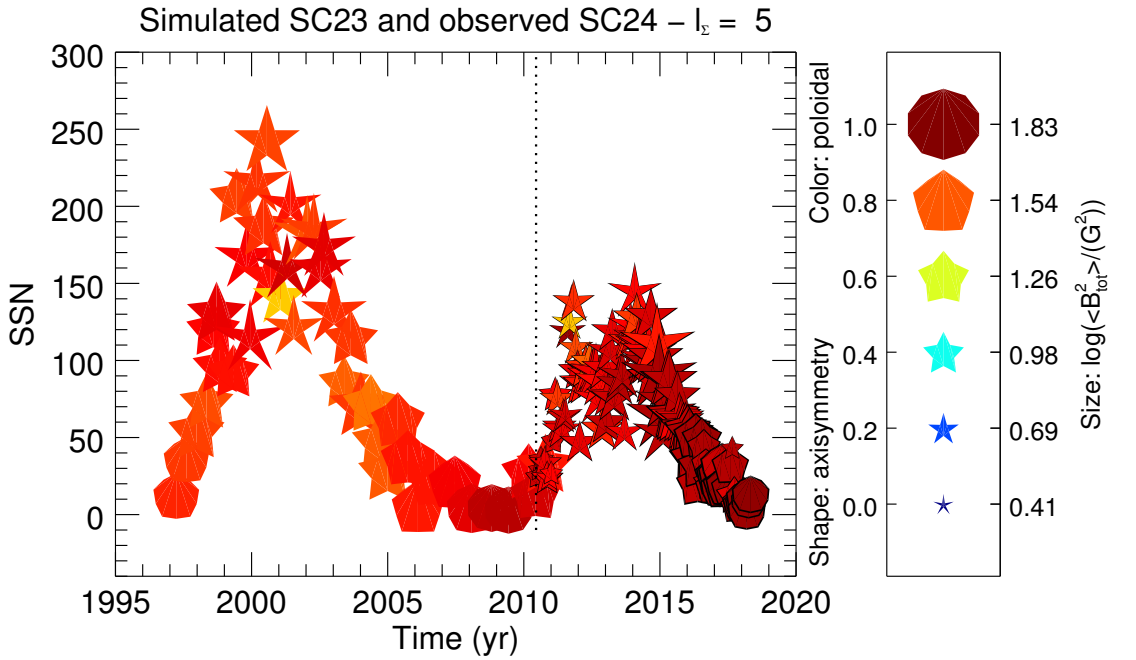

b.

Figure 5.18: The large-scale field magnetic field topology for the 41 simulated maps (open symbols) together with the observed sample of solar cycle 24 (black ringed symbols) presented by Vidotto et al. (2018): **a.** presents the dipolar mode $\ell = 1$ and **b.** the cumulative $\ell_\Sigma = 5$ mode. The dashed line separates the two data sets. The same format as in Fig. 5.7 is used with the exception that the symbol shape indicates the fraction of the axisymmetric field $f_{\rm axi}$. See also legend on the right.

5.3.3 Comparison with the observed of solar cycle 24

I was second author of the paper Vidotto et al. (2018), where we analysed observations of the solar cycle 24 (SC24) from 2010 to 2018. Here I want to compare some of the results with the simulations of the previous solar cycle 23 (SC23). We have a small overlap of a few maps for six months in 2010.

Figure 5.18 compares the large-scale magnetic field topology for both solar cycles using the format of Fig. 5.7. From Fig. 1.7 we already know that SC23 reaches a higher number of sunspots and that SC23 shows also higher magnetic energies for $\ell = 1$ and 2, see fig. 4 in DeRosa et al. (2012). I can confirm that the simulations for SC23 show higher magnetic energy values for the dipolar mode[6]. With each ℓ_Σ-mode the difference gets smaller until it is nearly equal for $\ell_\Sigma = 5$ with $\langle B^2_{\mathrm{tot},\ell_\Sigma=7}\rangle = 66.91\,\mathrm{G}^2$ for SC23 and $\langle B^2_{\mathrm{tot},\ell_\Sigma=7}\rangle = 61.85\,\mathrm{G}^2$ for SC24. Both solar cycles show a double peak during the activity maximum and the long and very quiet activity minimum of 2008–2010 is included. Most obvious is that the dipolar mode for SC24 shows much lower poloidal fractions than for SC23 during the maximum phase, see Fig. 5.18a. The dipolar mode is toroidal ($f_{\mathrm{tor}} = 1 - f_{\mathrm{pol}}$) dominated for several maps. For $\ell_\Sigma = 5$ the poloidal fraction is nearly equal again for the two solar cycles. SC24 shows even higher values for f_{pol} during the decreasing phase. SC24 seems to show slightly lower values for the axisymmetric fraction especially during the maximum phase. From only two cycles one cannot tell if they typical cycles or not. It is also difficult as we are comparing simulations with observations, see also discussion in the last paragraph of this Section.

Vidotto et al. (2018), figure 7, analyses the evolution of the poloidal and axisymmetric fraction and of the poloidal, axisymmetric, toroidal and total magnetic energy with SSN. I analysed the 118 simulated maps of solar cycle 23 (filled symbols) and their ZDI reconstructions (empty symbols) in the same manner, see Figure 5.19. I relate the first 40 maps and last ten maps (1996.61–2001.42 and 2009.80–2011.04) to the rising sample (black circles and pentagons) and the other maps to the decaying sample (red squares) similar to Vidotto et al. (2018). As Vidotto et al. (2018) and I used slightly different definitions of the SSN, I reproduced their data using my SSN definition[7] used here in Figure 5.20. This allows a direct

[5] Usually sunspots dominate at one hemisphere which gives the sign of the toroidal dipolar mode.

[6] The maximum of the dipolar total magnetic energy for SC23 is $\langle B^2_{\mathrm{tot},\ell=1}\rangle = 10.18\,\mathrm{G}^2$ and for SC24 $\langle B^2_{\mathrm{tot},\ell=1}\rangle = 3.35\,\mathrm{G}^2$.

[7] I used the monthly mean total sunspot number, while Vidotto et al. (2018) uses the monthly smoothed sunspot number.

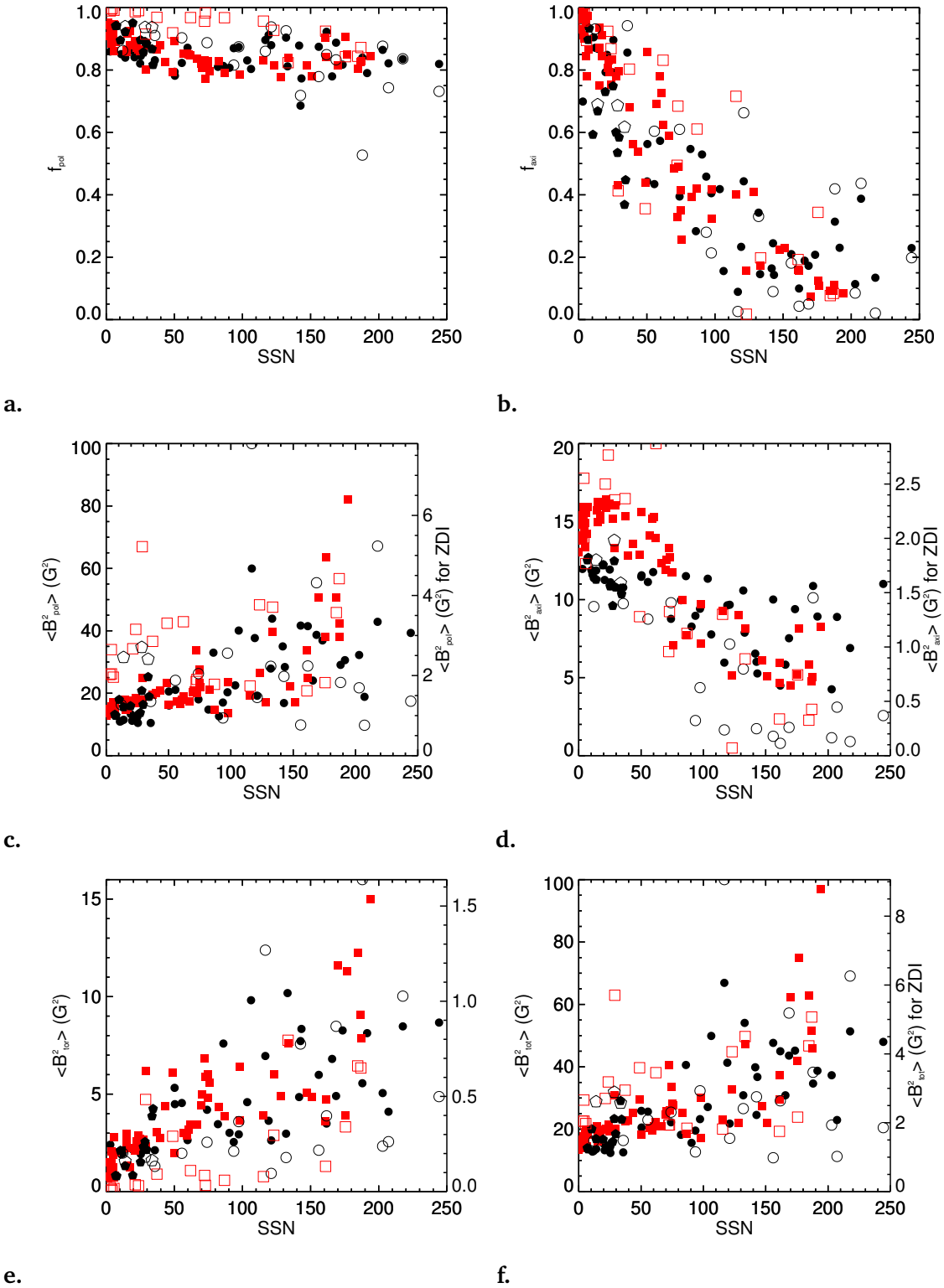

Figure 5.19: I compare the rising (black symbols) and decaying sample (red symbols) for different fractions and energies against sunspot number (SSN). The filled symbols indicate the simulations (left y-axis) and the empty symbols the ZDI reconstructed maps (right y-axis) for solar cycle 23. I show **a.** the poloidal $f_{\rm pol}$ and **b.** axisymmetric fraction $f_{\rm axi}$, **c.** the poloidal $\langle B^2_{\rm pol}\rangle$, **d.** axisymmetric $\langle B^2_{\rm axi}\rangle$, **e.** toroidal $\langle B^2_{\rm tor}\rangle$ and **f.** total magnetic energy $\langle B^2_{\rm tot}\rangle$.

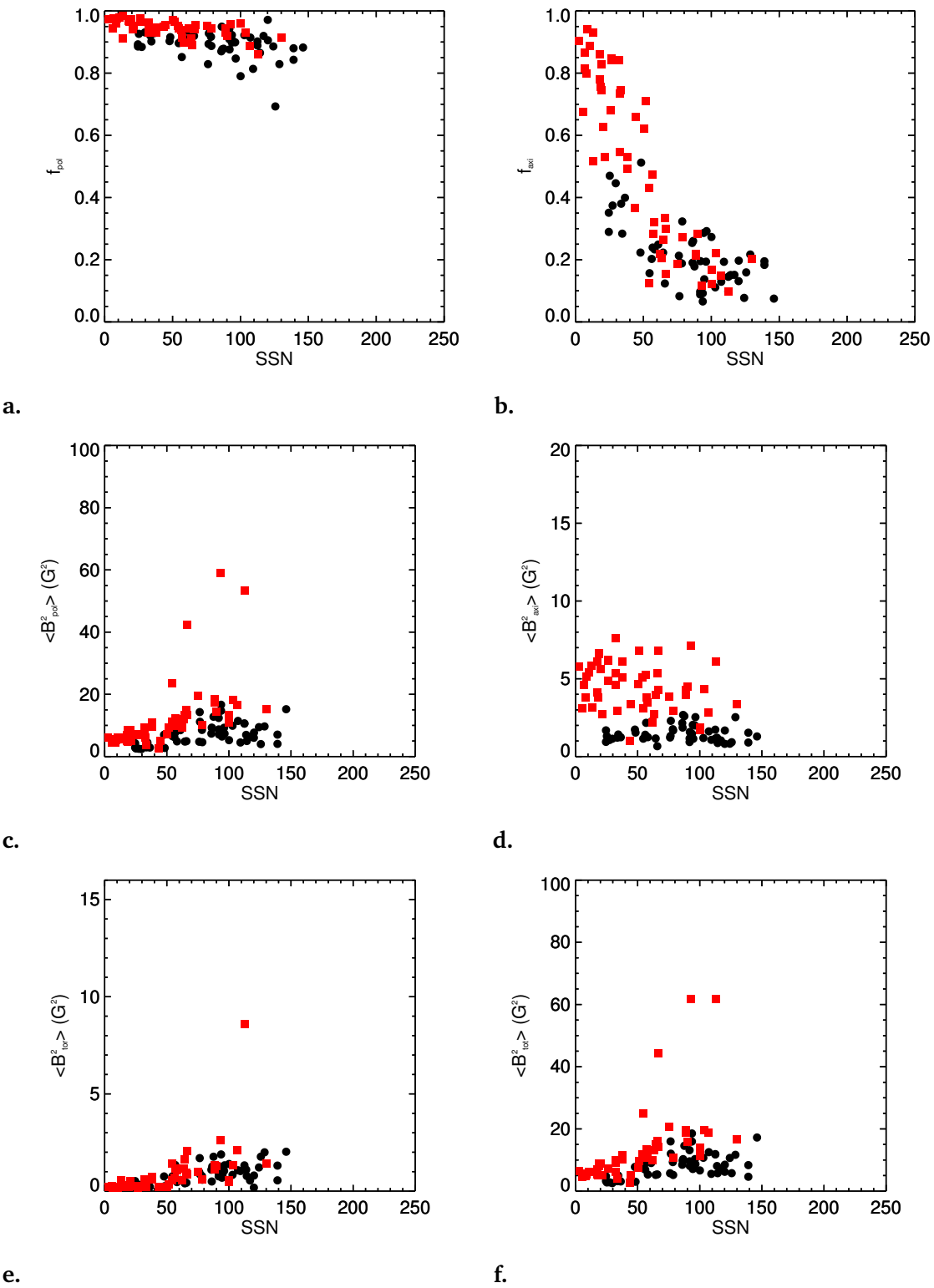

Figure 5.20: Comparing the rising (black symbols) and decaying sample (red symbols) for the solar cycle 24. This figure reproduces figure 7 of Vidotto et al. (2018) with the definition of SSN used here for a direct comparison with solar cycle 23 in Fig. 5.19.

comparison of the two cycles.

Most obvious again is that SC23 obtains higher SSN and magnetic energies than SC24. The differences between the rising and decaying sample are not seen for SC23 with exception of the axisymmetric magnetic energy $\langle B^2_{\rm axi}\rangle$, see Fig. 5.19d and Fig. 5.20d. Both cycles show here that $\langle B^2_{\rm axi}\rangle$ is higher for the decaying sample for SSN < 100. The reversed global axisymmetric dipole is already very strong for low SSN during the decreasing phase. SC23 shows this trend less well than SC24, but there is no clear separation for $f_{\rm axi}$ and the other plotted variables for SC23. The shallow decay of $f_{\rm pol}$ and strong decay of $f_{\rm axi}$ with SSN is seen for both cycles, see Fig. 5.19a,b and Fig. 5.20a,b. The simulations of SC23 show higher values for the magnetic energy parameters, see Fig. 5.19c,d,e,f and Fig. 5.20c,d,e,f. The energy values for low SSN are approximately $10\,\mathrm{G}^2$ higher for SC23 and SC23 shows a wider spread and higher maximum values as well. The ZDI reconstructed maps recover the trends with SSN although showing a higher spread and again much lower magnetic energy values, see Fig. 5.19.

It is hard to drive reliable conclusions as we are comparing simulation (SC23) with observations (SC24) and knowing that the solar cycles differ in SSN and magnetic energy. This includes the danger of seeing and analysing the differences between simulations and observations as differences between the two cycles. However, I proved that the simulations do a very good job of representing the observations, see e.g. Chapter 3 and Fig. 5.10a. Also the splitting between the decaying and rising sample is debatable as it was done by hand. If I assume that the differences between SC23 and SC24 are real, it could be that the different behaviour of the rising and decaying phase for SC24 is due to the long activity minimum between 2008–2010. This caused an unusually strong dipolar toroidal mode (see Fig. 5.18) and a less axisymmetric increasing phase, which is in agreement with Janardhan et al. (2018). However, both cycles show that the poloidal fraction decreases slightly with SSN and the axisymmetric fraction decreases strongly with SSN, which shows once more that $f_{\rm axi}$ is a good parameter to analyse solar cycles.

5.4 Conclusion and summary

To detect a solar-like cycle via ZDI is challenging but most likely to be possible. Most challenging is to get enough successful observations covering the long time range of the activity cycle with high enough S/N. If we are looking at slightly more active stars than the Sun it will be

much easier. The analysis of the axisymmetric and non-axisymmetric magnetic energy over time is very promising to detect solar-like cycles as both parameters show well distinguished and anti-phase trends. Of course $\langle B^2_{\rm axi}\rangle = 1 - \langle B^2_{\rm nax}\rangle$ but is a good start to check both as they have different parameter ranges (the non-axisymmetric field covers two orders of magnitudes more than the axisymmetric field). A second but closely-related parameter is the fraction of poloidal axisymmetric field. This parameter is one of the best recoverable parameters via ZDI and shows a clear trend over time covering nearly the whole range from 0.0 to 1.0, which makes it probably the best tracer for solar-like cycles. To confirm the detection of the activity maximum, one should check if the maximum of the toroidal field fraction $f_{\rm tor}$ appears at the same time.

In the following I summarise the main points and conclusions:

- The 3D non-potential surface magnetic field simulations of Yeates & Mackay (2012) reproduce the SC23 very well and are in agreement with other cool stars magnetic topology observations.

- The amplitude of the Stokes V profiles varies along the cycle and is lowest around activity maximum due to flux cancellation. The ZDI reconstructed maps are therefore most affected by noise during the phase of high SSN.

- ZDI reconstructs best for SSN < 100. ZDI tends to underestimate poloidal and axisymmetric poloidal fractions by a few percent for high SSN.

- The surface averaged magnetic field $\langle B_{\ell_\Sigma=5}\rangle$ increases linearly with SSN for the simulations but ZDI is blind to this trend. The ZDI reconstructed maps show a consistent range of $\langle B_{\ell_\Sigma=5}\rangle = 0.8 - 2.4\,$G against SSN.

- ZDI recovers approximately one order of magnitude less toroidal and poloidal magnetic energy of the large-scale field but recovers their trends with SSN.

- With decreasing SSN the large-scale toroidal magnetic energy decreases as well while the large-scale poloidal energy shows a lower limit for SSN < 50 most likely given by the global dipolar field. The large-scale toroidal field seems to be driven to a significant proportion by small-scale magnetic field structures like active regions as the toroidal energy increases with SSN.

- The higher the SSN the lower the fraction of axisymmetric field, which is very well recovered by ZDI.
- The best tracer for solar-like cycles is the fraction of the axisymmetric poloidal field or to analyse the evolution of the axisymmetric and non-axisymmetric magnetic energy over time. The total magnetic energy $\langle B^2_{\rm tot} \rangle$ is inappropriate for detecting solar-like cycles or to estimate cycle phases.
- The analysis of the ratio between the toroidal and poloidal magnetic energy for the single ℓ-modes $\ell = 1, 2$ gives hints of the interplay between the global dipolar field and the small-scale flux emergence pattern for stars similar to the Sun.
- For both solar cycles 23 and 24 the fraction of poloidal field shallowly decreases with SSN while the fraction of axisymmetric field strongly decreases with SSN, which is recovered by ZDI for SC23.
- SC24 shows a much higher toroidal dipolar mode during the increasing phase compared to SC23. This could be a result of the unusually long minimum phase between the cycles and the following asymmetric polar field reversal.
- The differences between the rising and decaying sample for SC24 shown by Vidotto et al. (2018) could not be confirmed for SC23 with the exception of the higher axisymmetric energy for the decaying sample for low SSN.

6

Conclusions and outlook

In this thesis I investigated the magnetic field topology of solar-like stars by connecting non-potential flux transport simulations with the observational technique of the Zeeman-Doppler-Imaging. I started with the analysis of the large- and small-scale magnetic field topology of solar-based 3D non-potential flux transport simulations under varying flux emergence, differential rotation and meridional flow rates. In the next step, I 'observed' the simulations by modelling Stokes IV time series and applying the ZDI technique onto them, which allows me to perfectly reflect, what ZDI is and is not able to observe. Finally, I examine if and how the ZDI technique would observe solar-like activity cycles using again flux transport simulations covering now 15 years of the solar cycle 23 and 24.

I review and conclude my main results and set them in context to each other in Section 6.1 followed by a short outlook in Section 6.2.

6.1 Connecting simulations and observations for solar-like stars

In the beginning of my thesis I asked: What can we learn from the large-scale field topology about the small-scale field distribution and how are they linked for solar-like stars? The following results start to answer these questions and some more.

First of all, I showed that the photospheric large-scale field of the solar-based non-potential flux transport simulations, (Gibb et al., 2016; Yeates & Mackay, 2012), fits very well the topology of observed solar-type stars. The spherical harmonic decomposition, (Vidotto, 2016), allows the analysis of the magnetic field topology regarding different length scales given by the ℓ and m modes of the spherical harmonics.

I discovered that the large-scale field of the simulations is dominated by the behaviour of the axisymmetric poloidal dipolar mode and the axisymmetric toroidal quadrupolar mode. The dipolar mode reflects the global stellar dipole field and the quadrupolar mode the global properties of the small-scale flux emergence at the active latitudes for solar-like stars. The small-scale flux emerges at mid to low latitudes showing the opposite polarity at the different hemispheres. This solar flux emergence pattern is best captured by the axisymmetric toroidal quadrupolar mode. I showed that with increasing flux emergence rate the quadrupolar mode becomes stronger and more toroidal reflecting the higher population of active latitudes.

Furthermore, I investigated the effects of the differential rotation and meridional flow onto the magnetic field topology. An increased differential rotation causes a decrease of the poloidal energy across all ℓ-modes and enhances the axisymmetry of the field. The higher differential rotation stretches the active regions (bipoles) and enlarges the region where the radial/poloidal component of the two spots with opposite polarity cancel, while the azimuthal/toroidal component remains or slightly increases. A higher differential rotation increases therefore the toroidal and azimuthal energy fraction.

The meridional flow causes a more complex change to the magnetic field topology: the axisymmetric toroidal fraction of the dipolar mode decreases and the even low toroidal modes ($\ell = 2, 4, 6, \ldots$) are enhanced. Both effects result from the transport of the active regions towards higher latitudes. The higher located active latitudes are best represented by the combination of several even axisymmetric toroidal modes, which form two toroidal rings of opposite polarity at high latitudes. The equatorial region is then nearly empty and causes the decrease

of $f_{\mathrm{tor,axi}}$ for the dipolar mode. The changes of the magnetic topology for higher meridional flow strongly demonstrates that the large-scale field topology reflects the global properties of small-scale flux emergence pattern.

The next questions to answer is: How much of the large-scale field is robustly observed with the Zeeman-Doppler-Imaging technique and how do we interpret the resulting magnetic field maps for solar-like stars? The highly resolved non-potential flux transport simulations are the perfect data set to benchmark ZDI as their large- and small-scale field topology is known in great detail and fits the observations. First, I visually showed that the Stokes V profiles of slow rotators are literally blind for small-scale field structures and that the coefficients of the magnetic field description needs to be freely fitted to the Stokes profiles to guarantee the correct reconstruction of the azimuthal and meridional field for solar-like stars in any case.

I found that ZDI does a good job in reconstructing the large-scale field topology ($\ell_{\Sigma} = 3{-}5$) but recovers approximately one order of magnitude less magnetic energy. The axisymmetric poloidal energy fraction is the best recovered magnetic field parameter. Only $6 - 17\,\%$ of the total averaged magnetic field is captured by ZDI, which is in line with previous analyses. Comparing the two inclination angles 60° and 20°, the more equator-on inclination (60°) provide the better results. For slow rotating stars with a solar flux emergence pattern, the axisymmetric and toroidal fraction (due to a lack of poloidal energy) is overestimated for lower inclination angles. The power law relation between the toroidal and poloidal energy with stellar activity is well recovered by ZDI. The more active the star, the higher the axisymmetric and toroidal fraction. Keep in mind that the trends with inclination and activity are only evaluated for slow rotating stars with solar flux emergence pattern.

In general, one needs to be aware of the following points when interpreting ZDI maps: Using a ZDI code in connection with the maximum entropy regularisation very likely underestimates the magnetic energy for solar-like stars. The Stokes V profiles can be equally well fitted with a range of magnetic energy values and the maximum entropy ansatz chooses the lowest possible one. Further, the maximum entropy prevents the detection of the correct energy distribution. Each magnetic field topology can be described by an infinite number of magnetic energy distributions as this is an ill-posed problem. The maximum entropy regularisation finds the simplest one and tries to put as much energy as possible into the lowest ℓ-modes enable to recover the original distribution. Surprisingly, I discovered that ZDI is able to recover the

distribution of the different energy fractions across the ℓ-modes mostly within a 20 % error for solar-like stars. This is very encouraging for dynamo theorists. They can trust better the observed energy fractions by comparing their dynamo models to the observations and improve our understanding of the stellar magnetic field generation. In addition, one needs to be aware of the obscuration effects due to the inclination angle by interpreting ZDI maps.

Another astonishing result is that ZDI is able to recover the global properties of the small-scale flux emergence pattern for solar-type stars under very good observing conditions. I showed that ZDI recovers the signature of the active latitudes for stars five times more active than our Sun (in terms of differential rotation and flux emergence rate). This raises the question if other striking signatures (e.g., toroidal rings for faster rotating stars) also point to active latitude phenomena. To answer these questions further stellar models needs to be analysed.

In the last step, I examined if and how ZDI observes the solar large-scale field variations over 15 years covering solar cycle 23 and the beginning of solar cycle 24. I used the non-potential flux transport simulations modelling the solar magnetic field evolution from 1996–2011 of Yeates & Mackay (2012).

I discovered that the Stokes V profiles show the lowest amplitudes and are most affected by noise during the activity maximum. ZDI recovers the large-scale magnetic field topologies best for sunspot numbers (SSN) below 100. The reconstructed magnetic energy is again one order of magnitude too low but ZDI captures the trends of the poloidal and toroidal energy with SSN. The poloidal energy of the large-scale field shows a lower limit for SSN < 50, which is most likely given by the global dipolar field. The toroidal energy of the large-scale field increases with SSN, which is another strong hint that the large-scale toroidal field is driven by the small-scale flux emergence. I further showed that the dipolar and quadrupolar mode reflect the interplay between the dipolar field and the global properties of the small-scale flux emergence along the solar cycle. ZDI seems just to be able to recover these trends under top conditions. To get enough high S/N observations over the long rotational and cycle period will be most challenging for the detection of solar activity cycles. Selecting targets slightly more active than our Sun will make the detection of solar activity cycles much easier.

My results suggest that the best strategy to trace solar activity cycles is to go for the axisymmetric poloidal energy fraction or the axi- and non-axisymmetric energy. These parameters are

well recovered by ZDI and show decently distinguished trends with time covering a good fraction of the parameter range, respectively. In addition, the detection of the activity maximum can be confirmed by maximum of the toroidal energy fraction. The averaged large-scale magnetic field or the total magnetic energy are not able to uncover solar-like cycles. ZDI observes these parameters with no to little variations over time or they even show misleading trends. These results will help to interpret the ZDI observed stellar activity cycles for solar-type stars, which currently become more and more available (e.g., Boro Saikia et al. 2018), and to find a true second Sun.

All in all, I showed that the global properties of the small-scale flux emergence, i.e., preferable emergence region and polarity pattern, affect the large-scale field and are most likely detectable for solar-like stars with ZDI. However, this is very challenging for stars similar to our Sun, but for stars that are a few times more active, the likelihood to detect remarkable signatures of the small-scale in the large-scale field significantly increases. Even the tracing of solar-like activity cycles seems to be possible. Under the consideration of the ZDI limitations and an improved knowledge about the stellar flux emergence patterns, the interpretation of observed stellar magnetic field maps appears in a new light and closes the circle to stellar dynamo simulations.

6.2 Outlook

ZDI detections of cool stars magnetic field topologies as well as dynamo and flux transport simulations widely improved our knowledge and understanding of stellar magnetic fields in the last decades. There are still open questions like the coexistence of two contrary topologies for fully convective M dwarfs or the origin of toroidal rings for faster rotating F, G and K stars.

My discovery, that the large-scale field can reflect the global properties of the small-scale flux emergence for solar-like stars, raises the question if the observed toroidal rings are signatures of active latitudes, too. Unfortunately, the stellar properties of the simulations used here are far from representing the magnetic field topologies of stars with toroidal rings (e.g., in terms of large-scale magnetic energy and rotation period). Further, it is remarkable that the higher cumulative ℓ_Σ-modes show a similar power law relation between the toroidal and poloidal energy to the M dwarfs. This might suggest that M dwarfs are covered with randomly distributed small-scale field structures. Both theories need to be tested with further

simulations representing the corresponding star types.

Furthermore, the benchmarking tests of the ZDI technique presented here need to be continued to avoid misinterpretations of the observed magnetic field topologies. I plan to examine the effect of varying S/N and phase gaps as well as to determine how much the magnetic field maps are affected by fast (on time scales shorter than one stellar rotation) evolving surface magnetic fields.

I would also advise to compare the different ZDI codes currently in use to prove if a given Stokes IV time series results in similar magnetic field topologies. In addition, the effects of different regularisation methods for the ZDI codes, e.g., on the magnetic energy distributions, would be good to check.

The research about cool star magnetic field topologies looks towards exciting times. The ZDI surveys start to run long enough to detect stellar activity cycles in the time range of our 11 year solar cycle. This will improve our understanding of stellar activity cycles in general as well as of our own solar activity cycle. It will also help to find not only a second Sun but also a second Earth as the signal of earth-mass planets in the habitable zones around a solar-like stars is similar the signal of the host star's activity, (Haywood et al., 2014; Klein & Donati, 2019). A good knowledge about the host star is therefore essential.

Bibliography

Afram N., Berdyugina S. V., Fluri D. M., Semel M., Bianda M., Ramelli R., 2007, A&A, 473, L1

Altschuler M. D., Newkirk G., 1969, Solar Physics, 9, 131

Alvarado-Gómez J. D., et al., 2015a, A&A, 582, A38

Alvarado-Gómez J. D., et al., 2015b, A&A, 582, A38

Arzoumanian D., Jardine M., Donati J.-F., Morin J., Johnstone C., 2011, MNRAS, 410, 2472

Babcock H. W., 1947, ApJ, 105, 105

Babcock H. W., 1961, ApJ, 133, 572

Babcock H. W., Babcock H. D., 1955, ApJ, 121, 349

Baklanova D., Plachinda S., 2015, Adv. Space Res., 55, 817

Baliunas S. L., et al., 1995, ApJ, 438, 269

Barnes J. R., Collier Cameron A., Donati J.-F., James D. J., Marsden S. C., Petit P., 2005, MNRAS, 357, L1

Barrera R. G., Estevez G. A., Giraldo J., 1985, European Journal of Physics, 6, 287

Baumann I., Schmitt D., Schüssler M., Solanki S. K., 2004, A&A, 426, 1075

Beckers J. M., 1969, A table of Zeeman Multiplets. Sacramento: Peak Observatory and Air Force Cambridge Research Laboratories

Berdyugina S. V., 2005, Living Rev Sol. Phys, 2, 8

Berdyugina S. V., 2009, in Strassmeier K. G., Kosovichev A. G., Beckman J. E., eds, IAU Symposium Vol. 259, Cosmic Magnetic Fields: From Planets, to Stars and Galaxies. pp 323–332, doi:10.1017/S1743921309030683

Berdyugina S. V., Usoskin I. G., 2003, A&A, 405, 1121

Berdyugina S. V., Frutiger C., Solanki S. K., Livingstone W., 2000, A&A, 364, L101

Berdyugina S. V., Fluri D. M., Afram N., Suwald F., Petit P., Arnaud J., Harrington D. M., Kuhn J. R., 2008, in van Belle G., ed., Astronomical Society of the Pacific Conference Series Vol. 384, 14th Cambridge Workshop on Cool Stars, Stellar Systems, and the Sun. p. 175 (arXiv:astro-ph/0703559)

Böhm-Vitense E., 2007, ApJ, 657, 486

Boro Saikia S., Jeffers S. V., Petit P., Marsden S., Morin J., Folsom C. P., 2015, A&A, 573, A17

Boro Saikia S., et al., 2016, A&A, 594, A29

Boro Saikia S., et al., 2018, A&A, 620, L11

Brandenburg A., 2005, ApJ, 625, 539

Brandenburg A., Saar S. H., Turpin C. R., 1998, ApJ, 498, L51

Brown B. P., Miesch M. S., Browning M. K., Brun A. S., Toomre J., 2011, Astrophys. J., 731, 69

Cameron R. H., Jiang J., Schmitt D., Schüssler M., 2010, ApJ, 719, 264

Carrascal B., Estevez G. A., Lee P., Lorenzo V., 1991, European Journal of Physics, 12, 184

Carrington R. C., 1858, MNRAS, 19, 1

Carroll T. A., Strassmeier K. G., Rice J. B., Künstler A., 2012, A&A, 548, A95

Chabrier G., Küker M., 2006, A&A, 446, 1027

Chandrasekhar S., 1961, Hydrodynamic and Hydromagnetic Stability. International Series of Monographs on Physics, Oxford: Clarendon

Collier Cameron A., 2007, Astronomische Nachrichten, 328, 1030

DeRosa M. L., Brun A. S., Hoeksema J. T., 2012, ApJ, 757, 96

DeVore C. R., Sheeley Jr. N. R., Boris J. P., Young Jr. T. R., Harvey K. L., 1985, Sol. Phys., 102, 41

Deutsch A. J., 1958, in Lehnert B., ed., IAU Symposium Vol. 6, Electromagnetic Phenomena in Cosmical Physics. p. 209

Donahue R. A., Saar S. H., Baliunas S. L., 1996, ApJ, 466, 384

Donati J.-F., 2010, Proc. Int. Astron. Union, 6, 23

Donati J.-F., Brown S. F., 1997, A&A, 326, 1135

Donati J.-F., Collier Cameron A., 1997, MNRAS, 291, 1

Donati J.-F., Landstreet J., 2009, Annu. Rev. Astron. Astrophys., 47, 333

Donati J. F., Semel M., Praderie F., 1989, A&A, 225, 467

Donati J. F., Brown S. F., Semel M., Rees D. E., Dempsey R. C., Matthews J. M., Henry G. W., Hall D. S., 1992, A&A, 265, 682

Donati J.-F., Semel M., Carter B. D., Rees D. E., Collier Cameron A., 1997, MNRAS, 291, 658

Donati J.-F., et al., 2003, MNRAS, 345, 1145

Donati J.-F., Forveille T., Collier Cameron A., Barnes J. R., Delfosse X., Jardine M. M., Valenti J. A., 2006a, Science, 311, 633

Donati J.-F., et al., 2006b, MNRAS, 370, 629

Donati J.-F., et al., 2008a, MNRAS, 385, 1179

Donati J.-F., et al., 2008b, MNRAS, 390, 545

Donati J.-F., et al., 2011, MNRAS, 417, 472

Dunstone N. J., Hussain G. A. J., Collier Cameron A., Marsden S. C., Jardine M., Stempels H. C., Ramirez Velez J. C., Donati J.-F., 2008, MNRAS, 387, 481

Elsasser W. M., 1946, Physical Review, 69, 106

Fares R., et al., 2009, MNRAS, 398, 1383

Fares R., et al., 2010, MNRAS, 406, 409

Fares R., et al., 2012, MNRAS, 423, 1006

Fares R., Moutou C., Donati J.-F., Catala C., Shkolnik E. L., Jardine M. M., Cameron A. C., Deleuil M., 2013, MNRAS, 435, 1451

Farrish A. O., Alexander D., Maruo M., DeRosa M., Toffoletto F., Sciola A. M., 2019, ApJ, 885, 51

Finley A. J., Matt S. P., See V., 2018, ApJ, 864, 125

Finley A. J., See V., Matt S. P., 2019, ApJ, 876, 44

Folsom C. P., et al., 2016, MNRAS, 457, 580

Folsom C. P., et al., 2018, MNRAS, 474, 4956

Frick P., Soon W., Popova E., Baliunas S., 2004, New Astron., 9, 599

Gastine T., Wicht J., 2012, Icarus, 219, 428

Gibb G. P. S., Jardine M. M., Mackay D. H., 2014, MNRAS, 443, 3251

Gibb G. P. S., Mackay D. H., Jardine M. M., Yeates A. R., 2016, MNRAS, 456, 3624

Gleissberg W., 1958, Z. Astrophys., 46, 219

Güdel M., 2007, Living Reviews in Solar Physics, 4

Hale G. E., 1908, ApJ, 28, 315

Hale G. E., Ellerman F., Nicholson S. B., Joy A. H., 1919, ApJ, 49, 153

Hartmann L. W., Noyes R. W., 1987, Annual Review of Astronomy and Astrophysics, 25, 271

Haywood R. D., et al., 2014, MNRAS, 443, 2517

Hébrard É. M., Donati J.-F., Delfosse X., Morin J., Moutou C., Boisse I., 2016, MNRAS, 461, 1465

Hill C. A., Carmona A., Donati J. F., Hussain G. A. J., Gregory S. G., Alencar S. H. P., Bouvier J., Matysse Collaboration 2017, MNRAS, 472, 1716

Hill C. A., Folsom C. P., Donati J. F., Herczeg G. J., Hussain G. A. J., Alencar S. H. P., Gregory S. G., Matysse Collaboration 2019, MNRAS, 484, 5810

Hoeksema J. T., et al., 2014, Sol. Phys., 289, 3483

Hussain G. a. J., 2004, Astron. Nachr., 325, 216

Hussain G. A. J., Donati J.-F., Collier Cameron A., Barnes J. R., 2000, MNRAS, 318, 961

Hussain G. A. J., Jardine M., Collier Cameron A., 2001, MNRAS, 322, 681

Hussain G. A. J., van Ballegooijen A. A., Jardine M., Collier Cameron A., 2002, ApJ, 575, 1078

Hussain G. A. J., et al., 2016, A&A, 585, A77

Işık E., Schmitt D., Schüssler M., 2011, A&A, 528, A135

Janardhan P., Fujiki K., Ingale M., Bisoi S. K., Rout D., 2018, A&A, 618, A148

Jardine M., Vidotto A. A., van Ballegooijen A., Donati J.-F., Morin J., Fares R., Gombosi T. I., 2013, MNRAS, 431, 528

Jeffers S. V., Petit P., Marsden S. C., Morin J., Donati J.-F., Folsom C. P., 2014, A&A, 569, A79

Jeffers S. V., et al., 2018, MNRAS, 479, 5266

Jetsu L., Pelt J., Tuominen I., Nations H., 1991, The spot activity of FK Comae Berenices. Springer-Verlag, Berlin, Germany; New York, NY, p. 381, doi:10.1007/3-540-53955-7_161

Jiang J., Cameron R. H., Schmitt D., Schüssler M., 2013a, Space Sci. Rev., 176, 289

Jiang J., Cameron R. H., Schmitt D., Işık E., 2013b, A&A, 553, A128

Johnstone C. P., 2012, Phd thesis, University of St Andrews

Johnstone C., Jardine M., Mackay D. H., 2010, MNRAS, 404, 101

Johnstone C. P., Jardine M., Gregory S. G., Donati J.-F., Hussain G., 2014, MNRAS, 437, 3202

Kakad B., Kakad A., Ramesh D. S., Lakhina G. S., 2019, Journal of Space Weather and Space Climate, 9, A1

Karak B. B., Miesch M., 2017, ApJ, 847, 69

Keller C. U., Harvey J. W., Giampapa M. S., 2003, in Keil S. L., Avakyan S. V., eds, Proc. SPIEVol. 4853, Innovative Telescopes and Instrumentation for Solar Astrophysics. pp 194–204, doi:10.1117/12.460373

Kitchatinov L. L., Olemskoy S. V., 2011, MNRAS, 411, 1059

Klein B., Donati J. F., 2019, MNRAS, 488, 5114

Kochukhov O., 2015, A&A, 580, A39

Kochukhov O., Bagnulo S., Wade G. A., Sangalli L., Piskunov N., Landstreet J. D., Petit P., Sigut T. A. A., 2004, A&A, 414, 613

Kochukhov O., et al., 2017, Astronomische Nachrichten, 338, 428

Konstantinova-Antova R., et al., 2010, A&A, 524, A57

Korhonen H., Berdyugina S. V., Strassmeier K. G., Tuominen I., 2001, A&A, 379, L30

Küker M., Rüdiger G., 2011, Astronomische Nachrichten, 332, 933

Lang P., Jardine M., Morin J., Donati J.-F., Jeffers S., Vidotto A. A., Fares R., 2014, MNRAS, 439, 2122

Larmor J., 1919, Rep Brit Assoc Adv Sci, 159, 412

Lehmann L. T., 2013, Bachelor thesis, Universität Potsdam

Lehmann L. T., 2015, Master thesis, Universität Potsdam

Lehmann L. T., Künstler A., Carroll T. A., Strassmeier K. G., 2015, Astron. Nachrichten, 336, 258

Lehmann L. T., et al., 2017, MNRAS, 466, L24

Lehmann L. T., Jardine M. M., Mackay D. H., Vidotto A. A., 2018, MNRAS, 478, 4390

Lehmann L. T., Hussain G. A. J., Jardine M. M., Mackay D. H., Vidotto A. A., 2019, MNRAS, 483, 5246

Lehtinen J., Jetsu L., Hackman T., Kajatkari P., Henry G. W., 2016, A&A, 588, A38

Leighton R. B., 1964, ApJ, 140, 1547

Leighton R. B., 1969, ApJ, 156, 1

Livshits I. M., Obridko V. N., 2006, Astronomy Reports, 50, 926

Llama J., Jardine M., Mackay D. H., Fares R., 2012, MNRAS, 422, L72

Lockwood G. W., Radick R. R., Henry G. W., Baliunas S. L., 2004, in American Astronomical Society Meeting Abstracts #204. p. 03.04

Lockwood G. W., Skiff B. A., Henry G. W., Henry S., Radick R. R., Baliunas S. L., Donahue R. A., Soon W., 2007, ApJS, 171, 260

Mackay D., Yeates A., 2012, Living Reviews in Solar Physics, 9

Mackay D. H., van Ballegooijen A. A., 2001, ApJ, 560, 445

Mackay D. H., van Ballegooijen A. A., 2006, ApJ, 641, 577

Mackay D. H., Jardine M., Collier Cameron A., Donati J.-F., Hussain G. A. J., 2004, MNRAS, 354, 737

Mancuso S., Garzelli M. V., 2007, A&A, 466, L5

Marsden S. C., Mengel M. W., Donati F., Carter B. D., Semel M., Petit P., 2006a, in Casini R., Lites B. W., eds, Astronomical Society of the Pacific Conference Series Vol. 358, Solar Polarization 4. p. 401

Marsden S. C., Donati J.-F., Semel M., Petit P., Carter B. D., 2006b, MNRAS, 370, 468

Marsden S. C., et al., 2011, MNRAS, 413, 1939

Marsden S. C., et al., 2014, MNRAS, 444, 3517

Matt S. P., Brun A. S., Baraffe I., Bouvier J., Chabrier G., 2015, ApJ, 799, L23

Mekkaden M. V., 1985, Ap&SS, 117, 381

Mengel M. W., et al., 2016, MNRAS, 459, 4325

Middelkoop F., 1981, A&A, 101, 295

Miesch M. S., Teweldebirhan K., 2016, Advances in Space Research, 58, 1571

Moon Y.-J., et al., 2007, PASJ, 59, S625

Morgenthaler A., Petit P., Morin J., Aurière M., Dintrans B., Konstantinova-Antova R., Marsden S., 2011, Astronomische Nachrichten, 332, 866

Morgenthaler A., et al., 2012, A&A, 540, A138

Morin J., et al., 2008a, MNRAS, 384, 77

Morin J., et al., 2008b, MNRAS, 390, 567

Morin J., Donati J.-F., Petit P., Delfosse X., Forveille T., Jardine M. M., 2010, MNRAS, 407, 2269

Morris B. M., Hebb L., Davenport J. R. A., Rohn G., Hawley S. L., 2017, ApJ, 846, 99

Moss D., Kitchatinov L. L., Sokoloff D., 2013, A&A, 550, L9

Noyes R. W., Hartmann L. W., Baliunas S. L., Duncan D. K., Vaughan A. H., 1984, ApJ, 279, 763

Oláh K., Strassmeier K. G., Granzer T., Soon W., Baliunas S. L., 2007, Astronomische Nachrichten, 328, 1072

Oláh K., et al., 2009, A&A, 501, 703

Ossendrijver M., 2003, Astronomy and Astrophysics Review, 11, 287

Pallavicini R., Golub L., Rosner R., Vaiana G. S., Ayres T., Linsky J. L., 1981, ApJ, 248, 279

Parker E. N., 1955, ApJ, 122, 293

Pesnell W. D., Thompson B. J., Chamberlin P. C., 2012, Sol. Phys., 275, 3

Petit P., Donati J.-F., Collier Cameron A., 2002, MNRAS, 334, 374

Petit P., et al., 2008, MNRAS, 388, 80

Petit P., Dintrans B., Morgenthaler A., Van Grootel V., Morin J., Lanoux J., Aurière M., Konstantinova-Antova R., 2009, A&A, 508, L9

Phillips K. J. H., 1995, Guide to the Sun. Cambridge, UK: Cambridge University Press

Phillips M. J., Hartmann L., 1978, ApJ, 224, 182

Piskunov N., Kochukhov O., 2002, A&A, 381, 736

Plachinda S., Pankov N., Baklanova D., 2011, Astronomische Nachrichten, 332, 918

Reader J., Sugar J., 1975, Journal of Physical and Chemical Reference Data, 4, 353

Reiners A., 2006, A&A, 446, 267

Reiners A., 2012, Living Reviews in Solar Physics, 9, 1

Reiners A., Basri G., 2006, ApJ, 644, 497

Reiners A., Basri G., 2009, A&A, 496, 787

Rice J. B., 2002, Astronomische Nachrichten, 323, 220

Robinson R. D., Worden S. P., Harvey J. W., 1980, ApJ, 236, L155

Rosén L., Kochukhov O., Wade G. A., 2015, ApJ, 805, 169

Rosén L., Kochukhov O., Hackman T., Lehtinen J., 2016, A&A, 593, A35

Saar S. H., 1988, ApJ, 324, 441

Saar S. H., 1996, in Strassmeier K. G., Linsky J. L., eds, IAU Symposium Vol. 176, Stellar Surface Structure. p. 237

Scalia C., Leone F., Gangi M., Giarrusso M., Stift M. J., 2017, MNRAS, 472, 3554

Schrijver C. J., Liu Y., 2008, Sol. Phys., 252, 19

Schrijver C. J., Title A. M., 2001, ApJ, 551, 1099

Schrijver C. J., Zwaan C., 2000, Solar and Stellar Magnetic Activity. New York : Cambridge University Press

Schrijver C. J., De Rosa M. L., Title A. M., 2002, ApJ, 577, 1006

Schüssler M., Baumann I., 2006, A&A, 459, 945

Schüssler M., Vögler A., 2008, A&A, 481, L5

Schwabe M., 1849, Astronomische Nachrichten, 28, 302

See V., et al., 2015, MNRAS, 453, 4301

See V., et al., 2016, MNRAS, 462, 4442

See V., et al., 2017, MNRAS, 466, 1542

See V., et al., 2019, ApJ, 876, 118

See V., Lehmann L. T., Matt S. P., Finley A. J., 2020, arXiv e-prints, p. arXiv:2002.11774

Semel M., 1989, A&A, 225, 456

Sheeley Neil R. J., 2005, Living Reviews in Solar Physics, 2, 5

Sing D. K., 2010, A&A, 510, A21

Skumanich A., 1972, ApJ, 171, 565

Snodgrass H. B., 1983, ApJ, 270, 288

Spörer F. W. G., 1879, Astronomische Nachrichten, 96, 23

Stenflo J., 1994, in Astrophysics and Space Science Library. , doi:10.1007/978-94-015-8246-9

Stokes G. G., 1852, Annalen der Physik, 163, 480

Strassmeier K. G., 2009, Astron. Astrophys. Rev., 17, 251

Tsvetkova S., et al., 2019, Bulgarian Astronomical Journal, 30, 67

Unno W., 1956, PASJ, 8, 108

Valenti J. A., Marcy G. W., Basri G., 1995, ApJ, 439, 939

Vidotto A. A., 2016, MNRAS, 459, 1533

Vidotto A. A., Jardine M., Morin J., Donati J. F., Lang P., Russell A. J. B., 2013, A&A, 557, A67

Vidotto A. A., et al., 2014, MNRAS, 441, 2361

Vidotto A. A., Lehmann L. T., Jardine M., Pevtsov A. A., 2018, MNRAS, 480, 477

Vogt S. S., Penrod G. D., 1983, PASP, 95, 565

Vogt S. S., Penrod G. D., Hatzes A. P., 1987, ApJ, 321, 496

Wade G. A., Donati J.-F., Landstreet J. D., Shorlin S. L. S., 2000, MNRAS, 313, 823

Waite I. A., Marsden S. C., Carter B. D., Hart R., Donati J.-F., Ramírez Vélez J. C., Semel M., Dunstone N., 2011, MNRAS, 413, 1949

Walter F. M., Bowyer S., 1981, ApJ, 245, 671

Wang Y.-M., Nash A. G., Sheeley Jr. N. R., 1989, Science, 245, 712

Wiegelmann T., Petrie G. J. D., Riley P., 2017, Space Sci. Rev., 210, 249

Wilson O. C., 1968, ApJ, 153, 221

Wright N. J., Drake J. J., Mamajek E. E., Henry G. W., 2011, ApJ, 743, 48

Yadav R. K., Christensen U. R., Morin J., Gastine T., Reiners A., Poppenhaeger K., Wolk S. J., 2015, ApJ, 813, L31

Yang W. H., Sturrock P. A., Antiochos S. K., 1986, ApJ, 309, 383

Yeates A. R., 2014, Sol. Phys., 289, 631

Yeates A. R., Mackay D. H., 2012, ApJ, 753, L34

Yeates A. R., Mackay D. H., van Ballegooijen A. A., 2007, Solar Physics, 245, 87

Yeates A. R., Mackay D. H., van Ballegooijen A. A., 2008, Solar Physics, 247, 103

Zeeman P., 1897, ApJ, 5, 332

do Nascimento J. D., et al., 2014, in Petit P., Jardine M., Spruit H. C., eds, IAU Symposium Vol. 302, Magnetic Fields throughout Stellar Evolution. pp 142–143 (arXiv:1310.7620), doi:10.1017/S1743921314001902

van Ballegooijen A. A., Cranmer S. R., 2008, ApJ, 682, 644

van Ballegooijen A. A., Priest E. R., Mackay D. H., 2000, ApJ, 539, 983